Penn Center *for* Musculoskeletal Disorders

UNIVERSITY *of* PENNSYLVANIA

21st Annual Scientific Symposium/Retreat

Wednesday, November 12, 2025
Smilow Rubenstein Auditorium/Commons
8:00am-6:00pm
www.med.upenn.edu/pcmd/

Table of Contents

We gratefully acknowledge the financial support provided by the National Institute of Arthritis, Musculoskeletal and Skin Diseases of the National Institutes of Health and the University of Pennsylvania, Perelman School of Medicine for our Center.

Penn Center for Musculoskeletal Disorders
Scientific Symposium Agenda
November 12, 2025
Smilow Rubenstein Auditorium ♦ University of Pennsylvania

08:00 – 08:45am **Registration and Poster Set-up**

08:45 – 09:00am **Welcome and Overview**
Louis J. Soslowsky, Ph.D.

09:00 – 10:00am **Session I: New Member Session** (Moderator: Ling Qin, Ph.D.)
- *Julie Engiles, VMD, DACVP, "One-Health Approach to Orthopedic Disease: Translational Applications of Large Animal Veterinary Pathology"*
- *Flavia Vitale, Ph.D., "Engineering Novel High-Density Surface EMG Arrays and Machine Learning Models to Support Diagnosis and Rehabilitation of Achilles Tendon Pathologies."*
- *Christopher Madl, Ph.D., "Probing Biophysical Regulation of Myogenesis with Dynamic Biomaterials."*

10:00 – 10:30am **Session II: Translational Opportunities** (Moderator: Katie Reuther, Ph.D.)
- *Annamarie Horan, Ph.D., "RNA in Peripheral Blood as Prognostic for Fracture Outcome"*
- *Josh Baxter, Ph.D., "Next Generation Nerve Conduction Testing: Turning an Art into a Science"*
- *Riccardo Gottardi, Ph.D., "Charting a Translational Path for Decellularized Meniscus Biomaterials"*

10:30 – 11:40am **Break and Poster Session I (Poster Numbers 1-55)**

11:40 – 12:40pm **Session III: Affiliate Member Session** (Moderator: Rob Mauck, Ph.D.)
- *Benjamin Wheatley, Ph.D., Bucknell University, "Elucidating Structure-Function Mechanisms in Muscle and Aponeurosis Tissue with Finite Element Analysis."*
- *Valentina Graci, Ph.D., Drexel University, "Reclined Vehicle Occupants: Current and Future Risk of Injury in Motor Vehicle Crashes"*
- *Jonathan Grasman, Ph.D., New Jersey Institute of Technology, "Developing Biomimetic Scaffolds to Treat Volumetric Muscle Loss."*

12:40 – 01:40pm **Lunch and Poster Breakdown/Setup (provided) in Smilow Commons**

01:40 – 02:40pm **Session IV: Pilot Grantee Session** (Moderator: Maurizio Pacifici, Ph.D.)
- *Foteini Mourkioti, Ph.D., "Stem Cell Dynamics in Acute and Chronic Injuries."*
- *Kyle Vining, D.D.S., Ph.D., "Tuning the Fate of Immune Cells with Their Mechanical Environment."*
- *Joel Boerckel, Ph.D., "Maternal Exercise Rescues Fetal Akinesia-Impaired Skeletal Development."*

02:40 – 03:50pm **Break and Poster Session II (Poster Numbers 56-109)**

03:50 – 04:50pm **Keynote Speaker** (Moderator: Lou Soslowsky, Ph.D.)
Keynote Speaker Title: "The Current Status of Regenerative Medicine in Orthopaedics."
Scott Rodeo, M.D., Professor of Orthopaedic Surgery from Weill Medical College of Cornell University; Vice Chair of Orthopaedic Research, Hospital for Special Surgery

04:50 – 05:00pm **Closing Remarks Preceding Reception**

05:00 – 06:00pm **Reception and Presentation of Poster Awards in Smilow Commons**

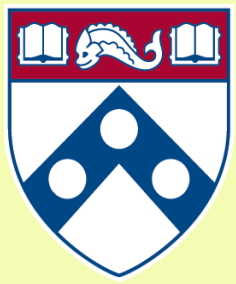

Penn Center *for*
Musculoskeletal Disorders

UNIVERSITY *of* PENNSYLVANIA

Center

Components

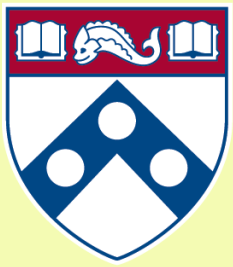

Penn Center *for*
Musculoskeletal Disorders
UNIVERSITY *of* PENNSYLVANIA

Center Overview

OVERVIEW OF THE PENN CENTER FOR MUSCULOSKELETAL DISORDERS

Director: Louis J. Soslowsky, PhD (soslowsk@upenn.edu)
Associate Director: Maurizio Pacifici, PhD (PacificiM@email.chop.edu)

Musculoskeletal-related conditions in the United States account for 132 million visits to physicians' offices, 29 million visits to emergency rooms, 15 million hospital outpatient visits, and cost over $850 billion each year. Further, musculoskeletal injuries in the United States cause workers to miss more than 440 million days of work annually. In fact, more than one in four Americans has a musculoskeletal impairment. With the widespread increase in athletic and recreational activities, and the increase of the elderly population at large, these numbers are expected to rise substantially. Musculoskeletal injuries represent a critical health concern which must be better understood and better treated. To do so, a dedicated and focused strategic effort is required that optimizes research translation from the bench to the bedside in an efficient and effective manner.

The Penn Center for Musculoskeletal Disorders (PCMD) will continue to enhance the research productivity of, and provide critical resources and programs to, investigators to address multidisciplinary research strategies for musculoskeletal problems. The overall goal of this Center is to promote cooperative interactions among investigators, accelerate and enrich the effectiveness and efficiency of ongoing research, foster new collaborations and new research, and ultimately, translate our research efforts into better and new therapies for musculoskeletal disorders. The central theme of the Center will continue to be "Musculoskeletal Tissue Injury and Repair". This theme is broad (as it includes all musculoskeletal tissue types, such as bone, cartilage, disc, ligament, meniscus, muscle, and tendon), focused (as takes advantage of commonalities in approaches across tissue types), and clinically significant (as it fosters development of assays, procedures and knowledge in preclinical animal and human models of translational relevance). It is important to note that our PCMD is not a "bone center" nor is it a "muscle center". Rather, it is truly a "musculoskeletal center" and has emerged as the recognized home for musculoskeletal research across the Penn campus and as a technical and intellectual resource for the broader Philadelphia musculoskeletal research community.

One focus of our Center is to translate research themes, approaches, and paradigms that are consistent across different tissues. Musculoskeletal tissues have much in common and their similarities are often overlooked when focus is restricted to a single tissue type. For example, the role of inflammatory cytokines is well studied in several tissue injury and repair scenarios; yet specific findings in one tissue-type are not always known and applied in other tissues. Similarly, the availability of technologies for imaging blood vessel formation in vivo to monitor healing in a given tissue is not always known and available to researchers focusing on other tissues. Given that approaches routinely used to evaluate mechanisms in one tissue could aid researchers in other areas, our Center will work to foster this critical cross-talk.

To provide a further focus for our Center, we will continue to develop programs with an emphasis on small animal models utilizing unique and sophisticated methods that can cross length scales to pre-clinical large animal models and human testing. Although large animal models for many human diseases exist and are essential for translational studies, small animals (e.g., mouse and rat) have become more commonly used for fundamental discovery of disease mechanism and initial therapeutic development due to availability of transgenic and knockout approaches and molecular tools, low cost, ease of handling and housing, and other practical issues. However, performing certain assays and experiments in mice and rats can be challenging and these difficulties often cannot be overcome in single investigator laboratories. The PCMD will provide unique expertise and sophisticated analytical tools to investigate musculoskeletal tissues across length scales.

Thus, the primary overall aims of this Center are to enhance and advance the research productivity of investigators in musculoskeletal tissue injury and repair by:

Aim 1: Providing innovation within critical resource core facilities in areas that cross disciplines, length scales, and hierarchies. These core facilities are μCT Imaging, Biomechanics, and Histology.

Aim 2: Developing a pilot and feasibility grant program for investigators, with direct mentorship, whereby new approaches, ideas, and collaborations can be developed prior to seeking extramural funding.

Aim 3: Developing educational and research enrichment programs spanning tissue types, research approaches, and paradigms, through which members can learn from national leaders and from each other.

High quality musculoskeletal research is currently being conducted by many groups at Penn. While many bring sophisticated approaches to bear on musculoskeletal problems, few groups have the required expertise and facilities to perform high quality and specialized assays in their own labs. Furthermore, most investigators are not aware of approaches utilized, and results obtained, in other tissues that may have direct relevance on their research questions. Ultimately, close cooperation, communication, and collaboration among researchers across musculoskeletal tissue types and from a wide variety of disciplines will significantly enhance the research of our members. The Center will provide opportunities to integrate multi-disciplinary techniques to determine mechanisms for tissue function, injury, degeneration, repair, and regeneration, with the ultimate goal of advancing the diagnosis, treatment, and prevention of diseases and injuries of the musculoskeletal system.

In addition to the specific features described in this proposal, there is an intangible feature of our Center that should not be overlooked. Although our musculoskeletal program is strong nationally, the Penn biomedical research community is large and diverse. As such, the Center serves as an essential mechanism to highlight our successes and the importance and excitement of musculoskeletal research across campus, as well as to institutional leadership. Having a strong voice for musculoskeletal researchers is critical to support our collective and individual research goals. In these ways, the Center - with essential support from the P30 - has become and remains an indispensable resource and advocate for our community.

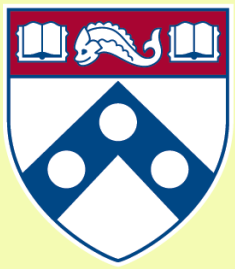

Penn Center *for*
Musculoskeletal Disorders
UNIVERSITY *of* PENNSYLVANIA

Core I

Biomechanics

Biomechanics Core

Core Director: Joel Boerckel, Ph.D. (boerckel@pennmedicine.upenn.edu)

The overall objective of the Biomechanics Core is to develop and provide a wide range of innovative biomechanical approaches to evaluate musculoskeletal tissue function in the context of damage, repair, and regeneration, and to provide training and funding for new projects and collaborations utilizing these assays. Over the last decade, our Biomechanics Core at the Penn Center for Musculoskeletal Disorders (PCMD) has grown into a thriving resource for the University of Pennsylvania and Philadelphia area musculoskeletal research community. In this submission, we will further expand our services to meet the increased demand for specialized techniques and develop new and innovative methods that address the multi-scale mechanics of musculoskeletal tissues. These developments will provide customized services that enhance the research productivity of our members. The Specific Aims of the Biomechanics Core are:

- To provide guidance and training on the capabilities, advantages, and disadvantages of the various methodologies to assess musculoskeletal tissue biomechanical function through formal educational enrichment programs and one-on-one interactions.

- To provide expertise and service for biomechanical assays of musculoskeletal tissues

- To develop innovative biomechanical testing techniques that will be applicable to Musculoskeletal research, and in particular those that provide information across tissue length scales.

- To provide funding for the development of new projects and collaborations and to develop preliminary and/or feasibility data for investigators.

Successful completion of these aims will significantly enhance the environment and the capabilities of researchers at the University of Pennsylvania, leading to new approaches to address musculoskeletal disorders and new collaborations between Center faculties who may have not previously included biomechanical function approaches in their musculoskeletal research programs.

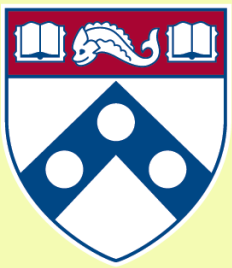

Penn Center *for*
Musculoskeletal Disorders
UNIVERSITY *of* PENNSYLVANIA

Core II

Histology

Histology Core

Overview and Mission

The mission of the Penn Center for Musculoskeletal Disorders (PCMD) Histology Core is to provide comprehensive, high quality histology services to musculoskeletal researchers at the University of Pennsylvania and the broader research community.

The Specific Aims of the core are:

- To provide guidance and training on the capabilities, advantages, and disadvantages of the various methodologies to assess musculoskeletal tissue structure and composition through formal educational enrichment programs and one-on-one interactions.
- To provide expertise and service for histological and histomorphometric assays of musculoskeletal tissues.
- To develop new histologically-based techniques that will be applicable to musculoskeletal research.
- To provide funding for development of new projects and collaborations and to develop preliminary and/or feasibility data for investigators.

Services Offered

The core offers a complete spectrum of services from sample preparation and processing, to sectioning, staining and analysis, with capabilities for paraffin, plastic and frozen histology. The core provides state of the art equipment in each of these areas, which can be accessed either on a self-service basis (upon completion of training) or a full-service basis through our full-time histology technician. Service fees are highly competitive, with significant subsidies offered for PCMD members.

- Consultation and protocol development (no charge for first 6 hours)
- Paraffin processing, embedding and sectioning
- Plastic processing and sectioning
- Frozen sectioning, including cryofilm method for undecalcified bone and teeth
- Routine histochemical staining
- Imaging and histoquantitation
- Training in histology techniques

If you are using the core for the first time, we highly recommend scheduling a meeting with one of the core co-directors and the core technician to discuss the scope of your project and specific needs.

We are very happy to provide letters of support for grant applications. To request a letter, please contact the core co-directors and provide the project title, a brief description of the project and core services you propose to use.

Please visit the core website for more information: www.med.upenn.edu/pcmd/histologymain.html

Co-Directors

Ling Qin, Ph.D. (Plastic and Frozen Histology)
Professor of Orthopaedic Surgery
qinling@pennmedicine.upenn.edu
215 898 6697

Lachlan Smith, Ph.D. (Paraffin Histology)
Associate Professor of Orthopaedic Surgery
lachlans@pennmedicine.upenn.edu
215 746 2169

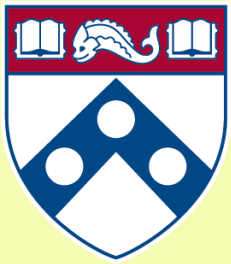

Penn Center *for*
Musculoskeletal Disorders
UNIVERSITY *of* PENNSYLVANIA

Core III

MicroCT

MicroCT Core

Director: X. Sherry Liu, Ph.D. (xiaoweil@pennmedicine.upenn.edu)

X-ray computed tomography (CT) imaging is an established and powerful tool to successfully analyze and clarify questions in musculoskeletal development, disease, injury and repair. In particular, the development of high-resolution micro-CT (μCT) over the last two decades has revolutionized the quantitative assessment of calcified and X-ray dense tissue morphology. With the capability of non-destructive, three-dimensional (3D) visualization of tissue structure, μCT has largely supplanted traditional histomorphometry and has become a gold standard for calcified tissue density and microstructure evaluation.

Due to the low intrinsic X-ray contrast of non-mineralized tissues, traditional applications of μCT in musculoskeletal research have been limited to mineralized tissue. However, the development of contrast-enhanced imaging methods has greatly broadened applications of μCT to include musculoskeletal soft tissues. This not only enables characterization of soft-tissue morphology, but also yields insight into tissue composition, such as glycosaminoglycan (GAG) density, which is essential for soft-tissue function and mechanics. Another important advance in the past decade is *in vivo* μCT imaging of living small animals, which enables longitudinal and non-invasive evaluation of changes in the same animal over time. This imaging strategy minimizes the number of animals required while enhancing statistical power. Further, high-resolution peripheral quantitative CT (HR-pQCT), a relatively recent μCT modality for clinical imaging of calcified tissue microstructure, has inaugurated a new era of non-invasive quantitative skeletal imaging and become a powerful tool for clinical research of musculoskeletal disorders. These new developments in μCT enable a detailed and quantitative understanding of the genetic influences on the skeleton, as well as modeling and remodeling events in hard and soft tissues during repair, treatment, and altered loading scenarios.

Over the past 4 years, our μCT Imaging Core (μCTIC) at the Penn Center for Musculoskeletal Disorders (PCMD) has grown into a thriving resource for the University of Pennsylvania and the region's musculoskeletal research community, serving a vibrant and growing base of 73 active PMCD faculty members and more than 170 trainees from their laboratories. The overall objective of the μCTIC is to develop and apply a wide range of standard and innovative μCT imaging approaches to evaluate musculoskeletal tissue development, disease, injury and repair, and to provide training and funding for new projects and collaborations utilizing these approaches.

The Specific Aims for the μCTIC are:

- To provide guidance and training on the capabilities, advantages, and limitations of using μCT imaging methods for musculoskeletal research through formal educational enrichment programs, online educational tutorials, and one-on-one interactions.
- To provide a range of μCT imaging resources, expertise, and services for the study of the structure, function, and physiology of the musculoskeletal system in laboratory animals and humans.
- To develop new μCT imaging-based techniques that support emerging needs and catalyze innovative musculoskeletal research.
- To provide funding for the development of novel, exploratory projects and collaborations, and to acquire preliminary and/or feasibility data for junior and senior investigators to seek external funding.

By implementing these Aims, the μCTIC will continue to serve as a unique and indispensable resource for researchers at UPenn, the Philadelphia region, and neighboring states, catalyzing innovative and high impact musculoskeletal research, and stimulating new collaborations between current and new PCMD members who may have not previously included μCT imaging approaches in their musculoskeletal research programs.

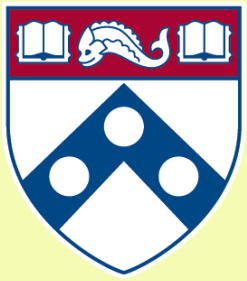

Penn Center *for*
Musculoskeletal Disorders

UNIVERSITY *of* PENNSYLVANIA

Pilot Grant Program

PENN CENTER FOR MUSCULOSKELETAL DISORDERS
PILOT AND FEASIBILITY GRANT PROGRAM

The Penn Center for Musculoskeletal Disorders has an ongoing Pilot and Feasibility Grant Program. Submissions should be related to musculoskeletal tissue injury and repair which is the broad focus of the Center and Grants are only eligible for Center members (if you are not a member but would like to become one, please contact pcmd@pennmedicine.upenn.edu). For more information on our Cores and Center in general, please see our web site at www.med.upenn.edu/pcmd . The next Center grant submission deadline is PENDING.

Eligibility

- Only Full Center members are eligible. If you are not currently a member, please go to the link: http://www.med.upenn.edu/pcmd/memberinfo.shtml
- Categories of applicants include: 1) Established investigators with a proposal to test the feasibility of a new or innovative idea in musculoskeletal tissue injury and repair representing a clear and distinct departure from their ongoing research, 2) Established investigators with no previous work in musculoskeletal tissue injury and repair interested in testing the applicability of their expertise on a problem in this area, and 3) New investigators without significant extramural grant support as a Principal Investigator to develop a new project.
- Pilot and Feasibility Grants must use at least one of the Center's Research Cores.
- Pilot project awardees are eligible for one year, with a second year to be considered (budgets will be for $20-50,000 per year and timelines should be for one or two years). The second year of funding, the dollar amount of which would only be for up to half the year one budget, will be considered based on the progress report submitted after the first year of funding and funding availability in the Center. Please note that second year funding will often not be awarded, and when awarded, will be done so primarily to new investigators; second year funding to senior investigators will be quite rare.
- It is expected that these Pilot grants will lead to funding through other independent, extramural mechanisms. Therefore, the likelihood of future extramural funding will enter into the evaluation of these proposals.

Format

- Applications should be formatted loosely in the style of an NIH R03 grant (http://grants.nih.gov/grants/guide/pa-files/PA-18-488.html). The main body of the application (Specific Aims through Research Design and Methods-sections 4-7 below) is limited to five pages. The application should be in a single pdf file. The format should be:

1) Cover Page (not NIH face page) with grant title, PI name (and co-PI name if applicable), affiliation, contact information
2) Budget and brief justification (note that equipment is not allowed) (Please use form PHS398, Page 4)
3) NIH Biosketch of PI (and co-PI if applicable) (in the new NIH format)
4) Specific Aims
5) Significance
6) Innovation
7) Approach
8) Brief Statement of Category of Investigator per guidelines above
9) Brief Statement of How this Funding will lead to other Extramural Funding
10) Human Subjects and/or Vertebrate Animal Subjects (if applicable)
11) Consultants (if applicable)
12) Literature Cited
13) Certification of Patient Oriented Research (if applicable)

The completed proposal is submitted via the PCMD website by going to the uploaded as a single PDF file.

Please do not hesitate to email pcmd@pennmedicine.upenn.edu with any questions or comments.

Penn Center for Musculoskeletal Disorders Pilot & Feasibility Grants
(all grants awarded since inception of Center)

Awarded 2025-2026
Suradip Das, Ph.D., Department of Neurosurgery: "Vascularized Innervated Tissue Engineered Muscle for Regeneration following Nerve Compression."

Liane Miller, M.D., Department of Orthopaedic Surgery: "Targeting Pathologic Synovial Fibrosis in Post-Traumatic Osteoarthritis Using Precision Biologics in a Small Animal Model."

Awarded 2024-2025
Damaris Lorenzo, Ph.D., Department of Cell, and Developmental Biology: "Contribution of Cytoskeleton Components and Adaptors to Structural and Energetic Adaptations of Skeletal Muscle During Exercise."

Lachlan Smith, Ph.D., Department of Orthopaedic Surgery: "Extended Release of Therapeutic mRNA to Treat Joint Disease in the Mucopolysaccharidoses."

Jennifer Kalish, M.D., Ph.D., Department of Pediatrics and Genetics, CHOP: "Mechanisms of Tongue Skeletal Muscle Overgrowth in Beckwith-Wiedemann Syndrome."

X. Sherry Liu, Ph.D., Department of Orthopaedic Surgery: "Interactions Between Bone and Marrow Adipose Tissue during Lactation and Post Weaning."

Awarded 2023-2024
Kyle Vining, Ph.D., Department of Preventive and Restorative Sciences, PDM and Materials Science and Engineering, School of Engineering and Applied Science: "Exploring Molecular and Mechanical Mechanisms of Myelofibrosis in Bone Marrow Diseases"

Joel Boerckel, Ph.D., Departments of Bioengineering/Orthopaedic Surgery, Perelman School of Medicine: "Determining the Effects of Maternal Exercise on Fetal Akinesia-Impaired Skeletal Development"

Foteini Mourkioti, Ph.D., Department of Orthopaedic Surgery, Perelman School of Medicine: "Mechanosensing Regulation in Skeletal Muscles"

Awarded 2022-2023
Chider Chen, Ph.D., Department of Oral and Maxillofacial Surgery/Pharmacology, School of Dental Medicine: "mTOR Mediated Ribosome Biogenesis Regulates CD4+ T Cell Activation in Osteoporotic Mice."

Carla R. Scanzello, M.D., Ph.D., Department of Medicine, Perelman School of Medicine: "Biophysical Regulation of Macrophage Fate and Function in OA"

Eiki Koyama, D.D.S., Ph.D., Translational Research Program in Pediatric Orthopaedics, Division of Orthopaedic Surgery, CHOP: "The Molecular Mechanisms Underlying Osteophyte Onset and Growth and its Pharmacologic Intervention."

Awarded 2021-2022
Christop Thaiss, Ph.D., Department of Microbiology, Perelman School of Medicine: "Microbiome Control of Musculoskeletal Physiology"

Melike Lakadamyali, Ph.D., Department of Physiology, Children's Hospital of Philadelphia, and Perelman School of Medicine: "Chromatin Structural Regulation of Chondrocyte Fate in Cell Therapy"

Michael Hast, Ph.D., Department of Orthopaedic Surgery, Perelman School of Medicine: "Development of Load-Bearing Trauma Implants Using Bioresorbable Zinc Alloy Scaffolds"

Awarded 2020-2021

Kyu Sang Joeng, Ph.D., Department of Orthopaedic Surgery, Perelman School of Medicine: "The Function of Mtorc1 Signaling in the Regulation of the Provisional Matrix During Tendon Healing" *(awarded extramural funding from NIH/NIAMS R01AR079486)*

Patrick Seale, Ph.D., Department of Cell and Developmental Biology, Institute for Diabetes, Obesity and Metabolism, Perelman School of Medicine: "Fat and Synovial Tissue Development and Disease Remodeling in Joints" *(awarded extramural funding from NIH/NIAMS R21 AR078650-01A1)*

Josh R. Baxter, Ph.D., Department of Orthopaedic Surgery, Perelman School of Medicine: "Stimulating Muscle-Tendon Healing by Prescribing Mechanical Loading" (awarded extramural funding from R21 AR081497-01)

Awarded 2019-2020
Jaimo Ahn, M.D., Department of Orthopaedic Surgery, Perelman School of Medicine: "The Interplay of Notch Suppression and Hypoxia on Bone Regeneration"

Riccardo Gottardi, Ph.D., Department of Pediatrics, CHOP Pulmonary Medicine: "Impact of Scaffold Microporosity in Guiding Local Stem Cell Differentiation for Osteochondral Repair"

Lachlan Smith, Ph.D., Departments of Neurosurgery/Orthopaedic Surgery: "Emergent Nucleus Pulposus Cell Heterogeneity during Intervertebral Disc Development and Growth" *(awarded extramural funding from NIH/NIAMS R21AR077261)*

Awarded 2018-2019
Miltiadis Zgonis, M.D., Department of Orthopaedic Surgery, Perelman School of Medicine: "Development, Maturation, and Function of Meniscal Radial Elements"

Joel Boerckel, Ph.D., Departments of Bioengineering/Orthopaedic Surgery, Perelman School of Medicine: "Role of Yap/Taz in Osteoprogenitor Cell-Induced Angiogenesis for Vascularized Bone Repair" *(awarded extramural funding from NIH/NIAMS R01AR074948 and R01AR073809)*

Awarded 2017-2018
Nathaniel Dyment, Ph.D., Department of Orthopaedic Surgery, Perelman School of Medicine: "Murine Anterior Cruciate Ligament Reconstruction Model to Understand the Cellular Origins and Mechanisms of Repair" *(awarded extramural funding from NIH/NIAMS R01 AR076381)*

Yangqing Gong, Ph.D., Department of Medicine, Perelman School of Medicine: "Role of Plasminogen in Mesenchymal Stem Cell Function and Post-Injury Bone Regeneration"

Carla Scanzello, M.D., Ph.D., Department of Medicine, Perelman School of Medicine: "Importance of Macrophage Responses in Osteoarthritis" *(awarded extramural funding from NIH/NIAMS R01 AR075737and T21 RX001757)*

Susan Volk, V.M.D., Ph.D., D.A.C.V.S., Department of Small Animal Surgery, School of Veterinary Medicine: "The Regulatory Roles of Type III Collagen in the Cartilage Collagen Network: Implications for Osteoarthritis Prevention and Treatment" (*awarded extramural funding from NIH/NIGMS R01 GM124091*)

Awarded 2016-2017
Joseph Baur, Ph.D., Department of Physiology Institute for Diabetes, Obesity and Metabolism, Perelman School of Medicine: "Targeting Nad Metabolism in Muscular Dystrophy" *(awarded extramural funding from Elysium Health)*

Yongwon Choi, Ph.D., Department of Pathology and Lab Medicine, Perelman School of Medicine: "Cell Adhesion Regulation of Multiple-Myeloma Induced Bone Destruction"

X. Sherry Liu, Ph.D., Department of Orthopaedic Surgery and Bioengineering, Perelman School of Medicine: "Mechanical Consequences of Modeling- vs. Remodeling-Based Bone Formation" *(awarded extramural funding from the NSF Award #1661858)*

Hongtao Zhang, Ph.D., Department of Pathology and Lab Medicine, Perelman School of Medicine: "Novel Cartilage-Targeting Fc Fusion Proteins as Novel and Effective Treatments For Osteoarthritis"

Awarded 2015-2016

Yejia Zhang, M.D., Ph.D., Department of Physical Medicine and Rehabilitation, Perelman School of Medicine: "Inhibition of Adam-8 to Reduce Intervertebral Disc Degeneration" *(Awarded extramural funding from the VA Meri t; VA Competitive Pilot Fund)*

Oren Friedman, M.D., Department of Otorhinolaryngology, Perelman School of Medicine: "Effect Of Injury To Cartilage And Recovery Treatment With Fgf-18"

Harvey Smith, M.D., Department of Orthopaedic Surgery, Perelman School of Medicine: "Impact of Pre-Culture and In Vivo Remobilization on Engineered Disc Replacement" *(Awarded extramural funding from the VA RX002274-01A1)*

Tejvir Khurana, M.D., Ph.D., Department of Physiology, Perelman School of Medicine: "Role of the Il-15 / Il-15rα Axis in Modulating Muscle-Tendon-Bone Adaptation and Repair"

Awarded 2014-2015

Joshua F. Baker, M.D., MSCE, Department of Rheumatology & Epidemiology, Perelman School of Medicine: "Assessment of Intramyocellular Fat Accumulation in Rheumatoid Arthritis Using MR Spectroscopy" *(Awarded extramural funding from American Federation for Aging Research Foundation)*

Russ P. Carstens, M.D., Department of Renal-Electrolyte and Hypertension Division, Perelman School of Medicine: "Roles of Epithelial Splicing Regulatory Proteins in Craniofacial Development" *(awarded extramural funding NIH 1R56DE024749 and awarded R01 NIDCR)*

Foteini Mourkioti, Ph.D., Department of Orthopaedic Surgery, Perelman School of Medicine: "A Novel Molecular Mechanism in Chronic Skeletal Muscle Injury" *(awarded extramural funding R01AR075914 NIH/NIAMS)*

Chamith Rajapakse, Ph.D., Department of Radiology, Perelman School of Medicine: "Biomechanics of Hip Fracture Assessed by MRI" *(Awarded extramural funding from the NIH R01 AR068382)*

Awarded 2013-2014

X. Sherry Liu, Ph.D., Department of Orthopaedic Surgery, Perelman School of Medicine: "Structure and Strength Recovery in Post-Lactation Bone" *(awarded extramural funding from the NIH R03 AR065145 and NSF Career Award #1653216)*

Ling Qin, Ph.D., Department of Orthopaedic Surgery, Perelman School of Medicine: "Novel Anabolic Treatment for Radiation-Induced Osteoporosis" *(awarded extramural funding from the NIH R01AR066098)*

Lachlan Smith, Ph.D., Departments of Neurosurgery/Orthopaedic Surgery, Perelman School of Medicine: "Molecular Mechanisms of Failed Vertebral Bone Formation in Mucopolysaccharidosis VII" *(awarded extramural funding from the NIH R03 AR065142 and the MPS Society)*

Hansell H. Stedman, M.D., Department of Surgery, Perelman School of Medicine: "Molecular Pattern Recognition in Acute and Chronic Injury to Muscle and Myotendinous Junction" *(awarded extramural funding from the NIH R01NS094705)*

Awarded 2012-2013

Jason Burdick, Ph.D., Department of Bioengineering, School of Engineering and Applied Science: "Acelluar Fibrous Scaffolds for Stem Cell Recruitment and Cartilage Repair" *(awarded extramural funding from the NIH R01 EB008722)*

James L. Carey, M.D., MPH, Department of Orthopaedic Surgery, Perelman School of Medicine: "Development of a Large Animal Model of Osteochondritis Dissecans" *(awarded extramural funding from the NIH R01 EB008722)*

Andrew Kuntz, M.D., Department of Orthopaedic Surgery, Perelman School of Medicine: "Effects of Intra-Articular Glenohumeral Injection of a Nonsteroidal Anti-Inflammatory Drug on Shoulder Joint Mechanics in a Rat Model"

Arjun Raj, Ph.D., Department of Bioengineering, School of Engineering and Applied Science: "Single Cell Analysis of Molecular and Micromechanical Heterogeneity in Mesenchymal Stem Cells and Engineered Tissues"

Awarded 2011-2012

Struan F.A. Grant, Ph.D., Department of Pediatrics, Children's Hospital of Philadelphia and Perelman School of Medicine: "Utilization of ChIP-seq to Identify Genes Regulated by Osterix"

Motomi Enomoto-Iwamoto, DDS, Ph.D., Department of Orthopaedic Surgery, Children's Hospital of Philadelphia and Perelman School of Medicine: "Tendon Repair by Retinoic Acid Receptor Agonists" *(awarded extramural funding from the NIH R21 AR062193)*

Ian N. Jacobs, M.D., Department of Otorhinolaryngology: Head and Neck Surgery, Children's Hospital of Philadelphia and Perelman School of Medicine: "A Pilot Study for the Development of a Rabbit In-Vivo Tissue- Engineered Cartilage Graft for Pediatric Laryngotracheal Reconstruction" *(awarded extramural funding from The Triological Society)*

Awarded 2010-2011

Susan W. Volk, VM.D., Ph.D., Dipl ACVC, Department of Small Animal Surgery, School of Veterinary Medicine: "The Role of Type III Collagen in Bone Repair and Regeneration"

Jaimo Ahn, M.D., Ph.D., Department of Orthopaedic Surgery, Perelman School of Medicine: "Toward the Identification of Molecular Pathway Alterations in Aged Fracture Healing: A Pilot Study Utilizing a Genetic Model of Senescence" *(awarded extramural funding from the NIH R03 AG040670)*

Shannon Fisher, M.D., Ph.D., Department of Cell and Developmental Biology, Perelman School of Medicine: "Requirement for Osterix in Skull Formation and Maintenance of Adult Bone in Zebrafish" *(awarded extramural funding from the NIH R21 DE021509)*

Awarded 2010-2011 (Jointly with IOA)

Olena Jacenko, Ph.D., Department of Animal Biology, School of Veterinary Medicine: "Aging of the Hematopoietic Niche" *(awarded extramural funding from the NIH R01 DK088334-01)*

Eileen M. Shore, Ph.D., Departments of Orthopaedic Surgery and Genetics, Perelman School of Medicine: "Modulation of Progenitor Cell Differentiation through BMP Signaling" *(awarded extramural funding from the NIH R01 AR041916-15)*

Kurt D. Hankenson, DVM, Ph.D., Department of Animal Biology, School of Veterinary Medicine: "Notch Signaling in Bone Regeneration" *(awarded extramural funding from the DOD CDMRP)*

Awarded 2009-2010

Ling Qin, Ph.D., Department of Orthopaedic Surgery, Perelman School of Medicine: "Mechanisms of EGFR Action on Bone" *(awarded extramural funding from the NIH R01 DK095803)*

Steven Scherer, M.D., Ph.D., Department of Neurology, Perelman School of Medicine: "Are N-cadherin and L1 Adhesion Molecules Required for Recovery of Muscle Strength after Nerve Injury?"

Nader M. Hebela, M.D., Department of Orthopaedic Surgery, Perelman School of Medicine: "A Pre-Clinical Rodent Model of Intervertebral Disc Autograft Transplant" *(awarded extramural funding from the DOD/CDMRP/PROP OR090090)*

Awarded 2008-2009

Sunday O. Akintoye, BDS, DDS, MS, Department of Oral Medicine, School of Dental Medicine: "Orofacial Bone Marrow Stromal Cells Promote Bisphosphonate-Associated Jaw Osteonecrosis" *(awarded extramural funding from the NIDCR R21 DE022826)*

Margaret M. Chou, Ph.D., Departments of Cell and Developmental Biology, Perelman School of Medicine: "Mechanisms of TRE17/USP6 Function in the Etiology of Aneurysmal Bone Cyst" *(awarded extramural funding from the NIH-NCI R01 CA168452 and R21-CA18601)*

Kenneth W. Leichty, M.D., Department of Surgery, Perelman School of Medicine: "The Role of Inflammation in Regenerative Fetal Tendon Wound Healing" *(awarded extramural funding from the NIH DP2 DK083085)*

Kathleen M. Loomes, M.D., Department of Pediatrics, Children's Hospital of Philadelphia: "The Role of Jag1 in Osteogenesis"

Eileen M. Shore, Ph.D., Departments of Orthopaedic Surgery and Genetics, Perelman School of Medicine: "Analysis of an ACVR1 Knock-in Mouse Model for FOP*" (awarded extramural funding from the NIH R01 AR041916-15S1)*

Awarded 2007-2008
Sherrill L. Adams, Ph.D., Department of Biochemistry, School of Dental Medicine: "Collagen III-deficient Mice as a Model for Musculoskeletal Wound Repair"

Kurt D. Hankenson, DVM, Ph.D., Department of Animal Biology, School of Veterinary Medicine: "Regulation of Bone Formation by Novel Activators of Canonical Wnt Signaling"

Awarded 2006-2007
Robert J. Pignolo, M.D., Ph.D., Department of Medicine, Perelman School of Medicine: "Stem Cell Rescue of the Osteoporotic Phenotype in a Mouse Model of Accelerated Aging" *(awarded extramural funding from the NIH R01 AG028873)*

Robert L. Mauck, Ph.D., Department of Orthopaedic Surgery, Perelman School of Medicine "Meniscus Repair with a Novel Aligned Nanofiber Scaffold" *(awarded extramural funding from the NIH R01 AR056624 and the VA RR & D)*

Christopher S. Chen, M.D. Ph.D., Department of Bioengineering, School of Engineering and Applied Science: "Mechanotransduction in Mesenchymal Stem Cells" *(awarded partial funding as Co-Investigator on NIH P41 EB001046)*

Pedro K. Beredjiklian, M.D., Department of Orthopaedic Surgery, Perelman School of Medicine: "Role of Hyaluronic Acid Receptors in Tendon Healing" (*awarded extramural funding from the NIH R21 AR052393*)

Penn Center *for* Musculoskeletal Disorders

University *of* Pennsylvania

Visiting Professorship Series 2025-2026

Visiting Professorship Series-Academic Year 2025-2026

Tuesday, January 13, 2026, 1:30 pm-2:30 pm / CRB Austrian Auditorium Joint with IRM
Investigating the PD-1/PD-L1 Immune Checkpoint Axis: Direct and Indirect Regulation of Bone Metabolism in Breast Cancer Metastasis
Rachelle Johnson, PhD, Associate Professor of Medicine, Division of Hematology and Oncology
Vanderbilt Center for Bone Biology; Program Director & Director of Graduate Studies
Program in Cancer Biology, Vanderbilt University School of Medicine

Tuesday, December 2, 2025, 1:30 pm-2:30 pm / CRB Austrian Auditorium
Title: "Repair Patrol: Sox9 Lineage Cells as Sentinels of Skeletal Regeneration"
Francesca Mariani, PhD, Associate Professor of Stem Cell Biology and Regenerative Medicine
Integrative Anatomical Sciences; Director for the Stem Cell Biology and Regenerative Medicine Master's Program
Keck School of Medicine, University of South California

Tuesday, October 21, 2025, 1:30 pm-2:30 pm / CRB Austrian Auditorium
Title: "Modulating Inflammatory Factors to Prevent the Painful Pathoanatomy in Discogenic Low Back Pain"
Simon Tang, PhD, MSCI, Associate Professor of Orthopaedic Surgery, Washington University

Monday, September 29, 2025, 11:00 am-12:00 pm / JMB Class of '62 Auditorium
Title: "Translational Opportunities at the Intersection of Immunoengineering, Mechanobiology, and Regenerative Medicine"
Robert E. Guldberg, PhD, Robert and Leona DeArmond Executive Director, Phil and Penny Knight Campus for Accelerating Scientific Impact; Director, Wu Tsai Human Performance Alliance at Oregon;
Professor, Department of Bioengineering; Vice President, University of Oregon

Visiting Professorship Series-Academic Year 2024-2025

Friday, June 27, 2025, 1:30 pm-2:30 pm / CRB Austrian Auditorium/Joint with IRM
Title: "Noodle Hop Hop - On the Development and Evolution of Skeletal Proportion"
Kimberly Cooper, PhD, Professor, Cell and Developmental Biology, University of California, San Diego

Tuesday, April 8, 2025, 1:30 pm-2:30 pm / CRB Austrian Auditorium
Title: "Pain Relief through Innovation: Harnessing Biological Pathways to Restore Function and Regenerate Tissue."
Fackson Mwale, M.D., Professor of Surgery, McGill University

Tuesday, March 11, 2025, 1:30 pm-2:30 pm / CRB Austrian Auditorium
Title: "Bone Building and Breakdown from the City of Brotherly Love to the Lone Star State."
Benjamin Levi, M.D., Dr. Lee Hudson-Robert R. Penn Chair and Director, Center for Organogenesis Regeneration & Trauma; Professor in Surgery and Bioengineering, University of Texas Southwestern Medical Center

Tuesday, February 25, 2025, 1:30 pm-2:30 pm / CRB Austrian Auditorium - Joint with IRM
Title: TBD
Matt Greenblatt, M.D., Ph.D., Associate Professor of Pathology and Laboratory Medicine Weill Cornell Medical College

Tuesday, January 14, 2025, 1:30 pm-2:30 pm / CRB Austrian Auditorium
Title: "Building Stronger Bones with Osteoblasts"

Joy Wu, M.D., Ph.D., Professor of Medicine and Vice Chair, Basic Science in the Department of Medicine
Stanford University

Tuesday, December 10, 2024, 1:30 pm-2:30 pm / CRB Austrian Auditorium
Title: Intraarticular Microbial Products: a Potential Driver of Osteoarthritis Pathogenesis
Matlock Jefferies, M.D., Clinical Associate Professor of Medicine, University of Oklahoma Health Services

Wednesday, November 20, 2024, 8:00 am-6:00 pm / Smilow Rubinstein Auditorium & Commons
Annual Scientific Symposium
Keynote Title: "Regulation of Post-Natal Growth Plate Maturation"
Keynote Speaker: **Marie DeMay, M.D.,** Professor of Medicine, Harvard Medical School

Tuesday, October 22, 2024, 1:30 pm-2:30 pm / CRB Austrian Auditorium - Joint with IRM
Title: "Interrogating Osteoclast Biology by Live Cell Imaging Reveals Novel Insight into their Cellular and Resorption Dynamics"
Sarah L. Dallas, Ph.D., University of Missouri Curator's Distinguished Professor and Lee M. and William Lefkowitz Endowed Professor, University of Missouri-Kansas City

Tuesday, September 10, 2024, 1:30 pm-2:30 pm / CRB Austrian Auditorium
Title: "Bone Microstructure, Mechanics, Mechanobiology, and Beyond"
Xiang-Dong Edward Guo, Ph.D., Professor of Biomedical Engineering, Columbia University

Visiting Professorship Series-Academic Year 2023-2024

Tuesday, June 18, 2024, 1:30 pm-2:30 pm / CRB Austrian Auditorium
Title: "Rotator Cuff Tear and Repair: From Bedside to Bench"
Kathleen Derwin, Ph.D., Department Vice Chair and Associate Staff, Biomedical Engineering
Director, Musculoskeletal Research Center, Lerner Research Institute, Cleveland Clinic

Tuesday, May 14, 2024, 130pm-230pm/CRB Austrian Auditorium/Joint with IRM
Title: "Interrogating Osteoclast Biology by Live Cell Imaging Reveals Novel Insight into their Cellular and Resorption Dynamics"
Sarah L. Dallas, Ph.D., University of Missouri Curator's Distinguished Professor, Lee M. and William Lefkowitz Endowed Professor, University of Missouri-Kansas City

Monday, April 15, 2024, 3pm-4pm/CRB Austrian Auditorium/Joint with Pennsylvania Muscle Institute
Title: "Mechanisms of Hippo Pathway Dysregulation in Sarcomas."
Munir Tanas, M.D., Associate Professor of Pathology, Carver College of Medicine, University of Iowa Health Care

Tuesday, March 19, 2024, 130pm-230pm/CRB Austrian Auditorium/Joint with IRM
Title: "Bone Building Molecular Targets: Lessons from Mechanical Signaling in Skeletal Tissues"
Alexander Robling, Ph.D., Chair, Anatomy, Cell Biology & Physiology, Indiana University, School of Medicine

~~**Tuesday, February 20, 2024, 130pm-230pm/CRB Austrian Auditorium**~~ Cancelled
Title: "Perspectives on Tendon Development"
Ronen Schweitzer, Ph.D., Interim Director of Research, Shriners Hospital for Children – Portland, Professor in Orthopaedics and Cell, Developmental and Cancer Biology, Oregon Health & Science University

Tuesday, January 23, 2024, 130pm-230pm/CRB Austrian Auditorium/Joint with IRM
Title: "Myostatin: A Molecular Rheostat for Muscle Mass"
Se-Jin Lee, M.D., Ph.D., Presidential Distinguished Professor, Genetics and Genome Sciences, Joint Appointment, The Jackson Laboratory for Genomic Medicine, MD/PhD Executive Committee Chair, University of Connecticut

Tuesday, December 12, 2023, 130pm-230pm/CRB Austrian Auditorium
Title: "Understanding Joint Health through Whole Joint Biomechanics and Mechanobiology"
Hai Yao, Ph.D., Professor and Ernest R. Norville Endowed Chair, Associate Chair for CU-MUSC Bioengineering Program, Department of Bioengineering, Clemson University

Wednesday, November 15, 2023, 8am-630pm/Smilow Rubinstein Auditorium & Commons
Annual Scientific Symposium
Title: "Navigating the NIH: The Program Director Perspective"
Keynote Speaker: Charles Washabaugh, Ph.D., Program Director, National Institute of Arthritis and Musculoskeletal and Skin Diseases, National Institute of Health

Tuesday, October 17, 2023, 130pm-2:30pm/CRB Austrian Auditorium
Title: "My Journey to Demystify the Marvelous Misunderstood Meniscus"
Suzanne Maher, Ph.D., Senior Scientist, Research Institute, Co-Director, Orthopedic Soft Tissue Research Program, Research Institute, Associate Director, Department of Biomechanics, Hospital for Special Surgery

Tuesday, September 12, 2023, 130pm-2:30pm/CRB Austrian Auditorium
Title: "Decorin: A Central Player of Cartilage Extracellular Matrix in Health and Disease"
Lin Han, Ph.D., Associate Professor, School of Biomedical Engineering, Science and Health Systems
Drexel University

Penn Center *for* Musculoskeletal Disorders

University *of* Pennsylvania

Symposium Participants 2025

Last Name	First Name	Email	Institution Name
Abdi	Farzad	abdi@udel.edu	UDelaware
Adomakoh	Celine	aceline@sas.upenn.edu	UPenn
Agnello	Kimberly	kagnello@vet.upenn.edu	UPenn
Ahn	Seongjue	ahn13@vet.upenn.edu	UPenn
Al Taie	Faisal	faisalrazaq9@gmail.com	Rowan-Virtua SOM
Alderfer	Sydney	alderfes@UPenn.pennmedicine.edu	UPenn
Aluoch	William	woa8@scarletmail.rutgers.edu	Rutgers University
Arroyo	Edgardo	arroyoe@pennmedicine.upenn.edu	UPenn
Ashford	Anna	aashford@seas.upenn.edu	UPenn
Augustin	Janai	janaiaug@seas.upenn.edu	UPenn
Azar	Reem	razar@seas.upenn.edu	UPenn
Azzouz	Aouss	Aouss.Azzouz@pennmedicine.upenn.edu	UPenn
Baccaglini	Emily	baccagle@pennmedicine.upenn.edu	UPenn
Bacchus	Zarah	Zsb20@scarletmail.rutgers.edu	Rutgers University
Basukala	Kebisha	basuka55@rowan.edu	Rowan University
Baxter	Josh	josh.baxter@pennmedicine.upenn.edu	UPenn
Bergstrom	Annika	abergs01@villanova.edu	Villanova University
Berlew	Erin	erin.berlew@pennmedicine.upenn.edu	UPenn
Bernstein	Ellie	elizabeth.bernstein@pennmedicine.upenn.edu	UPenn
Betts	Rebecca	rebecca.betts@pennmedicine.upenn.edu	UPenn
Bhangui	Varad	varad.bhangui@pennmedicine.upenn.edu	UPenn
Binder-Markey	Ben	bb983@drexel.edu	Drexel University
Blanch	Tyler	tblanch@seas.upenn.edu	UPenn
Blank	Jon	jonathon.blank@pennmedicine.upenn.edu	UPenn
Boakye	Lorraine	lorraine.boakye@pennmedicine.upenn.edu	UPenn
Boerckel	Joel	boerckel@pennmedicine.upenn.edu	UPenn
Bolanos-Campos	Alexander	alexbc@seas.upenn.edu	UPenn
Bonelli	Hannah	bonellih@chop.edu	CHOP
Camacho	Paula	paula.camachosierra@pennmedicine.upenn.edu	UPenn
Canonicco	Maria	Mjc7530@psu.edu	Penn State University
Capalbo	Maggs	mhc5270@psu.edu	Penn State University
Carey	James	james.carey@pennmedicine.upenn.edu	UPenn
Caronia	Lauren	lxc336@students.jefferson.edu	Thomas Jefferson University
Casila	Joseph	Jcasila@seas.upenn.edu	UPenn
Chan	Tiffany	tc995@scarletmail.rutgers.edu	Rutgers University - Camden
Charoensombut	Narintadeach	charoenson@chop.edu	CHOP
Chen	Mengcun	mengcc@pennmedicine.upenn.edu	UPenn
Chen	Chider	chenc10@upenn.edu	UPenn
Cheng	Zhiliang	zcheng@seas.upenn.edu	UPenn
Cheung	Catherine	catwxy@seas.upenn.edu	UPenn
Ching	Stephen	chings@seas.upenn.edu	UPenn
Choi	Eirene	exc125@students.jefferson.edu	Thomas Jefferson University
Chow	Lesley	lesley.chow@lehigh.edu	Lehigh University
Collins	John	john.collins2@jefferson.edu	Thomas Jefferson University

Last Name	First Name	Email	Institution Name
Cone	Stephanie	sgcone@udel.edu	UDelaware
Cook	Emily	esc6@seas.upenn.edu	UPenn
Cotney	Justin	cotneyj@chop.edu	CHOP
Cottrell	Christiana	clc456@drexel.edu	Drexel University
Croen	Brett	brett.croen@pennmedicine.upenn.edu	UPenn
Cullen	D. Kacy	dkacy@pennmedicine.upenn.edu	UPenn
Dehghani	Bijan	Bijan.dehghani@pennmedicine.upenn.edu	UPenn
Diallo	Mariama	lamarana17.2023@gmail.com	La Salle University
Dindarian	Sina	sina.dindarian@pennmedicine.upenn.edu	UPenn
Disser	Nathaniel	Nathaniel.disser@pennmedicine.upenn.edu	UPenn
Duah	Adrian	aad384@drexel.edu	Drexel University
Duffy	Michael	mpduffy@upenn.edu	UPenn
Dyer	Olivia	oldyer@udel.edu	UDelaware
Dyment	Nat	dyment@pennmedicine.upenn.edu	UPenn
Eekhoff	Jeremy	jeremy.eekhoff@pennmedicine.upenn.edu	UPenn
Engiles	Julie	engiles@vet.upenn.edu	UPenn
Fainor	Matthew	matthew.fainor@pennmedicine.upenn.edu	UPenn
Fan	Mingyue	mf988@seas.upenn.edu	UPenn
Felipe	Jack	felipej@udel.edu	UDelaware
Feng	Xiaotian	fengx@chop.edu	CHOP
Fischer	Nick	nfi@seas.upenn.edu	UPenn
Flannery	Kyle	flanneryk@chop.edu	CHOP
Forbes	Grace	grace.forbes@pennmedicine.upenn.edu	UPenn
Foster	Brad	brf5277@psu.edu	Penn State University
Freeman	Terry	theresa.freeman@jefferson.edu	Thomas Jefferson University
Fung	Stephanie	fungs@chop.edu	CHOP
Gabbard	Jackson	jgabbard@udel.edu	UDelaware
Gao	Zichen	gzc@seas.upenn.edu	UPenn
Garcia Collao	Miriam	mirigc95@upenn.edu	UPenn
Ghaeini-Hesaroueiye	Sobhan	sg3833@drexel.edu	Drexel University
Gibson	Eve	Eve.Gibson@pennmedicine.upenn.edu	UPenn
Godarzi	Jagger	jg3938@drexel.edu	Drexel University
Godshall	Stanton	Stanton.godshall@pennmedicine.upenn.edu	UPenn
Gonzalez-Fernandez	Tomas	Tog221@lehigh.edu	Lehigh University
Gottardi	Riccardo	gottardir@chop.edu	UPenn/CHOP
Gottlieb	Devin	deving26@seas.upenn.edu	UPenn
Graci	Valentina	graciv@chop.edu	Drexel University
Grant	Struan	grants@chop.edu	CHOP
Grasman	Jonathan	jonathan.m.grasman@njit.edu	NJ Institute of Technology
Greenberg	Elliot	greenberge@chop.edu	CHOP
Gullbrand	Sarah	sgullb@pennmedicine.upenn.edu	UPenn
Halloran	Daniel	hallorand@chop.edu	CHOP
Hallstrom	Grey	grey.hallstrom@pennmedicine.upenn.edu	UPenn

Last Name	First Name	Email	Institution Name
Han	Lin	lh535@drexel.edu	Drexel University
Harding	Warren	warren.harding@pennnedicine.uoenn.edu	UPenn
Haseeb	Abdul	haseeba@chop.edu	CHOP
Hassan	Ziad	ziad.hassan@pennmedicine.upenn.edu	UPenn
Hasson	Madeline	madeline.hasson@pennmedicine.upenn.edu	UPenn
Hast	Mike	hast@udel.edu	UDelaware
Haughan	Joanne	jhaughan@vet.upenn.edu	UPenn
He	Qi	qi.he@pennmedicine.upenn.edu	UPenn
Heo	Yuna	yunaheo@seas.upenn.edu	UPenn
Heo	Su Chin	heosc@pennmedicine.upenn.edu	UPenn
Hickok	Noreen	Noreen.Hickok@jefferson.edu	Thomas Jefferson University
Horan	Annamarie	HoranA@pennmedicine.upenn.edu	UPenn
Hu	Baofeng	baofeng.hu@pennmedicine.upenn.edu	UPenn
Hu	Haiying	haiyhu@seas.upenn.edu	UPenn
Huang	Darcy	ddhuang@seas.upenn.edu	UPenn
Huber	Payton	payton.huber@pennmedicine.upenn.edu	UPenn
Hullfish	Todd	todd.hullfish@pennmedicine.upenn.edu	UPenn
Ingerson	Samantha	ingersam@udel.edu	UDelaware
Isaacs	David	david.isaacs@pennmedicine.upenn.edu	UPenn
Iyer	Keerthana	keerthana.iyer@pennmedicine.upenn.edu	UPenn
Jalloh	Umu	jalloh79@students.rowan.edu	Rowan University
Jiang	Yichen	yichenj01@gmail.com	UPenn
Jin	Xi	Xi.Jin@Pennmedicine.upenn.edu	UPenn
Jin	Vincent	yvjin22@seas.upenn.edu	UPenn
Johnson	Talayah	talayahj@seas.upenn.edu	UPenn
Jones	Erica	emjones7@pennmedicine.upenn.edu	UPenn
Jordan	Jacob	Jacob.jordan@pennmedicine.upenn.edu	UPenn
Kalish	Jennifer	kalishj@chop.edu	UPenn/CHOP
Kalva	Srijan	srijankalva@gmail.com	UPenn
Kanakarajan Vijaya Kumari	Pratheesh	pkumari@alasu.edu	Alabama State University
Karvande	Anirudha	Karvandea@chop.edu	CHOP
Katsura	Kei	Kei.katsura@ucsf.edu	CHOP
Kazi	Farhan	Kazifa15@rowan.edu	Rowan/Osteopathic Medicine
Kehoe-Huck	Isabel	Isabelkh@udel.edu	UDelaware
Kenawy	Hagar	kenawyh@chop.edu	CHOP/UPenn
Kim	Sung Yeon	sungyk@seas.upenn.edu	UPenn
Kim	Jonathan	jonathankim865@gmail.com	UPenn
Kodama	Joe	JKodama@som.umaryland.edu	UMaryland
Kolasinski	Sharon	sharon.kolasinski@pennmedicine.upenn.edu	UPenn
Koo	Bonhyeock	bonhyeock.koo@pennmedicine.upenn.edu	UPenn
Korte	Scott	skorte@vet.upenn.edu	UPenn
Kotsaris	Georgios	georgios.kotsaris@pennmedicine.upenn.edu	UPenn
Koyama	Eiki	koyamae@chop.edu	CHOP

Last Name	First Name	Email	Institution Name
Kroll	Emma	krolle@seas.upenn.edu	UPenn
Kupratis	Meghan	meghan.kupratis@pennmedicine.upenn.edu	UPenn
Kust	Shu-Jin	shu-jin.kust@temple.edu	Temple University
Kwee	Brian	bkwee@udel.edu	UDelaware
Kwok	Bryan	kwokb@chop.edu	CHOP
Kwon	Michelle	michellekwon@pennmedicine.upenn.edu	UPenn
Lambeth	Emily	emily.lambeth@villanova.edu	Villanova University
Lan	Yanhua	Yanhua.Lan@PennMedicien.upenn.edu	UPenn
Larson	Thijs	thijs.larson@pennmedicine.upenn.edu	UPenn
Laslow	Brittany	brittany.laslow@pennmedicine.upenn.edu	UPenn
Lee	Wonsae	Wonsae.lee@pennmedicine.upenn.edu	UPenn
Lee	Ji-Hyung	ji-hyung.lee@pennmedicine.upenn.edu	UPenn
Lee	Rose	hl822@upenn.edu	UPenn
Lee	Hannah	hannah.lee1@pennmedicine.upenn.edu	UPenn
Lefebvre	Veronique	lefebvrev1@chop.edu	CHOP
Levis	Hunter	hunter.levis@utah.edu	UPenn
Li	Thomas	tl3242@drexel.edu	Drexel University
Li	Thomas	tl545@drexel.edu	Drexel University
Li	Siyan	sl3945@drexel.edu	Drexel University
Li	Zizhao	lizizhao@seas.upenn.edu	UPenn
Li	Qiaoli	qiaoli.li@jefferson.edu	Jefferson
Liang	Jiaming	Jiaming.Liang@PennMedicine.upenn.edu	UPenn
Liang	Jiahao	jhliang@seas.upenn.edu	UPenn
Liang	Qiushi	qiushil@seas.upenn.edu	UPenn
Liang	Dongming	dol@pennmedicine.upenn.edu	UPenn
Liu	Joshua	yuchungl@seas.upenn.edu	UPenn
Liu	Sherry	xiaoweil@pennmedicine.upenn.edu	UPenn
Long	Fanxin	longf1@chop.edu	CHOP
Lopez	Isabella	isalop@seas.upenn.edu	UPenn
Lorenzo	Damaris	damaris.lorenzo@pennmedicine.upenn.edu	UPenn
Love	Stacy	lovest@rowan.edu	Rowan
Lozano Perez	Mistica	mistica@seas.upenn.edu	UPenn
Lundquist	Olivia	oal226@lehigh.edu	Lehigh University
Madl	Christopher	cmadl@seas.upenn.edu	UPenn
Magarelli	Juliana	jnm227@lehigh.edu	Lehigh University
Maharjan	Shashwat	smahar02@villanova.edu	Villanova University
Marcolongo	Michele	michele.marcolongo@villanova.edu	Villanova University
Martin	Shaniqua	shaniquam22@gmail.com	Thomas Jefferson University
Massie	Anna	amassie@upenn.edu	UPenn
Mauck	Robert	lemauck@pennmedicine.upenn.edu	UPenn
McHugh	Emma	ehmchugh7@icloud.com	Penn State University
McLaughlin	Eri	exm557@jefferson.edu	Thomas Jefferson University
Mehta	Samir	Samir.Mehta@pennmedicine.upenn.edu	UPenn
Mejias Rivera	Loreilys	loreilys.mejias@pennmedicine.upenn.edu	UPenn

Last Name	First Name	Email	Institution Name
Melvage	Autumn	amelvage@gmail.com	Thomas Jefferson University
Meyers	Michelle	meyersm9@seas.upenn.edu	UPenn
Miller	Katelyn	katemill@udel.edu	UDelaware
Miller	Destiny	mdestiny@sas.upenn.edu	UPenn
Miller	Liane	liane.miller@pennmedicine.upenn.edu	UPenn
Moharrer	Yasaman	yasamanm@seas.upenn.edu	UPenn
Moniodes	Arianna	axm584@jefferson.edu	Thomas Jefferson University
Moreira Perez	Matheus	mym582@jefferson.edu	Thomas Jefferson University
Moser	Amanda	amanda.moser@pennmedicine.upenn.edu	UPenn
Mourkioti	Faye	fmour@pennmedicine.upenn.edu	UPenn
Mundy	Christina	matticolac@chop.edu	CHOP
Murphy	Lance	lam2248@columbia.edu	UPenn
Nandish	Nilan	nilann@sas.upenn.edu	UPenn
Nguyen	Vu	vunguyen@pennmedicine.upenn.edu	UPenn
Nixon	Jacob	jacobnix@seas.upenn.edu	UPenn
Nuethong	Sittinon	snueth@seas.upenn.edu	UPenn
Nuss	Courtney	cnuss@pennmedicine.upenn.edu	UPenn
Ocaranza-Nunez	Diego	ocaranza@seas.upenn.edu	UPenn
Ochman	Francis	fochman7@gmail.com	Thomas Jefferson University
O'Connell	Matthew	mao426@lehigh.edu	Lehigh University
Ojea Quintana	Julio	julio.ojeaquintana@pennmedicine.upenn.edu	UPenn
Okpara	Chiebuka	cho222@lehigh.edu	Lehigh University
Omar	Hisham	ayasrah@udel.edu	UDelaware
Orozco	Brianna	brianna.orozco@pennmedicine.upenn.edu	UPenn
Ortega Oviedo	Gerardo	feo222@lehigh.edu	Lehigh University
Pabon	Mariah	mpabon@seas.upenn.edu	UPenn
Pacifici	Maurizio	pacificim@chop.edu	CHOP
Panebianco	Christopher	christopher.panebianco@pennmedicine.upenn.edu	UPenn
Park	Joon	joonhyung.park@pennmedicine.upenn.edu	UPenn
Patel	Neil	nrp46@drexel.edu	Drexel University
Pearson	Ayla	ayp290@students.jefferson.edu	Thomas Jefferson University
Peterman	Amanda	apeterma@stevens.edu	Stevens Institute of Technology
Pham	Frank	fp352@drexel.edu	Drexel University
Piasecki	Liz	elizabeth.piasecki@pennmedicine.upenn.edu	UPenn
Pinto	Felicia	frpinto@seas.upenn.edu	UPenn
Ponakala	Mounika	mounika.ponakala@pennmedicine.upenn.edu	UPenn
Pondugula	Pushpak	pondugulapushpak@gmail.com	UPenn
Potter	Benjamin "Kyle"	benjamin.potter@pennmedicine.upenn.edu	UPenn
Qian	Jacob	jaqian@seas.upenn.edu	UPenn
Qin	Ling	qinling@pennmedicine.upenn.edu	UPenn
Ragbirsingh	Dana	ragbirsind@chop.edu	CHOP
Rajagopal	Karthikeyan	Karthikeyan.Rajagopal@Pennmedicine.upenn.edu	UPenn
Rajapakse	Chamith	chamith@pennmedicine.upenn.edu	UPenn
Ramon	Luis	lramon@vet.upenn.edu	UPenn

Last Name	First Name	Email	Institution Name
Recktenwald	Matthias	reckte75@rowan.edu	Rowan University
Reilly	Sean	seanpreilly27@gmail.com	Unity University
Reuther	Katie	kreuther@seas.upenn.edu	UPenn
Roberts	Doug	doug.roberts@pennmedicine.upenn.edu	UPenn
Rodeo	Scott	rodeos@hss.edu	Weil Medical College Cornell
Roots	Andre	amoroots@seas.upenn.edu	UPenn
Rosen	Alyssa	arosen22@sas.upenn.edu	UPenn
Roy	Avinava	avinavar@seas.upenn.edu	UPenn
Russo	Devyn	devyn.russo@pennmedicine.upenn.edu	UPenn
Saadipour	Misagh	ms5648@drexel.edu	Drexel University
Saha	Oli	olisaha.nsu@gmail.com	North South University
Saha	Badhan	badhan@udel.edu	UDelaware
Sathya Narayana	Vivek	vvs5446@psu.edu	Penn State University
Saunders	Cheri	saundersc1@chop.edu	CHOP
Sawant Dessai	Abhisha	abhisha.sawant@pennmedicine.upenn.edu	UPenn
Scanzello	Carla	cscanz@pennmedicine.upenn.edu	UPenn & CMCVAMC
Schaer	Thomas	tpschaer@upenn.edu	UPenn
Schifino	Albino	as6324@drexel.edu	Drexel University
Schoenberger	Rayna	schoenberr@chop.edu	UPenn
Sclafani	Marisa	mjs9782@psu.edu	Penn State University
Sedigh	Ashkan	asedigh@villanova.edu	Villanova University
Seidl	Elizabeth	eseidl@seas.upenn.edu	UPenn
Sharp	Emily	ees015@seas.upenn.edu	UPenn
Shore	Eileen	shore@pennmedicine.upenn.edu	UPenn
Sims	Myranda	simsmy89@students.rowan.edu	Rowan University
Sinad	Korina	kgs221@lehigh.edu	Lehigh University
Singh	Krishna Bhan	krishnabhan.singh@jefferson.edu	Thomas Jefferson University
Slaweski	Amber	amberjule1997@gmail.com	Thomas Jefferson University
Smith	Harvey	Harvey.Smith@pennmedicine.upenn.edu	UPenn
Smith	Kyra	smithkw@chop.edu	UPenn/CHOP
Smith	Tarence	tarence.smith@pennmedicine.upenn.edu	UPenn
Smith	Carly	cxs947@students.jefferson.edu	Thomas Jefferson University
Smith	Lachlan	lachlans@pennmedicine.upenn.edu	UPenn
Sodhi	Jaysukh	jps7986@psu.edu	Penn State University
Soriano	Abigail	ans268@scarletmail.rutgers.edu	Rutgers - Camden
Soslowsky	Lou	soslowsk@upenn.edu	UPenn
Spiller	Kara	kls35@drexel.edu	Drexel
Spitsin	Sergei	spitsins@upenn.edu	UPenn
Spurri	Amanda	amanda.spurri@temple.edu	Temple University
Stager	Thaddeus	thaddeusstager@gmail.com	Penn State University
Stewart	Holly	hstew@upenn.edu	UPenn
Stinger	Ellen	ellenstinger@yahoo.com	UPenn
Stoeckl	Brendan	bstoeckl@pennmedicine.upenn.edu	UPenn
Strand	Kathryn	strandk@seas.upenn.edu	UPenn

Last Name	First Name	Email	Institution Name
Struble	Sarah	shosler@upenn.edu	UPenn
Swiber	Olivia	livswiberdvm@gmail.com	UPenn
Szczesny	Spencer	ses297@psu.edu	Penn State University
Takac	Charlotte	cht33@drexel.edu	Thomas Jefferson University
Tam	Rachel	rachel.tam@pennmedicine.upenn.edu	UPenn
Tamburro	Margaret	Margaret.Tamburro@PennMedicine.upenn.edu	UPenn
Tertuliano	Ottman	oat@seas.upenn.edu	UPenn
Thellapally	Sai	thella65@rowan.edu	Rowan Virtua SOM
Thurlow	Nat	nthurlow@seas.upenn.edu	UPenn
Tichy	Elisia	tichye@chop.edu	CHOP
Tomlinson	Ryan	ryan.tomlinson@jefferson.edu	Thomas Jefferson University
Tsai	Christian	ctsai1@villanova.edu	Villanova University
Uggla	Spencer	snu001@students.jefferson.edu	Thomas Jefferson University
Uliano	Lola	ulianol@pennmedicine.upenn.edu	UPenn
Ural	Ani	ani.ural@villanova.edu	Villanova University
Utke	Eva	utkee@chop.edu	UPenn
Vega	Sebastian	vegas@rowan.edu	Rowan University
Velalopoulou	Anastasia	avela@pennmedicine.upenn.edu	UPenn
Vijayan	Vineeth	vviijayan@alasu.edu	Alabama State University
Vining	Kyle	viningk@upenn.edu	UPenn
Vitale	Flavia	vitalef@pennmedicine.upenn.edu	UPenn
Vo	Quan	vmquan@seas.upenn.edu	UPenn
Volk	Susan	swvolk@vet.upenn.edu	UPenn
Wagner	Maggie	magwag@seas.upenn.edu	UPenn
Wang	Bin	bin.wang@jefferson.edu	Thomas Jefferson University
Wang	Catherine	catwxy@seas.upenn.edu	UPenn
Wang	Dian	dian.wang@pennmedicine.upeen.edu	UPenn
Wang	Tianbai	tbwang9@seas.upenn.edu	UPenn
Wang	Chang	chanwang@seas.upenn.edu	UPenn
Wehrli	Felix W.	felix.wehrli@pennmedicine.upenn.edu	UPenn
Weiss	Steph	weisssn@gmail.com	UPenn
Westmoreland	Shaylyn	Shaylyn.westmoreland@temple.edu	Temple University
Wheatley	Ben	b.wheatley@bucknell.edu	Bucknell University
Whipple	Samantha	Whipples1@chop.edu	CHOP
Winslow	Asia	axw784@jefferson.edu	Thomas Jefferson University
Wu	Tiffany	tif5353@seas.upenn.edu	UPenn
Xiang	Jiaqi	jx338@drexel.edu	Drexel University
Xu	Lin	xulin7669@gmail.com	UPenn
Xu	Yiyang	yiyang.xu@pennmedicine.upenn.edu	UPenn
Xu	Xiaoyu	Xiaoyu.Xu@pennmedicine.upenn.edu	UPenn
Xue	Ting	xueting19104@gmail.com	UPenn
Yang	Shuying	shuyiny@upenn.edu	UPenn
Yang	Yanmei	yanmei.yang@jefferson.edu	Thomas Jefferson University
Yu	Chen	Chen.Yu@PennMedicine.upenn.edu	UPenn

Last Name	First Name	Email	Institution Name
Zawel	Max	max.zawel@pennmedicine.upenn.edu	UPenn
Zhang	Ping	zhangp@rowan.edu	CMSRU
Zhang	Xiao	xiao.zhang@pennmedicine.upenn.edu	UPenn
Zhang	Xiaohong	zhangx8@chop.edu	CHOP
Zhang	Kexin	zhkexin@seas.upenn.edu	UPenn
Zhang	Deyu	deyuz@pennmedicine.upenn.edu	UPenn
Zhang	Yuqi	yuqz@seas.upenn.edu	UPenn
Zhou	Ping	zhping@seas.upenn.edu	UPenn

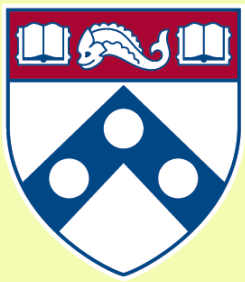

Penn Center *for*
Musculoskeletal Disorders
UNIVERSITY *of* PENNSYLVANIA

Speaker Abstracts

One-Health approach to orthopedic disease: translational applications of large animal veterinary pathology

Julie Engiles, VMD, DACVP
Large Animal Veterinary Pathologist

Abstract

Recent reports indicate rises in life-restricting, nonfatal musculoskeletal diseases[1], as well as pediatric osteoarticular infections[2] with concurrent increasing cost-burdens on individuals and society, highlighting the need for comprehensive musculoskeletal studies optimizing treatments to reduce debility and costs. Although complete postmortem examinations can confirm diagnoses and provide more complete pathoanatomic detail pertaining to disease contributing to an individual's death, the proportion of autopsies reported in human hospitals is extremely low (7.4%)[3] compared to the proportion performed on large animal hospital cohorts, and detailed pathoanatomic descriptions of human orthopedic disease are limited. Animals euthanized for musculoskeletal conditions often represent various stages of disease that either produced severe debilitation, poor prognosis for return to function, or financial constraints on the owner/producer. Large animal models better mimic human anatomic, physiologic, biomechanical, and pathologic skeletal conditions and, as clinical veterinary trials designed ethically and with owner consent can provide critical information pertaining to safety and efficacy of novel therapies intended for humans, conversely, diagnostics and therapeutic interventions can be translated to veterinary use. When correlated with clinical and radiological data, pathoanatomic lesions characterized by diagnostic veterinary pathologists with specialized training across multiple species can provide important insight into the etiopathogenesis, developmental timeline, and response to therapeutic interventions that can also inform the development and interpretation of translational animal models of comparable diseases in humans. This talk will present examples of spontaneous and experimental large animal disease models that leverage a One-Health, multidisciplined approach to orthopedic pathology and the advancement of orthopedic translational research.

1 https://www.ors.org/boneandjointburden/
2 Safdieh G, Silberman J, Nguyen J, et al. Pediatric Septic Arthritis and Osteomyelitis in the USA: A National KID Database Analysis. *HSS Journal*®. 2019;15(2):159-166. doi:10.1007/s11420-018-9644-2
3 Hoyert DL. Autopsies in the United States in 2020. National Vital Statistics Reports, 2023;72(5). doi: https://www.cdc.gov/nchs/data/nvsr/nvsr72/nvsr72-05.pdf

Bio:

Dr. Engiles is an ACVP-boards certified Professor of Anatomic Pathology PennVet- New Bolton Center. She completed her VMD in 2002 and Anatomic Pathology residency training in 2006 at UPenn with a Surgical Internship at the New Jersey Equine Clinic in 2003. As a boards-certified diagnostic pathologist specializing in orthopedic pathology, Dr. Engiles provides autopsy and biopsy services for the Pennsylvania Animal Diagnostic Laboratory System (PADLS), large animal teaching hospital, and research-related services supporting clinical and translational large animal models of axial and appendicular musculoskeletal diseases.

Flavia Vitale

Associate Professor, Departments of Neurology, Bioengineering, Physical Medicine and Rehabilitation. University of Pennsylvania.

Achilles tendinopathy (AT) is a common overuse injury that limits mobility and remains difficult to assess objectively. Current evaluations rely on pain reports and visual observation, providing limited insight into the neuromuscular changes that accompany tendon injury and recovery. To address this gap, we developed novel high-density surface electromyography (HDsEMG) arrays to quantify and investigate muscle activation patterns in the plantar flexor muscles during rehabilitation exercises. This HDsEMG technology is based on soft, conformable electrodes made of a high-performance nanomaterial named MXene, providing gel-free, low-impedance contact and high spatial resolution across large muscle regions. These flexible arrays enable stable, high-fidelity recordings over the gastrocnemius and soleus muscles during dynamic movements, offering significantly improved signal quality and spatial mapping compared to commercial, few-channels EMG sensors. In a study with patients with unilateral and bilateral AT, as well as healthy participants performing calf-raise tasks, the HDsEMG recordings revealed clear differences in activation patterns and coordination across conditions. Using custom-developed machine learning models, we found that these patterns emerging in the HDsEMG data could accurately distinguish between injury types and predict patient-reported functional scores. Moreover, the learned features correlated with clinical severity, suggesting that distinct muscle activation signatures reflect underlying tendon pathology. These results establish HDsEMG combined with data-driven analysis as a quantitative framework for diagnosis and rehabilitation monitoring in AT, with potential to guide more personalized and effective recovery strategies.

Madl, Christopher

Probing Biophysical Regulation of Myogenesis with Dynamic Biomaterials

Abstract: Muscle stem cells (MuSCs) are responsible for the maintenance and repair of skeletal muscle tissue throughout life. MuSCs are exquisitely mechanosensitive, with their regenerative potential dictated by the mechanical properties of their surrounding environment. However, the relevance of this mechanosensitivity to physiological conditions, such as in fibrotic muscle tissue, and the biochemical mechanisms underlying this response, remain poorly understood, hampering therapeutic translation. Using engineered biomaterials platforms with on-demand tuning of stiffness, we have identified a "mechanical memory" acquired by MuSCs during activation from the quiescent state that impairs the expansion of functional progenitor cells on substrates with fibrotic-like stiffness. Furthermore, we have demonstrated that MuSCs sense not only time-independent stiffness but also time-dependent viscoelastic mechanical cues using a family of hydrogels crosslinked by dynamic covalent bonds that span a relevant range of stress relaxation rates. Matching the viscoelastic properties of cell culture substrates to those of healthy muscle tissue results in a marked enhancement of progenitor cell expansion over substrates with static, elastic mechanical properties. We are leveraging these engineered materials platforms to determine the mechanisms by which MuSCs sense viscoelasticity to enhance ex vivo MuSC expansion for cell therapies and to identify new therapeutic targets to augment endogenous MuSC function in aged and diseased tissue.

Penn Center for Musculoskeletal Disorders Symposium Abstract (2025)

Title: RNA in Peripheral Blood as Prognostic for Fracture Outcome

Authors: Annamarie D. Horan, MPA, PhD and Samir Mehta, MD

Abstract

Background: Adult traumatic bone fractures are common, affecting about 6.3 million Americans each year. While approximately 85% of these injuries heal normally with standard care, 15% develop either delayed healing (around 10%) or non-healing fractures (nonunions, about 5%). The literature reports up to 50 risk factors for abnormal outcomes, making fracture prognosis very difficult. Experienced orthopedic trauma surgeons report anecdotally two conflicting outcomes: cases with no risk factors resulting in nonunion and cases with multiple risk factors healing normally. Numerous efforts were made to develop a prognosis method using protein or DNA biomarkers, serial radiology algorithms, and AI models; however, none to date have been satisfactory. We used an RNA-based approach to fracture prognosis.

Methods: Two discovery cohorts of patients with new traumatic fractures at Penn Medicine were enrolled in an observational study (Penn IRB #809094). Peripheral blood samples were collected at up to four timepoints from each patient between the day of injury and 84 days post-injury. Patients were monitored until the clinical outcome of healing was determined to be normal, delayed, or failed (nonunion). Multivariate logistic regression, the Chi-Square test, Fisher's exact test, and various data visualization methods, including Receiver Operating Characteristic (ROC) curves, were used to identify potential prognostic RNA signatures. At the same time, U.S., European, and Canadian patent applications were filed through the Penn Center for Innovation.

Results: Multiple RNA panels, up to four, demonstrate strong potential for predicting fracture outcomes, with ROC AUC scores over 0.90, Positive Predictive Value (PPV) above 0.90, and Negative Predictive Value (NPV) exceeding 0.9 across four post-injury time windows (0 to ≤7 days, 8 to ≤14 days, 15 to ≤42 days, and 43 to ≤84 days). A U.S. patent was issued on May 24, 2022. Other patents are pending.

Conclusions: The central hypothesis that "Early detection of impending delayed or nonunion is possible through the examination of RNA biomarkers and that the result of such testing is clinically actionable" has been supported by the single-center study conducted at Penn. A multicenter validation study is currently underway to further evaluate the existing models and guide future research and development.

Josh Baxter, PhD
Assistant Professor of Orthopaedic Surgery

Next generation nerve conduction testing: turning an art into a science

Abstract: Clinical treatments nerve health pathologies depend on accurate and accessible diagnostics. Diabetic polyneuropathy affects ~24 million Americans, radiculopathy affects ~17 million Americans, and peripheral nerve entrapment syndromes like carpal and cubital tunnel syndromes affect ~11 million Americans. These common pathologies are diagnosed using clinical assessments and nerve conduction studies. Nerve conduction studies are manually performed exams that require highly trained providers to locate the nerve of interest, deliver a series of electrical charges, and visually interpret results to make a clinical diagnosis. This approach has technical and practical limitations that reduce the reliability and use of this diagnostic tool. Our group has developed a novel platform to automate nerve conduction studies while addressing important limitations of the clinical standard. In this presentation, we will introduce the current clinical problem, how we developed our solution, and what our next steps are to develop our technology and begin fundraising.

Charting a Translational Path for Decellularized Meniscus Biomaterials

Riccardo Gottardi

Decellularized extracellular matrix (ECM) biomaterials have successfully reached clinical translation across multiple therapeutic domains. However, tissues with dense ECM architectures such as cartilaginous tissues, present a fundamental paradox: the dense, highly organized ECM that confers essential mechanical properties and biological functionality also creates a barrier to effective recellularization following decellularization. This challenge has limited the translational potential of cartilage-derived biomaterials.

We have developed a novel approach to engineer decellularized meniscus-based ECM scaffolds that resolves this paradox. Our method preserves much of the native tissue's structure while incorporating a network of microchannels that enable robust cell infiltration and tissue integration. This microchannel architecture transforms an otherwise impervious dense ECM into a scaffold with controlled porosity ideal for cellular engraftment.

Beyond the fundamental biomaterial innovation, successful clinical translation requires strategic planning that extends well beyond bench science. We will present our translational strategy, which began with identifying optimal initial clinical applications based on regulatory pathways, unmet clinical needs, and technical feasibility. This strategic approach led us to prioritize applications that leverage the unique properties of our platform while facilitating expedited regulatory approval and clinical adoption. We will discuss how participation in the Penn Health-Tech Accelerator Program has been instrumental in advancing pivotal preclinical studies, refining our regulatory strategy, and developing a commercialization pathway. This case study illustrates one approach to integrate scientific innovation with translational planning to accelerate the journey from laboratory discovery to patient impact.

Predicting how muscle-tendon units generate and transmit force requires a detailed understanding of the connective tissues that couples contractile fibers to tendon. Among these, the aponeurosis plays a central but still poorly characterized role. Despite decades of study on contractile muscle mechanics, passive muscle structure-function mechanisms are not fully understood, although passive stiffness alters how force is transmitted within and between muscles. This talk will present a research program that combines tissue-level experiments and finite element (FE) modeling to reveal multiscale structure–function mechanisms in both skeletal muscle and aponeurosis. We have shown that aponeurosis exhibits pronounced anisotropy and heterogeneity, and incorporating this heterogeneity in FE models can alter predicted muscle fiber strain and overall stiffness. Parallel studies of passive muscle demonstrate how biaxial tension, semi-confined compression, and strain-rate effects expose the interplay of extracellular matrix, intramuscular fluid pressurization, and fiber architecture in determining tissue stiffness and damage resistance. Building on these data, we developed microstructural, biphasic FE models that integrate fiber, matrix, and fluid domains to reproduce tensile and compressive responses and to explore mechanistic hypotheses, such as the contribution of fluid pressurization to compressive stiffness and the role of collagen fiber alignment in tensile behavior. Current and future work includes models of muscle-tendon unit damage accumulation and multiscale contributions of fluid pressurization to muscle stiffness. Together, these approaches demonstrate how tissue-level experiments and FEA can provide insight into structure-function mechanisms of muscle tendon units. By elucidating the coupled mechanical roles of muscle fibers, extracellular matrix, and aponeurosis, this work advances the long-term goal of accurate, predictive models of musculoskeletal mechanics relevant to locomotion, rehabilitation, and tissue engineering.

Reclined Vehicle Occupants: Current and Future Risk of Injury in Motor Vehicle Crashes

Valentina Graci, PhD,
Director of the Sled Laboratory
Children's Hospital of Philadelphia, Drexel University

The investigation into reclined seating configurations for automated vehicles has gained momentum after several studies found that in autonomous vehicles, occupants may prefer seats that allow for relaxing activities such as reading, resting, or sleeping. However, current restraints (e.g. seatbelt and airbag) are designed to protect vehicle occupants when seated upright and not in reclined postures. Most of the research examining the risk of injury in reclined occupants has been conducted in adults with the aim to understand how restraints will need to be modified. Children are different from adults at the musculoskeletal, neuromotor, and behavioral levels, therefore solutions designed for adults are not suitable for children. Our group at CHOP was the first to examine reclined children in simulated vehicle impacts and characterize unfavorable kinematics potentially leading to injuries.

A series of studies including both a child anthropomorphic test device (ATD) and child volunteers (6-8 years old) were conducted in frontal impacts and lateral impacts (i.e. in low acceleration conditions for the volunteers). Child occupants were seated on a production passenger seat with an integrated seatbelt and tested with sled-simulated pure frontal and lateral oblique impact (80° from frontal). A condition with nominal seatback angle (~25°) and two conditions with reclined seatback angles (~45°, and ~60°) with and without a backless BPB were compared. For the ATD, seatbelt and Anterior Superior Iliac Crest loads, abdominal pressure peak upper neck tension force and lateral moment, T1, T6, and T12 lateral rotation, lumbar axial and lateral shear forces, and lumbar axial moment (Mz) were extracted. For the child volunteers head and trunk displacements were recorded with a motion capture system.

Average peak abdominal pressures were smaller in reclined seatback configurations in the BPB condition compared to the no-BPB conditions. In the recline no-BPB conditions, both the peaks of the lap-belt force and ASIS forces occurred early and a a rapid reduction in forces followed the peaks. During the reduction of ASIS and lap-belt forces, there was an increase in abdominal pressure up to injurious values. This finding indicates that the lap-belt moved upward and off the ASIS and into the abdomen. While in the BPB condition, the belt stayed well engaged with the pelvis bones suggesting that the presence of the BPB could reduce abdominal injury even in reclined conditions. However, lumbar spine kinematics (in frontal impacts) and lumbar Mz (in lateral impacts) increased with the increase in reclined seatback angle. Lateral bending and/or flexion over the lap and/or shoulder belt, compression of the seat back, or the loads travelling axially to the spine through the seat pan are known to be injury causation injuries in BPB-seated children. Therefore, our findings suggest the presence of disadvantageous spinal kinematics in reclined seating particularly when the BPB. Reclined child volunteers' kinematics in low acceleration lateral impacts confirmed the child ATD kinematics by showing increased trunk rotation with greater reclined seatback angles.

In conclusion, although current countermeasures such as the BPB show efficacy in preventing abdominal injuries in reclined children, the pediatric spine shows an unfavorable kinematics in both frontal and lateral impacts, in particular thoracolumbar spine risk of injury could be a concern in reclined boosters seated children.

Developing Biomimetic Scaffolds to Treat Volumetric Muscle Loss

Natalie G. Kozan and Jonathan M. Grasman
Department of Biomedical Engineering, New Jersey Institute of Technology, Newark, NJ

Volumetric muscle loss (VML) is a condition resulting from traumatic injury where a significant loss of skeletal muscle mass occurs, leading to permanent loss of muscle functionality. The standard of care for VML is an autologous tissue transfer, which is limited by a relatively high risk of graft failure. Biomaterial scaffolds are being studied as alternative treatment methods to regenerate VML, however, current approaches are somewhat limited by their inability to recruit satellite cells and induce aligned myofiber formation. To overcome these limitations, we incorporated insulin-like growth factor-1 (IGF-1) into anisotropic collagen scaffolds with aligned porous architectures, which we hypothesize would promote organized tissue regeneration. To ensure IGF-1 could be released over long periods of time, we developed a biologically inspired delivery system to prolong its release, and demonstrate its active release for at least four weeks using *in vitro* assessments. To complement *in vitro* assessments, we next implanted these scaffolds into a murine model of VML. The regenerative response of IGF-1 enhanced the functional recovery of the injured limb eight weeks post-injury. Scaffolds containing our delivery system supported less fibrosis and higher expression of regenerative markers than muscles treated with control scaffolds. These results indicate that scaffolds released active IGF-1 throughout the eight week recovery period, which is significantly longer than previous approaches towards delivering this molecule. Further, the maintenance of a regenerative state at this time point has not been previously reported, suggesting that further remodeling could occur. These results emphasize the importance of sustained delivery of IGF-1 for muscle recovery and that these scaffolds could successfully be used to augment functional recovery after VML.

Stem Cell Dynamics in Acute and Chronic Injuries

F. Mourkioti[1, 2]

[1]Departments of Orthopaedic Surgery and Cell & Developmental Biology, Perelman School of Medicine, University of Pennsylvania, USA
[2]Institute for Regenerative Medicine, Musculoskeletal Program, Perelman School of Medicine, University of Pennsylvania, USA
email: fmour@pennmedicine.upenn.edu

A hallmark of advanced aging in humans is the progressive decline in skeletal muscle force production, leading to diminished functional capacity. Age-related muscle weakness is strongly associated with impaired physical function, increased risk of falls, fractures, and a higher degree of dependency among older adults. While much geriatric research has focused on muscle atrophy, accumulating evidence indicates that the decline in muscle stem cell function begins significantly earlier, around 30 years of age, and coincides with gradual muscle loss. Despite this, the mechanisms by which stem cells perceive mechanical stress from the surrounding myofibers, and how these processes are altered with age, remain poorly understood. Our lab investigates a fundamental yet understudied problem in aging biology: why aging cells lose their ability to sense and respond appropriately to microenvironmental mechanical cues. Our data indicate that the mechanosensitive ion channel Piezo1 plays a crucial role in muscle dysfunction, aligning with the phenotype of dynapenia, an early marker of muscle aging with unclear etiology in humans. These data define previously uncharacterized roles of mechanotransduction stimuli in adult stem cells within their native three-dimensional tissue context. By dissecting these mechanisms, we will present how mechanical cues are disrupted in acute and chronic injuries during aging and how restoring mechanosensation can enhance regeneration in the elderly.

Vining, Kyle

Tuning the Fate of Immune Cells with Their Mechanical Environment

The overall goal of Dr. Vining's research is to develop new strategies to target inflammation and promote tissue repair and regeneration. His research investigates mechanical regulation of tissue inflammation in bone marrow disease using fibrotic extracellular matrix hydrogel models and in vitro differentiation of hematopoietic stem and progenitor cells. Myelofibrosis develops in aggressive leukemias and other hematopoietic malignancies, which causes physical changes in the bone marrow. Myelofibrosis has been traditionally attributed to dysregulated inflammatory cytokine production by hematopoietic cells, which contributes to pathological activation of fibrogenic programs in mesenchymal stromal cells, as well as extracellular matrix (ECM) deposition and crosslinking. Using biomaterials and in vivo models, Dr. Vining identified a mechanical checkpoint of inflammatory signaling and monocyte fate in myelofibrosis. The Vining Lab currently investigates human myeloid differentiation from hematopoietic stem and progenitors in biophysical niches to understand how ECM changes influence the bone marrow niche. Further, our team recently identified that myelofibrosis is significantly associated with non-responders to CD19 chimeric antigen receptor T-cell therapies in acute B-cell leukemia, which suggests that mechanical cues in myelofibrosis may negatively impact cellular immunotherapies. Together, our work investigates immuno-mechanical regulation of inflammation and develops new strategies to harness immune cells for immunotherapies.

Maternal exercise rescues fetal akinesia-impaired bone and joint development

Christopher J. Panebianco[1], Yuming Huang[2], Nidal Khatib[2,3], Devin C. Gottlieb[1], Nathaniel Dyment[1], Joel D. Boerckel[1], Niamh C. Nowlan[2,3]

[1]University of Pennsylvania, Philadelphia, PA, USA | [2]Imperial College London, London, UK | [3]University College Dublin, Dublin, IRL

INTRODUCTION: During development, fetal movements provide the mechanical forces necessary for proper skeletal morphogenesis. Clinical conditions that limit fetal movement (*e.g.,* congenital muscle development defects, low amniotic fluid volume, breech position) can result in limited movement, "fetal akinesia".[1] Fetal akinesia can cause debilitating skeletal disorders, such as impaired bone development and multi-joint contractures.[2] Previously, we found that direct mechanical stimulation of explanted fetal limbs taken from muscle-less Pax3$^{spd/spd}$ (Spd) mice rescued effects of fetal akinesis on joint morphogenesis, suggesting that external mechanical stimulation can provide mechanobiological signals lost due to fetal akinesia.[3] Here, we tested the hypothesis that maternal exercise could be a non-invasive, *in utero* mechanotherapeutic intervention for fetal akinesia. Since maternal exercise may rescue skeletal deformities by directly restoring missing mechanical signals or by indirectly providing maternally secreted signals, the aims of this study were to determine the effects of maternal exercise on fetal akinesia-impaired skeletal development and evaluate the effects of maternal exercise on physiology-mediated signaling.

METHODS: To determine the effects of maternal exercise on fetal akinesia-impaired skeletal development, we used the muscle-less Pax3$^{spd/spd}$ (Spd) mouse.[4] Spd heterozygotes, which are phenotypically normal, were crossed to produce litters with wildtype (WT), heterozygous, and homozygous mutant progeny. Pregnant dams were subjected to 1 hr of daily wheel running exercise or sham exercise from E13.5 to E15.5, inclusive. Sham-exercised dams had locked wheels. Embryos were harvested at E16.5, then joint and bone shape were evaluated using whole-mount optical projection tomography. Follow-up analyses were conducted using C57BL/6J mice because it was easier to obtain sufficient sample sizes. C57BL/6J dams were exercised from E13.5 to E16.5, inclusive, with harvest at E17.5. We measured forelimb bone morphogenesis using microcomputed tomography (μCT, voxel size = 3 μm, x-ray tube potential = 70 kVp, x-ray intensity = 145 μA, integration time = 300 ms) and cryohistology. To evaluate the effects of maternal exercise on physiology-mediated signaling, we measured the fetal weight to placental weight ratio (FW:PW) and placental levels of IGF-1 and nutrient transporters. One-way ANOVA with Tukey's post-hoc test and Student's t-test were used to find significant differences for Spd and C57BL/6J experiments, respectively (α = 0.05). The Kolmogorov-Smirnov test was used for distributions.

RESULTS: Maternal exercise rescued bone mineralization and joint morphometry defects in homozygous Spd mutant embryos. Sham Spd embryos had significantly shorter humerus mineralization length and joint morphogenesis parameters (*e.g.,* lateral condyle height) than Sham WT controls. Exposing Spd embryos to maternal exercise rescued outcomes for bone and joint morphogenesis at E16.5 (Fig 1). Next, we evaluated the effects of maternal exercise in C57BL/6J mice at E17.5. Maternal exercise significantly increased mineralized length of the humeral primary ossification center, confirming the osteogenic effects of maternal exercise on developing WT embryos (Fig 2A). We also found significantly increased F-actin in the humerus primary ossification center, suggesting that maternal exercise enhances mechanoregulated bone development via cytoskeletal tension (Fig 2B). To evaluate the effects of physiology-mediated signaling, we first measured the FW:PW ratio, a measure of placental transport efficiency.[5] Maternal exercise increased FW:PW, suggesting increased placental transport efficiency (Fig 3A). However, maternal exercise did not significantly enhance placental levels of IGF-1, the major regulator of placental nutrient transporter expression[5] or amino acid and fatty acid transporter expression (*i.e.,* FATP4 and SNAT4, respectively) (Fig 3B,C).

DISCUSSION: Fetal akinesia affects 1 in 3000 live births. Prenatal screens for clinical conditions that cause fetal akinesia can identify at-risk pregnancies, but current treatments are limited to postnatal intervention (*e.g.,* physical therapy, surgery) and cannot reverse the debilitating skeletal deformities. Herein, we show that maternal exercise can function as a non-invasive, *in utero* therapeutic intervention to prevent fetal akinesia-induced skeletal deformities. Overall, our results show that maternal exercise enhances fetal skeletal development through a mechanism that likely involves both direct mechanical stimulation, consistent with our prior studies,[6] and maternal-placental transport. While we did not observe effects of exercise on the primary regulators of placental transport *per se*, maternal exercise may impact hormones and growth factors that pass to the fetus and regulate osteogenesis.[7] Future studies will elucidate the underlying cellular and molecular mechanisms.

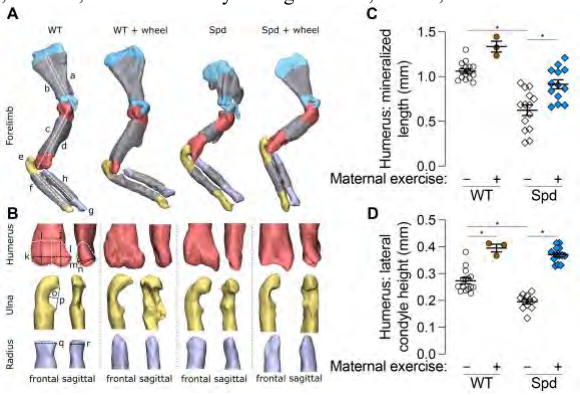

Figure 1. Maternal exercise rescues the effects of fetal akinesia-induced skeletal deformities. (A,B) *Optical projection tomography reconstructions showing forelimb morphogenesis.* ***(C,D)*** *Quantifications of humerus mineralized length and lateral condyle height. * = p<005.*

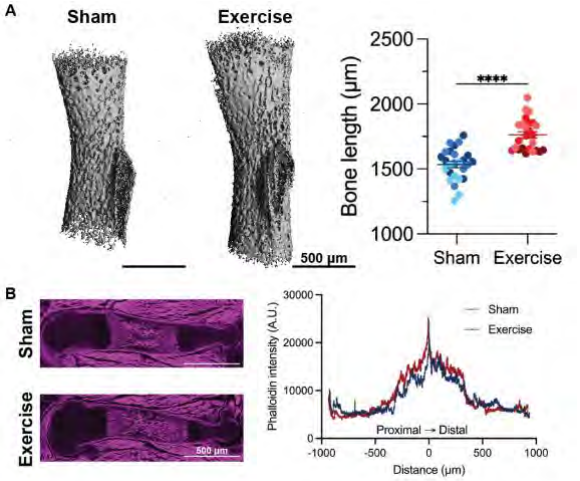

Figure 2. Maternal exercise promotes osteogenesis in WT mice. (A) *μCT reconstructions of the humerus with bone length quantification. **** = p<0.0001.* ***(B)*** *Phalloidin staining with intensity quantification.*

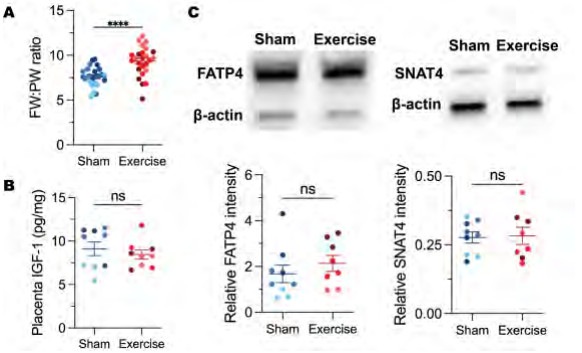

Figure 3. Maternal exercise affects placental transport efficiency, but not nutrient transporter expression. (A) *Fetal weight to placental weight (FW:PW) ratio. **** = p<0.0001.* ***(B)*** *Normalized IGF-1 expression.* ***(C)*** *Western blots for FATP4 and SNAT4 with quantifications.*

SIGNIFICANCE: Maternal exercise may function as a non-invasive, *in utero* therapeutic to treat the effects of fetal akinesia on skeletal development. Additionally, maternal exercise may represent a tractable model for studying developmental mechanobiology *in vivo*.

REFERENCES: [1] Nowlan+ *Eur Cell Mater* 2015; **[2]** Palacios+ *Teratology* 1990; **[3]** Ahmed+ *R Soc Open Sci* 2023; **[4]** Bober+ *Development* 1994; **[5]** Brett+ *Int J Mol Sci* 2014; **[6]** Collins+ *Dev Cell* 2023; **[7]** Babey+ *Nature* 2024

ACKNOWLEDGEMENTS: Work supported by the ERC EU's Seventh Framework Program [336306], NICHD [R01 HD113596], Penn IRACDA [NIH K12GM081259], Penn Center for Musculoskeletal Disorders [NIH P30-AR069691], and Penn Center for Undergraduate Research and Fellowships.

The Confusing Landscape of Orthobiologics

Scott A. Rodeo, MD
Hospital for Special Surgery

In recent years, there has been an explosion of interest in the use of "Orthobiologics" to treat symptoms in various difficult-to-treat conditions such as osteoarthritis, muscle injury, spinal disc disease, and tendinopathy. Interest is further heightened by the potential for these agents to augment structural tissue healing and even regenerate new tissue. The allure of "regenerative medicine" approaches has led to aggressive marketing and often indiscriminate use of these therapies. However, there are many unanswered questions and confusion remains due to: 1. Heterogeneity in current formulations, 2. Confusing terminology, 3. Aggressive marketing claims for unproven and unapproved therapies, and 4. Variable clinical outcomes data.

The single most important factor is likely the heterogeneity amongst different formulations. The composition and biologic activity is typically not quantified for a given dose, making it very difficult to know what the patient is really receiving. There are no universally agreed-upon markers of purity, potency, and biologic activity. We need to identify practical sentinel markers to allow characterization of the biologic activity of various formulations.

Variable nomenclature has also added to confusion. For example, autologous blood preparations include platelet-rich plasma (PRP), autologous conditioned plasma (ACP), autologous conditioned serum (ACS), platelet-rich fibrin matrix (PRFM), and alpha-2 macroglobulin (A2M). Cell therapy formulations, including cells derived from bone marrow, adipose tissue, and peri-natal sources such as umbilical cord blood and amniotic membrane, have been described as mesenchymal stromal cells, mesenchymal stem cells, and connective tissue progenitor cells. It should be understood that a true stem cell is a highly specialized cell, and all of the currently-available cell therapy formulations contain vanishingly few true stem cells by any cellular, molecular, or functional criteria.

The attraction of cutting edge "regenerative medicine" therapies, stem cells, etc. has led to aggressive marketing by commercial entities and even some medical providers. This is further aided by the economic incentive as these therapies are typically self-pay. These factors can lead to inaccurate and exaggerated claims for unproven therapies.

Lastly, as would be expected given the factors noted above, there is tremendous variability in the reported clinical outcomes of various orthobiologic therapies. Randomized trials in this area can be challenging because patients have a bias that these therapies work, and as a result are not willing to be randomized to a control group. There may also be a strong placebo effect in this area. Perhaps most importantly, only the minority of studies rigorously characterize and report the composition, biologic activity, etc. of the therapy that was actually given to the patient. Such information is critically important to correlate with clinical and imaging outcomes in order to improve our understanding of the risks and benefits of these therapies.

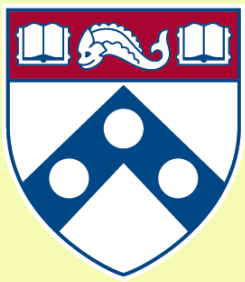

Penn Center *for*
Musculoskeletal Disorders
UNIVERSITY *of* PENNSYLVANIA

Other Research
(No P30 Core Use)
Abstracts

AM Session
Poster 1 to 21

Increasing Utilization Trends of Robotic-Assistance in Orthopaedic Surgery

Ponna A, Giakas A, Khoudary A, Uggla S, Ramtin S, Soliman Y, Illyas A

Abstract

Introduction

Robotic-assisted surgeries in orthopaedics have been increasing, particularly in hip and knee arthroplasty as well as spine surgeries. This study aims to evaluate the utilization of robotic-assisted orthopaedic surgeries and analyze the demographic and geographic distribution of patients undergoing these surgeries.

Methods

A retrospective cohort study was conducted of patients who underwent total hip arthroplasty, total and partial knee arthroplasty, or spine arthrodesis from 2017 to 2023 utilizing the TriNetX database. Relevant International Classification of Diseases, 10th revision (ICD-10) and Current Procedural Terminology (CPT) procedural codes identified patients who underwent a primary orthopaedic surgery with a corresponding robot-assisted code on the same day. Temporal trends in procedural volume were analyzed, and multivariate logistic regression assessed sociodemographic factors associated with receiving robotic surgery.

Results

A total of 809,802 patients were included, representing 1,072,714 surgeries, of which, 57,920 (5.1%) utilized robots. Overall, robotic surgery usage increased from 3.0% in 2017 to 6.7% in 2023 ($P < 0.0001$), with knee arthroplasties rising from 5.7% to 13.8% ($P < 0.0001$) and spine arthrodesis from 0.2% to 1.3% ($P < 0.0001$). Logistic regression demonstrated a statistically significant higher utilization among females (OR [Odds Ratio] 1.16), Asian patients (OR 1.15), and married individuals (OR 1.38). Black (OR 0.39) and Hispanic/Latino (0.63) patients were significantly less likely to receive robotic surgeries. Regionally, patients in the Midwest were significantly more likely to receive robotic-assisted surgeries compared to the Northeast (OR 2.43) while those in the South (OR 0.72) and West (OR 0.50) were significantly less likely.

Conclusions

Robotic-assisted surgery in orthopaedics have grown steadily in the subspecialties of hip and knee arthroplasty and spine surgery. Although advancements in surgical technology offer potential benefits, ensuring both clear demonstration of long-term clinical benefit and equitable access remains an ongoing challenge.

Evaluating the relationships between lesion size and location, muscle activation, and motor and cognitive impairment in stroke subjects

Azar R, Mendonca R, Cacchione P, Johnson M

Introduction:

Stroke is one of the most common causes of death and disability in America and in other countries around the world; on average, about 53 billion of dollars is spent every year to treat patients[1]. Stroke causes brain damage in the form of a lesion, which can be dissected into lesion size and location. Studies show that 77% of stroke survivors have upper limb motor deficits, and these deficits impede on stroke survivor's quality of life and function[2]. Stroke rehabilitation traditionally relies on "impairment-level treatments" based solely on their motor and cognitive performances, with an emphasis on motor performance[3]. After stroke, the neuronal damage can affect normal muscle activity in the affected limb. Electromyography (EMG), specifically surface EMG (sEMG), provides information about muscular activation, which can provide information on the biopotentials of affected muscles[4]. Even in subjects that have functional limbs, there is evidence that co-activation of agonist and antagonist muscles is not appropriate and leads to abnormal limb movements[5]. Furthermore, the literature supports that cognitive impairments may mask motor performance, which may lead to incorrect therapeutic intervention when relying on behavior alone[6-8]. Additionally, there is a relationship between brain structure and resulting function. Muscle activation and lesion metrics are left out of therapeutic decisions in traditional therapy, however, relying on behavior alone may lead to incorrect intervention techniques. Given that cognitive impairments may mask motor high motor performance, a subject may incorrectly categorize a patient's impairment level and possibly, therapeutic strategy. Thus, relying on behavior alone to assess function assumes a simplistic and unrealistic view of the brain. Robotic-assisted therapy is an emerging treatment for stroke patients, and feedback from these robots allows for a quicker and more personalized treatment plan. This study's goal is to collect lesion metrics from retrospective scans, acquire muscle activation through sEMG, and assess stroke subject impairment through robotic evaluation. We hypothesize that there is a relationship between lesion location and subject behavior. We also hypothesize that there is a relationship between muscle activation and lesion location.

Materials and Methods:
Subjects that had diagnosis of stroke were consented into the study. All subjects underwent robotic assessments with the Haptic Theradrive, a 1 degree of freedom (DOF) robot equipped with a crank arm that allows for movement of shoulder, elbow, and wrist. Muscle activation during robot activity were acquired using sEMG from the subject's impaired arm via two four-channel sensors (Trigno Quattro, Delsys, Inc., Natick, MA, USA), for a total of eight channels. The sEMG targeted muscles from the shoulder, elbow, wrist, and hand, covering flexion, abduction and extension to varying degrees. To collect lesion metrics, CT scans were acquired retrospectively from patient charts. ITK-SNAP was used to create the lesion masks. The Statistical Parametric Mapping (SPM Version 12) Clinical Anatomy toolbox in MATLA is used to register individual CT scans to a uniform space. After normalizing the images to a uniform space, ITK snap was used to compute lesion volume. To accomplish the goal of capturing whole brain regions of interest and subcortical brain regions, the Hammersmith 2003 atlwas was used. Region of interest volume involvement was acquired by using the layer tool in ITK Snap.

Results and Discussion:
Lesion metrics were harnessed from the radiological images of eleven subjects (70.3 ± 5.8 years old) manually. All subjects were 50 years or older, clinically diagnosed with stroke, had a CT scan, and able to voluntary move their upper extremity. All subjects were able to complete the robotic assessments with sEMGs equipped. Ten subjects had unilateral lesions, while eight subjects had bilateral lesions. Six of the identified lesions were characterized on the left brain, meanwhile four subjects displayed lesions on the right side of the brain. Interestingly, two subjects did not have identifiable lesions. The lesions spanned the entire brain, covering cortical, subcortical, and brain stem areas.

Conclusion: These preliminary results suggest that we can harness lesion metrics from acute CT scans, a contested topic in the literature. These results also suggest possible relationships between structure and function; however, a larger sample size is needed. Future analyses will be focused on understanding the connection between lesion location and muscle function (sEMG) and behavior (robotic assessments).

Acknowledgements
This work was made possible through the core services and support from the NIH-funded T32 grant (Training in Musculoskeletal Research), NIH-funded parent and diversity supplement grants R42 HD104325, University of Pennsylvania Fontaine Society, and the Departments of Bioengineering and Physical Medicine and Rehabilitation.

Financial Conflicts of Interest
Dr Michelle J Johnson and Dr. Rochelle Mendonca who are the PI and/or Co-I leading this study has a patent that uses devices inspired by the device being evaluated through this research. The PI is a co-founder of Recupero Robotics LLC.

DREAMER MRI for Pediatric Craniofacial Imaging: Rapid, Multi-Contrast, and Radiation-Free Assessment of Bone and Soft Tissue

Sina Dindarian[1], Brian-Tinh Duc Vu[1], Nada Kamona[1], Chamith S. Rajapakse[1], Scott P. Bartlett[2], Felix W. Wehrli[1]

[1] Department of Radiology, Perelman School of Medicine, University of Pennsylvania, Philadelphia, PA, USA
[2] Division of Plastic, Reconstructive and Oral Surgery, Children's Hospital of Philadelphia, Philadelphia, PA, USA

Introduction: Pediatric craniofacial imaging often requires both computed tomography (CT) for osseous detail and magnetic resonance imaging (MRI) for soft-tissue evaluation. This dual-modality workflow exposes children to ionizing radiation, increases cost, and complicates scheduling and image registration. We applied DREAMER MRI, a Dual Repetition and Echo Acquisition with Multi-contrast Encoding and Reconstruction sequence, recently developed in the authors' lab (Vu et al, Mag Res Med 2025) to achieve rapid, high-resolution, self-registered imaging of bone and soft tissue in a single scan. By providing CT-like bone detail alongside MRI-like soft-tissue contrast, DREAMER offers a radiation-free solution for comprehensive pediatric musculoskeletal assessment.

Methods: Nine pediatric subjects (10–17 years) with craniofacial or skull-base conditions including craniosynostosis, fibrous dysplasia, traumatic injury, and postsurgical reconstruction were scanned on a 3 T system using DREAMER. Acquisitions yielded isotropic (0.8–1.0 mm³) volumes in <3 min. Multi-contrast images were reconstructed into bone-selective, T_1-, and T_2-weighted volumes post-acquisition by judicious choice of the signal phase ψ. Bone contrasts were qualitatively compared with CT, and soft-tissue contrasts with conventional MR sequences (**Figure 1**). Automated 3D skull and soft-tissue segmentations were generated using a pre-trained U-Net model.

Results: DREAMER produced co-registered 3D datasets delineating osseous and soft-tissue structures. Bone-selective volumes closely matched CT morphology, revealing sutural fusion, cortical thickening, and dysplastic bone with high fidelity. T_1- and T_2-weighted reconstructions preserved muscular, vascular, and connective-tissue detail suitable for developmental and postoperative evaluation. Isotropic datasets enabled multiplanar reformation and surface modeling without additional registration. Automated skull segmentation showed consistent boundary accuracy across subjects, confirming reproducible bone contrast (**Figure 2**).

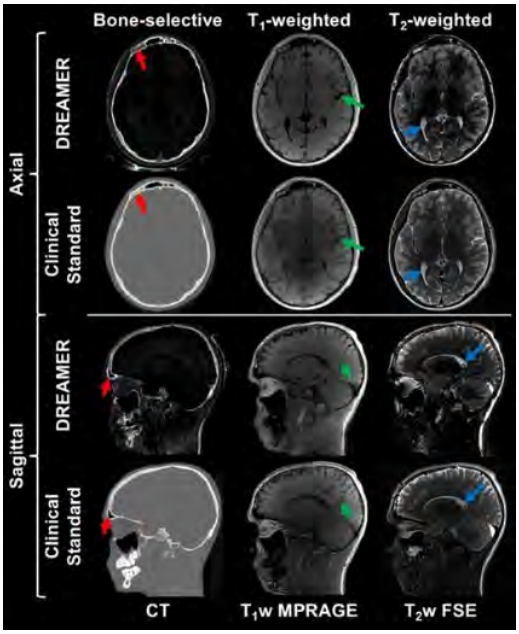

Figure 1. Comparison of DREAMER image contrasts with corresponding clinical standards in a 17-year-old male with a history of facial trauma. Bone-selective DREAMER images are compared with CT, while T_1-weighted and T_2-weighted DREAMER reconstructions are shown alongside conventional T_1-weighted MPRAGE and T_2-weighted multi-slice fast spin-echo (FSE) acquisitions ($\psi_{T1} = 114°$, $\psi_{T2} = 159°$). Comparable anatomical structures are visible across all modalities, including skull, cortical surfaces, and cerebrospinal fluid (highlighted by red, green, and blue arrows).

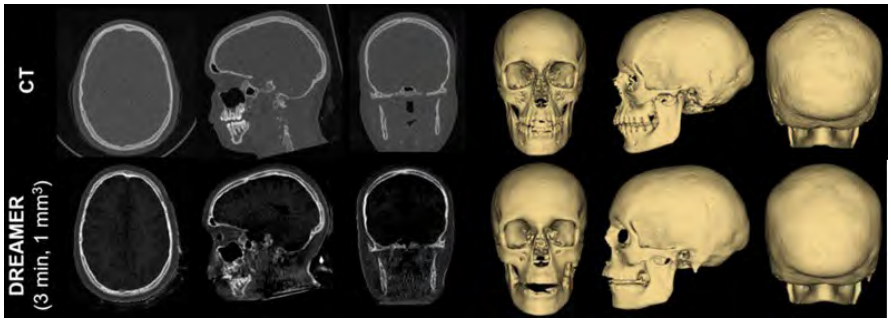

Figure 2. DREAMER bone-selective MRI validated against CT in a 16-year-old female with fibrous dysplasia and no prior cranial vault surgery. The strong bone-selective signal enabled automated 3D skull reconstruction using a pre-trained U-Net segmentation model.

Conclusion: DREAMER MRI enables rapid, radiation-free, multi-contrast visualization of bone and soft tissue in pediatric musculoskeletal imaging. It therefore has the potential to reduce dependence on CT, streamline imaging sessions, and improve assessment of craniofacial growth, surgical outcomes, and bone–soft-tissue interactions. Future work aims to adapt DREAMER to extremity and joint imaging for broader pediatric musculoskeletal application.

Effects of Age on Inflammation and Intervertebral Disc Tissue Morphology in the ADAM8-inactivation Mouse

Lutian Yao, MD, PhD*, Huan Wang*, Zuozhen Tian*, Frances S. Shofer, Ling Qin and Yejia Zhang
Hospital of the University of Pennsylvania.

Background. Back pain related to intervertebral disc (IVD) degeneration is a common clinical problem. Inflammatory cytokines and chemokines have been found in painful/degenerative human IVDs, and may account for some of the painful symptoms. A murine IVD injury model has been used to simulate the human disease, but an important question was raised whether older mice should be used to model the human disease, which is most prevalent in middle-aged people. The objective is to compare the effects of ADAM8 mutation on tissue responses to IVD injury in mice of different ages.

Methods. Inflammatory marker gene expression and morphological changes in response to IVD injury were compared between ADAM8 mutant (*Adam8*^{EQ}) and wild type (WT) mice. Specifically, mouse tail IVDs were injured at 3, 10 and 18 months of age, mice were sacrificed 1 week post injury, and IVD tissues harvested for histological and molecular studies.

Results. *Cxcl1*, *Il6*, and *Adam8* gene expression levels were higher in the injured tail IVDs of 3-month-old *Adam8*^{EQ} than WT mice ($p<0.01$); the injury-related differences are less marked following injury at > 3 months. Safranin O-staining was less intense in 10-month-old than in 3-month-old mice, in intact and injured IVDs ($p<0.01$), but no further decrease in 18-month-old mice of either genotype was observed ($p>0.05$; Fig. 1).

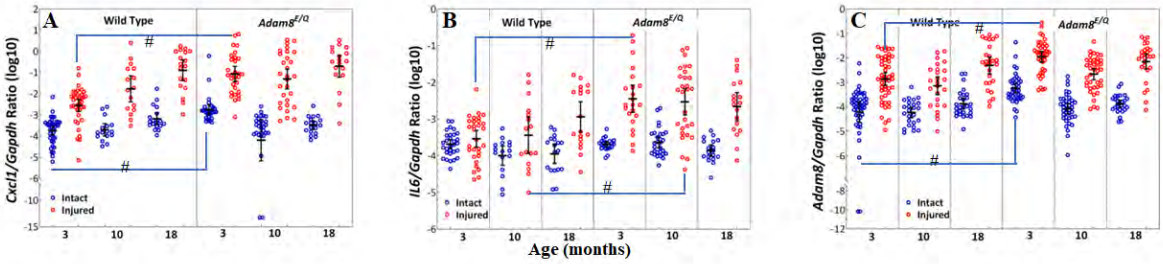

Figure 1. *Il6, Cxcl1* and *Adam8* Gene Expression in the 3-, 10- and 18-month-old wild type and Adam8-mutant (*Adam8*^{EQ}) Mouse Intervertebral Discs. A: *Cxcl1* gene expression; **B**: *Il6* gene expression; **C**: *Adam8* gene expression; Each symbol represents data from one mouse (wild type: n=38 mice for the 3 months age group; n=16 for the 10 months age group; n=18 for the 18 months age group; *Adam8*^{EQ} : n=30 mice for the 3 months age group; 29 for the 10 months age group; n=18 mice for the 18 months age group); intact discs are shown in blue, and injured discs in red; error bar: mean ± 95% confidence interval; $^{\#}p\leq0.01$.

Discussion. Herein, we have shown that significant differences in inflammatory marker gene expression between WT and *Adam8*^{EQ} mouse IVDs were detectable at age 3 months. However, these differences between mutant and WT mice were less evident at ages greater than 3 months. As expected, gene expression and disc morphology changed in response to injury in mice of both genotypes at all ages. Therefore, to identify differences in injury responses between WT and *Adam8*^{EQ} mouse IVDs, 3-month-old mice are superior to older mice.

*These authors contributed equally

Comparison of transport properties between human and tissue-engineered vertebral endplates

Brianna S. Orozco[1,2], Alexandra J. Baranyai[1], Matthew Fainor[1,2], Mohamed Habib[3], Aaron J. Fields[3], Sarah E. Gullbrand[1,2]
[1]University of Pennsylvania, Philadelphia, PA, [2]Corporal Michael J. Crescenz VA Medical Center, Philadelphia, PA, [3]Department of Orthopaedic Surgery, University of California, San Francisco, CA, USA

Disclosures: BSO (N) – brianna.orozco@pennmedicine.upenn.edu, AB (N), MF (N), MH (N), AJF (N), SEG (6)

INTRODUCTION: The vertebral endplates are the primary routes through which nutrients and metabolites enter and exit the intervertebral disc.[1] Changes in cartilaginous endplate (CEP) composition, including CEP fibrosis and calcification, can impair nutrient and metabolite transport[2,3] and associate with more severe disc degeneration.[4,5] As an alternative to spinal fusion surgery for the treatment of end-stage disc degeneration, our group has developed a composite tissue-engineered total disc replacement (eDAPS), which includes a porous poly(caprolactone) (PCL) scaffold as an endplate analog that provides an interface between the native vertebral bone and engineered disc. Our prior work has been focused on biomaterial modifications to this scaffold to promote integration *in vivo*; however, the transport properties of these engineered endplates in comparison to human endplates remains unknown.[6] Recapitulating the transport properties of healthy endplates will be essential to the long-term *in vivo* success of the eDAPS. We hypothesized that transport across engineered endplates would decrease with extracellular matrix deposition within the scaffold to reach equivalence with transport across healthy endplates.

METHODS: *Engineered endplate fabrication:* PCL endplate scaffolds (10 mm diameter x 1.5 mm in height) were fabricated according to a salt-leaching protocol and coated with hydroxyapatite (HA) according to our established protocols.[6,7] microCT and SEM imaging were used to characterize the formation of HA. HA-coated PCL scaffolds (n=6) were then seeded with goat mesenchymal cells and cultured in chemically defined media with TGF-β3 for 5 and 10 weeks to promote collagen and proteoglycan formation within the scaffold. *Human endplate acquisition:* Eight lumbar spines (L12-L5S1, 5 male, 3 female, 25-70yo) were obtained from human cadavers (Science Care and NDRI). T2-weighted MRIs were obtained for disc Pfirrmann grading, and T2 mapping was used to quantify nucleus pulposus (NP) T2 relaxation times.[8] Spinal motions segments (n=35) were dissected. From these segments, two cylindrical cores (10 mm diameter x 2.50 mm, n=66) were obtained that included the cartilage endplate and adjacent trabecular bone. *Passive diffusion experiments*: Human endplates (n=32), acellular HA PCL scaffold (n=6), and 5-week cell-seeded HA PCL scaffolds (n=4) were used for passive diffusion experiments using a custom diffusion chamber. The first passive diffusion experiment had an upstream chamber of 3.33 mg/mL of glucose (MW=180.16), following a second passive diffusion experiment of 1.1 mg/mL of sodium fluorescein (MW=367.27). From the experiments, triplicates of the downstream chamber were collected every hour for 6 hours. Fluorescence and absorbance were read via a microplate reader, and the concentration of the downstream chamber was calculated based on specific standard curves for each. Total diffusion was quantified by calculating the area under the curve (AUC). *Convection experiments:* A custom loading apparatus (**Figure 1A**) was used to control the driving hydraulic pressure against the native and engineered CEPs (4 mm diameter). The native human CEPs used in these tests were harvested from discs with a range of 93 < NP T2 < 236 ms. We applied a cyclic pressure (0.28–0.55 MPa) and sinusoidal frequency (0.5 Hz). The upstream solute reservoir had 0.1 mg/mL of sodium fluorescein; fluid and solute that passed through the CEPs were collected in a downstream reservoir containing PBS.[2] Permeation experiments were up to 80 minutes in duration. Outcomes included the net fluorescein transport and the hydraulic permeability.[2]

RESULTS: Passive diffusion experiments demonstrated that transport through tissue-engineered CEPs was variable but trended lower compared to native human CEPs. Cell-seeded HA PCL had significantly less glucose passive diffusion compared to endplates from degenerative discs, but not statistically different from endplates adjacent to healthy discs (**Figure 2B**). Sodium fluorescein passive diffusion was not statistically different across groups, but demonstrated that sodium fluorescein diffusion is variable within the 5-week cell-seeded HA PCL and that passive diffusion across cell-seeded HA PCL endplates trended higher than for acellular HA PCL (**Figure 2C**). Acellular HA PCL and 10-week cell-seeded HA PCL had significantly higher hydraulic permeability compared to native human CEPs (**Figure 1B**). For CEP porosity, acellular HA PCL had significantly lower porosity compared to native human CEPs (**Figure 1C**).

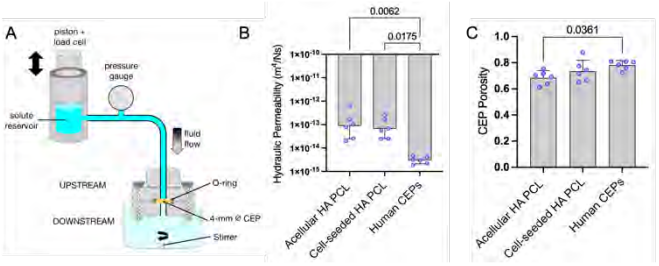

Figure 1. (A) Schematic of custom loading apparatus. (B) Hydraulic Permeability and (C) CEP Porosity for each experimental group.

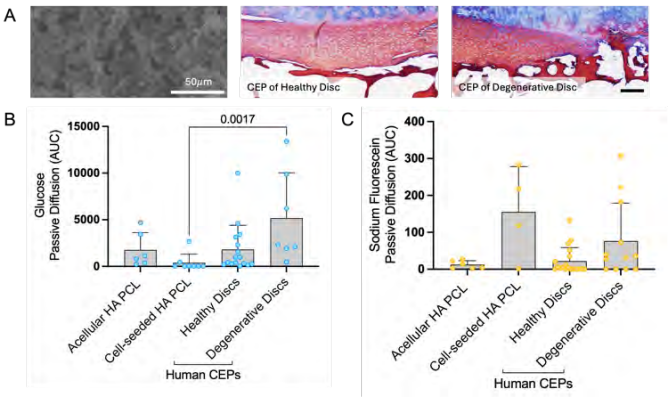

Figure 2. (A) SEM image of HA PCL scaffold and CEP histology images (Mallory Heidenhain). (B) Glucose and (C) Sodium Fluorescein passive diffusion for experimental groups. Endplate scale = 555 μm.

DISCUSSION: Passive diffusion experiments demonstrated trending reductions in glucose diffusion and increases in sodium fluorescein diffusion following chondrogenic pre-culture of MSC seeded endplates. Future work will quantify water, proteoglycan and collagen content to help explain some of these differences. In addition, we plan to study the effects of longer durations of endplate pre-culture (10 weeks) to determine how matrix maturation within the endplates affects diffusion. Endplates adjacent to degenerative discs also exhibited trending increases in diffusion compared to endplates adjacent to healthy discs, yet importantly, diffusion across engineered endplates was more similar to diffusion across endplates adjacent to healthy discs versus degenerative discs. The low hydraulic permeability of healthy human CEPs is consistent with the dense, negatively charged extracellular matrix, which resists fluid flow. With higher hydraulic permeability, the engineered CEPs had less resistance to fluid flow compared to native human CEPs, which may lead to greater convective transport. This may improve nutrient transport into tissue-engineered total disc replacements, but may come at the expense of increased creep deformation under physiologic loading. CEP porosity is an important factor that influences hydraulic permeability and solute transport[2]. Despite engineered CEPs having higher permeability, they have low porosity, which indicates that other factors affect permeability. Potential factors affecting permeability can include matrix maturity and cross-linking/fiber anisotropy. Future studies will focus on tuning factors that control porosity and permeability for engineered CEPs while also taking into consideration the contribution to biomechanical creep.

SIGNIFICANCE: Overall, the results from this study can inform design improvements to the endplate interface of composite, tissue engineered disc replacements to enhance their long-term in vivo performance. Ultimately if successful, composite engineered disc replacements such as the eDAPS offer a promising alternative to fusion surgery for patients with end-stage disc degeneration and back pain.

REFERENCES: [1] Maroudas+ *J. Anat*., 1975 [2] Sampson+ *J. of Biomechanics*, 2018 [3] Benneker+ *Spine*, 1976 [4] Antoniou+ Spine 1996 [5] Bonnheim+ Eur Spine J 2022 [6] Fainor+ *Cells Tissues Organs*, 2023 [7] Kim+ *Acta Biomater, 2020* [8] Ashinsky+ *J. Anat*., 2020

ACKNOWLEDGEMENTS: This study was supported by the Department of Veterans Affairs and the ORS Spine Section Travel Fellowship.

Simultaneous hard and soft tissue contrast musculoskeletal magnetic resonance imaging

Emily Baccaglini[1,2], Brian-Tinh Duc Vu[1,2], Nada Kamona[1,2], Chamith S. Rajapakse[1], Felix W. Wehrli[1]
[1]*Department of Radiology, Perelman School of Medicine, University of Pennsylvania, Philadelphia, PA*
[2]*Department of Bioengineering, School of Engineering and Applied Sciences, University of Pennsylvania, Philadelphia PA*

Purpose: Musculoskeletal (MSK) imaging involves assessment of skeletal and soft tissue anatomy, therefore, typically CT is required to assess bone, and MRI to assess soft tissue. The use of both modalities incurs longer patient examination times, increased scheduling complexity, and image co-registration and post-processing. This study proposes an MRI pulse sequence, DREAMER[1] (Dual Repetition and Echo Acquisition with Multi-contrast Encoding and Reconstruction), capable of generating multiple contrasts, including bone-selective, T_1-weighted, and T_2-weighted imaging. Moreover, levels of soft-tissue contrast are user-customizable at reconstruction. DREAMER combines the benefits of MRI and CT, simplifying clinical workflow in MSK applications and bypassing the need for ionizing radiation.

Methods: DREAMER modifies a dual-echo UTE sequence with an RF phase schedule driven by a small phase increment[2, 3], which encodes T_2-weighting along the phase of the steady-state magnetization. To remove background phase, $\varphi(\boldsymbol{r})$, induced by inhomogeneities in the static field and RF pulse excitation, the scan is repeated with the reversed sign of the steady-state signal phase[2, 3]. Hence, $\boldsymbol{x} = \frac{1}{2}\left[\boldsymbol{x}_{+}e^{-i\varphi(r)} + \left(\boldsymbol{x}_{-}e^{-i\varphi(r)}\right)^{*}\right]$, where $\boldsymbol{x}$ is the multi-contrast signal simultaneously encoding T_1- and T_2-weighting. Contrast is extracted by taking the component of the complex-valued image along an angle ψ, where $\boldsymbol{x}_{\psi} = \left|\Re\left(\boldsymbol{x}e^{i\psi}\right)\right|$. Modulation of ψ adjusts the T_1- or T_2-weighting of the resulting image $\boldsymbol{x}_{\psi}$. Additionally, images $\boldsymbol{x}_{\mathrm{UTE}}$ and $\boldsymbol{x}_{\mathrm{CTE}}$ are acquired during each TR from ultrashort and conventional echo time (UTE and CTE) readouts, which are used to isolate the bone signal as $\boldsymbol{x}_s = \frac{|x_{\mathrm{UTE}}| - |x_{\mathrm{CTE}}|}{|x_{\mathrm{UTE}}| + |x_{\mathrm{CTE}}|}$. Imaging was performed at 3T and implemented using golden-angle ordering and a center-out, ramp-up radial trajectory, an isotropic voxel size of 0.75 mm^3, field-of-view of 279 mm^3, and scan duration of 8 minutes[1]. SENSE-model reconstruction was performed with joint-L_0 wavelet regularization.

Results: DREAMER yields four image types: multi-contrast magnitude, T_1-weighted, T_2-weighted, and bone-selective, as shown for the knee in **Fig.1**. After acquisition, user-driven contrast extraction of T_1- and T_2-weighted images via modulation of ψ results in images with various soft tissue contrasts.

Conclusion: DREAMER performs simultaneous imaging of musculoskeletal solid and soft tissues, potentially obviating the need for additional CT imaging, thereby eliminating the use of ionizing radiation in clinical settings and removing logistical complexities related to scheduling examinations.

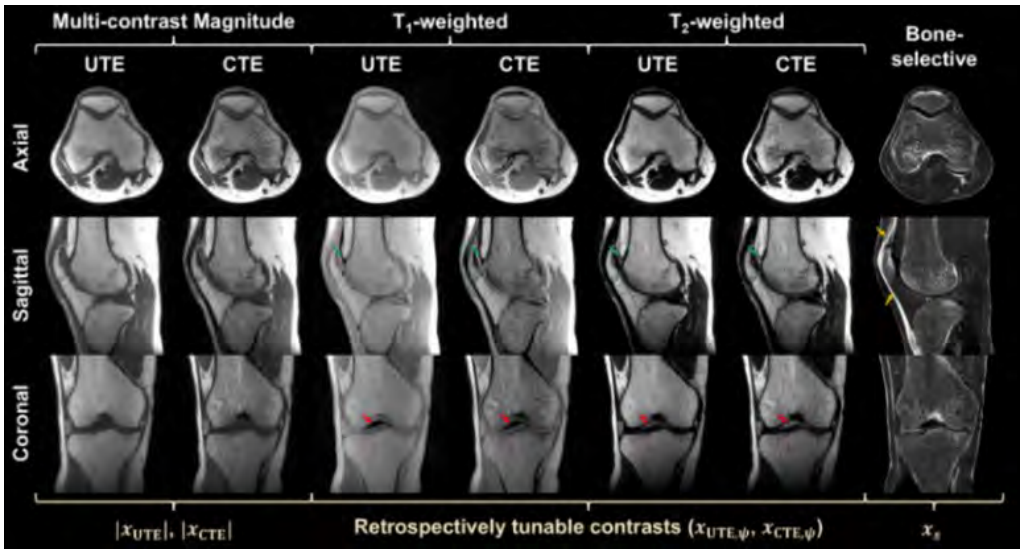

Fig 1. DREAMER acquisition at the right knee (25 y.o. healthy male). Synovial fluid appears dark on T_1w imaging and bright on T_2w imaging (ψ_{T1} = 117°, ψ_{T2} = 168°), visualized in the joint space between the femur and the tibia (red and green arrows). Quadriceps and patellar tendons (orange arrows), which have short T_2, are visualized in the bone-selective image.

References: **[1]** Vu BTD, Kamona N, Wehrli FW, Baccaglini E, Rajapakse CS. DREAMER: Rapid, high-resolution, and simultaneous multiple contrast magnetic resonance imaging of solid and soft tissues. Proc ISMRM 2025 May; Abstract #1278. **[2]** Tamada D, Field AS, Reeder SB. Simultaneous T(1) -weighted and T(2) -weighted 3D MRI using RF phase-modulated gradient echo imaging. Magn Reson Med 2022;87(4):1758-70. Epub 20211109. doi: 10.1002/mrm.29077. PubMed PMID: 34752639; PMCID: PMC9006307. **[3]** Wang X, Hernando D, Reeder SB. Phase-based T(2) mapping with gradient echo imaging. Magn Reson Med. 2020;84(2):609-19. Epub 20191224. doi: 10.1002/mrm.28138. PubMed PMID: 31872470; PMCID: PMC7180093.

Incidence and Predictors of Ulnar Neuropathy Within 12 Months Following Distal Humerus Fracture Fixation: A TriNetX Multi-Institutional Analysis

Ginder J, IIyas, Asif

Background

Ulnar neuropathy is a prominent complication after distal humerus fracture (DHF) fixation. Reported rates in literature are variable depending on the surgical approach and reporting methodology. This study aimed to quantify the incidence of postoperative ulnar neuropathy within 12 months of DHF fixation using a large multi-institutional database, while exploring potential reasons for discrepancies between our findings and previously published rates.

Methods

A retrospective cohort study was performed using the TriNetX Research Network, encompassing de-identified electronic health records from participating healthcare organizations. Adult patients undergoing operative fixation for DHF were identified using a combination of ICD and CPT codes. Those with pre-existing ulnar neuropathy were excluded. The primary outcome observed was ulnar neuropathy diagnosed within 12 months following surgical repair. Incidence was stratified by age group and fracture location.

Results

A total of 8,487 patients met inclusion criteria. The overall 12-month incidence of ulnar neuropathy was 6.3%. Incidence by age range was 7.2% (30–49 years), 6.6% (50–69 years), 4.6% (70–89 years), and 4.4% (>65 years). When stratified by CPT code, ulnar neuropathy rates vary across procedure types. Patients undergoing fixation for bicondylar distal humerus fractures demonstrated the highest incidence (9.1%), while those treated for epicondylar fractures had the lowest (4.5%). Procedures involving transcondylar and supracondylar fracture fixation showed intermediate rates (5.5% and 5.2%, respectively).

Conclusion

This multi-institutional analysis observed overall ulnar neuropathy rates post DHF fixation lower than previous reported literature. Differences in rates were also observed across DHF location and age group. These findings highlight the variability in reported ulnar neuropathy post DHF fixation and the importance of contextualizing these outcomes. A deeper understanding of surgical outcomes such as post DHF fixation ulnar neuropathy can help enhance patient-physician decisions. These results provide a foundation for future work aimed at identifying modifiable risk factors and standardizing definitions of postoperative nerve injury.

Cell Source-Specific Extracellular Vesicles Direct Zone-Specific MSC Differentiation for Rotator Cuff Enthesis Regeneration

Zizhao Li[1], Catherine Cheung[1], Lin Xu[1], Sung-Han Jo[1], Se-Hwan Lee[1], Jayden Shin[1], Felicia Pinto[1], Ellie MacMullan[1], Jina Ko[1], and Su Chin Heo[1]
[1]University of Pennsylvania, Philadelphia, PA
lizizhao@seas.upenn.edu

DISCLOSURES: Li (N), Cheung (N), Xu (N), Jo (N), Lee (N), Shin (N), Pinto (N), MacMullan (N), Ko (N), and Heo (5-4WEB Medical Inc.)

INTRODUCTION: The rotator cuff is essential for shoulder stability and mobility, yet tears at the tendon-to-bone insertion (enthesis) are highly prevalent and remain notoriously difficult to repair **[1]**. Despite advances in surgical techniques, re-tear rates remain high due to the formation of mechanically weak scar tissue, poor vascularization, and the inability to replicate the highly specialized, multi-zonal architecture of the native enthesis **[3–4]**. This tissue interface is composed of tendon, fibrocartilage, and bone regions, each defined by distinct biochemical and mechanical cues, underscoring the need for strategies that can address this structural complexity. Cell-based approaches have been explored to improve healing, but challenges with cell survival, delivery, and regulatory translation limit their clinical utility. Recently, extracellular vesicles (EVs), lipid-bound nanoparticles (50–200 nm) that carry functional RNAs, proteins and signaling molecules, have emerged as a promising alternative **[5]**. EVs offer many of the paracrine benefits of their parent cells while avoiding many of the logistical and safety barriers of direct cell therapies [**6**]. Notably, EVs from diverse cell sources have been shown to promote tenogenic and chondrogenic differentiation, making them particularly attractive for musculoskeletal repair **[7–10]**. In this work, we systematically characterized EVs derived from three enthesis-relevant cell types: tenocytes (T-EV), chondrocytes (C-EV), and mesenchymal stem cells (M-EV). We further examined their effects on MSC proliferation and lineage commitment to assess their therapeutic potential for promoting zone-specific regeneration of the rotator cuff enthesis.

METHODS: EVs were isolated from passage-1 juvenile bovine tenocytes (T-EV), chondrocytes (C-EV), and mesenchymal stem cells (M-EV) using our optimized ultracentrifugation protocol **(Fig. 1A) [11–12]**. Particle size and concentration were quantified by nanoparticle tracking analysis (NTA), and morphology was examined via scanning electron microscopy (SEM, FEI Quanta). EV identity was confirmed by immunostaining with tetraspanin markers (CD9, CD63, CD81) and validated by direct super-resolution stochastic optical reconstruction microscopy (dSTORM, ONI Nanoimager). EV uptake by recipient bovine MSCs (bMSCs) was assessed using DiO-labeled (DiO: a lipophilic carbocyanine DiOC18) EVs. For cell migration analysis, scratch closure assays were performed on passage-1 bMSCs treated with T-EV, C-EV, or M-EV (3×10^4 EV/cell), and wound closure was quantified over 24 h. Cell proliferation was assessed by seeding bMSCs with the same EV treatments and quantifying metabolic activity using the Cell Counting Kit-8 on Days 1 and 3. For differentiation analysis, bMSCs were treated with each EV type, followed by RNA extraction (TRIzol) and RT-qPCR to evaluate tendon, fibrocartilage, and cartilage-associated genes (COL1A2, COL2, COL3, Tenascin-C), normalized to GAPDH.

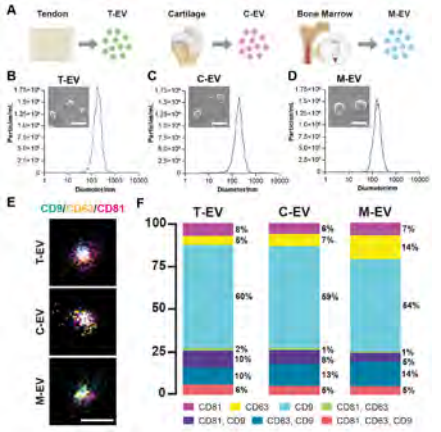

Fig. 1: (A) Schematic illustration of T-EV, C-EV and M-EV isolation process. (B-D) Quantitative NTA results and SEM images of T-EV, C-EV, and M-EV (scale bar = 200 nm). (E) Representative STORM images of individual T-EV, C-EV, and M-EV (Green: CD9, Yellow: CD63, Red: CD81; scale bar = 200 nm). (F) Tetraspanin co-localization analysis of T-EV, C-EV, and M-EV.

RESULTS: SEM confirmed successful isolation of T-EV, C-EV, and M-EV, which exhibited predominantly spherical to ovoid morphology with diameters <200 nm **(Fig. 1B-D)**. NTA analysis revealed mean particle sizes of 196.8 nm, 182.4 nm, and 195.2 nm, respectively. Super-resolution imaging (dSTORM) verified the presence of canonical EV tetraspanins (CD9, CD63, CD81) across all groups, with comparable distributions of single-, double-, and triple-positive subpopulations **(Fig. 1E-F)**. Among single-positive vesicles, CD9 predominated (T-EV: 60%, C-EV: 59%, M-EV: 54%), while CD9/CD63 was the most frequent double-positive subset (T-EV: 10%, C-EV: 13%, M-EV: 14%). DiO labeling demonstrated efficient uptake of all EV types by recipient bMSCs, with fluorescence distributed throughout the cytoplasm **(Fig. 2A)**. Functionally, EV supplementation significantly enhanced MSC motility, as evidenced by accelerated wound closure in scratch assays at 0 and 12 hours compared with untreated controls **(Fig. 2B-C).** Proliferation analysis revealed modest but consistent increases in MSC growth across all EV-treated groups, whereas control cells expanded more slowly over the same time points **(Fig. 2D)**. Gene expression analysis demonstrated distinct lineage-specific effects among the EV types. T-EV and M-EV treatment significantly upregulated Tenascin-C and COL3 compared to control and C-EV groups, reflecting enhanced tenogenic and fibrocartilaginous cues **(Fig. 3A)**. Notably, M-EV induced the highest expression of the chondrogenic marker COL2 (1.5–3-fold increase), whereas C-EV most strongly promoted COL1A2 expression **(Fig. 3A)**.

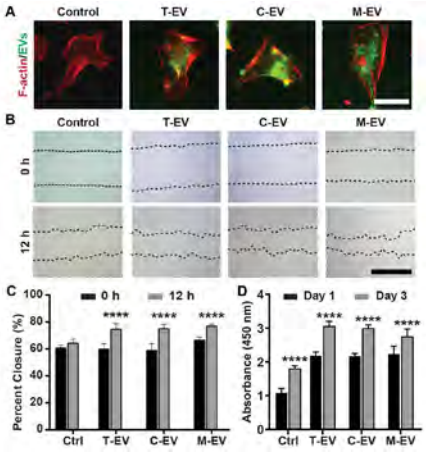

Fig. 2: (A) Representative fluorescence images of bMSCs treated with T-EV, C-EV, and M-EV (bar = 50 µm). (B) Representative images of scratch assay in bMSCs treated with T-EV, C-EV, and M-EV over 24 hours (scale bar = 1 mm). (C) Percent cell closure over 24 hours (*: $p < 0.05$, **: $p < 0.01$, ****: $p < 0.0001$). (D) Proliferation of bMSCs treated with T-EV, C-EV, and M-EV, determined by CCK8 assay (****: $p < 0.0001$, n = 5/group, mean ± SD).

DISCUSSION: This study systematically evaluated the functional potential of bovine-derived EVs from tenocytes (T-EV), chondrocytes (C-EV), and mesenchymal stem cells (M-EV) to direct MSC behavior in vitro, providing new insight into their application for rotator cuff enthesis repair. Comprehensively characterized confirmed nanoscale morphology and canonical tetraspanin markers across all EV types, which were efficiently internalized by MSCs without adverse effect. Functionally, all EV groups enhanced MSC migration and proliferation compared to untreated controls, underscoring their biocompatibility and general pro-regenerative effects. Importantly, gene expression profiling revealed source-dependent differentiation cues. M-EV strongly promoted chondrogenic and tenogenic markers, T-EVs favored tenogenic and fibrogenic signatures, and C-EV induced fibrous and cartilage-related genes. These results suggest that EV cargo reflects the molecular identity of the donor cell and can selectively bias MSC lineage commitment. Such source-dependent effects highlight the potential of EV-based therapies to achieve spatially tailored regeneration of the multi-zonal enthesis, where tendon, fibrocartilage, and bone must be restored in a coordinated manner. Future work will employ proteomic and transcriptomic profiling to define the molecular cargo of these vesicles and guide the design of zonal biomimetic scaffolds incorporating specific EV subtypes. Together, these findings establish EVs as promising non-cellular therapeutics capable of orchestrating zone-specific differentiation, addressing one of the major challenges in rotator cuff repair and tendon-to-bone integration.

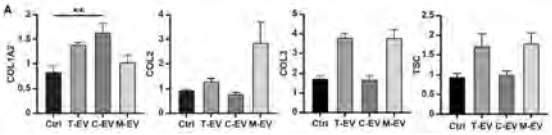

Fig. 3: Gene expression in bMSCs treated with T-EVs, C-EVs, and M-EVs on day 7, normalized to GAPDH (**: $p < 0.01$, n = 5/group, mean ± SD).

SIGNIFICANCE: This work establishes a non-cellular, EV-mediated strategy to promote lineage-specific differentiation of MSCs, offering a promising platform for zone-specific tendon-to-bone interface regeneration. By harnessing the intrinsic bioactivity of cell source–dependent EVs, and integrating them into biomaterial systems, this approach may overcome current limitations in enthesis repair and accelerate translation toward clinically relevant therapies.

REFERENCES: [1] Apostolakos+, *M.L.T.J.* 2014; [2] Sahoo+, *JSES Int.* 2015; [3] Sambandam+, *World J Orthop.* 2015; [4] Oh+, *Clin Orthop Surg.* 2018; [5] Nakase+, *Sci Rep.* 2016; [6] Zou+, *J. Nanobiotechnology* 2023; [7] Kodama+, *Bone Rep.* 2022; [8] Xu+, *CT.* 2019; [9] Yu+, *Acta Biomater.* 2020; [10] Connor+, *J. Bone Miner.* 2019; [11] Ko+, *Adv. Biosyst.* 2020; [12] Reynolds+, *J of Extracellular Bio.* 2023.

ACKNOWLEDGEMENTS: This work was supported by NIH (P50 AR080581) and NSF (CMMI-1548571).

Emergent Cell Subpopulations and Time-Evolving Biophysical Cues in the Developing Porcine Meniscus

Meghan E. Kupratis[1,2], Jiaqi Xiang[3], Kevin G. Burt[1,2], Yuqi Zhang[1], Bryan Kwok[3,4], Sara F. Tufa[5], Douglas R. Keene[5], Nathaniel A. Dyment[1], Lin Han[3], Eiki Koyama[4], Robert L. Mauck[1,2]

[1]University of Pennsylvania, Philadelphia, PA, [2] CMC VA Medical Center, Philadelphia, PA, [3]Drexel University, Philadelphia, PA, [4]The Children's Hospital of Philadelphia, Philadelphia, PA, [5]Shriners Hospital for Children, Portland, OR

meghan.kupratis@pennmedicine.upenn.edu

Disclosures: RL Mauck (5, *4Web Medica*); no other disclosures

INTRODUCTION: Precise cell patterning and extracellular matrix organization are critical to establish and maintain proper function of dense connective tissues, such as the knee meniscus. Although robust, cell-mediated regeneration can occur various fetal connective tissues, this capacity declines rapidly with maturation and is largely absent in the adult meniscus.[1-2] Therefore, defining the molecular pathways and biophysical cues underlying initial formation and expansion of the meniscus during fetal development may reveal new strategies to promote endogenous tissue repair in adults. We demonstrated previously that regionalization of murine meniscus extracellular matrix (ECM) composition and cellular identity are established prenatally,[3-4] and that mechanical forces arising from cellular contraction and muscle loading are required for meniscus patterning and persistence.[5] However, the translatability of the murine model is limited due to the animals' short gestation time, small size, and resultant morphological distinctions relative to humans. To bridge this gap, we recently established a pipeline for timed acquisition of fetal Yorkshire pigs and determined the timing of joint formation and meniscus specification.[6] Here, we expand our porcine model by establishing the single-cell transcriptomic profile of meniscus progenitors as a function of gestational state and quantifying the concurrent emergence and evolution of multiscale ECM structure and micromechanical properties of the developing meniscus.

METHODS: All live animal work was carried out at the National Swine Resource and Research Center (NSRRC, Columbia, MS) under approved protocols. Yorkshire gilts (n=10, ~1yo) were artificially inseminated, and pregnancy was confirmed via ultrasound. Gilts were euthanized during the fifth (embryonic day E34), seventh (E45), ninth (E63-69), twelfth (E84), and sixteenth (P0) weeks of gestation. Animal sex was not delineated for prenatal time points. Hindlimb tissues were collected from the gilts at time of sacrifice. Hind limbs from ≥3 individual fetuses per time point were assayed in all experiments. Freshly isolated menisci were digested for single cell RNA sequencing (scRNA-seq, 10X Genomics).[7-8] Cellularity, proteoglycan distribution, and proteoglycan content were assessed via Safranin-O/Fast Green (SO/FG) and Alcian Blue/Picrosirius Red (AB/PSR) staining. Spatial gene expression was assessed by RNAscope *in situ* hybridization. Phalloidin staining and second harmonic generation (SHG) imaging were used to visualize actin and collagen fibril distribution in the transverse plane. Collagen fibril nanostructure was assessed using transmission electron microscopy (TEM). Atomic force microscopy (AFM) nanoindentation was performed in 1X PBS using polystyrene microspherical tips (Ø25μm, *k*~0.6N/m), and the effective indentation modulus (E_{ind}) was calculated from the finite thickness-corrected Hertz model. Differences between groups were assessed via two-way ANOVA with multiple comparison-corrected α=0.05.

RESULTS: Single cell transcriptomic profiling of meniscal tissues identified cell populations of mesenchymal, hematopoietic, and endothelial lineages. The majority (>80%) of profiled cells comprised a population enriched for classical fibrochondrocyte markers, including *COL1A1, COL2A1, COMP,* and *TNMD* (**Fig. 1a**). Further analysis of this population revealed distinct subpopulations high in canonical outer zone markers (including *TNMD* and *KERA*) vs. inner zone markers (such as *UCMA* and *TGM2*). The relative proportion of inner zone cells increased during late fetal development, from 10% at E45 to 35% by P0 (**Fig. 1b**). To better understand the spatial variation in these cells' transcriptome, we also sequenced cells from E84 menisci that had been segmented into putative inner and outer zones prior to digestion. In inner zone cells, this analysis uncovered enrichment of a *TNMD*-low population high in chondrogenic markers, including *COL2A1* and *HAPLN1* (**Fig. 1c-d**, cluster 0) and a smaller *TNMD*-low population with high expression of *PRG4* that may correspond to the emerging superficial layer (**Fig. 1c-d**, cluster 4). RNAscope *in situ* hybridization showed *COL2A1, ACAN, and TNMD* expression localized to the outer two-thirds of the meniscus and no staining in the inner zone (**Fig. 1e**). At the nanoscale, collagen fibrils were significantly thicker in the outer meniscus (p<0.0001, **Fig. 2a-b**), and fibril diameter within both regions increased with gestational age (p<0.0001). AFM nanoindentation revealed rapid stiffening of the primitive meniscus during mid- to late-gestation, with E_{ind} increasing 2-fold from E62 to E84 and an additional 3-fold by P0 (p<0.01, **Fig. 2c**). Furthermore, regional micromechanical distinctions were present by E45, such that the outer zone was significantly stiffer than the age-matched inner zone at all time points (p<0.01).

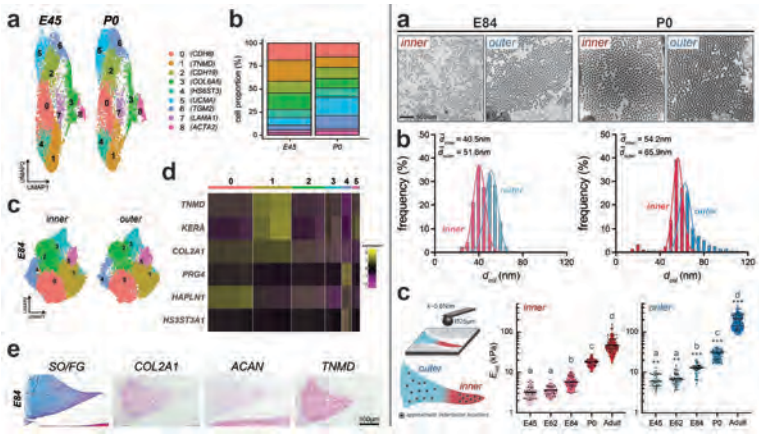

Fig. 1. Single cell transcriptomic analysis of developing meniscus. (a) Subpopulations of MFCs and **(b)** relative proportions, revealing expansion of inner zone cells later in gestation. **(c-d)** Sequencing of segmented inner and outer zone cells identified enrichment of *TNMD*-low cells in the inner zone. **Fig. 2. Nanostructural and micromechanical assessments. (a)** TEM images of E84 and P0 meniscal regions. **(b)** Collagen fibril diameter increased with gestational age and was greater in the outer zone. **(c)** AFM nanoindentation revealed zonal specification at E45 and stiffening within each zone during gestation.

DISCUSSION: This study demonstrates that transcriptional, ultrastructural, and micromechanical regionalization of the primitive meniscus are established early in fetal development. We show that porcine meniscus specialization occurs through rapid microenvironmental refinement during initial tissue formation and gestational growth. Namely, increased transcriptional heterogeneity emerges concurrently with the growth-mediated expansion and refinement of the extracellular matrix during gestation, particularly in the inner zone. Furthermore, high *in situ* expression of *TNMD* in the outer zone shown by RNAscope confirms our scRNA-seq data provides a degree of spatial information. Finally, the observed associations between microstructural and micromechanical properties of the inner and outer zones support a role for mechano-adaptation of meniscus progenitor cells during development. We previously observed greater intrinsic cellular contractility of embryonic porcine cells derived from the outer zone that increases with gestational age.[6] Together with the present findings, this observation suggests that residence within the stiffer, more aligned collagen microenvironment of the outer zone may prime meniscus progenitor cells towards enhanced mechanosensitivity and drive specification of cells distinct from those of the inner zone.

SIGNIFICANCE: This work provides insight to the transcriptional and biophysical mechanisms underlying meniscus formation and regional specification in a large animal model and reveals that regionalization of ECM and resident cells initiates early in embryonic development and is refined during prenatal growth.

REFERENCES: [1] Ionescu+ *Tissue Eng A*, 2011. [2] Qu+ *Sci Rep*, 2018. [3] Tsinman+ *FASEB J*, 2021. [4] Kwok+ *Acta Biomater*, 2023. [5] Tsinman+ *J Orthop Res*, 2023. [6] Kupratis+ *Trans ORS*, 2025. [7] Stuart+ *Cell*, 2019. [8] Knights+ *Ann Rheum Dis*, 2022.

ACKNOWLEDGEMENTS: This work was supported by the NIH (R01AR075418, P30AR069619, S10OD021633). The authors gratefully acknowledge Dr. Kristin Whitworth (NSSRC), Dr. Gordon Ruthel (Penn Vet Imaging Facility), and the CHOP Center for Applied Genomics Sequencing Core.

IMAGING BONE TISSUE COMPOSITION USING FOURIER TRANSFORM INFRARED (FTIR) HYPERSPECTRAL IMAGING

Amanda Peterman
Department of Biomedical Engineering, Stevens Institute of Technology
Dr. William Querido

Introduction: This study shows a new approach to image bone tissue composition at high resolution using minimally prepared samples. Bone tissue composition is a key factor underlying bone health—properties of the mineral phase (hydroxyapatite) and organic matrix (primarily collagen) are the building blocks of bone structure and mechanical function. [1] Fourier transform infrared (FTIR) imaging is a powerful label-free vibrational spectroscopy method to assess the chemical and molecular composition of samples. The FTIR spectrum shows the unique spectral fingerprint of the sample, where absorbance bands reflect the presence and relative amounts of components based on their inherent chemical bonds. In bone, analysis of spectral band intensities, shapes, and peak ratios can directly inform on tissue-level compositional properties key to bone function, such as mineral content, mineral crystallinity and maturity, and collagen integrity. [2] A current limitation in the field is that conventional FTIR imaging in transmission or transflectance modes require the sample to be thin-sectioned, which due to the mineralized bone matrix, is often cumbersome and produces artifacts such as loss of tissue. This study aims to address this limitation by applying ultrafast FTIR hyperspectral imaging in reflection mode to map bone tissue composition in thick specimens at high spatial resolution.

Methods: This experimental study analyzed cross-sections of mouse bone embedded in polymethyl methacrylate (PMMA) using the Bruker LUMOS II FTIR microscope, equipped with a focal plane array (FPA) detector. Non-contact reflection mode imaging was used with Kramers-Kronig correction, while attenuated total reflectance (ATR) imaging with a macro-ATR germanium crystal (1000 µm) required no correction. Spectral data were collected across a mid-infrared range of 1800-800 cm^{-1} with pixel resolution set to 5 µm for reflection and 1.25 µm for ATR imaging, targeting vibrational modes associated with hydroxyapatite, collagen, and PMMA. Cluster analysis maps were generated to visualize spatial distribution of different components.

Results & Discussion: FTIR spectra collected in reflectance of the thick PMMA-embedded bone had excellent quality, showing typical peaks of bone mineral and protein, as well as of the embedding PMMA (Fig. 1a). Hyperspectral imaging and cluster analysis was able to clearly identify and distinguish bone tissue from surrounding soft tissue and PMMA (Fig. 1b). Moreover, the high spatial resolution achieved by ATR imaging enabled identifying microporosity (each pore is 5–10 µm in diameter) throughout the tissues (Fig. 1c), based on the intensity of the PMMA peak present only inside of the pores (Fig. 1d). This pilot experiment shows the feasibility of applying this method to imaging bone tissue composition in minimally prepared samples, without the need to thin sectioning. Compared to recent studies using reflection-based IR imaging modalities [3], in which imaging a 20×20 µm region can take about 20 hours, the approach we describe here offer a much faster acquisition time, enabling imaging a 1500×1500 µm region in about 30 minutes.

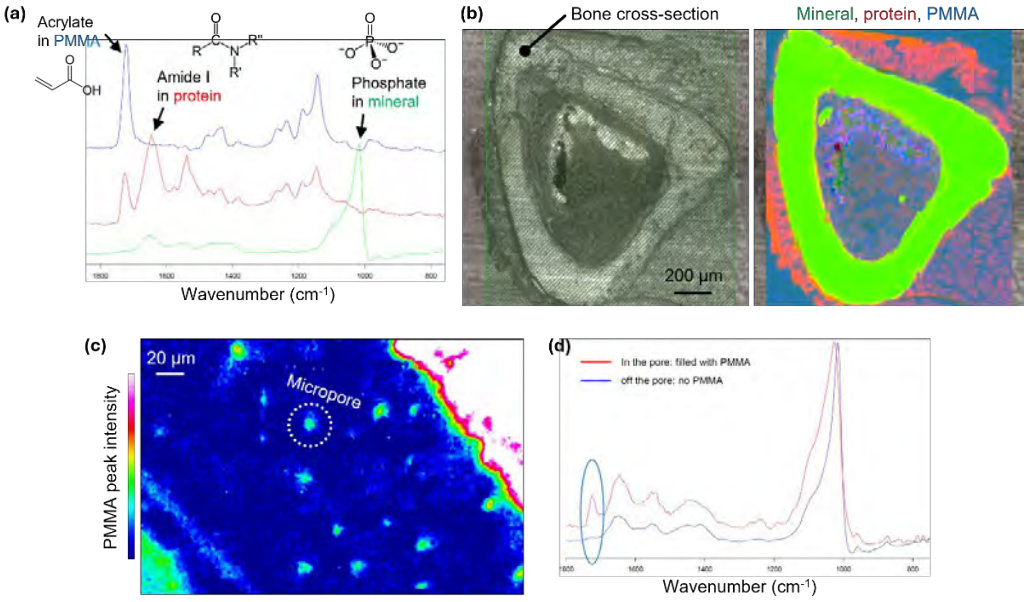

Fig. 1: (a) Typical FTIR spectra of bone tissue (green), surrounding soft tissue (red), and PMMA (blue). (b) FTIR imaging and cluster analysis identify and distinguish bone from soft tissue and PMMA. (c) ATR imaging based on the PMMA peak intensity shows bone microporosity at high resolution. (d) Spectra show the presence of PMMA inside of the tissue microporosity.

Impact: This work advances the field of biomedical imaging and bone tissue analysis by demonstrating the utility of reflection-based FTIR imaging as a valuable tool for characterizing the biochemical composition and microstructure of minimally processed bone.

Acknowledgements: Supported by NIH/NIAMS award R21AR082129

References: [1] Reznikov et al. Acta Biomater, 2014, 10(9):3815-26. [2] Querido et al. Molecules, 2021, 26(4):922.[3] Dev et al. JSBX, 2024, 100111

Natural vs Experimental Contamination of External Fixator Pins in a Sheep Model

Seongjue Ahn[1], Kaylee N. Philbrick[1], Samir Mehta[2], Thomas P. Schaer[1]
[1]Department of Clinical Studies New Bolton Center University of Pennsylvania School of Veterinary Medicine, Kennett Square, PA; [2]Department of Orthopaedic Surgery, University of Pennsylvania, Perelman School of Medicine, Philadelphia, PA
ahn13@upenn.edu

Disclosures: TPS (1-PSI, 2-Neuromed Vet, 1,3B,4,5-ReGelTec, 3B-Peptilogics, 3B,4,5-Acuitive Technologies, 3C-PAX Therapeutics, 3C-OrimTech, 3C,5-SINTX Technologies, 3C-OsteoCentric Technologies, 5-DePuy Synthes, 5 Stryker, 5-Alcyone Therapeutics, 5 Aravis, 5-Camber Spine, 6-Heraeus, Altus Spine, Elute, Vet-Len, Qentoros Inc.); SM (3B-DepuySynthes, Smith&Nephew, Stryker; 3C-Curvafix, AgNovos).

Introduction: Orthopedic-related infections (ORIs) cause significant economic impact and remain the leading cause of revision procedures following orthopedic implant placement in both humans and animals. Currently accepted models for evaluating ORIs include using abnormally high bacterial inoculation levels and lab-grown bacterial strains[1]. It is well known that even with proper surgical technique and postoperative management of external fixator pins, there is a high rate of pin tract infection, with a range of 45-71%[2,3] for localized infections with up to 4% developing osteomyelitis[2]. The pin site infection rate remains consistent across various postoperative pin care practices and is higher in periarticular pins or pins placed through larger soft tissue envelopes. Establishing a consistent model of a naturally occurring ORI can enhance the evaluation of both local and systemic immune responses to ORIs, as well as assess the effectiveness of proposed treatments. **Methods:** *Animal Model:* In this pilot study, four healthy, 2-year-old castrated male Dorset sheep were divided into two groups: Cohort 1 (natural infection, n = 2) and Cohort 2 (*S. aureus* inoculation, n = 2). Each animal underwent a mid-shaft tibial osteotomy stabilized with a half-pin monoplanar external fixator construct (2 pins proximal and 2 pins distal) without perioperative antibiotics. Cohort 2 was iatrogenically inoculated with 0.2 mL of *S. aureus* at 2.5×10^6 CFU/mL at each of the pin sites at the conclusion of the surgical procedure. Clinical monitoring involved daily exams and weight-bearing assessments. Pin sites were evaluated twice weekly for pain and sensitivity, swelling, heat, and redness, with results combined into daily scores. Radiographs, graded blindly for cortical lucency and periosteal reaction, were taken at scheduled intervals. Cohort 2 was euthanized at 4 weeks, Cohort 1 at 8 weeks, for postmortem analysis, including pin site histology and micro-CT **(Figure 1)**. *Inoculum Preparation: S. aureus* (ATCC 25923) was grown overnight in tryptic soy broth at 36.5°C with agitation (235 rpm). A 15 mL aliquot was centrifuged at 1200×g for 10 minutes; the supernatant was discarded. The pellet was resuspended in 10 mL sterile 1X Phosphate-Buffered Saline (PBS) by vortexing and diluted tenfold in PBS before Optical Density (OD) measurement at 600 nm. The bacteria were further diluted to an OD of 0.3, then subjected to three serial tenfold dilutions to reach 2.5×10^6 CFU/mL. Inoculum concentration was confirmed via colony counting. *Pathogen Identification:* Pins were sampled at post-op and during necropsy using aseptic technique **(Figure 1 B1&B2)**. At the time of sacrifice, microbial samples were taken from all pin sites and the tibial medullary cavity and immersed in 1 mL PBS, inoculated onto tryptic soy blood agar, and incubated overnight at 36.5°C. Pins were washed three times by vortexing in sterile PBS, sonicated at 40 kHz and 37°C for 10 min, and streaked onto blood agar. Selected colonies were subcultured on mannitol salt agar. **Results:** One sheep from Cohort 1 was euthanized at 2 weeks due to pin loosening and frame failure, leaving three sheep for analysis. Pin evaluation scores varied in severity and onset between cohorts. Radiographs **(Figure 2)** showed progressive bone changes consistent with septic pin tract infection in both groups. Radiographic scores were higher in Cohort 2 (iatrogenic infection) at 1 week, while Cohort 1 (natural infection) showed minimal changes initially but reached higher scores by 4-7 weeks compared to Cohort 2 at 4 weeks. Postmortem findings included mucopurulent discharge from all pin sites, notably copious at proximal sites in both cohorts. In Cohort 1, all pins were loose, and *S. aureus* was isolated from the pin sites. In Cohort 2, one sheep had all four pins loosened; the other sheep had only the proximal first and second pins loosened. On blood agar, all pins from Cohort 2 cultured positive for β-hemolysis, while 56% of pins from Cohort 1 were β-hemolysis positive. Subculture on mannitol salt agar revealed mannitol-fermenting bacteria on 38% of pins in Cohort 2 and 68% in Cohort 1. Overall, this indicates *S. aureus* was present in all pin site infections, with approximately 20% of pin site infections in Cohort 1 potentially co-infected with *S. epidermidis* **(Table 1)**. Remarkably, Cohort 1 showed signs of infection within 1 month, earlier than the 49-day average reported in our previous study involving a sheep cohort of 35 animals that received intravenous amikacin throughout the 18-week study period of a critical segmental defect fracture healing study stabilized with a uniplanar skeletal fixation frame[4]. **Discussion:** Both Cohort 1 and Cohort 2 exhibited clinically relevant features of pin site infection in sheep, although disease progression and severity differed between the cohorts. Cohort 1 experienced *S. aureus* infection 19 days earlier than in our previous study, highlighting the importance of experimental design in deciding whether to include systemic antimicrobial therapy when modeling clinical pin site infections. The high reproducible rate of pin tract infections is consistent with previous reports in human patients with tibia fractures stabilized with external skeletal fixation[5]. The risk of intramedullary infection of orthopedic hardware increases substantially following pin tract infection[6,7]. We observed all infections at the proximal pin sites with greater soft tissue coverage. The cranial tibialis muscle movement at the proximal pin sites contributes to a soft tissue-pin interface in constant motion. **Significance**: Our findings present the opportunity for a potential large animal model to study naturally occurring ORI, which can be used in future research to evaluate new technologies for reducing implant-related infections. A naturally occurring implant infection model removes the need for supraphysiological inoculum levels that are not reflective of clinical reality and reduces the burden on the investigative team. **References:** [1] Moriarty FT, et al. JOR. 2019 Feb. 37(2):271-287. [2] Kazmers NH, et al. Strat Traum Limb Recon. 2016. 11:75-85. [3] Sims M, et al. J Ortho Nursing. 2000 Aug; 4(2):59-63. [4] Boyes M, et al. VetSurg. ACVS Proceedings 2021. [5] Parameswaran, A. et al. J Orthop Trauma 2003 Aug. 17(7):503-507. [6] Clasper JC, et al. J of Orthop Research. 1999 17:947-952. [7] Maurer D, et al. JBJS (6):835-838. **Acknowledgements:** This work was funded by the U.S. Department of Defense DM220115 - CDMRP Award.

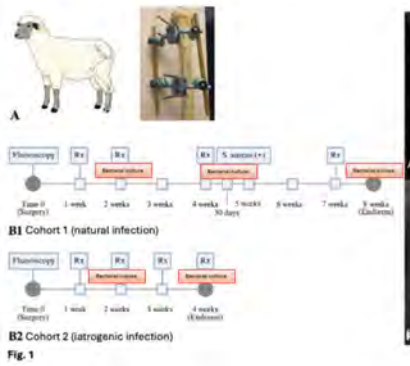

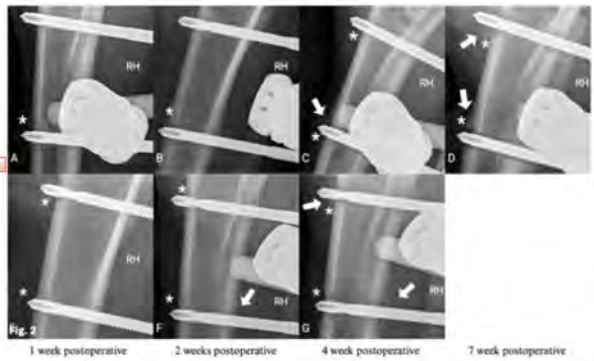

Table 1: Pin Site Microbial Culture Results

	Cohort1	Cohort2
Hemolysis		
α	20%	0%
β	56%	100%
γ	24%	0%
Mannitol Fermentation		
-	32%	63%
+	68%	38%
Organism		
Indeterminate	12%	0%
S. aureus	68%	100%
S. epidermidis	20%	0%

Figure 1. A: Diagram of tibial osteotomy model with half-pin external fixator box construct. **B1:** Cohort 1 imaging and infection confirmation (30 days postoperatively) timeline. Study duration was 8 weeks postoperatively. **B2:** Cohort 2 imaging timeline. Study duration was 4 weeks postoperatively. **Figure 2.** Caudocranial radiographs of the proximal first and second tibial pin sites at four timepoints: 1, 2, and 4 weeks postoperatively for both cohorts, and 7 weeks postoperatively for Cohort 1 only. **A–D:** Cohort 1. **E–G:** Cohort 2. Asterisks indicate cortical lucency; arrows indicate periosteal reaction around pin sites. **Table 1:** Infection in external fixator pins with reported incidences between 3% and 80% occurs when planktonic bacteria adhere to external fixator pins and subsequently produce a biofilm, which protects the bacteria from host defences. The most commonly implicated organisms are *Staphylococcus aureus* and *Staphylococcus epidermidis.* Both of these clinically relevant organisms were recovered from pin sites of animals in the naturally occurring infection cohort.

Using Machine Learning for Automated Femur Geometry Analysis in the Context of Atypical Femoral Fracture

Alyssa Rosen[1], Ruoyu Xu[1], Frank Pham[1], Stephen Falkner[1], Jonathan Gao[1], Jayden Yu[1], Maggie Jiang[1], Jason Li[1], Tania Lokesh[1], Olivia Rosen[1], Makayla Clark[1], Jason Xu[1], Iris Yang[1], Rashad Madi[1], Rebecca Willcocks[2], Ani Ural[3], Bruce Kneeland[1], Neil Sheth[1], Elena Taratuta[1], Rui Feng[1], Chamith S Rajapakse[1]

[1]University of Pennsylvania Perelman School of Medicine, Philadelphia, PA, [2]University of Florida, Gainesville, FL, [3]Villanova University, Villanova, PA arosen22@upenn.edu

Disclosures: Alyssa Rosen (N), Ruoyu Xu (N), Frank Pham (N), Stephen Falkner (N), Jonathan Gao (N), Jayden Yu (N), Maggie Jiang (N), Jason Li (N), Tania Lokesh (N), Olivia Rosen (N), Makayla Clark (N), Jason Xu (N), Iris Yang (N), Rashad Madi (N), Rebecca Willcocks (N), Ani Ural (N), Bruce Kneeland (N), Neil Sheth (N), Elena Taratuta (N), Rui Feng (N), Chamith S Rajapakse (N)

INTRODUCTION: Osteoporosis is a disease characterized by the deterioration of bone microarchitecture, decreased bone mass, and increased bone fragility. Bisphosphates are the standard pharmacological treatment for osteoporosis, but long-term consumption has been associated with adverse effects, including atypical femoral fracture (AFF). Femur geometry is also recognized as an important risk factor for AFF. For example, long-term bisphosphonate users with acute femoral neck-shaft angles were associated with AFF [1]. While X-ray analysis of proximal femoral geometry is valuable in the study of AFF prediction and diagnosis, manual landmark detection and measurement are labor- and time-intensive processes. To address this, we propose a convolutional neural network for fully automated landmarking and measurement of proximal femur geometry from X-ray.

METHODS: To train and evaluate the model, 382 anteroposterior pelvic radiographs from the publicly available Osteoarthritis Initiative (OAI) Dataset were used. For each image, 20 measurements were taken manually, including femoral medial and lateral cortical thicknesses, shaft width, head diameter, horizontal and vertical offsets, neck width, hip axis length, neck axis length, and neck-shaft angle for both left and right sides. The images were split into three datasets for training (n = 314), validation (n = 39), and testing (n = 40). Since the model was designed to learn the left femur measurements, each image was included in its original form in addition to a horizontally flipped version, effectively doubling the size of data. A convolutional neural network (CNN) with four convolutional layers and two fully connected layers was used. Each convolutional layer used 3x3 kernels and doubled the number of filters of the previous layer (except for the first layer, which used 32 filters), followed by a ReLU activation function and a 2x2 max pooling. The final feature maps were flattened and passed through a fully connected layer of 4096 units (with ReLU) and followed by a second fully connected layer with 11 units. Instead of directly predicting the 10 left femur measurements, the model produced 11 outputs corresponding to the coordinates of predefined landmark points in a relative coordinate system. In this system, the femoral head center (point A) served as the origin, and the femoral shaft axis defined the y-axis (Fig. 1). The ground-truth measurements were used to reconstruct the true locations of these points in the relative coordinate space, and the loss was computed as the sum of the L2 norms between each predicted point and its corresponding true point.

RESULTS SECTION: After training for 10 epochs, with the stopping point determined by early stopping based on validation loss, the model predicted each of the 10 left femur measurements with the following percent errors relative to the ground truth values for the testing set: 3.1 (femoral neck-shaft angle), 5.9 (femoral neck axis length), 6.1 (femoral head diameter), 7.1 (hip axis length), 7.9 (shaft width), 8.5 (femoral neck width), 9.3 (vertical offset), 10.9 (horizontal offset), 18.2 (lateral cortical thickness), 21.8 (medial cortical thickness). Figure 2 also shows the predicted (red) and true (blue) points in the relative coordinate space for one image.

DISCUSSION: The proposed model is able to efficiently extract the 10 measurements of interest. However, its accuracy is limited by the absence of explicit locational data. Because landmark coordinates were not manually annotated in the images, we had to rely on a relative coordinate system that preserved the geometric relationships among points but did not specify their actual positions within the radiograph. Future work could explore unsupervised key point detection models to enable the network to better capture the structural geometry of the hip and femur or incorporate explicit landmark annotations during training to provide locational guidance. Additionally, future work could involve a larger dataset to potentially improve model accuracy and contribute to its viability in clinical AFF prediction.

SIGNIFICANCE/CLINICAL RELEVANCE: This convolutional neural network automates femoral geometry landmark detection and measurement for potential use in AFF prediction.

REFERENCES: [1] Taormina DP, Marcano AI, Karia R, Egol KA, Tejwani NC. Symptomatic atypical femoral fractures are related to underlying hip geometry. Bone. 2014 Jun;63:1-6. doi: 10.1016/j.bone.2014.02.006. Epub 2014 Feb 21. PMID: 24565751.

IMAGES AND TABLES:

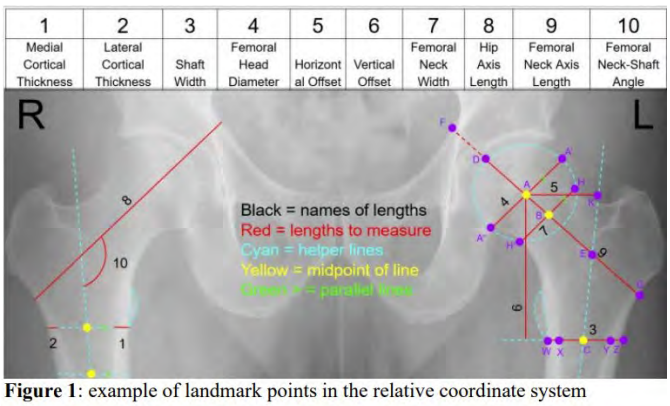

Figure 1: example of landmark points in the relative coordinate system

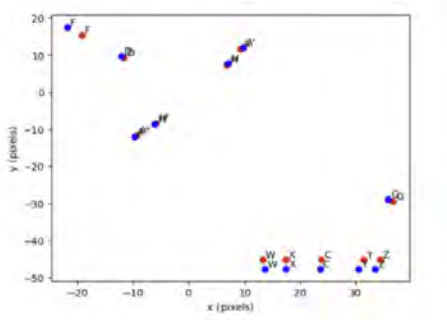

Figure 2: the predicted (red) and true (blue) points in the relative coordinate space for an image in the testing set

The Impact of Non-Tobacco Nicotine Dependence on Postoperative Outcomes Following Ankle Fracture Fixation

Ponna A, Mehta A, Mody K, Baidya J, Amponsah N, Thomas G, Pedowitz D, Daniel J, Parekh S

Introduction: Ankle fractures are among the most common orthopaedic injuries, frequently requiring surgical management through open reduction and internal fixation (ORIF). While the negative impact of cigarette smoking on bone healing is well established, the effects of non-tobacco nicotine dependence (NTND)—including the effects of electronic nicotine delivery systems (ENDS)—remain poorly understood. This study aims to evaluate the impact of NTND on postoperative outcomes following ankle ORIF.

Methods: A retrospective cohort study was conducted using the TriNetX database. Patients undergoing ankle ORIF (CPT: 27766, 27792, 27814, 27823) were divided into two cohorts: NTND (ICD-10: F17, excluding tobacco-specific subcodes) and nonsmokers (no history of nicotine use). Following 1:1 propensity score matching for demographic and comorbid conditions, postoperative outcomes were analyzed at 90 days and 2 years using risk ratios (RR) with 95% confidence intervals (CI).

Results: After matching, 7,549 patients were included in each cohort. At 90 days, NTND patients experienced significantly higher rates of opioid prescriptions (RR 1.30, 95% CI: 1.26 – 1.33), emergency department visits (RR 1.54, 95% CI: 1.40 – 1.69), inpatient hospitalizations (RR 1.27, 95% CI: 1.19 – 1.35), infections (RR 1.44, 95% CI: 1.17 – 1.77), wound complications (RR 1.48, 95% CI: 1.19 – 2.10), and pneumonia (RR 1.58, 95% CI: 1.19 – 2.10) (all $P < 0.005$). Over 2 years, NTND patients had increased risk of pseudoarthrosis (RR 2.49, 95% CI: 1.78 – 3.49), mechanical implant failure (RR 1.42, 95% CI 1.23 – 1.64), infection-related implant failure (RR 1.39, 95% CI: 1.17 – 1.67), and periprosthetic fracture (RR 1.38, 95% CI: 1.32 – 1.45) (all $P < 0.005$).

Conclusions: Non-tobacco nicotine dependence is associated with significantly higher rates of short- and long-term complications following ankle ORIF. These findings highlight the importance of preoperative screening and cessation counseling for patients with NTND to optimize surgical outcomes.

Deep Learning and Wearable Sensing Accurately Classify Tendon Loading in Immobilizing Boot Walking

Stanton Godshall[1], Michelle P. Kwon[1], Eni Halilaj[2], Lorraine AT Boakye[1], Casey Jo Humbyrd[1], Josh R. Baxter[1]
[1]University of Pennsylvania, Philadelphia, PA, [2]Carnegie Melon University, Pittsburgh, PA
stanton.godshall@pennmedicine.upenn.edu

DISCLOSURES: Stanton Godshall (N), Michelle P. Kwon (N), Eni Halilaj (N), Lorraine AT Boakye (1,9), Casey Jo Humbyrd (1,9), Josh R. Baxter (N)

INTRODUCTION: The Achilles tendon is the most frequently ruptured tendon, and incidence rates are increasing [1]. This injury causes permanent functional deficits in two of three patients [2]. To improve outcomes, clinicians have attempted earlier mobilization and loading to limit muscle atrophy and promote tendon regeneration [3]. Despite this innovation, recommendations remain generalized in the absence of evidence-based guidelines. We developed a wearable-sensing paradigm that uses an inertial measurement unit (IMU) secured to the immobilizing boot shortly after surgery to monitor patient activity. Our group uses a similar paradigm to accurately track step count and boot wear time, but those measures fail to capture the variability in tendon loading. Our force-sensing insole data reveal that rupture patients adopt varying strategies that differentially load the Achilles tendon. Some transfer less than 0.5 bodyweights through the tendon, while others exceed 2 bodyweights. These insoles, however, are impractical for clinical care or large studies because of their cost and burdens for patients. To overcome this, we built a custom one-dimensional (1D) convolutional neural network (CNN) that classifies IMU signals into low, medium, and high tendon-loading steps (<1, 1-2, and >2 bodyweights). This approach offers a scalable, low-burden alternative to force-sensing insoles and moves us closer to individualized rehabilitation guidelines after Achilles tendon rupture.

METHODS: We analyzed previously published data [4] from ten healthy adults (3 females, age 25+\-2.4, BMI 23.9+\-6.56) to establish proof-of-concept and plan a follow-up clinical study. This dataset included 6154 steps with paired force-sensing insole data and boot-mounted IMU data that were collected in a controlled laboratory environment. These steps span varying gaits (fast, medium, slow, and pathological) and heel wedges (0, 5, and 30 degrees). We trained 1D CNN models to classify tendon loading using an ordinal classification scheme (low <1 BW, medium 1-2 BW, high >2 BW). IMU signals were segmented and normalized prior to training, and step duration and boot wedge height were included as metadata. Hyperparameters (filter size, kernel size, fully connected nodes, and learning rate) selection and model evaluation were done via nested cross-validation. To reflect our intended deployment and to improve performance, we deliberately incorporated a small portion of each validation/test subject's data into training, enabling subject-specific calibration. This mirrors the clinical use case, where a brief in-clinic snapshot of tendon loading would be used to retrain a generalized model for individual patients.

RESULTS: Across all subjects, classification accuracy was 85.8+/-3.3% and balanced accuracy was 82.1+/-7.9%. Classification accuracy was highest for low- and high- load steps (sensitivities: 96.0%, 93.1%, respectively), with reduced accuracy for medium-load steps (sensitivity: 62.8%) (**Figure 1**). All misclassifications occurred with a neighboring class (**Figure 1**). Errors clustered near the decision boundary, with the average distance from a misclassified step to the nearest boundary being 18.1% bodyweight (**Figure 2**).

DISCUSSION: Our study demonstrates that 1D CNNs are good candidates to estimate Achilles tendon loading in an immobilizing boot with only IMU signals and wedge height. This approach lays the groundwork for future studies to continuously monitor Achilles tendon loading without relying on burdensome sensors that restrict data collection and patient inclusion. The model reliably distinguished low- and high-load gait patterns, suggesting potential to identify patient-specific strategies that modulate tendon loading in the early therapeutic window after rupture repair. Although overall accuracy metrics did not exceed 90% accuracy, most errors occurred near decision thresholds. We suspect that when summarizing over day- and week-long recovery periods, this model will provide sufficient granularity to support clinical decision-making. By connecting motion signals to tendon load, our findings highlight a promising direction for individualized rehabilitation monitoring. This study has several limitations. First, step segmentation relied on force-sensing insoles, limiting complete deployment in IMU-only applications. Additionally, models were trained with healthy subjects, and their generalizability to rupture patients remains unknown. Future work will focus on evaluating tendon load estimation using IMU-only segmentation, external validation in rupture cohorts, and identifying daily loading metrics that may guide long-term healing outcomes.

SIGNIFICANCE/CLINICAL RELEVANCE: This experiment is a necessary step towards developing precision rehabilitative care for patients with Achilles tendon ruptures. We expect that by linking real-world tendon loading to tendon healing and symptoms, we will establish evidence-based tendon-loading profiles that improve patient outcomes by supporting clinical decision making. Additionally, these data provide important practical rehabilitative information that can inform preclinical models and serve as clinically relevant outcome measurements for longitudinal clinical research.

REFERENCES: [1] Whitmore+, *Orthop J Sports Med*, 2025; [2] Brorsson+, *Am J Sports Med,* 2017; [3] Willits+, *J Bone Jt. Surg.,* 2010; [4] Kwon+, *Sci Rep*, 2023

ACKNOWLEDGEMENTS: This research was supported by NIH/NIAMS P50AR080581

IMAGES AND TABLES:

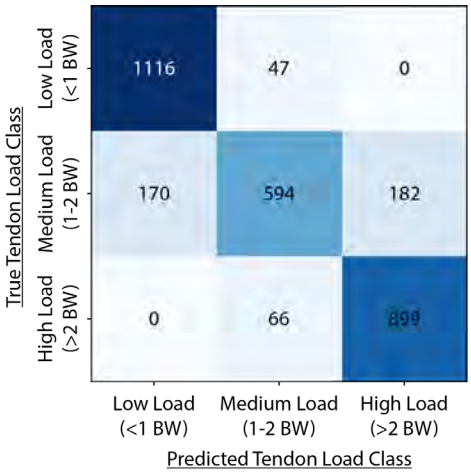

Figure 1. Confusion matrix showing classification performance. Correct predictions lie across the diagonal. Low load is never classified as high load.

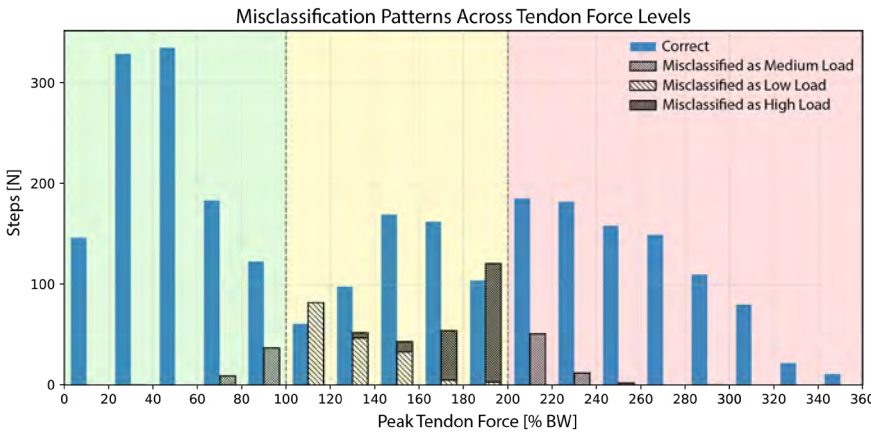

Figure 2. Histogram of classification outcomes by peak tendon force (% BW). Misclassifications are concentrated near threshold boundaries, indicating transitional ambiguity between load regions.

EPDA 2.0: Peptide-Responsive Synthetic Receptors for Spatial Gene Expression in 3D Materials

Kebisha Basukala[1], Matthias Recktenwald[1], Sebastián L. Vega[1,2]
[1]Department of Biomedical Engineering, Rowan University, Glassboro, NJ, USA
[2]Department of Orthopaedic Surgery, Cooper University of Rowan University, Camden, NJ, USA

Introduction

Precise spatial control of gene expression within biomaterials could transform musculoskeletal tissue engineering by directing bone and cartilage formation where needed. The Extracellular Peptide-ligand Dimerization Actuator (EPDA) is a modular synthetic receptor platform developed in the Vega Lab that enables cells to sense and respond to peptide ligands tethered to 3D biomaterials. The first-generation EPDA (Recktenwald et al., *ACS Synthetic Biology* 2024) demonstrated reversible activation and inhibition of split GFP through peptide-induced receptor dimerization, providing the foundation for dynamic cell-material communication. The second-generation system, EPDA 2.0, expands this capability by coupling ligand binding directly to transcriptional activation, enabling extracellular peptides to control gene expression and potentially drive lineage-specific differentiation.

Methods

EPDA 2.0 receptors were engineered with extracellular recognition domains for peptide epitopes and intracellular domains containing either a leucine-zipper recruitment motif or a kinase activation domain. The receptor includes a zinc-finger DNA-binding domain fused to a nuclear localization sequence (NLS) and an SH2 domain linked to the VP64 transcriptional activator. Constructs were transiently transfected into HEK293T cells and treated with cognate peptide ligands. Flow cytometry quantified YFP fluorescence as a readout of transcriptional activation.

Results

Ligand binding induced receptor dimerization, recruiting intracellular signaling components that translocated to the nucleus and activated YFP transcription. To date, we have demonstrated peptide-induced receptor dimerization that activates an internal phosphorylation circuit (EPDA 1.0) and ligand-induced transcriptional activation of a YFP reporter gene. Ongoing work focuses on integrating these modules into a unified receptor platform. Future studies will incorporate EPDA 2.0-programmed cells into 3D thiol-norbornene hydrogels, where patterned peptides will define transcriptional “on” and “off” zones mimicking native musculoskeletal tissues.

Conclusions

EPDA 2.0 establishes a programmable synthetic receptor platform that links extracellular biochemical cues to transcription, enabling localized control of cell fate within 3D biomaterials. By replacing YFP reporter with osteogenic (e.g., RUNX2) or chondrogenic (e.g., SOX9) targets, this system could direct region-specific differentiation to generate osteochondral interfaces and other musculoskeletal tissues. This ligand-responsive, spatially tunable platform represents a powerful new tool for engineering complex tissue architectures in regenerative medicine.

Mechanoregulation of endosome dynamics during endothelial cell motility

Paula Camacho, Erin Berlew, Devon E. Mason, Amber N. Stratman, Melike Lakadamyali, Joel D. Boerckel

Introduction

Mechanical stimuli and endothelial cell (EC) mechanotransduction are essential for vascular development. [1, 2] New techniques for measuring cellular forces combined with advances in RNA sequencing have enabled rapid progress in mechanobiology, with studies elucidating how mechanical cues drive cell function through changes in gene expression dominating the field. However, increasing evidence indicates that intracellular membranous organelles can receive, modulate, and even initiate mechanotransduction signaling.[3] Here, we investigated the mechanoregulation of endosomes during EC migration. Endosomes internalize proteins from the cell membrane and sort them for recycling or degradation. Thus, endosome trafficking plays crucial roles in cell signaling, polarization, and migration.

Small GTPases function as molecular switches that govern many fundamental cellular processes, including vesicular transport. They toggle between active (GTP-bound) and inactive (GDP-bound) states through activating GEFs and inactivating GAPs to enable spatially and temporally defined activation of downstream effector molecules.[4] The Rab family of small GTPases orchestrates endosome dynamics (e.g. identity, maturation, and motility) by localizing to diverse endosomal structures and recruiting various effectors. For example, Rab5, Rab7, and Rab11 mark early, late, and recycling endosomes, respectively.[5] Of the Rho family, RhoB localizes to endosomal membranes and has been shown to regulate vesicle motility.[6] In this work, we leveraged Rabs to track changes in endosome dynamics in response to mechanical perturbations and investigated the role of RhoB in EC migration.

Materials and Methods

We previously identified YAP and TAZ as mechanosensitive mediators of a feedback loop that modulates cytoskeletal tension and focal adhesion (FA) formation through transcriptional control of RhoA signaling. [7, 8] This homeostatic feedback loop is necessary for persistent EC motility and vascular morphogenesis. To identify the immediate transcriptional targets of YAP/TAZ mechanotransduction, ECs received either YAP/TAZ-silencing siRNA or scrambled control, were seeded onto 1 kPa or 18 kPa methacrylated hyaluronic acid (MeHa) hydrogels and collected for RNA-sequencing 4 hours after attachment. Transcriptional changes were analyzed using DESeq package in R and Gene Ontology. We identified genes whose mechanoresponsiveness on stiff substrates was ablated by YAP/TAZ depletion, revealing genes specifically regulated by YAP/TAZ mechanotransduction.

To characterize endosome mechanoregulation, we performed adhesion-spreading-polarization-migration (ASPM) assays on substrates of varying stiffness and migration assays on transfected or inhibitor-treated cells. ASPM assay was performed by seeding HUVECs onto 5 kPa or 30 kPa polyacrylamide (PA) hydrogels and fixing 4 hours later for immunocytochemistry. For wound migration assays, HUVECs received combinations of YAP, TAZ, RhoB-silencing siRNA, or scrambled control for 24 hours before or were treated with Blebbistatin or Y-27632 when migration was initiated. We measured the number, morphology, and localization of early, late, and recycling endosomes labeled with antibodies for Rab5, Rab7, and Rab11, respectively. We also used phalloidin and vinculin staining to characterize the actin cytoskeleton and FAs. Finally, we expressed fluorescently tagged Rab5, Rab7, and Rab11 using pcDNA transfer vectors and tracked endosome motility in inhibitor-treated migrating cells.

Results/Conclusions/Discussion (50-350 words)

RNA-sequencing revealed that YAP/TAZ depletion upregulated genes associated with Rho signaling and altered the expression of RhoA GEFs and GAPs, consistent with our previously described model of YAP/TAZ mechanotransduction. Interestingly, it revealed RhoB, Rab11b, and several Rab and Rho family GAPs and GEFs as direct transcriptional targets of YAP/TAZ mechanotransduction. Additionally, genes upregulated by YAP/TAZ depletion on stiff matrices were enriched for GO cellular component terms associated with the endomembrane system and endosomes. These data suggest that YAP/TAZ mechanotransduction regulates the endosomal system.

We next sought to determine how mechanical perturbations affect early, late, and recycling endosomes. Culturing cells on stiff substrates altered endosome distribution compared to soft substrates, especially of Rab5-positive endosomes. Both myosin and ROCK inhibition altered endosome distribution, morphology, and motility. Depletion of TAZ and YAP/TAZ increased Rab7 intensity compared to controls, with TAZ depletion also increasing Rab11 intensity compared to controls. Together, these data indicate that mechanical cues, cytoskeletal dynamics, and YAP/TAZ signaling regulate endosome function.

Finally, we knocked down RhoB to explore how altering endosome dynamics affects EC migration. Cell motility requires formation of new FAs at the cell's leading edge and coordinated adhesion disassembly at the trailing edge. In a wound migration assay, depletion of RhoB accelerated wound closure compared to control. RhoB-depleted cells had fewer and smaller vinculin+ FAs, suggesting that endosomal RhoB signaling regulates migration by coordinating FA dynamics.

Only limited knowledge exists regarding endosome mechanoregulation and their contribution to cellular mechanotransduction. Our data suggests that mechanical cues, through either YAP/TAZ signaling or cytoskeletal dynamics, regulate endosome function. Future studies will explore the molecular mediators of endosome mechanoregulation and validate our findings *in vivo*. Answering these fundamental questions will have broad implications for physiology and disease, as endosome dynamics dictate essential functions such as nutrient uptake, the rate of flow of signaling molecules, and collective cell migration.

References

[1] Barrasa-Ramos, el at. (2022) J R Soc Interface, 19:20220360. [2] Phng & Belting (2021) Semin Cell Dev Biol, 120:32-43. [3] Phuyal, et al. (2023) Trends Cell Biol, 33:1049-1061. [4] Müller & Goody (2018) Small GTPases, 9:5-21. [5] Wandinger-Ness & Zerial (2014) Cold Spring Harb Perspect Biol, 6:a022616. [6] Fernandez-Borja, et al. (2005) J Cell Sci, 118:2661-2670. [7] Mason, et al. (2019) JCB, 218:1369-1389. [8] Mason, Camacho, et al. (2024) eLife, 86668.2.

Chemical Targeting of Hypoxic Signaling to Enhance Chondrocyte Repair Potential

Samantha Ingerson[1], Stephanie Richardson-Solorazano[2], Ernestina Schipani[3], Justin Parreno[1,2]
1Department of Biomedical Engineering, University of Delaware
2Department of Biological Sciences, University of Delaware
3Department of Orthopedic Surgery, University of Pennsylvania

Osteoarthritis (OA) is a debilitating degenerative joint disease with limited reparative therapies. Current chondrocyte transplantation results in fibrocartilage, which is biomechanically inferior to native articular cartilage. Native cartilage is in a lower oxygenated environment, and previous studies demonstrated that hypoxia induces expression of cartilage matrix and suppresses expression of hypertrophic matrix molecules by monolayer passaged cells.

In this study, we aimed to chemically induce hypoxic cellular signaling in passaged chondrocytes to promote cartilage matrix deposition. Prolyl Hydroxylase Domain enzymes (PHDs) regulate the degradation of hypoxia-inducible factors (HIFs) in oxygen rich environments. Roxadustat is a hypoxia-inducible factor prolyl hydroxylase inhibitor developed for chronic kidney disease that pharmacologically mimics hypoxia under normoxic conditions, by preventing HIF-1a degradation. We hypothesize that Roxadustat will prevent HIF-1a degradation in passaged chondrocytes to stimulate the expression of cartilage matrix genes and prevent hypertrophy.

To assess Roxadustat's effect on chondrocytes, we exposed passage 2 chondrocytes cultured in a 2D monolayer to varying concentrations of Roxadustat (0–50 μM). Real-time RT-PCR analysis revealed a concentration-dependent increase in chondrogenic (aggrecan, chondroadherin, and Sox9) mRNA levels. Roxadustat also reduced proliferation molecule (Ki67) and degradative enzyme (Matrix Metalloproteinase 3) mRNA levels. Similarly, exposing passaged chondrocytes in 3D culture to Roxadustat, enhanced the expression of Collagen-2, Aggrecan, and Sox9 while repressing Collagen-X by 25 days of culture. Currently, we are assessing the efficacy of Roxadustat treatment on improving the quality of *in vitro* grown tissue by passaged chondrocytes. Triggering hypoxic signaling in passaged chondrocytes may lead to superior tissue engineered cartilage constructs.

HIF-1α controls somitogenesis and spine development by regulating levels of intracellular oxygen in the presomitic mesoderm.

Matthew J. Anderson[1], Angela Yao[2], Brittany Laslow[3], Ernestina Schipani[2,3], and Mark Lewandoski[1]
[1]Genetics of Vertebrate Development Section, Cancer and Developmental Biology Lab, National Cancer Institute, National Institutes of Health, Frederick, Maryland
[2]Department of Orthopedic Surgery, School of Medicine, University of Michigan, Ann Arbor, Michigan
[3]Department of Orthopaedic Surgery, University of Pennsylvania, Perelman School of Medicine, Philadelphia, Pennsylvania

Formation of the vertebral column requires precise coordination between presomitic mesoderm (PSM) development and somite segmentation during embryogenesis. According to the *Clock and Wavefront* model, rhythmic waves of gene expression propagate from the posterior to the anterior of the embryo, driving the sequential formation of somites. These oscillations are regulated by the segmentation clock, a molecular oscillator primarily driven by the Notch signaling pathway that directs the periodic patterning of somites. Disruption of this process leads to severe segmentation defects and congenital spinal malformations. Although hypoxia is known to interfere with segmentation clock oscillations, how oxygen availability influences somitogenesis remains poorly understood.

Here, we investigated the role of hypoxia-inducible factor 1α (HIF-1α), a master regulator of cellular adaptation to low oxygen, during PSM formation and segmentation. Conditional deletion of HIF-1α in nascent mesoderm using T-Cre (Brachyury-driven) caused vertebral malformations including butterfly and hemivertebrae, scoliosis-like curvature, and an additional thoracic vertebra at E18.5. At E10.5, mutants displayed asymmetric Tbx18 and Uncx4.1 expression and misaligned somite pairs, despite minimal cell death in the PSM. Loss of HIF-1α markedly increased hypoxia within the PSM, likely due to elevated mitochondrial respiration and a diminished vascular network around the developing area—both classical outcomes of HIF-1α loss in other tissues. These alterations were accompanied by a pronounced reduction and phase disruption of Hes7 and Lfng oscillations, indicating impaired Notch clock activity.

To test whether restoring oxygenation could mitigate these defects, pregnant dams carrying E9.5 embryos were exposed to hyperoxia (80% O_2) for three hours. In all treated mutants, hypoxia in the PSM was substantially reduced and Hes7 oscillations normalized. Embryos that developed to E18.5 showed noticeably fewer vertebral abnormalities in the lumbar region, corresponding to somites formed during the period of hyperoxia exposure.

These findings establish HIF-1α as a critical regulator of the Notch-dependent segmentation clock and somite formation through control of intracellular oxygen homeostasis. Ongoing experiments will test whether genetically inhibiting mitochondrial respiration can reduce oxygen consumption, restore intracellular oxygen balance, and rescue the HIF-deficient phenotype to normalize vertebral development.

Understanding the Effects of Pain from Deep Sensory Nerve Fibers on Cutaneous Pain and Sensation- a Case Study

Todd J Hullfish, BSME; Quinn Tate, MD; Josh R Baxter, PhD
University of Pennsylvania

Introduction: The posterior interosseous nerve (PIN) is commonly considered a motor-only nerve. Some anatomic studies have suggested there are deep sensory fibers that innervate the wrist joint capsule and ligaments. However, the understood impact of these deep sensory fibers on cutaneous pain and sensation remains limited. This case report describes the effects of high frequency alternating current (HFAC) electrical stimulation of the PIN on cutaneous sensation, offering further insight into the interaction between deep sensory nerve fibers and cutaneous sensory pathways.

Methods: A single case study was conducted involving the electrical stimulation of the PIN before piercing the supinator muscle. Localization of the PIN was confirmed by motor stimulation. For sensory disruption, we set the HFAC stimulation parameters at 5 kHz frequency, 40 mA current, and 20 µs pulse width. The primary outcome was the induction of paresthesia and the effect on cutaneous sensation. Sensory testing was performed using a 4-g monofilament to assess pressure sensation and a pinprick test to evaluate nociceptive response. Mapping of the area of altered sensation allowed us to find the areas of the skin most affected along the known path of the PIN.

Results: Initial motor stimulation of the PIN resulted in extension of the thumb and wrist. Sensory blocking stimulation of the PIN resulted in the induction of paresthesia localized to the proximal forearm and continuing to the dorsum of the wrist, without extending beyond this region. Notably, there was intermittent disruption of cutaneous sensation, specifically affecting pressure and pinprick sensation on the dorsum of the wrist proximal to the hand (**Figure 1**). The case study participant described a pathway of paresthesia that aligned with the sensory changes noted. These followed a narrow band along the forearm that ended at the dorsum of the wrist, consistent with the anatomical trajectory of the PIN.

Conclusion: This case report highlights the potential interactions of deep sensory fibers of the PIN in influencing cutaneous sensation, and how wrist joint pain may cause radicular symptoms, providing additional insight into the traditional view of the PIN as a solely motor nerve. The observed sensory alterations suggest a complex interaction between deep and cutaneous sensory pathways, which may have implications for understanding pain mechanisms and the development of neuromodulation therapies. Further research is warranted to explore the clinical significance of these findings and their potential applications in pain management.

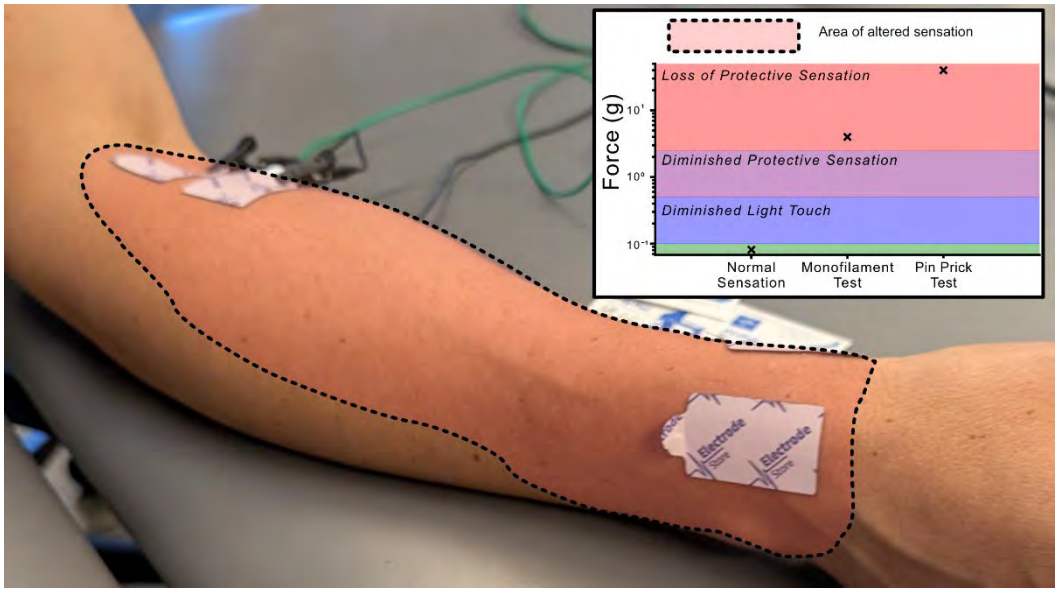

Figure 1. Electrodes are placed over the PIN distal to the elbow. High Frequency Alternating Current (HFAC) of the PIN reduces sensation to below protective levels in the shaded area as confirmed by both monofilament and pin prick testing.

Synthetic Gene Circuit for Remodeling Fibrotic Tissue

Christopher M, Albert L, Jacob Q

Background and Significance:

The interdependent relationship between cells and the extracellular matrix (ECM) is a crucial component of tissue regulation that is disrupted by aging and diseases. Cells sense and respond to mechanical cues within the ECM, which trigger downstream biochemical and biophysical signaling to regulate cellular function via enzyme secretion. In turn, cells actively remodel their microenvironment through ECM proteolysis and synthesis of new ECM molecules. One of the responses is the nuclear localization of the Yes-associated protein (YAP). In soft substrates, YAP is present in the cytoplasm, but under a stiff substrate, YAP localizes to the nucleus. Working in conjunction with TEAD transcription factors, they can control the transcription of key genes in cell proliferation and differentiation.

A disease that directly disrupts the cell-ECM relationship is fibrosis. Fibrosis arises when normal wound-healing processes fail, leading to excessive ECM deposition. In healthy tissue repair, transient fibrosis promotes wound healing within days, but prolonged or unresolved fibrosis can result in pathological ECM accumulation and scarring, stiffening tissue and impairing tissue function. Synthetic ECM platforms offer a promising way to mimic these interactions by presenting specific mechanical cues to direct cell behavior. While existing hydrogel systems can be dynamically stiffened in response to external stimuli, there has yet to be a native-like, reciprocal feedback between cells and engineered ECM.

Purpose: The purpose of this research is to understand how diseases and aging dysregulate the mechanobiology in tissue regeneration and homeostasis.

Goal: The goal is to engineer a self-regulating loop in which cells alter the ECM, sense changes in the ECM, and then respond by restoring the ECM to a stable state that has not yet been developed.

Methods:

- Engineer cells that respond to changes in stiffness in the ECM
- Design a photo-responsive hydrogel
- Using the time delay in transient fibrosis, we will integrate a split dCas9 system along with YAP into a coherent type 1 feed-forward loop to trigger a softening response using the Sortase A enzyme

YAP/TAZ Signaling Affects Cytoskeletal Feedback in Tenocytes

Elizabeth Seidl[1], Nathaniel Dyment[1], Joel Boerckel[1]
[1]University of Pennsylvania, Philadelphia, PA,
eseidl@seas.upenn.edu

INTRODUCTION: Tendon fibroblasts (tenocytes) exist within a highly organized collagen matrix. Healthy tenocytes experience load and exist in a state of tensional homeostasis. However, when the matrix of the tendon is damaged either through degradation or trauma the matrix and tenocytes de-tension. After de-tensioning matrix metalloproteinases (MMPs) remodel the tendon matrix leaving it disorganized with reduced mechanical properties. Previous work has shown that after blebbistatin treatment, tenocytes experience an upregulation in MMP and downregulation YAP/TAZ gene expression [1]. Within tendon healing it is understood that after an initial de-tensioning even tenocytes will eventually regain cytoskeletal tension, however this mechanism is poorly understood. RhoA signaling regulates myosin phosphorylation and subsequent cytoskeletal tension. RhoA-inactivating GAP proteins regulate the cytoskeletal feedback loop by repressing RhoA activity.

METHODS: Human tendon fibroblasts from adult donor patellar and Achilles tendons were obtained commercially and cultured in sterile conditions. Cells were transfected with either SMARTpool ONTARGETplus siRNA. One group of tenocytes was treated with siRNA to repress YAP1 and WWTR1 (TAZ). Another experimental group was treated with siRNA to repress Tead1, Tead2, Tead3, and Tead4. Finally, non-targeting control siRNA was used as a control group. Additionally, cells were either treated with 20 uM Blebbistatin or DMSO to simulate a de-tensioning effect. Transfection was performed using Lipofectamine RNAiMAX. 48 hours after transfection, cells were lysed and purified using Qiagen RNeasy Mini Kit. RNA was converted to cDNA with Applied Biosystems' HighCapacity cDNA Reverse Transcription Kit. Gene expression was evaluated using quantitative real-time PCR and Applied Biosystems' PowerTrack SYBR PCR Master Mix on a QuantStudio 6 Pro machine. Fold change values were obtained through the delta delta Ct method and compared by unpaired, two-tailed t-tests ($\alpha = 0.05$).

RESULTS SECTION: All siRNA significantly downregulated their targets within tenocytes. Cells with YAP/TAZ downregulated had a significant increase in MMP expression (MMP3 & MMP14). Both experimental groups treated with siRNA to target YAP/TAZ or Teads (1-4) showed significant downregulation for Cyr61, Ctgf and DLC1. All groups treated with blebbistatin demonstrated significant downregulation of Cyr61, Ctgf, and DLC1 compared to those treated with DMSO.

DISCUSSION: Overall these results demonstrate the effect of both loss of tension and inhibition of YAP/TAZ signaling on tenocytes. Having a better understanding of a tenocyte's cytoskeletal feedback loop better elucidates tenocyte's regulation tensional homeostasis and MMP expression.

REFERENCES: [1] Jones+ J PNAS. 2023

ACKNOWLEDGEMENTS: Work Supported by Grant NIH/NIAMS P50AR080581 from the National Institute of Arthritis and Musculoskeletal and Skin Diseases of the NIH and PCMD grant P30 AR069619

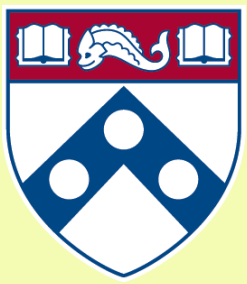

Penn Center *for*
Musculoskeletal Disorders
UNIVERSITY *of* PENNSYLVANIA

Biomechanics Core Abstracts

AM Session

Poster 22 to 33

Coordination of Collagens V and XI Guide Fibril Assembly during Mouse Patellar Tendon Postnatal Development

Nat A. Thurlow, Jeremy D. Eekhoff, Meera Ratnagiri, Courtney A. Nuss, Stephanie N. Weiss, Nathaniel A. Dyment, Louis J. Soslowsky
McKay Orthopaedic Research Laboratory, University of Pennsylvania, Philadelphia, PA
nthurlow@seas.upenn.edu

Disclosures: None

INTRODUCTION: Collagens V and XI are minor fibril-forming collagens that assemble with major collagens, such as collagens I and II, to facilitate fibrillogenesis. Interestingly, collagens V and XI have related roles in fibril assembly including fibril nucleation, organization, lateral growth, and fusion [1]. In tendons, lack of *Col5a1* expression leads to larger diameter fibrils, smaller tendon cross-sectional area, and reduced mechanical properties [2]. Lack of *Col11a1* expression leads to tendons with disrupted fibril organization, more fibrils with small diameters, and decreased elastic properties [3]. Collagens V and XI also have similar structures, can assemble together in triple helices, and have comparable gene expression levels in tendon until postnatal day 30 (p30) [1]. Together, this suggests that a potential interaction between these two collagen types during early development is critical for proper fibril growth and mechanical response. However, the structural and functional outcomes due to cooperation between collagens V and XI in tendon are unclear. The objective of this work is to assess the impact of cooperation between collagens V and XI during early development by comparing tendons with tendon-specific knockdown of *Col5a1* and *Col11a1* (VHet-XIHet and VKO-XIHet) to tendons with altered expression of *Col5a1* only (VHet and VKO). We hypothesized that tendons with compound deficiencies would have more severe dysregulation of fibril growth, altered tendon structure, and mechanical deficits compared to their counterparts lacking only *Col5a1*.

METHODS: Animals: Male and female p30 mice with tendon specific (ScxCre) alterations in *Col5a1* and/or *Col11a1* expression were collected (VHet, VHet-XIHet, VKO, and VKO-XIHet; n=12/genotype) and ScxCre- littermates served as controls (Ctrl, n=12; IACUC approved). Mechanics: Patella-patellar tendon-tibia complexes were finely dissected from hindlimbs, and cross-sectional area was measured using a custom laser device. The patella was secured in neoprene with cyanoacrylate glue, and the tibia was potted in polymethyl methacrylate. Tendons were tested with a viscoelastic protocol consisting of preloading to 0.05N, preconditioning for 10 cycles, stress relaxations at 2% and 4% strain followed by a frequency sweep of 10 cycles at 0.1, 1, 5, and 10 Hz, and quasistatic ramp-to-failure at 0.1% strain/sec. VKO-XIHet patellar tendons (PTs) only underwent preconditioning and ramp-to-failure due to tissue fragility. Transmission Electron Microscopy: PTs (n=4/genotype) were isolated, fixed, embedded, sectioned, stained, and imaged as described [4]. Fibril diameters were measured in MATLAB (n=10 images/PT). Tendon Morphology: Knees were fixed, cryoembedded, sectioned at 8 µm, and stained with toluidine blue to visualize morphology. Statistics: Mechanical properties were compared using ANOVA followed by Bonferroni corrected t-tests when appropriate ($p \leq 0.05$).

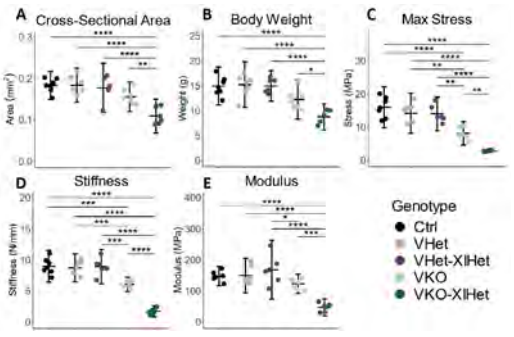

Figure 1. VKO-XIHet mice had (A) reduced tendon CSA and (B) body weight. (C) Maximum stress and (D) stiffness were lower in the VKO compared to VHet. Maximum stress, stiffness, and (E) modulus were lower in VKO-XIHet compared to VKO (* p<0.05, ** p<0.01, *** p<0.001, **** p<0.001).

RESULTS: Mechanical changes due to the addition of *Col11a1* knockdown were larger than *Col5a1* knockout alone: VKO-XIHets had smaller PT cross-sectional areas (CSA) (Figure 1A) and lower body weight (Figure 1B) than the other four genotypes. There were no differences detected in maximum stress, stiffness, or modulus in Ctrl, VHet, and VHet-XIHet tendons (Figure 1C-E). VKO tendons had reduced maximum stress and stiffness compared to Ctrl and VHet (Figure 1C-D). Compared to VKO tendons, VKO-XIHet had dramatically lower maximum stress, stiffness, and modulus. Viscoelastic properties were similar between genotypes (data not shown). VHet-XIHet and VKO-XIHet had populations of larger fibrils: Ctrl, VHet, and VKO fibril diameters were similar with only small deviations (~5nm) in Q1, median, and Q3 values (Figure 2A-B). Conversely, the VHet-XIHet distribution had a large population of larger fibrils with a shift of 23.4nm in median diameter compared to VHet fibrils (Figure 2C, F, G, J). Similarly, the VKO-XIHet fibril sizes shifted toward larger fibrils with a shift of 18.6nm in median diameter and an increase in 22.6nm in the interquartile range (Figure 2D, H-J). Tendon morphology was altered in VKO-XIHet PTs: VKO and VKO-XIHets had visibly smaller anterior-posterior thickness which approximated the differences in CSA measured during mechanical testing (Figure 3). VKO-XIHet PTs also appeared shorter than the other four genotypes and had abnormal morphology at the tibial insertion.

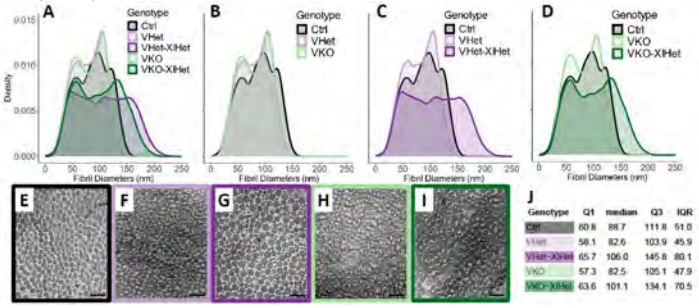

Figure 2. Fibril diameter distributions of (A) all genotypes. (B) *Col5a1* knockdown had little effect on fibril diameters, but (C, D) the addition of *Col11a1* knockdown caused larger fibril diameters. These changes are reflected in (E-I) representative images (scale bar = 400nm) and (J) a numerical summary.

DISCUSSION: We demonstrated that VKO-XIHet PTs have considerable deficits in mechanical properties and dysregulation of fibril assembly, while the effects of collagen V alone are comparatively minor. During the first 30 days of postnatal growth, tendon fibrils are organized and undergo a phase of lateral growth. Both collagen V and XI have N-terminal regulatory domains that extend to the fibril surface [3] and have been hypothesized to regulate fibril growth and assembly. Fibril diameters in p30 PTs were largely unchanged due to *Col5a1* knockout; however, the addition of *Col11a1* knockdown to *Col5a1* knockout led to dramatic fibril growth beyond 150nm suggesting that collagen V/XI interaction is a critical regulator of fibril growth. Interestingly, the increases in fibril diameters in the VHet-XIHet and VKO-XIHet tendons are coupled with unchanged and decreased overall cross-sectional areas, respectively. In previous work, tendon-targeted knockdown of a single copy of *Col11a1* (XIHet) in PTs caused no differences in maximum stress, stiffness, or modulus by p30 [5], while knockout of both copies (XIKO) resulted in significant decreases in the same properties. In this study, the mechanical property changes due to *Col5a1* knockout alone were minor, but the addition of *Col11a1* knockdown caused drastic decreases in mechanical properties. Together, these results indicate that there is a coordinated role between collagens V and XI during this phase of tendon growth, with collagen XI having a more prominent role. Given the abundance of collagen I in tendon, this finding is surprising given the canonical roles of collagen V and XI in regulating collagen I and II fibrillogenesis, respectively.

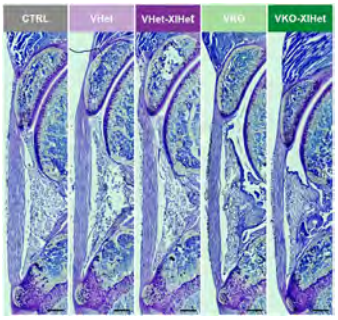

Figure 3. Tendon morphology is similar between Ctrl, VHet, and VHet-XIHet. VKO and VKO-XIHet PTs show a slight narrowing in anterior-posterior thickness. VKO-XIHet tendons also appear shorter and have abnormal bone morphology near the insertion (scale bar = 250µm).

SIGNIFICANCE: Collagen fibril organization and structure are vital to proper tendon function. Collagens V and XI have known roles in the regulation of fibrillogenesis, and their similar structure, expression levels, and roles suggest that coordination of these two collagen types occurs during tendon development. Defining these interactions is essential to understanding the mechanisms of collagen fibril formation and establishment of tendon structure.

REFERENCES: 1. Wenstrup et al., J Biol Chem, 2011. 2. Connizzo et al., J Ortho Res, 2016. 3. Sun et al., Matrix Biol, 2020. 4. Dunkman et al., Matrix Bio, 2014. 5. Cohen et al., ORS, 2023.

ACKNOWLEDGEMENTS: This study was supported by NIH/NIAMS (R01AR073231) and Penn Center for Musculoskeletal Disorders (P30AR069619).

Durability and Impact of Annulus Fibrosus Repair with Functionalized Hydrogels Under Loading

Emily E. Sharp[1-3], Marcia Muerner[4,5], Barbora Kubincova[4,6], Junxuan Ma[4], Emily S. Cook[1-3], Sarah E. Gullbrand[2,3], Robert L. Mauck[1-3] and Sibylle Grad[4,5]
[1]Dept. of Bioengineering, [2]Dept. of Orthopaedic Surgery, University of Pennsylvania, Philadelphia, PA, [3]Translational Musculoskeletal Research Center, Corporal Michael J. Crescenz VA Medical Center, Philadelphia, PA, [4]AO Research Institute, Davos, Switzerland, [5] ETH Zurich, Zurich, Switzerland, [6]University of Zurich, Zurich, Switzerland

Disclosures: RLM (5- 4WEB Medical), SEG (6- DiscGenics and Zurimed), SG (8- JOR Spine)

INTRODUCTION: During intervertebral disc (IVD) herniation, the nucleus pulposus (NP) extrudes beyond the boundaries of the annulus fibrosus (AF), compressing neighboring spinal elements and inducing pain. Microdiscectomy can relieve the immediate symptoms of herniation but fails to promote long-term healing as it does not restore mechanical integrity of the AF or address the associated inflammation.[1] While a variety of repair materials have been developed to improve IVD mechanical stability following microdiscectomy,[2,3] few utilize localized therapeutic delivery to combat these adverse biologic changes. We previously developed a hyaluronic acid (HA)-based hydrogel capable of spatiotemporal controlled delivery via secondary reactions between the streptavidin-modified hydrogel backbone and biotin-modified therapeutics.[4] Here, we investigated the *ex vivo* retention of these functionalized hydrogels in injured AF in living discs that were subjected to dynamic uniaxial compression over an extended duration.

METHODS: Hydrogel Fabrication: HA synthesis and hydrogel fabrication were accomplished using established protocols.[5] Streptavidin modification was achieved by incorporating 1% thiol-streptavidin (TS) into the hydrogel precursor solution and was covalently attached via reaction with norbornene residues on the HA backbone. Unless otherwise specified, hydrogels were 3 wt% with a crosslinking density of 50% using MMP-degradable crosslinks.[6] 30 μM biotin-modified Cy5 was also incorporated to visualize the hydrogel via the biotin-streptavidin secondary reaction. IVD Tissue Preparation: IVD motion segments were isolated from bovine tails. The vertebral bodies were carefully removed to enhance nutrient diffusion through the endplates and prepared for sterile organ culture.[6] AF Injury and Repair: A 5 mm x 2.5 mm cruciate laceration was made in the AF (Depth = 2 mm) followed by a 7 mm deep puncture with a 14G needle into the NP. Hydrogel repair was performed immediately following injury by injecting 25 μL of the sterile hydrogel precursor solution and photocrosslinking for 10 minutes at 5 mW/cm^2. Samples were incubated overnight prior to loading. Uniaxial Compressive Loading: Physiologic loading (0.02–0.2 MPa, 0.2 Hz) was applied for 2 hours each day for 3 consecutive days.[7] After the final loading cycle, samples were incubated overnight prior to processing. Outcomes: Disc height was measured before and after loading (n=8 per group). Stress-strain data were collected during each loading cycle (n=8 per group). Half of the samples were processed for PCR (n=4 per group) while the remaining were processed for histology (n=4 per group). Statistical Analysis: Significant differences ($p<0.05$) were detected using two-way ANOVA (Disc Height Reduction, Mechanics) or unpaired t-tests (PCR) in GraphPad Prism.

RESULTS: The cruciate-puncture injury substantially disrupted AF structure without significant injury to the NP (1A). Injury coupled with physiologic loading resulted in a clear increase in expression of matrix remodeling (ADAMTS5, MMP-1, and MMP-13) and inflammatory (IL-6) genes (1B-E). There were no differences in disc height reduction with loading between intact and injured discs (1F). On the first day of loading, the linear modulus for injured samples increased with increasing cycles of compression while intact samples remained constant (1G, p=0.078). The maximum strain for injured samples decreased with increasing cycles of compression to eventually reach the same level as intact controls (1H, Day 1 p=0.0614, Day 2 p=0.0318). On all three days of loading, the amount of energy dissipated was significantly higher at every cycle for injured discs compared to intact controls (1I, p<0.0001). The hydrogel remained in place over three days of loading (2A), with histological analysis confirming that the hydrogel penetrated through the depth of the AF injury and remained resident over this time course (2B). At this early timepoint, there were trends towards increasing ECM deposition markers expression (COL1, ACAN) with hydrogel repair (2C-D). ADAMTS5, IL-6, and MMP-1 gene expression were unchanged compared to injured samples, while MMP-13 was significantly decreased with hydrogel repair (2E-H).

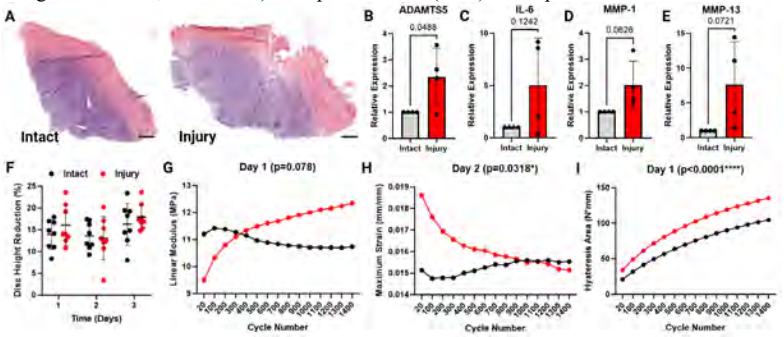

Figure 1: A) H&E histology of intact and injured discs. Scale = 2.5 mm B-E) Gene expression in the injured AF normalized to the intact AF. F) Disc height reduction during loading. G-I) Mean mechanical changes with injury (n=8/group).

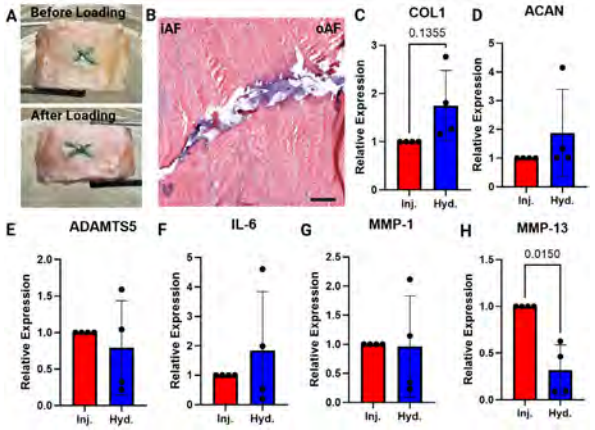

Figure 2: A) Hydrogel repair before and after loading. B) H&E histology of hydrogel retention. Scale= 0.5 mm C-H) Gene expression in the repaired AF normalized to the injured AF.

DISCUSSION: Our data supports prior findings that acute AF injury increases matrix remodeling and initiates an inflammatory cascade that hinders endogenous repair.[8] At the onset of loading, injured discs were softer and experienced higher strain, which normalized at later cycles (likely due to compaction of the injured disc). Injured discs also dissipated more energy than intact discs across all cycles. Altogether, these differences highlight how acute AF injury impacts the mechanical integrity of the disc even at early timepoints. These changes to the mechanical stability of the disc could compound with time and further contribute to inferior tissue repair – motivating the need for novel AF repair biomaterials. Importantly, we demonstrated that TS hydrogels can effectively seal the AF injury and are retained with physiologic loading.

The introduction of this hydrogel did not worsen inflammation and matrix remodeling following injury. Instead, hydrogel repair decreased MMP-13 expression, suggesting less collagen degradation, and exhibited trends towards increased ECM deposition that may promote tissue repair. Future studies will further probe the mechanical and biologic response of the disc to injury and repair via immunofluorescence and RNAScope to better understand the consequence of rapid and sustained delivery of biologics from functionalized hydrogels. We also plan to utilize this methodology to evaluate the efficacy of localized therapeutic delivery using the secondary reactions between our streptavidin-modified hydrogels and a biotin-modified therapeutic.

SIGNIFICANCE: In addition to characterizing the effects of acute AF injury, this study demonstrates that functionalized hydrogels are a promising repair material for the AF as well as other dense connective tissues. The ability of this hydrogel to penetrate and remain in place under loading suggests that such materials are promising for providing spatiotemporal controlled delivery of a therapeutic throughout the tissue to promote endogenous healing. This development could transform clinical practice by creating superior surgical alternatives and outcomes for patients.

REFERENCES: 1. Peredo, AP *et. al.* JOR Spine (2021) 2. Sloan, SR *et. al.*, Sci. Trans. Med. (2020) 3. Panebianco, CJ *et. al.* Euro. Cells & Mat. (2020) 4. Sharp, EE *et. al.* ORS (2025) 5. Gramlich, WM, *et. al.*, Biomaterials (2013) 6. Loebel, C *et. al.* Nat. Mater. (2019) 7. Saravi, B *et. al.* Jove (2021) 8. Bonnevie, ED *et. al.* Nat. Biomed. Eng. (2019)

A novel measurement of altered Achilles subtendon load-sharing 6-12 months following rupture

Kathryn S. Strand[1], Todd J. Hullfish[1], Maggie M. Wagner[1], Devyn Russo[1], Max Zawel[1], Douglas E. Schaubel[1], Casey Jo Humbyrd[1], Josh R. Baxter[1]
[1]University of Pennsylvania, Philadelphia, PA
strandk@seas.upenn.edu

Disclosures: KSS (N), TJH (N), MMW (N), DR (N), MZ (N), DES (N), CJH (7B, 8, and 9), JRB (N).

INTRODUCTION: Achilles tendon ruptures cause functional deficits which persist years following injury and likely arise from compromised native tendon structure and function[1]. In a healthy Achilles tendon, the three subtendons arising from the medial (GM) and lateral (GL) gastrocnemii and soleus (SOL) muscles experience semi-independent relative sliding during passive and active plantar flexion, but this sliding is reduced following rupture and repair[2]. This reduced sliding may result from the formation of intratendinous adhesions and disorganized collagen. Prior work suggests that increased interfascicular adhesions within the Achilles tendon alter triceps surae muscle dynamics[3]. However, clear, quantifiable measures of intratendinous load sharing and altered subtendon function are lacking. The purpose of this study was to apply prior validated methods[4] combining neuromuscular electrical stimulation (NMES) of individual triceps surae muscles and transverse plane ultrasound imaging to quantify lateral load sharing in both injured and uninjured tendons. We hypothesized that Achilles tendons healing 6-12 months following rupture and repair would display more homogenous behavior within the tendon cross section in response to individual triceps surae stimulations due to increased lateral load sharing between adjacent subtendons compared to the uninjured, contralateral side.

METHODS: Eighteen adults with acute unilateral Achilles tendon rupture (15M, 3F, age 38±11 years) provided informed, written consent to participate in this IRB-approved study. Thirteen patients received surgical repairs, and the remaining five received conservative treatment. We evaluated patients between 6 and 12 months post-injury. An additional eleven adults (5M, 6F, age 26±5 years) with no history of Achilles tendon injury consented to participate as a control group. We used our validated NMES protocol[4] to elicit isolated plantar flexor muscle contractions of the GM, GL, and SOL, and simultaneously acquired transverse-plane B-mode ultrasound images of the Achilles tendon. Subjects laid prone on a bed with their ankle in a neutral, relaxed position. We fixed a 21 MHz linear ultrasound transducer (L6-24, GE LOGIQ) perpendicular to the free tendon and applied 1 second monophasic pulse trains (100 Hz, 400 µs pulse width) via hydrogel electrode pairs placed over the muscle bellies of the GM, GL, and SOL muscles. To stimulate a single triceps surae muscle, we increased the stimulation amplitude stepwise by 1-2 mA until there was localized movement of the Achilles tendon visible via ultrasound video, but no plantar flexion of the foot. We repeated these steps separately for each muscle and delivered the respective chosen stimulation amplitudes with the ultrasound probe placed 1, 3, and 5 cm proximal to the Achilles tendon calcaneal insertion point. We used an automated Kanade-Lucas-Tomasi point tracking algorithm to calculate the displacement of 900 corner point eigenfeatures across all stimulation frames[4]. We then applied k-means clustering (k=3) to classify point behavior in the transverse plane. The three clusters represented non-stimulated tissue (lowest total displacement), the subtendon of interest (highest total displacement), and intermediate tissue influenced by intratendinous load sharing. We calculated the difference between the mean displacement vector angles of the points in the clusters experiencing the least and greatest total displacement at the time of peak point velocity immediately following stimulation onset (**Figure 1**). A greater angular difference indicates a higher degree of subtendon independence. To evaluate the bilateral differences in subtendon responses within the control and injured cohorts, we performed a Wilcoxon signed-rank test to compare the angular difference values calculated for each leg. To evaluate the predictive capabilities of angular difference and imaging position along the free tendon on the tendon injury status in the injured cohort, we performed multiple logistic regression analysis (1=uninjured, 0=injured) for each stimulated muscle. All significance levels were set to $p<0.05$.

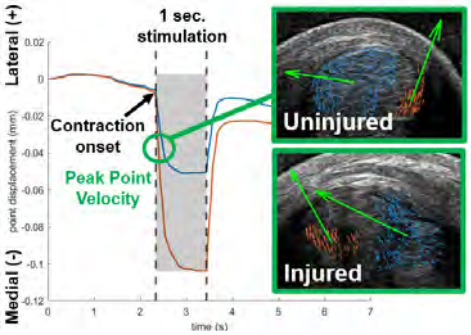

Figure 1. Point displacement during a representative trial. Mean point displacement trajectories in clusters experiencing least (blue) and greatest (red) total displacement differ between uninjured and injured tissue.

RESULTS SECTION: Injured tendons displayed a significantly lower angular difference compared to the contralateral, uninjured tendon during GL ($p=0.0003$) and GM ($p=0.0028$) stimulations (**Figure 2**). Angular difference values did not differ between right and left legs in the control cohort during any muscle stimulation (**Figure 2**). Logistic regression analysis revealed that angular difference was a significant predictor of injury status during GL stimulations only ($p=0.039$, Odds Ratio: 1.010) (**Table 1**).

Table 1. Logistic regression output for GL stimulations.

	Estimate	Std. Error	p-value	Odds Ratio
(Intercept)	-0.207	0.349	0.552	0.813
3 cm position	-0.271	0.496	0.585	0.763
5 cm position	-0.106	0.490	0.828	0.899
Angular Difference	0.010	0.005	0.039	1.010

DISCUSSION: Our results support the possibility of muscle-specific influence on tendon injury. For example, logistic regression revealed that a 10 degree increase in angular difference during GL stimulations decreases odds of identifying an injured tendon by a factor of $e^{(-0.010*10)}=0.906$. We found significantly greater angular differences in uninjured compared to injured legs during both GL and GM stimulations, but this outcome measure was only a significant predictor of injury status during GL stimulations, potentially due to structural differences between the triceps surae muscles. For example, the GL has longer fascicles with lower pennation angles compared to the GM[5], so similar activation levels produce less GL excursion and, consequently, more longitudinal tendon motion. Prior studies also found significant reduction in GL physiological cross-sectional area and activation compared to the GM and SOL in tendinopathic patients, suggesting a relationship between GL contribution to triceps surae dynamics and Achilles tendon injury development[5]. Finally, the absence of bilateral differences in this outcome in uninjured controls suggests that angular difference may be a biomarker of tendon healing post-rupture using the uninjured, contralateral limb as a reference.

SIGNIFICANCE/CLINICAL RELEVANCE: We developed a novel outcome measure to quantify Achilles subtendon function which is sensitive to injury status. These results suggest that changes in lateral load sharing between subtendons may be a new biomarker of tendon health and injury recovery status.

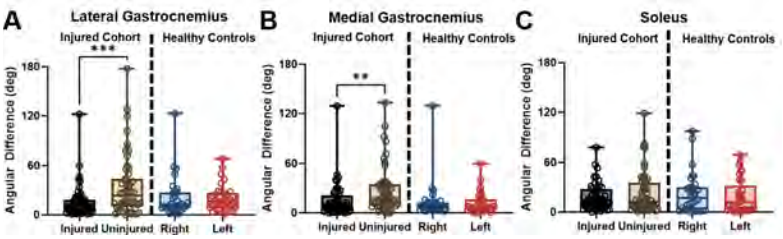

Figure 2. Angular difference values calculated for each leg in the injured and uninjured cohorts during A) GL stimulations, B) GM stimulations, and C) SOL stimulations. **p<0.01, ***p<0.001.

REFERENCES: 1. Suydam et al. (2015) Sports Traumatol. Arthrosc. 2. Khair et al. (2022) J. Appl. Physiol. 3. Franz & Thelen (2016) J. Biomech. 4. Strand et al. (2025) J. Appl. Physiol. 5. Crouzier et al. (2020) Med. Sci. Sports Exerc.

Acknowledgements: This work was supported by NIH/NIAMS P50AR080581 and NSF Grant DGE-223 6662.

Understanding the Relationship between Pore Water, Bound Water and Atypical Femoral Fractures Utilizing MRI-Based Finite Element Modeling

Ashkan Sedigh[1], Nada Kamona[2], Christiana Cottrell[3], Jonathan Gao[3], Hansen Liu[3], Allison Tang[3], Chamith S. Rajapakse[4] and Ani Ural[1]

[1] Department of Mechanical Engineering, Villanova University, USA
[2] Department of Bioengineering, University of Pennsylvania, USA
[3] Department of Radiology, University of Pennsylvania, Philadelphia, PA, USA
[4] Departments of Radiology and Orthopaedic Surgery, University of Pennsylvania, Philadelphia, PA, USA

Abstract:

Atypical femoral fracture (AFF) is a rare fracture associated with prolonged bisphosphonate treatment that occurs in the subtrochanteric and midshaft regions of the femur. Previously, we identified that anterior bowing angle and bone volume fraction (BVF) measured by magnetic resonance imaging (MRI), are significantly correlated with AFF fracture load. MRI also provides novel measures including bound water (BW), associated with collagen density, and pore water (PW) that reflects microporosity. In this study, we aim to assess the relationship between PW, BW and AFF fracture load by establishing the first fracture mechanics-based MRI finite element model (FEM) that incorporates these novel compositional and microstructural measures.

UTE MRI of ten female human cadaveric femora (isotropic resolution=980 mm) at the potential AFF regions were obtained and segmented to provide the BW and PW at each voxel (Fig. 1a,b). The segmented images were converted to FE models (~500k elements) using Simpleware and were subjected to stance loading (Fig. 1c). The fracture process in the UTE region was modeled by the cohesive extended finite element method (XFEM) using Abaqus incorporating experimental data from the literature. The sections outside the AFF region were assigned material properties based on their MRI-measured BVF. The stiffness, fracture load, displacement at fracture load, strain at crack location were extracted.

The simulation results showed that the fracture load at the AFF site has a negative partial correlation (controlled for BVF and geometrical features) with mean PW ($R=-0.72$, $p<0.05$) and positive partial correlation with mean BW ($R=0.65$, $p<0.05$) (Fig. 1d,e). Mean BW is also significantly partially correlated with strain at crack location ($R=-0.90$), displacement at fracture load ($R= -0.85$), and stiffness ($R=0.74$).

This study established a novel modeling approach that integrates UTE MRI measures of BW and PW with FEM. The results showed that the fracture load at AFF sites decreases with increasing cortical porosity and decreasing collagen density measured via PW and BW, respectively. Our method captures novel MRI-based compositional and microstructural features of cortical bone that cannot be measured by other clinical imaging modalities and demonstrates their significant impact on fracture resistance at the AFF site. These noninvasively measurable MRI-based markers have the potential to enable personalized AFF risk assessment and interventions.

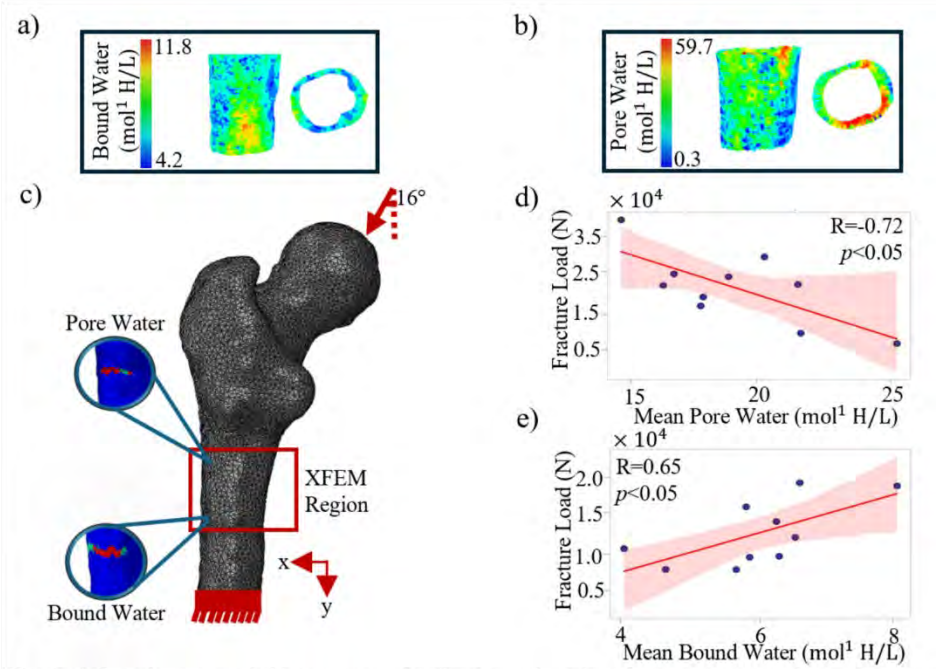

Fig 1. a) Bound water and (b) pore water distribution at the subtrochanteric region and a transverse cut at the crack site c) Femur FE model with the applied load (red arrow) and XFEM region (red box) showing the crack formation location based on bound water and pore water distribution. Partial correlation of fracture load with mean (d) pore water and (e) bound water controlled for geometry and bone volume fraction.

Meso-scale Viscoelastic Properties of Achilles Tendon Matrix Reveal Local Contributions to Tissue Mechanics

Tyler E. Blanch[1], Yu-Chang Chen[1], Jonathon L. Blank[1], Kyle H. Vining[1], and Su Chin Heo[1]
[1]University of Pennsylvania, Philadelphia, PA
tblanch@seas.upenn.edu

Disclosures: Blanch (N), Chen (N), Blank (N), Vining (N), Heo (5-4WEB Medical)

INTRODUCTION: Tendons are dense connective tissues that transmit muscle forces onto bone, facilitating efficient movement **[1]**. To achieve this, tendon relies on an anisotropic collagen matrix with high elasticity to minimize energy loss during force transfer. In the context of tendon pathologies such as tendinopathy, matrix organization and composition are significantly disrupted, leading to reduced load transmission efficiency and altered material properties **[2]**. Beyond force transmission, tendon viscoelastic properties also play a critical role in regulating resident cell behavior, including mechanotransduction and matrix synthesis. Changes in viscoelasticity can therefore influence how cells sense and remodel their microenvironment. Despite this importance, how viscoelastic properties are altered in tendon disease, and how such changes contribute to tendon degeneration, remain poorly understood. Although tendon mechanics have been widely studied at the whole-tissue level under tensile loading, bulk measurements often obscure meso-scale mechanical properties arising from extracellular matrix composition and organization **[3]**. Consequently, there is a gap in our understanding of how local viscoelastic changes at the cell level contribute to disease-associated matrix remodeling. To address this gap, we employ shear rheology on Achilles tendon biopsies to determine how viscoelastic matrix contributions are affected in the case of tendon homeostasis and disuse. Here, we present our preliminary characterization of healthy tendon tissue across multiple biological donors to establish the feasibility and reproducibility of this approach. Male animals were used in this validation phase to reduce biological variability prior to extending the study to overloaded and underloaded tendon models.

		D3.1	D3.2	D4.1	D4.2	D5.1	D5.2
3% Axial Strain	Relaxation, %	55.46	56.38	68.42	59.54	55.63	60.35
	|E*|, Mpa	170.25	91.38	124.38	62.29	122.92	105.10
	tan δ	0.0652	0.0820	0.0780	0.0930	0.0638	0.0833
6% Axial Strain	Relaxation, %	45.74	52.21	49.80	55.24	48.09	53.15
	|E*|, Mpa	284.93	143.74	240.85	103.72	200.56	165.02
	tan δ	0.0495	0.0697	0.0507	0.0784	0.0525	0.0690
	GAG content (ug/mg)	6.89	7.36	14.21	8.35	7.82	8.90

Figure 1: Table outlining results from whole-tendon tensile testing, including stress relaxation, dynamic modulus (E*), and phase shift (tan(δ)) at 3% and 6% tensile strain, and glycosaminoglycan (GAG) content assay. (n=3 biological replicates with 2 contralateral limbs each, D: donor, 1: left limb, 2: right limb).

METHODS: Left and right Achilles tendons were isolated and harvested from four 10-week-old male Sprague Dawley rats (IACUC approved). For whole-tendon testing, the hindpaw was secured in polymethylmethacrylate at 120° and the proximal tendon clamped in sandpaper grips in a 37°C 1×PBS bath. Whole-tendon tensile testing consisted of a 1 N preload, 10 cycles of preconditioning at 0.5% strain, stress relaxations at 3% and 6% grip strain, followed by frequency sweeps at 0.1, 1, 5, and 10 Hz as previously reported **[4]**. Viscoelastic properties (dynamic modulus (E*), phase shift (tan(δ)), and percent relaxation) were measured. Following tensile testing, two biopsy punches (1.5mm diameter, ~0.8 mm height) were extracted from the tendon midsubstance of each tissue. Biopsies were tested in a shear rheometer under shear and compression in a 37°C 1×PBS water bath with normal force perpendicular to fiber orientation. Rheological testing consisted of a 0.01N compressive preload followed by either (1) shear strain sweeps from 0.01% - 20% (0.00063 - 1.257rad) at 0.1Hz (n=1) or (2) shear frequency sweeps from 0.01Hz – 25Hz at 0.5% strain (0.0314rad) (n=3), shear stress relaxation at 3% strain (0.1885rad), and axial compression to 90% strain at 1% strain/sec rate for two technical replicates per tissue. Viscoelastic (shear storage modulus (G′), shear loss modulus (G″), tan(δ), and percent relaxation) and elastic (stiffness, Young's modulus) properties were measured. All remaining tendon tissue was digested in proteinase K overnight at 60°C prior to quantifying glycosaminoglycan (GAG) content using the 1,9-dimethylmethylene blue assay and chondroitin sulfate as standard. Absorbance was read at 525 and 595 nm and normalized to the tendon dry weight **[5]**.

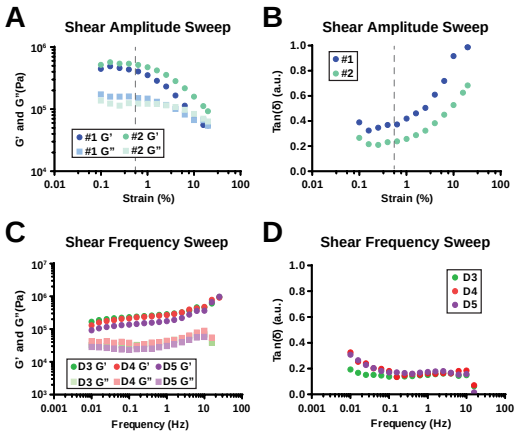

Figure 2: (A, B) Shear storage (G') and loss (G") moduli **(A)**, and phase shift (tan(δ)) **(B)**, of Achilles tendon biopsy punches measured across increasing strain magnitudes. Dashed line indicates 0.5% strain (0.0314rad). (n=2 technical replicates). **(C, D)** Shear storage (G') and loss (G") moduli **(C)**, and tan(δ) **(D)**, of Achilles tendon biopsy punches measured across increasing strain frequencies. (n=3 biological replicates, colors indicate individual donors, D: donor).

RESULTS: Whole-tendon tensile testing revealed consistent viscoelastic properties between contralateral limbs and individual donors. Tendons reached an average of 59.3% stress relaxation after 10 minutes, and phase shift (tan(δ)) averaged 0.08 (3% strain) **(Fig. 1)**. In shear, tendon biopsy punch tissues displayed linear strain behavior up to 1% strain (0.0628rad), beyond which nonlinear responses manifested **(Fig. 2A, B)**. Based on this, 0.5% strain (0.0314rad) was selected for subsequent shear measurements. Frequency sweeps of punch tissues revealed reproducible complex modulus values across samples, with tan(δ) averaging 0.18 **(Fig. 2C, D)**. Shear stress relaxation was rapid, reaching 50% relaxation within 5 minutes in all samples **(Fig. 3A)**. Axial compression of biopsy punch tissues yielded a consistent Young's modulus of 4.75 MPa (standard deviation = 0.217) averaged across biological replicates **(Fig. 3B, C)**. GAG content, measured biochemically, showed a strong correlation with stress relaxation in both tensile (3%, R^2=0.9518) and shear (R^2=0.7303) testing, linking matrix composition to viscoelastic behavior **(Fig. 1, 3)**.

DISCUSSION: Shear rheological analysis of tendon tissue provides an underexplored and complementary approach to characterizing matrix material properties, with unique sensitivity to meso-scale effects. Both whole-tendon and biopsy punch testing demonstrated consistent trends across biological samples, including relative ordering based on stress relaxation times and tan(δ). However, notable differences in the value of tan(δ) and Young's modulus between whole-tendon and biopsy-scale tests underline how bulk tissue structure can mask local mechanical properties. Meso-scale forces are particularly important to define, as they directly regulate resident tendon fibroblast mechanotransduction, gene expression, and matrix synthesis, while tissue-scale forces primarily govern macroscopic tendon function **[6]**. Disruption of local viscoelastic properties may shift tenocyte transcriptional programs away from homeostasis toward disease-associated remodeling **[7]**. Thus, shear rheology offers a powerful platform to investigate localized or heterogeneous alterations in tendon mechanics and to link matrix composition with functional outcomes in both health and disease.

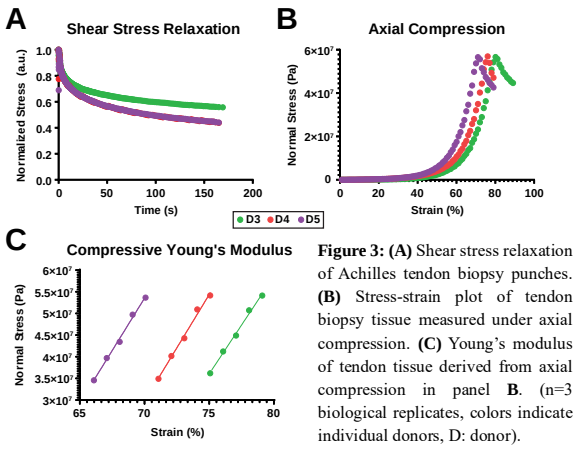

Figure 3: (A) Shear stress relaxation of Achilles tendon biopsy punches. **(B)** Stress-strain plot of tendon biopsy tissue measured under axial compression. **(C)** Young's modulus of tendon tissue derived from axial compression in panel **B**. (n=3 biological replicates, colors indicate individual donors, D: donor).

SIGNIFICANCE: This study demonstrates the use of shear rheology to characterize novel meso-scale mechanical properties of the Achilles tendon. This work provides new insight into how tendon mechanics are altered in heterogeneous conditions such as tendinopathy, with the potential to link matrix composition to disease progression.

References: **[1]** Bordoni+, *StatPearls*, 2024; **[2]** Xu+, *Clin Orth Rel Res*, 2008; **[3]** Basoli+, *Front Physio*, 2018; **[4]** Blank+, *J Physiol*, 2025; **[5]** Zheng+, *Eur Cell Mat*, 2015; **[6]** Nelson+, *Cell*, 2024; **[7]** Gardner+, *JOR*, 2012.

Acknowledgements: This work was supported by the NIH (P50 AR080581, K01 AR077087, F32 AR082671) and NSF (CMMI-1548571).

Foot Structure Changes and Links to Patient-Reported Pain Interference during Pregnancy and Postpartum

Michelle Meyers[1], Devyn Russo[1], Celeste Durnwald, M.D.[2], Casey Humbyrd, M.D., M.B.E.[1], Josh Baxter, Ph.D.[1]

[1]Department of Orthopaedic Surgery and [2]Department of Obstetrics and Gynecology, University of Pennsylvania, Philadelphia, PA

meyersm9@seas.upenn.edu

Disclosures: CH: 7B, 8, and 9; all other authors have no disclosures according to ACCME guidelines.

INTRODUCTION: Forty-two percent of pregnant patients report having foot/ankle pain during pregnancy [1,2]. Pregnancy also has lasting effects on the foot with thirty-three percent of the postpartum population reporting foot pain, which is hypothesized to contribute to the prevalence of musculoskeletal disorders in the parous population [1,3]. Studies have identified changes in foot structure throughout pregnancy and postpartum, most notably changes in length, width, arch, and volume which are hypothesized to be caused by a combination of mass increase, postural adjustment, and circulating hormones. Pregnant individuals undergo approximately a twenty percent increase in weight which also contributes to an anterior shift in the center of mass, leading to a compensatory postural adjustment to maintain an upright position [4-6]. Additionally, the reproductive hormone relaxin significantly increases during pregnancy to promote laxity in the pelvic ligaments to prepare the body for birth but also affects stabilizing ligaments in the foot and ankle [7]. Last, foot swelling or edema affects up to eighty percent of pregnant patients [8]. Accurately and reliably tracking foot structure is critical to understanding the effects of pregnancy on the foot and to identify patients at risk of chronic pain and disability. The goal of this study was to identify changes in foot structure throughout pregnancy and postpartum to link to patient-reported pain interference.

METHODS: We recruited a cohort of 25 pregnant individuals (age = 35.2 4 ± 4.03 years, gestational age = 12.91 ± 1.84 weeks) from Penn Medicine obstetrics clinics in Philadelphia and a cohort of 23 non-pregnant female control participants (age = 27.52 ± 3.53 years). Participants provided written informed consent, and the University of Pennsylvania's Institutional Review Board approved this study. Pregnant participants visited the Human Motion Lab during their 1st, 2nd, and 3rd trimester as well as 12-weeks postpartum to capture foot structure and patient-reported pain interference. Control participants visited the Human Motion Lab at least twice, 12-weeks apart, to perform a repeatability analysis on the camera-based foot structure measurement system. Patient reported-outcomes were collected via REDCap at the beginning of each in-lab visit. Participants completed the Patient-Reported Outcome Measurement Information System (PROMIS) Pain Interference survey, which is designed to assess how much pain interferes with an individual's daily activities and life. Pregnant participants with increases in PROMIS Pain Interference t-scores above 10 from their 1st to 3rd trimester were considered to have a significant increase in pain interference during pregnancy. We used 10 to distinguish significant changes in pain interference since PROMIS scores are scaled to a standard deviation of 10. We designed and built a camera-based foot structure measurement system consisting of two mirrors at 45° angles, foot plates, and a webcam. This system allows us to capture top and medial views of both feet in the standing position. Using a custom MATLAB script, we labeled key landmarks of the foot to identify width, length, and medial area (Figure 1A). When comparing medial foot area across groups we normalized this value by shoe size provided during the participants first visit. To test the repeatability of the camera-based system, we calculated the Intraclass Correlation Coefficient (ICC) using two visits from the control cohort. We tested for normality and used appropriate statistical test according to Shapiro-Wilk results. Paired t-test/Wilcoxon signed-rank tests ($\alpha = 0.05$) were used to longitudinally assess changes in foot width, foot length, and medial foot area throughout pregnancy and postpartum. Independent t-test/Mann-Whitney U tests were used to identify differences in normalized medial foot area between groups.

RESULTS: Using the camera-based system, we found that foot length (left: ICC = 0.96, right: ICC = 0.95), foot width (left: ICC = 0.94, right: ICC = 0.98), and medial foot area (left: ICC = 0.89, right: ICC = 0.93) have excellent repeatability. We found that left foot length and width increased during pregnancy, however no significant differences were detected in the right. Left foot length significantly increased from the 1st to the 3rd trimester ($p = 0.003$) as well as from the 1st trimester to postpartum ($p = 0.006$). Left foot width significantly increased from the 1st to 3rd trimester ($p = 0.005$) and from the 2nd to 3rd trimester ($p= 0.005$). When investigating the medial area of the foot, which represents increased swelling, we found that area increased in both feet from the 1st to 2nd trimester (left: $p = 0.002$, right: $p < 0.001$), 1st to 3rd trimester (left: $p < 0.001$, right: $p < 0.001$), and 1st trimester to postpartum (left: $p < 0.001$, right: $p < 0.001$). Additionally, we observed that the left medial foot area decreased from the 3rd trimester to postpartum ($p = 0.006$). 15 pregnant participants sustained significant increases in pain interference while 10 had no significant changes. During the 3rd trimester, the increased pain group had a significant elevation in normalized medial foot area compared to the non-pregnant control cohort (left: $p = 0.003$, right: $p = 0.005$) and the no pain change group (left: $p = 0.043$, right: $p = 0.028$) (Figure 1B). We observed that this increased normalized medial foot area was sustained postpartum in which the increased pain group again had significantly higher normalized medial foot area compared to non-pregnant controls (left: $p = 0.027$, right $p = 0.012$) and no pain change postpartum individuals (left: $p = 0.011$, right: $p = 0.031$) (Figure 1C).

DISCUSSION: Through this longitudinal study, we observed significant alterations in foot structure including increased foot length and width, as well as consistent increases in foot medial area or swelling during pregnancy and into the postpartum period. Changes in foot length and width may be attributed to increased levels of relaxin compounded with elevated mass which contribute to the fall of the transverse and longitudinal arches of the feet. We also observed side to side differences in the length and width of feet, which may be explained by foot dominance. Foot swelling is a very common symptom of pregnancy and effects up to eighty percent of patients, as we observed by significant increases in medial foot area throughout pregnancy [8]. However, pregnant individuals who had significant increases in PROMIS Pain Interference t-scores from their 1st to 3rd trimester also experienced increased normalized medial foot area during the 3rd trimester compared to non-pregnant controls and 3rd trimester pregnant individuals with no change in pain interference. These results suggest that foot swelling contributes to increased pain interference during pregnancy and should be targeted to enhance quality of life for these individuals. Additionally, foot medial area remained elevated at 12-weeks postpartum highlighting the lasting effects of pregnancy on the foot and need for specialized care for this population to address structural changes that contribute to increased pain interference during pregnancy.

SIGNIFICANCE/CLINICAL RELEVANCE: This study provides clinicians with an easy to use and low-burden tool to longitudinally measure and monitor foot structure to screen for risk factors and predictors of foot pain. This study offers insight to why patients experience increased pain interference during pregnancy and mechanisms to target with specialized care for this population.

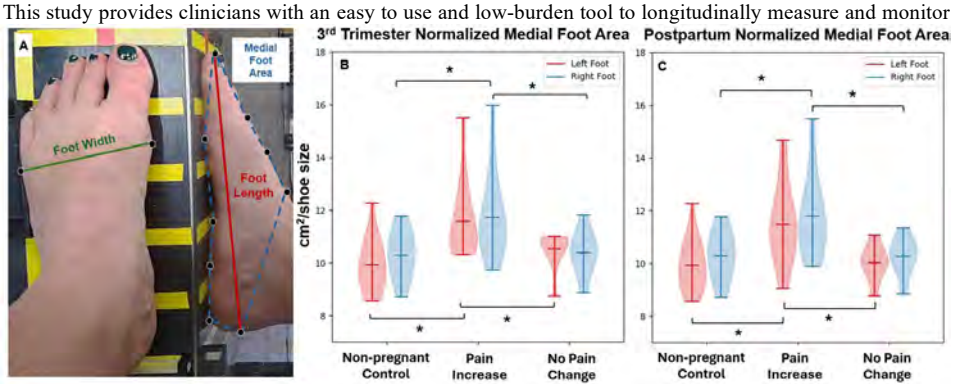

Figure 1. Foot width, length, and medial area measurements (A). Normalized medial foot area is increased during the 3rd trimester (B) and postpartum (C) in individuals with increased pain interference scores. *$p<0.05$

REFERENCES: [1] Vullo+1996, [2] Ponnapula+2010, [3] Segal+2023 [4] Anselmo+2017, [5] Fitzgerald+2015, [6] Shah+2020, [7] Kristiansson+1996, [8] Sahr+2024.

ACKNOWLEDGEMENTS: We thank the Ruth Jackson Orthopaedic Society (RJOS) and the American Orthopaedic Foot & Ankle Society (AOFAS) for their funding in this project.

Dynamic and Reversible Boundary Constraints to Guide Engineered Meniscus Microtissue Formation

Darcy D. Huang*[1,2], Yuqi Zhang[1,2], Georgios Kotsaris[2], Meghan E. Kupratis[2], Elizabeth R. Bernstein[1,2], Robert L. Mauck[1,2]

Departments of [1]Bioengineering and [2]Orthopaedic Surgery, University of Pennsylvania, Philadelphia, PA

Introduction: The meniscus is one of the most frequently injured structures in the knee,[1] with altered joint loading accelerating the onset of osteoarthritis.[2] Its wedge-shaped, semilunar architecture and attachment to the tibia enable the meniscus to convert compressive forces from the femur into hoop stresses, generating significant tensile loads.[3] In meniscus tissue engineering efforts, incorporating tensile loading, such as mechanical anchoring,[4] can enhance functional properties. However, the role of tensile loads in tissue formation and cellular contraction remains poorly understood. Constrained microtissue models provide a valuable platform for investigating these processes by enabling real-time, in situ measurements of tissue force generation.[5] Here, we present a novel constrained microtissue model that combines dynamic and reversible boundary stiffness with pre-strain capabilities to investigate how boundary constraints influence meniscus microtissue formation and force generation.

Materials and Methods: 3D-printed microtissue devices were fabricated using the biocompatible VisiJet SL Clear resin on a 3D Systems ProJet 6000 printer. Silicone tubing served as the elastic string, while stainless steel rods were used to adjust both the effective bending stiffness and the positioning of the string. Meniscus fibrochondrocytes (MFCs) were encapsulated in a 1.5 mg/mL collagen gel, and contractile force was quantified by measuring string deflection from images captured with a stereo microscope.

Results and Discussion: First, we characterized tissue force generation under static boundary stiffnesses and assessed their impact on tissue contraction. When cultured under either soft or stiff conditions for 5 days, axial tissue contraction—and, consequently, force generation—remained relatively stable after Day 1 (Fig. 1E). In contrast, lateral compaction progressed throughout culture, with only minimal differences in cross-sectional area between the two conditions (Fig. 1F). Notably, MFCs generated less force under stiff boundary conditions, in contrast to other tissues, such as cardiac tissue, where stiffer boundaries promoted higher force generation (Fig. 1G).[6] We also explored the effects of dynamic boundary stiffnesses, where tissues were primed at one stiffness for 4 days before transitioning to the opposite stiffness for an additional 2 days (Fig. 1H). Stiffening significantly reduced force generation in the control group, with a similar trend observed in TGF-β3-treated tissues (Fig. 1J). Conversely, the effects of softening were less pronounced, particularly in TGF-β3-treated tissues (Fig. 1J).

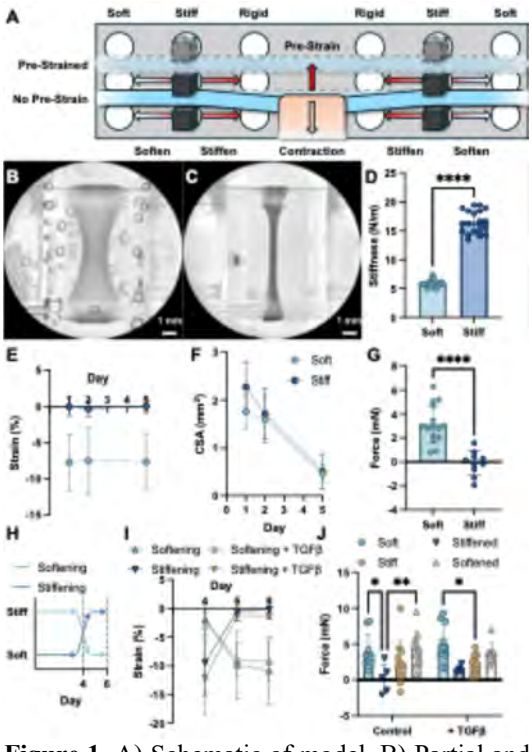

Figure 1. A) Schematic of model. B) Partial and C) full tissue compaction. D) Effective stiffness of soft and stiff configurations. E) Axial strain over time. F) Cross-sectional area over time. G) Day 5 force generation. H) Schematic of dynamic culture conditions. I) Axial strain over time. J) Day 4 and 6 force generation. * $p < 0.05$, ** $p < 0.01$, **** $p < 0.0001$ by t-test, or 2-way ANOVA.

Conclusion: In this work, we developed a novel constrained microtissue model to explore how boundary constraints influence meniscus microtissue formation and force generation. Our findings demonstrate that meniscus microtissues generate distinct levels of contractile force depending on boundary stiffness, and that this force generation adapts to dynamic boundary stiffnesses. Future work will further explore the influence of boundary constraints—particularly pre-strain—on tissue development and mechanical behavior. Techniques such as confocal imaging and RT-qPCR will be used to gain deeper insight into how boundary conditions affect tissue organization and cellular responses.

Acknowledgements: This work was supported by a National Science Foundation Graduate Research Fellowship and the National Institutes of Health (R01 AR075418).

References: [1] Bilgen B+, *Adv Healthc Mater*, 2018. [2] Lohmander L+, *Am J Sports Med*, 2007. [3] Makris E+, *Biomaterials*, 2011. [4] Puetzer J+, *J Biomech*, 2015. [5] Legant W+, *Proc Natl Acad Sci U S A*, 2009. [6] Eyckmans J+, *J Cell Sci*, 2017.

Anakinra Protects Against Mechanical Degradation of Articular Cartilage in an *In Vitro* Inflammatory Environment

Emily S. Cook[1,2], Brendan D. Stoeckl[1,2], Austin C. Jenk[1,2], David R. Steinberg[1,2], Robert L. Mauck[1,2]
[1]University of Pennsylvania, Philadelphia, PA. [2]CMC Veterans Administration Medical Center, Philadelphia, PA.
esc6@seas.upenn.edu

Disclosures: RLM (5- 4WEB Medical)

INTRODUCTION: Articular cartilage is essential for the proper mechanical function of the knee, but is prone to degradation following injury and exhibits poor healing capabilities. These injuries can lead to a "red knee" inflammatory environment [1], which exacerbates damage and hinders clinical cartilage repair strategies. Recently Anakinra, a recombinant version of Interleukin-1 receptor antagonist (IL-1Ra) has shown promise as a therapeutic to reduce post-traumatic arthritis [2-4] and limit disease progression. We recently showed that application of Anakinra in a large animal model of osteochondral repair (using the osteochondral autograft transfer system (OATS) procedure, in which cartilage is explanted from a non-bearing region and implanted into the damaged load-bearing region), improved graft functional properties five weeks following implantation [5,6]. However, given the complicated inflammatory and mechanical post-surgical environment, it was difficult to say with certainty whether the specific effects of Anakinra were on the articular cartilage or working through other joint structures (i.e., synovial inflammation, boney remodeling). To directly test the effects of Anakinra on cartilage functional properties, here we cultured cartilage *in vitro* in media containing either IL-1β alone or a combination of IL-1β and Anakinra. We hypothesized that provision of Anakinra would preserve the mechanical properties of cartilage cultured in a simulated inflammatory environment.

METHODS: Articular cartilage explants were sterilely isolated from juvenile bovine femoral condyles using a 4mm diameter biopsy punch and cut into cylinders 2mm in height from the cartilage surface. Explants were pre-cultured in basal media (BM) for 4 days before media was supplemented at day 0. Explants were split into 4 groups, with explants from each joint (N = 6 joints, ~16 explants/joint) split evenly across all 4 groups (N = 8-10/group/timepoint): Control (BM only), +IL-1β/-Anakinra (BM + 50ng/mL IL-1β), -IL-1β/+Anakinra (BM + 1000ng/mL Anakinra), and +IL-1β/+Anakinra (BM + 50ng/mL IL-1β + 1000ng/mL Anakinra). Media was changed and supplemented 3 times/week and explants were removed from culture on day 0 (baseline Control) and days 7 and 14 (all groups). Explants were frozen in 1x PBS at -20˚C until mechanical testing, at which time they were thawed and immersed in PBS in a custom fixture on an Instron mechanical test frame. Creep indentation testing [7] was performed on all samples at a constant force of 0.1N for 15 minutes, after which samples were allowed to swell to their original thickness prior to refreezing at -20˚C. After testing, samples were then thawed and split into sections for biochemical assays and histology. Samples for biochemical analysis were digested overnight with Proteinase-K followed by measurement of GAG content via a DMMB assay and DNA content via a PicoGreen assay [8]. Samples for histology were fixed in 10% formalin, processed into paraffin, and sectioned to 10 microns. Staining included Safranin O/Fast Green and Alcian Blue/Picrosirius Red [9]. All quantitative data was analyzed in GraphPad Prism using a Kruskal-Wallis test ($p<0.05$) followed by Dunn's multiple comparison post hoc test between groups at each timepoint.

RESULTS: Treatment with IL-1β significantly altered cartilage explant mechanical properties over time, including a reduction in compressive and tensile moduli and an increase in permeability by day 14. While treatment with Anakinra protected against IL-1β mediated-degradation, the compressive modulus and permeability were more noticeably affected than the tensile modulus (**Fig. 1**). Notably, application of Anakinra alone (in the absence of IL-1β) did not protect against the progressive loss of properties that explants experience during free-swelling culture over 2 weeks. That is, properties in the IL-1β/+Anakinra group on day 14 were significantly different from controls at day 0 ($p=0.001$). Histological analysis showed that IL-1β treatment significantly degraded the cartilage throughout the full thickness of the cartilage explants (**Fig. 2A, B**) and reduced the concentration of glycosaminoglycans (GAGs), as seen in both Alcian Blue staining (**Fig. 2C**) and direct quantification of GAG content (**Fig. 2D**). Samples treated with +IL-1β/+Anakinra retained more proteoglycans/GAG than the +IL-1β/-Anakinra treated samples ($p<0.0001$ for staining quantification and $p=0.0033$ for GAG content) and did not differ significantly from the control (-IL-1β/-Anakinra) group in either measure.

DISCUSSION: Here, we demonstrate the protective effects of Anakinra, an IL-1 receptor antagonist, against inflammation-induced degradation of cartilage and loss of mechanical integrity. Although explant cartilage samples experienced some loss of mechanical properties in culture over the 14-day period as expected [10], supplementation with Anakinra was sufficient to protect the cartilage from significant degradation across all outcomes, including mechanical properties and GAG content, when exposed to IL-1β. While this study focused primarily on the macroscale effect of Anakinra in an inflammatory environment, it will be important to investigate microscale changes in extracellular matrix mechanics to determine whether treatment preserves both depth-dependent and pericellular mechanics of the native tissue. Additionally, while the work presented here shows that Anakinra protects against IL-1β-induced degradation when administered at the same time, future studies will investigate whether Anakinra can rescue (or stabilize) mechanical properties when administered hours or days after inflammation begins, to more accurately represent a realistic injury state. Importantly, however, this study does support our initial hypothesis that Anakinra can protect articular cartilage from the loss of mechanical integrity and consequently supports the use of Anakinra as an adjuvant therapeutic during *in vivo* cartilage repair procedures.

SIGNIFICANCE: This *in vitro* investigation of the protective effects of Anakinra against cartilage degradation in an inflammatory environment supports further *in vivo* studies of its application as an adjuvant therapeutic used in combination with cartilage repair procedures to improve outcomes in the "red knee" joint environment.

REFERENCES: [1] Martín+ *NPJ Regen Med*, 2019. [2] Chevalier+ *Arthritis Care Res*, 2009. [3] Kraus+ *Osteoarthr Cartil*, 2012. [4] *Caron+ Arthritis Rheum*, 1996. [5] Stoeckl+ *ORS*, 2025. [6] Stoeckl+ *SB3C*, 2025. [7] Moore+ *J Tribol*, 2016. [8] Huang+ *Eur Cell Mater*, 2012. [9] Stoeckl+ *Acta Biomater*, 2021. [10] Meloni+ *Eur Cell Mater*, 2019.

ACKNOWLEDGEMENTS: This work was supported by the NIH (R01 AR077362 and P30 AR069619) and the VA (I50 RX004845, I01 RX003375, and I21 RX004628).

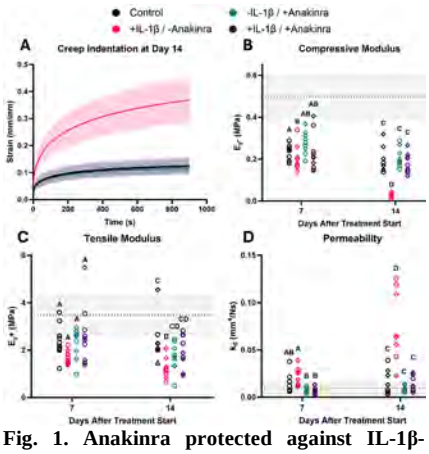

Fig. 1. Anakinra protected against IL-1β-mediated loss of mechanical properties. (A) IL-1β reduced resistance to creep deformation compared to all other groups. IL-1β lowered the compressive (B) and tensile moduli (C) and increased permeability (D) of the cartilage, while co-supplementation with Anakinra somewhat (C) or significantly (B, D) protected the cartilage mechanical properties. Letters indicate significant differences between groups; $p<0.05$. Grey box indicates day 0 control values; mean +/- SD.

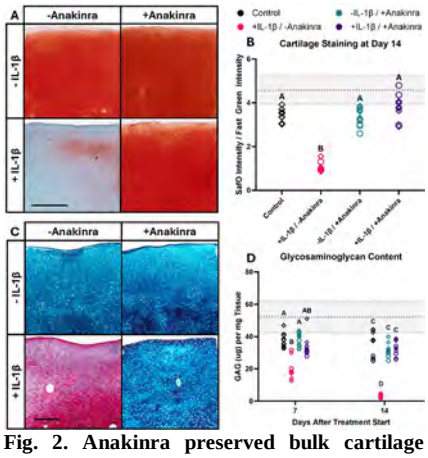

Fig. 2. Anakinra preserved bulk cartilage matrix proteoglycans. Safranin-O (A, B) and Alcian Blue staining intensity (C) was reduced by IL-1β treatment but preserved by treatment with both IL-1β and Anakinra. GAG content (D) was similarly affected by IL-1β, while Anakinra co-supplementation protected against GAG loss. Letters indicate significant differences between groups; $p<0.05$. Scale = 500 microns. Grey box indicates day 0 control values; mean +/- SD.

Trade-offs Between Compression and Relaxation: The Role of Screw Angle in Long-Oblique Fracture Fixation

Rachel Bonfini[1], Karl E. Hoenecke[2], Farzad Abdi[1], Badhan Saha[1], Elizabeth Silvestro[3], Anna M. Massie[2], Michael W. Hast[1]
[1]University of Delaware, Newark, DE, [2]University of Pennsylvania, Philadelphia, PA, [3]Children's Hospital of Philadelphia, Philadelphia, PA
Email of Presenting Author: rbonfini@udel.edu

Disclosures: Bonfini (N), Hoenecke (N), Abdi (N), Saha (N), Silvestro (N), Massie (N), Hast (N)

INTRODUCTION: A long-oblique fracture, defined as a fracture with at least twice the length of the cross-sectional diameter of the bone, is a common bone fracture resulting from compressive forces along a bone axis. Multiple fixation techniques are available to stabilize long-oblique fractures, each with distinct advantages and limitations. Primary bone healing through reconstruction and compression of the fractured bone can be achieved with either lag screw placement or cerclage wiring. Lag screw fixation is achieved by placing screws across the fracture line using specially designed lag screws or by over-drilling the cis/glide cortex. Perpendicular drilling is achieved subjectively in a clinical setting and can be additionally skewed by fracture exposure/visualization and soft tissue impingement. The significance of screw angle to interfragmentary contact forces remain unclear. This study sought to determine changes in compressive forces caused by 6 different screw insertion angles to better understand the relationship between lag screw placement and contact forces. We hypothesized that interfragmentary compression of lag screw fixation will rise with increasing angulation of screw placement compared to a screw placed perpendicular to the fracture line.

METHODS: 48 two-part cylindrical specimens (1 cm dia × 4 cm h) were created with a 27° oblique fracture pattern (**Fig. 1A**). Parts were fabricated via 3D printing using materials that closely mimic the mechanical properties of cortical and cancellous bone (BoneMatrix and VeroWhite (BV) filaments). To model over-drilling of the cis cortex, a 3.5 mm glide hole was created in the proximal fragment and a 2.5 mm pilot hole was created in the trans-cortex. Five groups (n=8) were aligned at angles of 60°, 75°, 90°, 105°, and 120° relative to the fracture line, while a sixth group was aligned at 90° and incorporated a 30° oblique offset with respect to the axial plane. Reduction was achieved with two point-to-point bone holding forceps, after which a 3.5 mm cortical screw was inserted with an instrumented screwdriver to a torque of 0.4 Nm. Forceps were then released, and the construct was allowed to relax. To measure interfragmentary forces, thin-film pressure sensors were placed between the bone fragments (**Fig. 1B**). Force data was collected (1) after reduction using forceps, (2) after screw fixation with the forceps in place, and (3) for 30 seconds after removal of the reduction forceps. Statistical analyses were performed using one-way ANOVAs with Tukey's multiple comparison tests.

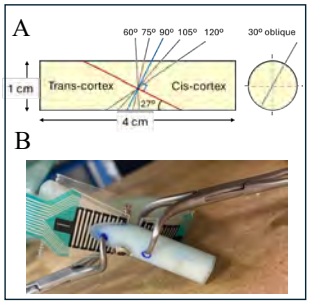

Figure 1: *(A) Schematic of screw trajectories used in the study. (B) Photograph of pressure sensors within constructs fixed by a lag screw and reduction forceps.*

RESULTS: There were no significant differences between groups during forceps reduction (**Fig. 2A**). Interfragmentary forces increased for all groups during screw fixation, but the 120° group had significantly lower contact forces than the 105°, 90°, and 75° groups (**Fig. 2B**). After removal of forceps, all groups experienced decreases in contact forces. The 120° group had significantly lower contact forces than the 105°, 90°, 75°, and 60° groups, while the 30° oblique offset group was significantly lower than the 90° and 75° groups (**Fig. 2C**). Contact force loss rates were the lowest for the 120° group, with no significant differences between other groups (**Fig. 2D**).

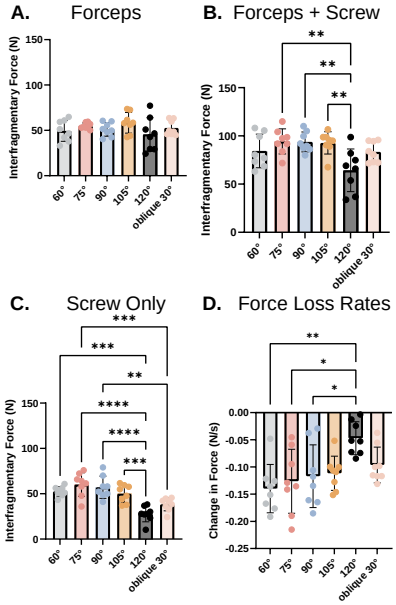

Figure 2: *Measures of interfragmentary forces using (A) forceps, (B) forceps and screw fixation, and (C) screw fixation alone. (D) Rates of force losses caused by relaxation. * $p<0.05$, ** $p<0.01$, *** $p<0.001$, **** $p<0.0001$.*

DISCUSSION: This study demonstrated that lag screw orientation significantly influenced both interfragmentary compression and reduction alignment across oblique fracture models. Results support the biomechanical principle that alignment closer to normal against the fracture plane maximizes interfragmentary compression. Similar studies have observed the effects of lag screw placement on fixation strength but differ in that non-bone surrogate materials were used, post-placement relaxation patterns were not assessed, and long oblique fracture models were not incorporated [1],[2]. Interestingly, the lowest compressive relaxation rates over time were observed in the 60° and oblique 30° groups, suggesting that angled screws may generate greater surface engagement with bone, thereby resisting early screw migration despite lower overall compression. Clinically, this raises the question of whether maximizing compression (as with perpendicular screws) is preferable to minimizing relaxation (as with more oblique screws), as both factors influence long-term stability and healing. Excessive shear generated at more oblique angles may compromise fixation, emphasizing the delicate balance between compression and stability in lag screw placement. Limitations of this study include the short 30-second observation period, which may not fully capture long-term relaxation patterns. Overall, these findings suggest that perpendicular placement is biomechanically advantageous for maximizing initial compression and minimizing displacement after fixation, though oblique orientations may confer unique stability benefits that warrant further investigation.

SIGNIFICANCE/CLINICAL RELEVANCE: This study demonstrates that lag screw insertion angle directly influences compressive force, relaxation behavior, and length offset in long oblique fractures, providing critical insight into how fixation geometry impacts mechanical stability. These findings highlight the potential clinical value of optimizing screw orientation—possibly through custom 3D printed drill guides—to maximize compression and improve fracture healing outcomes. This is particularly important in articular fractures where perfect anatomic reduction and compression to promote primary bone healing is critical to long-term outcomes.

REFERENCES: [1] Kuzma+, *J Orthop Trauma*, 2019; [2] Chang+, *Vet Comp Orthop Traumatol,* 2018

Glycosaminoglycan content decreases with age in the mouse Achilles tendon but does not alter mechanical properties

Jonathon L. Blank, Jeremy D. Eekhoff, Louis J. Soslowsky
McKay Orthopaedic Research Laboratory, University of Pennsylvania, Philadelphia, PA
jonathon.blank@pennmedicine.upenn.edu

DISCLOSURES: None.

INTRODUCTION: Injuries are common in repetitive and high load-bearing tendons such as the Achilles tendon,[1] and injuries in middle-aged and older adults are prevalent due to increased lifespans and activity.[2] Glycosaminoglycans (GAGs) are long, negatively charged polysaccharides found in musculoskeletal tissues such as cartilage and meniscus and decrease in number with age,[3,4] corresponding to altered mechanics.[5,6] Decreasing GAG content with age has also been observed in human rotator cuff.[7] While GAGs have been shown to modulate viscoelasticity in mature patellar tendon[8] and tail tendon fascicles,[9] the relationship between GAG composition and aging Achilles tendon mechanics remains unknown. Therefore, the objective of this study was to investigate the role of GAGs in dynamic tensile loading in mouse Achilles tendons. We hypothesized (1) that GAG content would decrease with age and (2) that GAG-depleted tendons would exhibit a decrease in tensile viscoelasticity, but that this effect would wane with increasing age.

METHODS: Animals: Achilles tendons from male postnatal (P) day 150, 300, and 570 C57BL/6 Charles River mice were used (IACUC approved). These age ranges correspond to roughly 25, 45, and 65 years of human age. Biochemistry: GAGs were cleaved from their proteoglycan core proteins using chondroitinase ABC (cABC). Tendons from each age group were incubated in a tris buffer (pH=8) supplemented with protease inhibitors (control buffer) or a solution of control buffer with the addition of 0.5U/mL cABC (treatment buffer) for 18 hours under gentle agitation at 37° C. Tendons were then dissected from the calcaneus and digested in a Proteinase K solution overnight at 60°C prior to quantifying GAG content using the 1,9-dimethylmethylene (DMMB) blue assay and CS as standard (n=6/group). Absorbance was read at 525 and 595 nm.[10] Mechanics and Collagen Fiber Realignment: Following digestion, cross-sectional areas (CSAs) were measured using a custom laser device. Verhoeff stain lines were applied to denote the tendon insertion (0-1 mm) and midsubstance (1-3 mm) for regional, optical strain analysis. Tendons were mounted on a loading device (4 mm gauge length) with the calcaneus fixed and the proximal tendon clamped in a sandpaper grip in a 37° C 1X PBS bath. Our protocol consisted of 10 preconditioning cycles followed by stress relaxations at 1.5% and 3% strain. Following a 10-minute hold, tendons were subjected to frequency sweeps at 0.1, 1, 5, and 10 Hz, followed by a 5-minute rest period and a ramp-to-failure at 0.1%/s (n=8-10/group). Elastic (stiffness, regional modulus) and viscoelastic properties (dynamic modulus, phase shift, and percent relaxation) were measured from the test. Fiber realignment during the ramp-to-failure in the insertion and midsubstance regions were measured using reflectance mode quantified polarized light imaging.[11] Statistics: Comparisons across age and digestion groups were conducted using two-way ANOVAs followed by Bonferroni post-hoc tests. Significance was set at $p \leq 0.05$.

RESULTS: GAG content in the Achilles tendon decreased throughout aging ($p = 0.001$) and was reduced by 50% ($p < 0.001$) following cABC treatment (**Fig. 1a**). Tendon cross-sectional area increased with age ($p = 0.01$) but was unaffected by cABC treatment (**Fig. 1b**). There were no changes in elastic mechanical properties of the Achilles tendon following cABC treatment (**Fig. 1c-e**). We did not detect any change in viscoelastic mechanical properties following cABC treatment in any age group (results for 3% strain and 1 Hz shown, **Fig. 1f-h**). cABC treatment had no effect on fiber realignment independent of strain in P150 mice in the insertion and midsubstance regions (**Fig. 1j-k**). Fiber realignment patterns were similar in P300 and P570 mice with the exception of a higher variance in angle of polarization (AoP) in the P300 insertion group at 50% of the max grip strain ($p = 0.03$, data not shown).

DISCUSSION: GAG content in the Achilles tendon decreases similarly across age as in cartilage and meniscus,[3,4] yet the role of GAGs in aging tendon mechanics in this study is minimal. We did not detect an effect of GAG depletion on elastic mechanical properties, as reported in prior studies.[12,13] Contrary to our hypothesis, GAG digestion did not alter the viscoelastic mechanical properties of the Achilles tendon in any age group, including stress relaxation, which has been reported in tendon fascicles.[9] Prior studies have shown that GAGs promote collagen fiber realignment in cartilage under tension.[14] However, a higher-than 50% digestion yield may be necessary to uncover any changes in fiber realignment and resulting changes in mechanical properties following cABC treatment in tendon, where there are fewer GAGs than in cartilage and meniscus. Future work will extend our measurements of fibril kinetics using atomic force microscopy and investigate the mechanical role GAGs serve in tendon overuse and injury.

SIGNIFICANCE: GAGs are a minor constituent in tendon and are found in abundance in tendinopathy and following injury. Understanding the role of GAGs in aging tendon structure-function is critical for developing therapies to restore tendon function.

REFERENCES: [1] Möller+ *Acta Orthop. Scand.* 1996. [2] Huttenen+ *Am. J. Sports Med.* 2014. [3] Riedler+ *Laryngoscope* 2017. [4] Muller-Lutz+ *J. Magn. Reason. Imaging* 2015. [5] Lee+ *J. Struct. Biol.* 2013. [6] Boxberger+ *J. Biomech.* 2009. [7] Riley+ *Ann. Rheum. Dis.* 1994. [8] Muljadi+ *J. Biomech.* 2023. [9] Legerlotz+ *Acta. Biomater.* 2013. [10] Zheng+ *Eur. Cell. Mater.* 2015. [11] Ianucci+ *Biomed. Optic. Exp.* 2024. [12] Lujan+ *J. Orthop. Res.* 2007. [13] Fessel+ *J. Theor. Biol.* 2011. [14] Schmidt+ *J. Orthop. Res.* 1990.

ACKNOWLEDGEMENTS: Penn Center for Musculoskeletal Disorders (NIH/NIAMS P30AR069619).

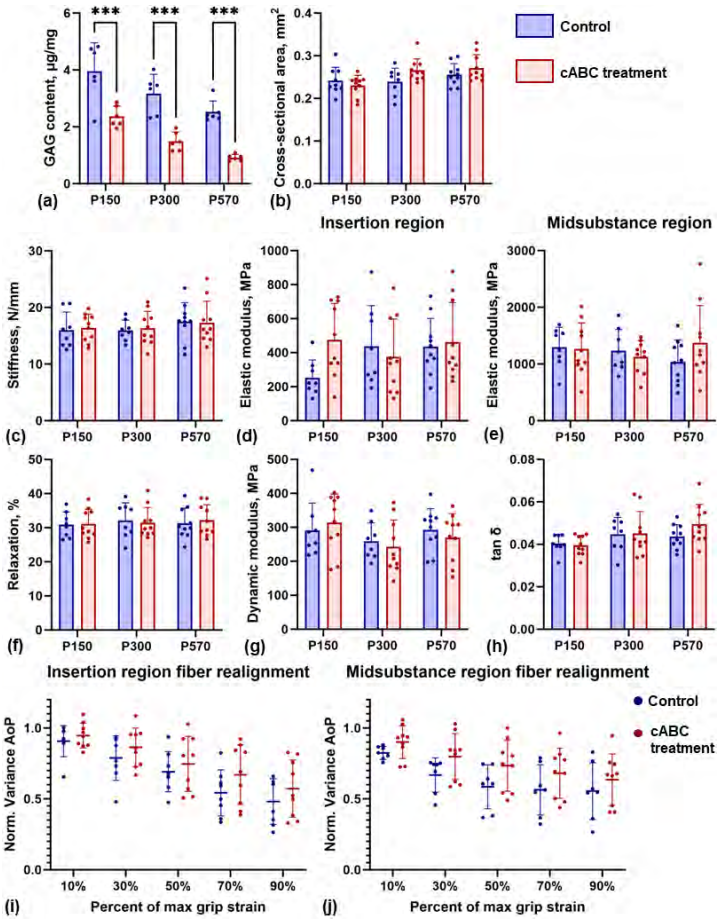

Figure 1: (a) cABC treatment reduced GAGs in the Achilles tendon, which decreased similarly across age. **(b)** CSA was unaffected by cABC treatment. **(c-e)** Elastic properties were unaffected by cABC treatment in all age groups. **(f-h)** Viscoelastic properties were unaffected by cABC treatment (properties at 3% strain and 1 Hz shown) in all age groups. **(i-j)** cABC treatment had no effect on fiber realignment independent of strain (P150 results shown) determined by variance in angle of polarization (AoP) (* $p \leq 0.05$, ** $p \leq 0.01$, *** $p \leq 0.001$).

Deep Learning–Based Markerless Motion Tracking as a Cost-Effective Alternative for Large Animal Gait Analysis

Farzad Abdi[1], Badhan Saha[1], Jacob Sommer[1], Isabel Kehoe-Huck [1], Karl Hoenecke[2], Zoe Araujo[2], Anna M. Massie[2], Kimberly A. Agnello[2], Michael W. Hast[1]

[1]University of Delaware, Newark, DE, [2]University of Pennsylvania, Philadelphia, PA

abdi@udel.edu

Disclosures: FA (N), BS (N), JS (N), IK-H (N), KH (N), ZA (N), AMM (N), KAA (N), MWH (N)

INTRODUCTION: Quantitative gait analysis in large preclinical animal models is an important tool for assessing experimental surgical outcomes and long-term rehabilitation progress. Conventional tools such as marker-based motion capture and instrumented walkways provide accurate kinetic and kinematic data, but are costly, time-intensive, and impractical for routine use – especially in veterinary clinics and farms [1]. Markerless motion tracking enables precise detection of joint trajectories from standard video recordings [2]; however, its reliability and validity in this context remain unproven. The purpose of this study was to evaluate the feasibility of a markerless motion tracking framework for large animal gait analysis. We hypothesized that markerless motion tracking would provide gait measurements that were equally as sensitive to changes in healing as conventional methods (force plate data) while offering improved efficiency and practicality.

METHODS: In an ongoing IACUC-approved study, thirteen adult dogs have been enrolled, including seven with a cranial cruciate ligament (CCL) rupture and reconstruction and 6 controls. This pilot study evaluated one CCL-injured dog within the cohort, which was assessed longitudinally at five time points: (1) pre-operatively, (2) day of surgery, (3) 6 weeks, (4) 8 weeks, and (5) 6 months post-operatively. During each visit, the dog walked across a pressure-sensitive walkway (Tekscan) while being simultaneously recorded in the sagittal plane using a smartphone camera recording at 30 Hz. Kinematic analysis was performed with DeepLabCut™ (DLC), a deep learning-based markerless pose estimation framework. To create a training dataset, 1–2 representative videos were selected, and 80–140 frames were manually labeled with hip, knee, ankle, and toe landmarks. Models were trained using the optimal ResNet-101 architecture for 50,000–100,000 iterations with image augmentation to enhance generalization. Once trained, DLC automatically tracked all joints in the remaining trials and joint angles were derived in MATLAB. To assess gait symmetry, root mean square errors (RMSE) were calculated for the ipsilateral and contralateral joint angles. Separately, symmetry indices were calculated from the walkway kinetic data. The linear correlation between kinetic and kinematic symmetry indices were calculated and one-way ANOVAs with post hoc Tukey's pairwise tests were performed to evaluate differences within groups across time points.

RESULTS: ***Kinematic Analysis:*** At baseline, the dog demonstrated reduced peak knee and ankle flexion compared to later time points (e.g. **Fig. 1A**). Longitudinal tracking revealed progressive recovery following surgery, with knee flexion partially restored by 6–8 weeks and approaching normal patterns by 6 months. RMSE between injured and healthy legs decreased significantly from Visit 1 to Visit 5 for all joints (e.g. **Fig. 1B**). The knee showed the largest reduction, from 21.8± 3.1° at Visit 1 to 5.3 ± 0.9° at Visit 5 ($p<0.0001$). ***Kinetic Analysis:*** Symmetry indices derived from maximum hindlimb forces (ideal score = 0) showed marked asymmetry at baseline, with a normalized score of 29.04 at Visit 1. This asymmetry index progressively decreased following surgery, reaching a mean score of 0.28 at Visit 5 (**Fig. 1C**). ***Correlation between kinematics and kinetics:*** Best-fit linear regression revealed weak-to-moderate associations between RMSE and maximum force symmetry. The hip demonstrated a regression of $R^2 = 0.07$, the knee $R^2 = 0.14$, the ankle $R^2 = 0.17$, and the toe $R^2 = 0.10$ (**Fig. 1D**).

DISCUSSION: This case study demonstrated that markerless motion tracking was sensitive to changes in post-operative rehabilitation. Analysis of joint trajectories showed the joint's angles progressively normalized across visits, with RMSE values decreasing significantly from baseline to 6 months. The most pronounced improvements were observed in the knee, which makes sense, given the nature of the injury. Similarly, pressure-sensing walkways were also able to quantify functional recovery following CCL reconstruction by measuring substantial improvements in limb-loading symmetry. Correlations between RMSE and maximum force symmetry demonstrated that reductions in kinematic variability were paralleled by improvements in kinetic balance, with data clustering tightly by Visit 5. Although the regression fits were not strong, the trend confirmed that joint-level recovery and limb-loading restoration converge over time. Together, these findings demonstrate a relationship between kinematic and kinetic measures for quantitative monitoring of rehabilitation. The implications of a reliable, low-cost analysis of kinematics are substantial. A DLC-based kinematic analysis has potential to not only improve preclinical animal model experiments, but it also provides a new tool in standard veterinary clinics. Limitations of this study include a subject-specific DLC training protocol, and the evaluation was limited to the sagittal plane. Future work will expand to a larger cohort and explore model generalization for cross-subject use.

SIGNIFICANCE/CLINICAL RELEVANCE: This study shows that reduced kinematic variability (RMSE) aligns with improved limb-loading symmetry, underscoring the sensitivity of markerless motion tracking with low-cost equipment. This scalable, cost-effective approach enables remote, longitudinal monitoring, with significant potential to enhance experimental and clinical assessments of rehabilitation following surgery.

REFERENCES: [1] Gillette+, *Vet. J.*, 2008; [2] Spinella+, *Vet. Sci.*, 2021,

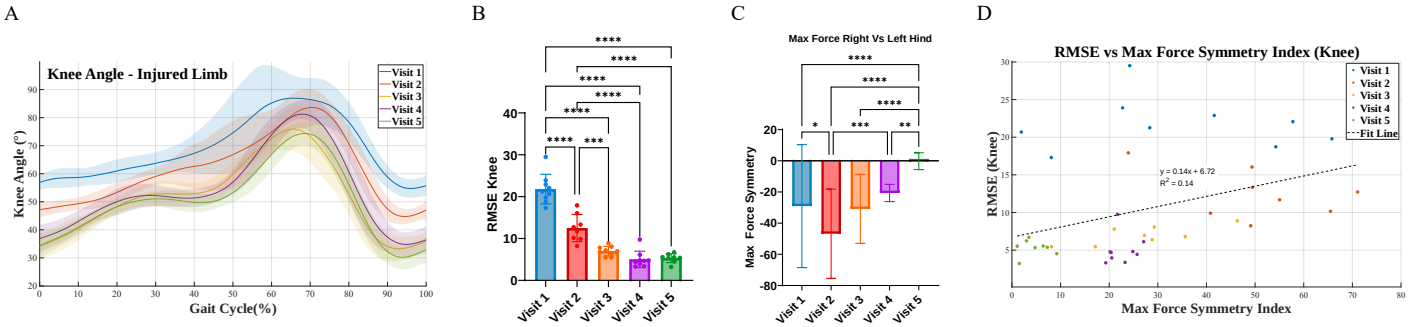

Figure 1*: Quantitative analyses of the knee joint in this pilot study included (A) knee angle trajectories from all strides for the injured limb; (B) RMSE analysis of the knee considering the injured and contralateral limb; (C) Maximum force symmetry index (right vs. left hind); (D) Correlation between RMSE values and maximum force symmetry index.*

Influence of Zinc Coating on Bone Volume Loss and Mechanical Stability Across Different Screw Designs in a Cadaveric Rabbit Femur Model

Badhan Saha[1], Farzad Abdi[1], Andrew Cagliostro[1], Chet S. Friday[2], Karl Hoenecke[2] Anna M. Massie[2], Michael W. Hast[1]
[1]University of Delaware, Newark, DE, [2]University of Pennsylvania, Philadelphia, PA
badhan@udel.edu

Disclosures: BS (N), FA (N), AC (N), CSF (N), KH (N), AMM (3B; Movora), MWH (N)

INTRODUCTION: Osteoporosis is a chronic skeletal disorder characterized by reduced bone mass and structural deterioration, leading to increased fragility and fracture risk. Hip and femoral fractures are among the most severe, often requiring surgical fixation with metallic hardware [1]. However, fixation in osteoporotic bone is challenged by poor screw anchorage, reduced osseointegration, and poor clinical outcomes [2]. Zinc (Zn) has emerged as a promising coating material due to its osteogenic and antibacterial properties [3]. While Zn coatings on screws and Kirchner wires may improve bone regeneration longitudinally, it remains unclear if additional thickness and roughness of the coatings cause immediate microdamage during the insertion process. The purpose of this study was to investigate the efficacy of Zn coatings on cortical screws, locking screws, and K-wires. Our null hypothesis was that Zn-coatings would have no effect on bone loss or bone mechanics compared to uncoated controls.

METHODS: Thirty-six femora were harvested from skeletally mature New Zealand White rabbits (all female) obtained post-mortem from an unrelated study. Specimens were dissected and bones were randomly assigned to six groups (n=6/group) based on implant type (2.0 mm cortical screws, 2.0 mm locking screws, and 2.0 mm K-wires) and material (stainless steel (SS, control) or zinc-coated (Zn)). Zinc coatings were applied using an electrodeposition process following ASTM B633-19 guidelines. To create pilot holes, bones and a surgical drill were mounted to custom fixtures on a universal test frame and the drill was depressed at 0.5 mm/s. K-wires were inserted directly without pilot holes to mimic a percutaneous technique. Cortical and locking screws were inserted with a torque-limiting driver set to 1.2 Nm. After hardware was removed from the bones, femora were scanned using microCT (10.4 µm voxel size) and 312 slices were analyzed for each specimen. To evaluate localized bone loss, volumetric analyses were performed with standardized segmentation thresholds (Dragonfly v.1.31.0). Following imaging, femora were potted and tested in an axial/torsional load frame. Each specimen was preloaded axially to simulate 35% of body weight and then subjected to external rotation at 10°/s until failure. Torque and angular displacement were continuously recorded to calculate stiffness, yield torque, ultimate torque, and torsional rigidity. Statistical analysis was performed using two-way ANOVA with Tukey pairwise comparisons. Normality was assessed with Shapiro–Wilk tests, and significance was defined as $p<0.05$.

RESULTS: ***Micro-CT Analysis:*** Quantitative analysis of normalized total bone volume loss showed that Zn-coated K-wires (14.0 ± 1.4%) exhibited significantly greater bone loss compared to SS K-wires (10.8 ± 0.7%, p=0.023, **Fig. 1A&B**). Cortical screws caused more bone loss than locking screws for the SS (p=0.035) and Zn (p=0.033) groups. There were no significant coating-related differences within cortical or locking screw groups. No evidence of zinc coating delamination was observed in any of the micro-CT scans. ***Mechanical Testing:*** Ultimate torque was significantly higher in SS K-wires (2.49 ± 0.25 Nm) compared to Zn-coated K-wires (1.61 ± 0.31 Nm, p=0.009, **Fig. 1C**). Similarly, torsional rigidity was significantly greater in SS K-wires (0.026 ± 0.004 N·m²/deg) than Zn-coated K-wires (0.019 ± 0.004 N·m²/deg, p=0.014, **Fig. 1D**). No other significant differences were observed between Zn and SS for cortical or locking screws.

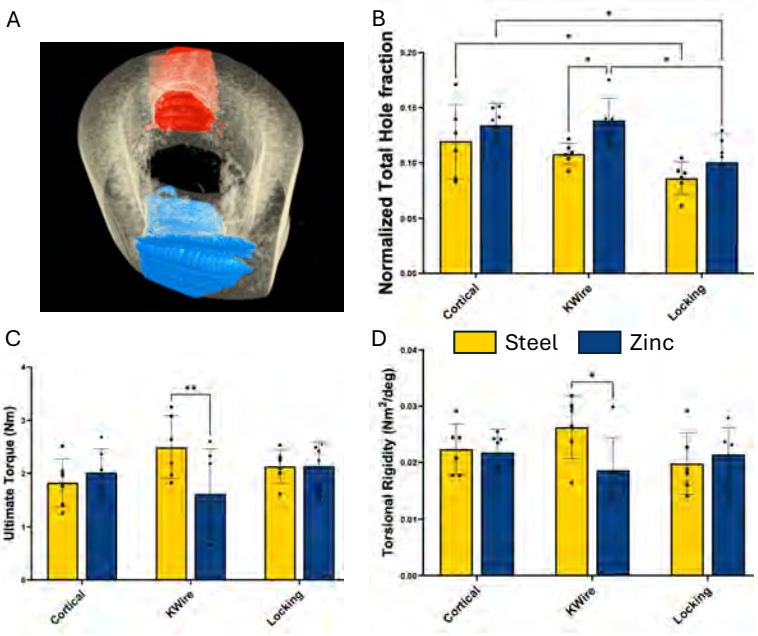

Figure 1. *(A) Representative micro-CT reconstruction of a rabbit femur drilled with a cortical stainless steel (SS) screw, showing insertion hole (red), secondary hole (blue), and surrounding bone. (B) Normalized total bone volume fraction (BV/TV) across fixation types and materials. (C) Ultimate torque of femora implanted with SS and zinc-coated (Zn) fixation devices. (D) Torsional rigidity of femora implanted with SS and Zn fixation devices. $p<0.05$, ** $p<0.01$*

DISCUSSION: This study investigated the influence of screw design and Zn surface coating on bone loss and torsional stability in cadaveric rabbit femora. A rabbit model was selected for this study because the brittle nature of rabbit bone provides a clinically relevant environment for evaluating fixation stability and failure mechanisms. Interestingly, micro-CT analysis revealed that Zn-coated K-wires caused the greatest total bone volume loss, but this did not result in significant losses in mechanical strength in comparison to locking or cortical screws. Among SS implants, cortical screws produced greater bone loss than locking screws, highlighting the role of implant geometry in preserving bone. These findings suggest that K-wires, particularly when Zn-coated, may compromise bone integrity by enlarging insertion volumes, while locking screws are less disruptive to surrounding bone. Mechanical testing demonstrated that SS K-wires achieved significantly higher ultimate torque and torsional rigidity than Zn-coated K-wires, consistent with their reduced bone loss. No significant coating effects were observed in cortical or locking screws, reinforcing the interpretation that any deleterious effects of coatings are minimal and are likely to be offset by improved biological properties including osteogenic stimulation and antibacterial activity. Limitations of this study include the in vitro design, which does not capture bone remodeling or biological integration, as well as the limited sample size. Future in vivo studies are needed to determine whether the biological effects of Zn can improve fixation outcomes, particularly in osteoporotic bone.

SIGNIFICANCE/CLINICAL RELEVANCE: Zn coatings increased bone loss and slightly weakened mechanical properties, but their biological potential to promote healing suggests value for future in vivo applications in osteoporotic fracture fixation.

REFERENCES: [1] Varacallo+, *Med. Clin. North Am.*, 2014; [2] Prince+, *J. Bone Miner. Res.*, 2019; [3] Pisani+, *World J. Orthop.*, 2016.

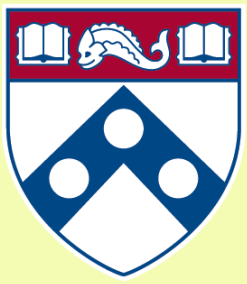

Penn Center *for*
Musculoskeletal Disorders
UNIVERSITY *of* PENNSYLVANIA

Histology Core Abstracts

AM Session

Poster 34 to 48

Application of an Electric Current in the Developing Chicken Embryo Induces Spinal Deformity

Carly Ciociola[1], Jacob V. Jordan[2,3], Giuseppe Orlando[4], Andrea Ketschek[5], Gianluca Gallo[5], Jason Anari[2,3], Brian D. Snyder[6], Thomas P. Schaer[1], Patrick J. Cahill[2,3]
[1]Department of Clinical Studies New Bolton Center, University of Pennsylvania School of Veterinary Medicine, Kennett Square, PA; [2]Department of Orthopedic Surgery, Children's Hospital of Philadelphia, Philadelphia PA;[3]Perelman School of Medicine at the University of Pennsylvania, Philadelphia PA; [4]Casilino Hospital, Rome, Italy; [5]Shriners Hospitals Pediatric Research Center, Lewis Katz School of Medicine at Temple University, Philadelphia PA; [6]Boston Children's Hospital and Beth Israel Deaconess Medical Center, Harvard Medical School, Boston, MA;
ciociol1@vet.upenn.edu

Disclosures: All authors have no conflicts to disclose related to this research project.

Introduction: Congenital scoliosis is a relatively rare condition, affecting 1 in 1000 live births, where vertebral anomalies present at birth involve either a failure of vertebral formation, such as a hemivertebra, or a failure of vertebral segmentation, such as a unilateral unsegmented bar, where different parts of the vertebral body and posterior elements can be affected to varying extent [4] creating complex spinal deformity. Congenital vertebral malformations result in unbalanced spinal growth, leading to deformities that can range from mild, asymptomatic curves to severe curves requiring surgical intervention in infancy [2]. Imaging of the spine pathoanatomy on bi-planar X-rays is described as scoliosis when projected onto the coronal plane and kyphosis when projected in the sagittal plane [1]. Congenital anomalies of the thoracic spine may involve rib cage deformities that result in thoracic insufficiency syndrome (TIS), where anatomic constriction of the thorax prevents uniform lung inflation and impedes lung growth, leading to extrinsic restrictive lung disease and increased childhood mortality [3]. The risk of spine deformity progression depends on various factors, including the morphology and anatomical location of the vertebral anomalies as well as the rate of spine growth. Given that little is known about the pathophysiology of congenital spine deformity, clinicians are unable to make informed treatment decisions. Our understanding of congenital spine deformity is limited by a lack of relevant animal models to study mechanisms contributing to congenital spine pathoanatomy. The purpose of this study is to examine the effects of applying targeted electric current on the formation and location of congenital spinal deformities in the developing chicken embryo.

Methods: 47 specific pathogen-free (SPF) eggs were incubated until embryonic day 3 (E3) when the shell was windowed for intervention. Electroporation parameters were set to 50V, with 50 ms pulses x 3 separated by a 950 ms interval. In the intervention group (n=42), an electrical current was delivered through electrodes placed above (n=11), below (n=12), and at an oblique angle to the vitelline vessels (n=19). Five eggs served as controls, with electrodes placed but no current applied. Eggs were sealed and incubated until E10, then the embryos were sacrificed. At E17, 11 eggs were assessed to specifically and accurately characterize the 3D nature of induced deformity using µCT, with 7 receiving intervention and seven controls. For histologic analysis, select specimens harvested at E10/E11 were sectioned and stained using both standard H&E and Alcian blue / Picrosirius red to observe morphological defects of the vertebrae at the apex of the deformity. To facilitate standardization, specimens were sectioned coronally through the spinal canal. Alcian blue was used to stain the vertebral cartilaginous anlagen, delineating the primitive spine from surrounding tissue. In the cohort of eggs assessed at E10/E11, descriptive statistics determined proportions for survival and deformity induction, at a 95% confidence interval, calculated using the Wilson score method. To account for the small sample size, overall survival proportions of treated vs control specimens were compared using Fisher's exact test. Additionally, among the surviving specimens, Fisher's exact test was used to compare deformity proportions between the treated and control groups ($p<0.05$).

Results: The electroporation protocol resulted in high survival rates (n=33/46, 72%) and high spinal deformity rates (n=29/33, 88%). Spinal defects (n=30/33, 90%) were region-specific, based on electrode placement (**Fig. 1**). All control embryos survived (5/5) without spine deformity (0/5), highlighting the significant difference in deformity rates between groups ($p<0.0001$, **Fig. 1**). Control chicks did not exhibit aberrant morphology of vertebral anlagen or curvature of the spine. µCT assessment of the inferior orientation group @ E17 identified unsegmented bars and block vertebrae at the thoracolumbar region. In scoliotic chicks, laterality comparisons were made between sides exhibiting aberrant vertebral development compared to the opposite side. Bilateral defects were observed in 4/9 specimens with fusion, and unilateral defects were observed in 5/9 specimens with fusion. Histologic evaluation of specific regions in representative specimens confirmed segmentation defects between adjacent cartilaginous vertebral anlagen, not present in controls **(Figs. 2&3)**.

Discussion: Since scoliosis can occur without vertebral malformations from changes in the disc or surrounding muscles, we verified that the deformities observed during dissection were due to bony abnormalities mimicking the vertebral defects seen in patients with congenital scoliosis. HE and Alcian blue staining of E10/E11 specimens revealed morphological abnormalities in the vertebral cartilaginous anlagen at the deformed region of interest, which were absent in controls. In the sectioned samples, fusions of adjacent vertebral segments were observed, indicating failure of segmentation as the cause of the pathoanatomy. These patterns were consistent across the targeted region and were not seen in areas of the spine not operated on, indicating local regional control of electroporation. A disruptive vascular pathogenesis has been widely hypothesized as a cause for the development of congenital spine anomalies, such as Klippel-Feil syndrome (5,6). During re-segmentation (membranous phase), pairs of dorsal intersegmental arteries arise from the dorsal aorta and supply blood to the respective somites. In a histological study by Tanaka et al, a relationship between abnormal intersegmental artery distribution and vertebral segmentation defects was observed in 40 of 266 human embryos and fetuses (5), where cells closest to the arteries differentiated more rapidly. During the membranous phase, obstruction or delay in the development of the vertebral arteries could cause ischemia and halt morphogenesis, leading to segmentation failure. The extent and location of vertebral fusion can be explained by the location and severity of the vascular lesion (6), which could be controlled through targeted electrode placement. We suggest that vascular injury is the mechanism inducing vertebral segmentation defects in this chick model, supported by mild bleeding events observed in our study when applying electric current. Although not all deformed specimens experienced a bleeding event, microvascular injury to the intersegmental arteries remains plausible and deserves further investigation.

Significance/Clinical Relevance: The ability to produce region-specific thoracolumbar malformations that persist through late-stage development provides a valuable platform for investigating disease progression, biomechanical consequences, and potential therapeutic interventions in a clinically relevant form of congenital scoliosis.

References: 1. Mackel++*Childs Nerv Syst*. 2018; 2. Kose++*Med Sci Monit Int Med J Exp Clin Res*. 2004; 3. Hedequist++ *J Pediatr Orthop*. 2007; 4. Hensinger++*Spine*. 2009; 5. Tanaka++Acta Orthop Scand. 1981; 6. Bavinck++*Am J Med Genet*. 1986;

Acknowledgements: The Wyss/Campbell Center for Thoracic Insufficiency (Children's Hospital of Philadelphia).

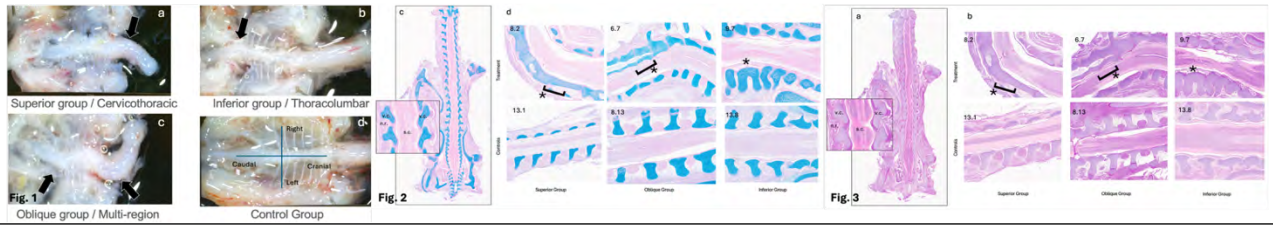

Fig. 1 Shows representative gross specimens from the dissection of the superior group (a), the inferior group (b), and the oblique group (c). Each display coronal plane structural curves. Control specimens (d) showed no signs of scoliosis. **Fig. 2 & 3** Display coronal H&E (a, b) and Alcian blue / Picrosirius Red (c, d) sections from the respective groups, illustrating abnormal vertebral morphology. In the superior group, sections are taken from the cervical/cervicothoracic region; in the oblique group, from the thoracic region; and in the inferior group, from the thoracolumbar region. Adjacent segments in the scoliotic region of interest show fusion of the vertebral cartilaginous anlagen, not seen in controls, indicating vertebral failure of segmentation as the structural cause of scoliosis observed at gross dissection. Sample normal, unoperated embryos (a, c) were used for relevant comparisons (s.c. (spinal cord); v.c. (vertebral cartilage); n.r. (nerve root); *Areas of abnormal morphology).

Imaging Mass Cytometry Reveals a Dynamic Synovial Cellular Landscape in Canine Cruciate Ligament Disease

Lola Uliano[1,2,3], Kevin G. Burt[1,2], Elisabeth A. Lemmon[1,2,3], Janai Augustin[1,2], Carla R. Scanzello[2], Sarah Gullbrand[1,2], Kim Agnello[3], Robert L. Mauck[1,2]
[1]Dept. of Ortho. Surgery, Perelman School of Medicine, University of Pennsylvania, Philadelphia, PA; [2]Translational Musculoskeletal Research Center, Crescenz VA Medical Center, Philadelphia, PA; [3]University of Pennsylvania School of Veterinary Medicine, Philadelphia, PA.
Disclosures: LLU (N) - ulianol@pennmedicine.upenn.edu, KGB (N), EAL (N), JA (N), CS (N), SEG (6), KA (N), RLM (5 – 4WEB Medical).

INTRODUCTION: Disease of the canine cranial cruciate ligament (CCL), the functional equivalent of the human anterior cruciate ligament (ACL), results in marked synovial inflammation and fibrosis, both of which are thought to drive progressive joint degeneration and pain in CCL disease (CCLD).[1,2] In a recent clinical case review, we found a strong correlation between the duration of clinical symptoms and arthroscopic scores of synovial inflammation.[3] Analysis of explanted synovial biopsies from CCL dogs also showed increased inflammation and fibrosis (evaluated on H&E-stained sections), greater stiffness (evaluated by atomic force microscopy), and clear inflammatory/immune cell activation (evaluated by bulk RNA sequencing).[4] However, these prior studies did not evaluate cellular phenotypes or spatial organization in the diseased canine synovial microenvironment. Prior work, using multiplex imaging mass cytometry (IMC) of mouse synovium, showed dynamic changes to the murine joint synovium following injury, inclusive of fibroblast activation and immune cell infiltration.[5] Here, we used IMC to evaluate changes in the cellular landscape of naturally occurring diseased CCL canine synovium, with a particular focus on fibrotic (COL1, α-SMA, fibronectin), inflammatory/immune (CD68, CD14, CD11B/C, CD20), and vascular (VEGF) markers. To our knowledge, this represents the first application of imaging mass cytometry to the analysis of canine tissue in a musculoskeletal context. We hypothesized that CCLD synovium from patients with advanced disease would show increases in cell populations expressing fibrotic, immune, and vascular markers.

METHODS: CCLD Samples: Synovium from canine patients with CCLD (n=8) and healthy canine patients (n=7) were collected from a cohort of dogs (3-6 years old), as previously described.[4] Synovial Scoring: H&E-stained synovial sections were scored for fibrosis and inflammation, with samples from each cohort spanning the range of disease severity within each category. Region of Interest (ROI) Selection: 400 x 400 µm ROIs were selected based on adjacent H&E sections, with two ROIs in the intima and two in the subintima for each sample. Biomarker Selection: Markers of interest were selected from a Hyperion-compatible human IMC panel based on confirmed cross-reactivity with canine targets. Cross-reactivity was further confirmed by the detection of markers within canine spleen (not shown). IMC (n=7-8): Paraffin-embedded synovial sections were subjected to heat-induced antigen retrieval and then incubated overnight with a 14-marker panel of metal-tagged antibodies. Nuclei were counterstained with Intercalator-IR, and imaging was subsequently carried out on a Hyperion Imaging System (Standard BioTools). Spatial Protein Expression and Cellular Phenotype Analysis: Single-cell masks were generated using the nuclear stain via DeepCell (deepcell.org). Data was normalized using arcsin transformation, and clustering was performed with t-distributed stochastic neighbor embedding (t-SNE) dimensionality reduction in IMACytE software.[6] Statistical Analysis: Welch's t-test or Pearson's correlation, with $p<0.05$ significant.

RESULTS: Histologic evaluation demonstrated structural features of synovitis, including synovial lining hyperplasia and expansion of the sub-synovial stroma with collagen deposition, all of which were more pronounced in sections from CCLD patients whose synovia had higher inflammation and fibrosis scores (**Fig. 1f).** IMC based cellular phenotyping of these samples revealed 8 distinct immune and non-immune cell clusters that were separated via unique levels of protein marker expression (**Fig. 1a, b**). Specifically, synovial fibroblast clusters (Clusters 1, 2, 3) were characterized by low expression of CD45 and other immune defining markers and higher expression of COL-1 and αSMA. The immune focused panel identified a possible $CD20^{high}$ B cell cluster (Cluster 6) and multiple likely macrophage clusters (Clusters 7 & 8) expressing CD45, CD68, and CD163 (**Fig. 1a, c)**. Comparing across groups showed an overall greater number of cells per ROI in CCLD samples compared to healthy controls (**Fig. 1c**). Quantification of subpopulations across groups revealed dynamic changes in likely fibroblast clusters (Clusters 1 & 2), where CCLD samples had a significantly greater number of cells (Cluster 2: p=0.0098) compared to healthy controls (**Fig. 1d**). When IMC results were correlated with synovial histopathologic scoring, a significant negative association was found for Cluster 1 (Undefined stromal cell, $r_p = -0.8335$, $p = 0.0296$) and a positive correlation for Cluster 4 (CD68+ Fibroblast, $r_p = 0.8335$, $p = 0.0496$) (**Fig. 1e**). It was not clear if this is a proper fibroblast population or if IMC is capturing fibroblasts and macrophages in close proximity to one another. Mapping these clusters back to the anatomic specimen showed an increase in Cluster 4 cells located both in the subintima and intima of the most diseased samples (**Fig. 1f).**

DISCUSSION: Simultaneous detection of multiple proteins in a spatially discretized manner with imaging mass cytometry can identify diverse cellular populations within a single tissue sample. Here, IMC revealed a significant increase in fibroblasts within the synovium of CCLD patients compared to healthy controls. These findings align with expectations of synovial remodeling under diseased conditions, where fibroblasts proliferate and deposit extracellular matrix — processes that are absent in healthy joints.[5] In addition, combining standard histopathologic metrics with IMC quantification revealed that a CD68+VEGF+ macrophage and/or fibroblast population (or the two cells in close proximity) positively correlated with histological measures of synovial inflammation. These results support the hypothesis that macrophage cell populations, possibly localized near VEGF+ endothelial cells and fibroblasts, are present in higher numbers within the inflamed synovium, and that their numbers scale with disease severity.[8] These findings are consistent with prior work describing the pro-inflammatory synovial landscape following human ACL injury, supporting the similarity in the post-injury synovial pathologic response across species. supporting the translational relevance of canine synovium as a model of human pathology and a testbed for therapeutic evaluation.[7]

SIGNIFICANCE: Our findings support the translational relevance of the canine CCLD model of spontaneously occurring joint injury as a testbed for evaluation of novel therapeutics, particularly those targeted to synovial inflammatory processes. This work demonstrates that imaging mass cytometry can serve as a novel tool to detect subtle changes in the synovial cell landscape during disease progression and treatment, while also establishing its application to canine tissue in a musculoskeletal context, thereby broadening the framework for analyzing joint disease and informing the development of targeted therapeutic strategies.

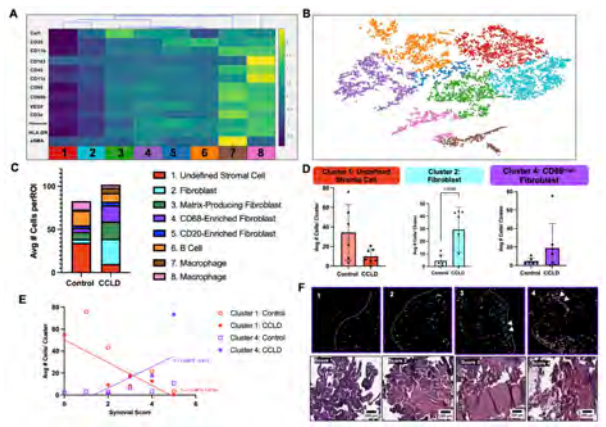

Figure 1: ***IMC analysis of synovial cell phenotypes with CCLD.*** *A) Marker expression heatmap identifying clusters and B) t-SNE plot showing all cells identified. (C) Average number of cells per ROI for each group (and distribution of subclusters). D) Comparisons within individual cell clusters showing change across disease state. E) Correlation of cells within clusters relative to H&E-assigned synovial score (Cluster 1: r = -0.8335, p = 0.0393; Cluster 4: r = 0.8305, p = 0.0406). F) Cell cluster assignment in synovium and corresponding H&E-stained sections (1 = less pathology, 4 = more pathology). Synovial lining = white dashes.*

REFERENCES: [1]Wright+ J Small Anim Pract (2023), [2]Johnston+, Vet Clin (1974), [3]Lemmon+ Vet Surg (2025) [4]Lemmon+ OA&C (2024), [5]Burt+ Biorxiv (2025), [6]Somarakis+ IEEE Trans Vis (2020), [5]Magarian+ Knee (2011), [6]Cialdi+ Front Bioeng Biotechnol (2022), [7]South+ OA&C Open (2023), [8]Zhao+ Front Immunol (2023).

ACKNOWLEDGEMENTS: Funding – NIH (T35 OD010919) and the Penn Center for Musculoskeletal Disorders (P30 AR069619).

Inflammatory and Overuse Tendinopathy Impair Chondrocyte Function in Shoulder Crosstalk

Felicia Pinto[1], Yuna Heo[1], and Su Chin Heo[1]
[1]University of Pennsylvania, Philadelphia, PA
frpinto@seas.upenn.edu

Disclosures: Pinto (N), Y. Heo (N), S.C. Heo (5-4WEB Medical)

INTRODUCTION: Shoulder musculoskeletal disease is highly prevalent, with approximately 20% of the population reporting shoulder pain at any given time **[1].** Rotator cuff disease, characterized by inflammation, degeneration, or acute injury of muscles or tendons in the shoulder, is the primary clinical cause of shoulder pain **[2]**. Osteoarthritis of the shoulder (glenohumeral OA) is the second most common cause, affecting more than 30% of the population over the age of 60 **[3]**. These two conditions frequently coexist and are major contributors to shoulder dysfunction. Tendinopathy in the rotator cuff, characterized by chronic matrix degeneration with or without inflammation, frequently develops in response to repetitive overuse **[4]**. While mechanical destabilization of the rotator cuff (e.g. tendon degeneration) is a recognized driver of OA (cartilage degradation), the biochemical crosstalk between degenerative tendon and cartilage in the shoulder remains underexplored **[5]**. To address this, we modeled degenerative tendon phenotypes using cytokine-induced inflammation and mechanical overuse via a tensile loading bioreactor to generate conditioned media (CM). Chondrocytes were treated with tenocyte-derived CM, and their response was assessed through histone modification imaging and gene expression analysis. We hypothesized that inflammatory and overuse CM would impair chondrocyte health and transcriptional capacity. This study aims to determine tendon–cartilage crosstalk as a contributor to shoulder degeneration to ultimately inform future therapeutics.

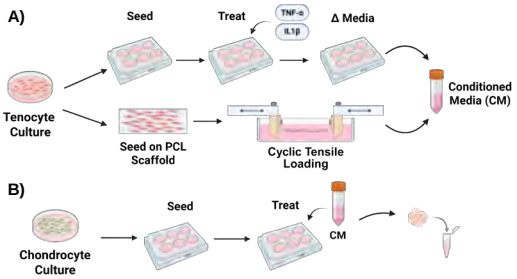

Figure 1: (A) Workflow of inflammatory (top) and overuse (bottom) tendinopathic models to generate conditioned media (CM). **(B)** Chondrocyte culture workflow with CM treatment.

METHODS: Inflammatory tendinopathy model: Juvenile bovine tenocytes were seeded on tissue culture plastic, incubated for 24 hours, and then cultured for 3 days in basal cell growth media (BM, Control) or inflammatory media. Inflammatory media consisted of BM supplemented with both TNFα and IL1β (Sigma) at either 10 ng/mL (10) or 20 ng/mL (20). After 3 days, all media were replaced with BM to create conditioned media (CM) from each group (CM Control, CM 10, CM 20) **(Fig. 1A)**. CM was collected following a 24-hour incubation. **Overuse tendinopathy model**: Tenocytes were seeded onto aligned poly(ε−caprolactone) (PCL) nanofibrous scaffolds and cultured for 2 days in BM. A custom tensile loading bioreactor applied cyclic uniaxial force at 8% strain (at 2 Hz) to seeded scaffolds for 4 hours/day for 1 or 3 days **(Fig. 1A)**. Additionally, unloaded scaffolds cultured in BM served as static controls. CM was collected following static culture (CM Static) and after 1 or 3 days of loading (CM DL 1, CM DL 3), then filtered and spun down. **Chondrocyte treatment**: Juvenile bovine chondrocytes were seeded on tissue culture plastic and incubated for 24 hours in BM, followed by 3-day culture in BM (Control) or CM (CM Control, CM 10, CM 20, CM Static, CM DL 1, CM DL 3) **(Fig. 1B)**. RNA was extracted post-treatment for RT-qPCR analysis. Cells were fixed for immunofluorescence (IF) imaging to assess expression level of histone modifications H3K9ac, a marker of gene activation, and H3K27me3, a marker of gene repression (Invitrogen); fluorescent intensity was quantified using Image-J. Statistical analyses were performed using one-way ANOVA with post-hoc testing.

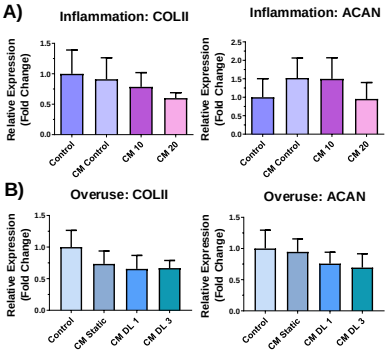

Figure 2: Fold change in collagen II (COLII) and aggrecan (ACAN) in chondrocytes, normalized to GAPDH and Control. **(A)** Cells cultured in BM (Control) or inflammatory conditioned media (CM Control, CM 10 or 20). **(B)** Cells cultured in BM (Control) or overuse conditioned media (CM Static, CM DL 1, CM DL 3). n = 9-20 (technical replicates). Mean ± SD.

RESULTS: RT-qPCR analysis of chondrocytes treated with tenocyte-derived CM from inflammatory and overuse conditions revealed a consistent decreased trend of collagen type II (COLII) and aggrecan (ACAN) expression, both essential proteins for cartilage structure and function **(Fig. 2A, B)**. IF analysis demonstrated epigenetic alterations in chondrocytes exposed to inflammatory CM with reduced H3K9ac (gene activation) and increased H3K27me3 (gene repression) with CM from 10 ng/mL of inflammatory stimulation **(Fig. 3A, B)**. Both H3K9ac and H3K27me3 expression were reduced with CM from Days 1 and 3 of loading, indicating distinct chromatin remodeling patterns associated with overuse. **(Fig. 3C, D).**

DISCUSSION: Our findings demonstrate an interaction between tendinopathic conditioned media and chondrocyte response, suggesting tenocyte-derived biochemical signals can drive both genetic and epigenetic changes in chondrocytes. Reduced expression of COLII and ACAN reflect a shift toward cartilage degradation under both inflammatory and overuse conditions. However, histone modification analysis revealed distinct patterns between tendinopathy models. Inflammatory CM decreased H3K9ac and increased H3K27me3, consistent with transcriptional repression, while overuse-derived CM reduced both activation (H3K9ac) and repression (H3K27me3) marks, suggesting locus-specific disruption of chromatin regulation. CM from lower inflammatory stimulation (CM 10) induced more pronounced histone changes, while CM from higher inflammatory stimulation (CM 20) elicited greater transcriptional responses, suggesting early epigenetic shifts may prime subsequent transcriptional responses. Mechanical loading produced consistent effects at Days 1 and 3, indicating persistent alterations in the genomic and epigenomic state of chondrocytes with overuse. Together, these results suggest that tendon-derived inflammatory and mechanical cues can influence cartilage degeneration through distinct but converging mechanisms. To expand on these findings, future studies will combine inflammatory and overuse conditions, employ ChIP-seq to map locus-specific epigenetic changes, and develop co-culture systems that better recapitulate tendon–cartilage interactions *in vivo*. Such approaches will deepen understanding of tendon–cartilage crosstalk and inform future therapeutic strategies.

SIGNIFICANCE: This study reveals biochemical crosstalk from tendinopathic media alters chondrocyte gene expression and epigenetic state under inflammatory and overuse conditions. These insights highlight tendon–cartilage interactions as contributors to shoulder degeneration and suggest new avenues for developing targeted therapies to prevent or slow the progression of shoulder degeneration.

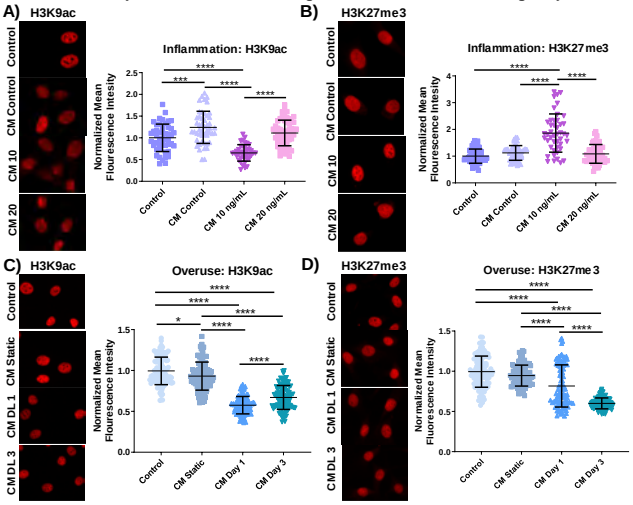

Figure 3: Representative IF images and quantification of **(A)** H3K9ac (n=39-57) and **(B)** H3K27me3 (n=46-57) in chondrocytes cultured in BM (Control), CM Control, or CM from tenocytes treated with 10 or 20 ng/mL of inflammation (CM 10, CM 20). Representative IF images and quantification of **(C)** H3K9ac (n=99-112) and **(D)** H3K27me3 (n=91-104) in chondrocytes cultured in BM (Control), CM Static, or CM from Day 1 or 3 of loading (CM DL 1, CM DL 3). Mean ± SD, *:p≤0.05, ***:p≤0.001, ****:p≤0.0001.

REFERENCES: [1] Pope+, *Ann. Rheum. Dis.,* 1997; **[2]** Whittle+, *Ann. Intern. Med.,* 2015; **[3]** Chillemi**+,** *Arthritis,* 2013. **[4]** Plachel+, *J. Ortho. Res.,* 2019. **[5]** Spiegl+**,** *KSSTA,* 2015. **[6]** Russo+, *Cells*, 2022.

ACKNOWLEDGEMENTS: This work is supported by the NIH (P50 AR080581) and NSF (CMMI-1548571).

IL-1β Does Not Exacerbate Cell Death in a Large-Scale Tissue-Engineered Intervertebral Disc

Matthew Fainor[1,2], Alexandra J. Baranyai[1], Robert L. Mauck[1,2], Harvey E. Smith[1,2], Sarah E. Gullbrand[1,2]
[1]University of Pennsylvania, Philadelphia, PA; [2]Corporal Michael J. Crescenz VA Medical Center, Philadelphia, PA
Disclosures: MF – Matthew.Fainor@pennmedicine.upenn.edu (N), AJB (N), RLM (5), HES (N), SEG (6)

INTRODUCTION: Much work has been completed assessing how mesenchymal stromal cells (MSCs) respond to the challenges inherent to large-scale (>4mm diameter) tissue engineering, including the presence of stark oxygen [1-2] and glucose gradients [2-3]. However, the transition of tissue-engineered intervertebral discs from nutrient-rich in vitro cultures to low nutrient in vivo environments leads to changes in cell morphology, decreases in cell viability, and alterations to extracellular matrix post-implantation [4-5]. It's unclear how the interplay of nutrient deprivation, inflammatory molecules, and immune cell infiltration contribute, both independently and synergistically, to MSC death and tissue remodeling. Here, we hypothesized that inflammation would exacerbate cell death and matrix loss in a large tissue-engineered intervertebral disc made from MSCs when deployed in conjunction with oxygen and glucose deprivation.

METHODS: Mesenchymal stromal cells (MSCs) were obtained from the bone marrow of six skeletally-mature goats and previously screened using a chondrogenic pellet assay [6]. Endplate-modified Disc-like Angle Ply Structures (eDAPS) (16 mm diameter x 9 mm height) were then fabricated and seeded with the P3 MSCs from the most chondrogenic goat donor, as previously described [7]. Tissue-engineered discs were matured under normoxic conditions (21% oxygen) in high-glucose (4.5g/L) chondrogenic media supplemented with TGF-β3 (10ng/mL) under constant mechanical agitation for 10 weeks. After 10 weeks of culture, eDAPS were subject to either in vitro or in vivo challenges. During the in vitro challenge, eDAPS were cultured in hypoxia (2% oxygen) using low-glucose (1g/L) chondrogenic media supplemented with IL-1β (50ng/mL), which was refreshed every 3 days, for up to 2 weeks. At 0, 1, and 2 weeks eDAPS were removed from hypoxic culture. Half of each eDAPS (n=3-4) was utilized for quantification of DNA, glycosaminoglycan (GAG), and collagen content in the NP and AF regions. The NP and AF analogs from the second half of each eDAPS were separated for live/dead staining and MTT quantification, respectively (n=3-4). Additional full eDAPS were taken for histological staining at each time point (n=3). Additional full eDAPS (n=3) were processed for paraffin histology and stained with alcian blue, picrosirius red, and hematoxylin/eosin. Sections also underwent immunofluorescence staining for human collagens I, II, and X, as well as human chondroitin sulfate and rat CD68. During the in vivo challenge, eDAPS were implanted in the subcutaneous space of 8-week-old athymic rats, as approved by IACUC. After 0 and 5 weeks of subcutaneous implantation, eDAPS were processed as described above (n=3).

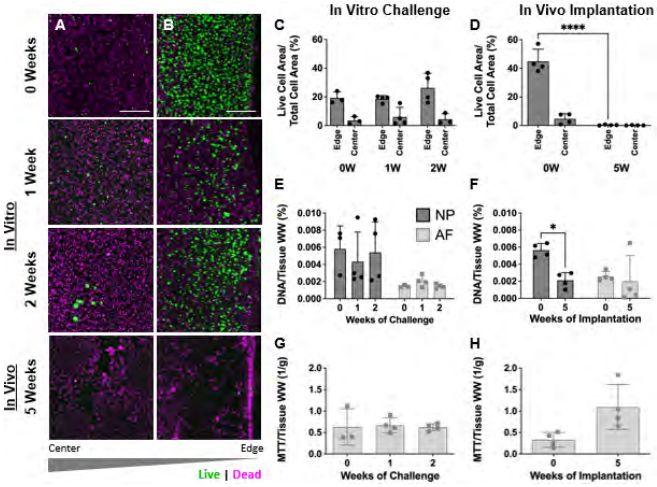

Figure 1: Cell Viability. Live (green)/Dead (pink) staining at the (A) center and (B) edge of eDAPS' NP-analog cross sections at 1 and 2 weeks following in vitro challenge and 5 weeks following in vivo subcutaneous implantation (scale = 300 μm). Quantification of (C-D) NP live cell area/total cell area, (E-F) DNA content, and (G-H) AF metabolism measured via MTT for in vitro and in vivo challenges, respectively.

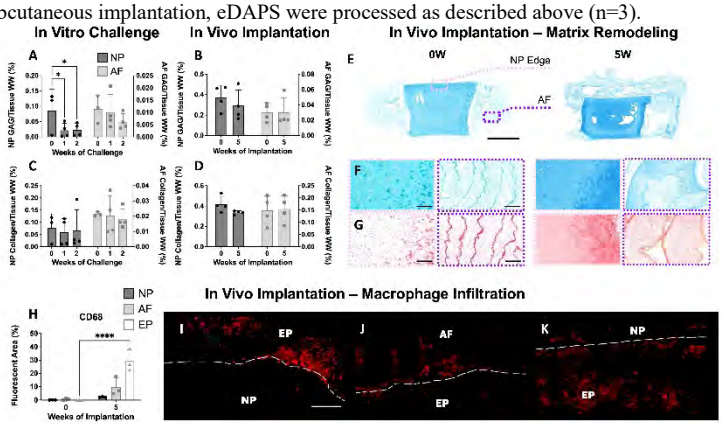

Figure 2: Extracellular Matrix Changes. (A-B) GAG and (C-D) collagen content for eDAPS subjected to in vitro and in vivo challenges, respectively. Histologic staining of eDAPS subjected to in vivo subcutaneous implantation at 0 and 5 weeks using (E-F) alcian blue and (G) picrosirius red of the NP-analog (left inset) and AF-analog (right inset) [scale=3mm (E), 500μm (F-G)]. Immunofluorescence (IF) (H) quantification of CD68 positive macrophages (red) in the (I) NP-analog, (J) AF-analog, and (K) endplate (EP)-analog (scale=400μm).

RESULTS: After 10 weeks of in vitro preculture, the vast majority of goat MSCs were dead in the center of the constructs (Figure 1A) but were alive at the constructs' edge (Figure 1B). After two weeks of in vitro challenge, cell viability in the NP was unchanged (Figure 1C,E), whereas 5 weeks of in vivo subcutaneous implantation killed every MSC in the NP-analog (Figure 1D,F). Following in vitro challenge, MSC metabolism and DNA content in the AF was unchanged (Figure 1E,G), whereas overall cell metabolism in the AF of the in vivo implantation group increased from 0 to 5 weeks (Figure 1H). Glycosaminoglycan content decreased significantly in the NP of in vitro-challenged eDAPS after 1 week but was unchanged in the NP and AF of in vivo-challenged eDAPS (Figure 2A-B). Hydroxyproline (collagen) content was stable over time in all compartments of both experimental groups (Figure 2C-D). Both alcian blue and picrosirius red stained more intensely after 5 weeks of subcutaneous implantation, particularly in the NP-analog (Figure 2E-G). Collagen I, collagen X, and chondroitin sulfate all decreased significantly in quantity by 5 weeks, indicating that extracellular matrix proteins of all kinds, while present in higher quantities, are non-functional and fragmented. Finally, CD68 positive macrophages were found in the DAPS NP-, AF-, and EP-analogs after 5 weeks in the subcutaneous space (Figure 2H-K).

DISCUSSION: Surprisingly, there was no change in goat MSC survival in a low oxygen, low glucose, IL-1β-induced inflammatory environment over the course of two weeks in vitro, which may indicate that the cells unfit to survive these conditions already perished during the preculture period. Both in vitro- and in vivo-challenged eDAPS lost functional GAG content over time, indicating that even if cells are not dying, they are struggling to maintain ECM integrity, likely in response to upregulated MMPs from IL-1β stimulation [8-9]. Although T cell deficient athymic rats are a useful model to study an in vivo challenge, it is clear that local macrophages responded to the presence of these xenogenic implants. When hMSCs were delivered intraarticularly to the knees of T and B cell deficient SCID mice, their number was reduced by 87% one month following transplantation [10], supporting the theory that local macrophages likely contributed to cell death across the NP-analog in this study. The eDAPS provide a system to test the performance of cell therapies in 3D hypoxic, hypoglycemic environments, and this data provides a critical baseline against which to compare the future performance of eDAPS seeded with native disc cells, as well as eDAPS seeded with CRISPR-modified MSCs [11] with edits targeting cell proliferation, senescence, metabolism, and fibrocartilaginous matrix production, in order to better understand what mechanisms enable cells to thrive in inflammatory/low glucose/low oxygen environments.

SIGNIFICANCE: Characterization of MSC response to inflammation in low glucose and low oxygen environments will allow us to better understand what phenotypes allow cells to thrive under duress in order to engineer more successful cell therapies for large-scale tissue engineering interventions.

REFERENCES: [1] Buckley+ *Tissue Eng: Part A,* 2012. [2] Farrell+ *OA&C,* 2015. [3] Nims+ *Tissue Eng: Part C,* 2015. [4] Gullbrand+ *STM,* 2018. [5] Moriguchi+ *Plos One,* 2017. [6] Frehner & Fainor+ *Tissue Eng: Part A*, 2025. [7] Gullbrand, *Acta Biomater,* 2018. [8] Pattappa+ *Cells*, 2019. [9] Ries+ *Stem Cells in Hematology,* 2007. [10] Toupet+ *A&R,* 2013. [11] Levis+ *Acta Biomater,* 2025.
ACKNOWLEDGEMENTS: This work was supported by the Department of Veterans' Affairs and the Penn Center for Musculoskeletal Disorders.

Synovium-Cartilage Crosstalk in Facet Joint Osteoarthritis and Correlations with Adjacent Disc Degeneration

Janai Augustin[1], Kevin Burt[1,2], Matthew Fainor[1,2], Brianna S. Orozco[1,2], Sung Yeon Kim[1] , Carla R. Scanzello[1,2], Sarah E. Gullbrand[1,2]
[1]Department of Orthopaedic Surgery, Perelman School of Medicine, University of Pennsylvania, Philadelphia, PA; [2]Translational Musculoskeletal Research Center, Philadelphia Veterans Affairs Medical Center, Philadelphia, PA.

Disclosures: JA (N), KB (N), MF (N), BSO (N), SYK (N), CRS (N), SEG (6)

INTRODUCTION: Low back pain (LBP) affects up to 85% of individuals and is the leading cause of disability worldwide, often stemming from degeneration of the spinal motion segment[1]. The facet joints (FJs) are synovial articulations posterior to the intervertebral disc (IVD) that play a critical role in load transmission and constrain range of motion in the spine (**Fig 1A**)[2]. These joints gradually undergo degenerative changes characterized by cartilage erosion, subchondral sclerosis, and synovial remodelling compounded by inflammatory responses and biochemical alterations that stimulate nociceptive pathways ultimately leading to chronic pain[3]. This pathology is called facet joint osteoarthritis (FOA), and contributes to back pain in 15-41%[4] of patients. In other synovial joints such as the knee and hip, synovitis is tightly linked to symptoms and structural progression of osteoarthritis (OA)[5], yet the contribution of the synovium to osteoarthritic changes in the facet joint and degeneration of the adjacent intervertebral disc remains poorly understood. ***We hypothesized that FJ synovium pathology initiates and drives inflammatory and catabolic changes in FOA and severity of FOA correlates with adjacent IVD degeneration.***

METHODS: *Cadaveric spine acquisition:* Five lumbar spines (2 male, 3 female, 27-70yo), were obtained from human cadavers (Science Care and NDRI). *IVD qMRI:* To assess disc degenerative changes, 3T MRI with sagittal T2 mapping (resolution = 0.5 mm, TEs = 13, 26, 39, 52, 71 ms) were obtained for disc Pfirmann grading[6], and to quantify nucleus pulposus (NP) T2 relaxation times[7]. Spinal motions segments (n = 22) were dissected into discs and facet joints. One facet joint from each spinal level was left intact, and its contralateral joint was disarticulated. *Facet cartilage creep indentation:* The articular surface was indented using a 2 mm spherical indenter (0.1 N creep load for 15 minutes at four locations per surface)[8]. *Facet qMRI and histopathology*: Following mechanical testing, T2 mapping of the facet articular cartilage was performed on a 4.7T preclinical MRI scanner (resolution = 117µm, TE = 15ms, 10 echoes). Evaluation of cartilage damage[9] and synovial inflammation and damage [10] was performed on paraffin embedded axial sections of intact facets (**Fig1B)**. *Imaging mass cytometry (IMC)*: Additional axial sections underwent heat-mediated antigen retrieval and overnight incubation with a basic immune cell panel to delineate myeloid and lymphoid cells generally (CD3, CD20, CD45, CD68), a myeloid subset panel (CD11b, CD11c, CD14, CD66b, CD163, HLA-DR) and a tissue architecture panel (fibronectin, Col1, αSMA, VEGF) of metal-conjugated antibodies. This was followed by incubation with Intercalator-Ir nuclear stain, and imaging using a Hyperion Imaging System. *Statistical analysis:* Differences in quantitative outcomes stratified by OARSI score were assessed via a student's t-test ($p<0.05$). Principal component analysis (PCA) biplots were generated in Python.

RESULTS: Facet cartilage mechanical testing demonstrated that increased OARSI scores were accompanied by increased cartilage permeability and reduced tensile and compressive moduli **(Fig1 C, D, E**). Although synovial inflammation, synovial damage, and cartilage T2 values did not differ significantly when stratified by OARSI score, PCA biplots (**Fig 2**) demonstrated that more degenerative facet cartilage (higher OARSI scores and macroscopic grades) and higher synovial damage scores were associated with reduced IVD NP T2 values indicating more extensive disc degeneration. Synovial inflammation was not correlated with synovial damage but was inversely correlated with facet cartilage mechanical properties. PCA analysis revealed distinct phenotypes: healthy, hydrated IVDs with little facet pathology (cluster C); concomitant disc degeneration and facet synovium damage (cluster B); facet synovial inflammation with minimal disc and facet degeneration (cluster A), and severely degenerated discs and facets marked by high synovial inflammation, and compromised cartilage mechanics (cluster D). IMC demonstrated strong expression of collagen I, fibronectin, αSMA, and VEGF, as well as abundant immune and myeloid lineage cells within the facet synovium **(Fig 3**).

DISCUSSION: Our data revealed distinct phenotypes of spinal disease, with synovial damage and inflammation driving disparate phenotypes of degeneration, consistent with knee OA[10]. The presence of elevated synovial inflammation in samples with only modest structural damage suggests that synovial inflammatory signaling may contribute to subsequent tissue breakdown. These findings parallel knee OA where inflammatory cells can drive articular extracellular matrix degradation, pain and progression of disease[5]. The negative correlation between NP T2, synovial damage and cartilage degeneration provides evidence for facet–disc crosstalk, however, the biological mechanisms driving this relationship remain unclear and warrant further investigation. IMC further revealed ECM remodeling proteins (collagen I, fibronectin), myofibroblast activation (αSMA), angiogenic factors (VEGF), and immune cell infiltration, features consistent with synovial remodeling in knee OA, where fibroblast activation and neovascularization sustain inflammation and nociception[5]. Ongoing IMC analyses will quantify changes in tissue architecture and synovial cell populations as FOA progresses and will be compared to healthy facets to define molecular and cellular signatures of disease.

SIGNIFICANCE: Together, these results highlight the contribution of synovial inflammation and damage to FOA progression and adjacent disc degeneration, positioning the synovium as both a driver of pathological changes and a potential therapeutic target for low back pain.

REFERENCES:[1] Shahidi+ J Orthop Res., 2017, [2] Jaumard + J Biomech Eng., 2011, [3] Gelhorne + Nat Rev Rheumatol., 2013, [4] Du + J Pain Res., 2022, [5] Scanzello + Bone., 2012, [6] Pfirrmann + Spine (Phila Pa 1976)., 2001, [7] Martin + J Orthop Res., 2015 [8] Gupta + J Orthop Res., 2023 [9] Pritzker + Osteoarthritis Cartilage., 2006 [10] Philpott + Osteoarthritis Cartilage., 2024.

ACKNOWLEDGEMENTS: This study was supported by the Department of Veterans Affairs and the Penn Center for Musculoskeletal Disorders.

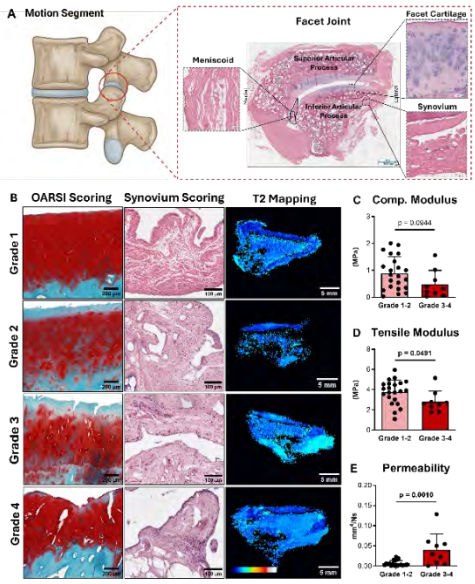

Fig 1: A) Facet Joint location and Anatomy. **B**) Facet cartilage, synovium scoring and T2 maps stratified by OARSI scores. Facet Cartilage Mechanical Properties stratified by OARSI score, **C)** Compressive Modulus, **D)** Tensile Modulus, **E)** Permeability.

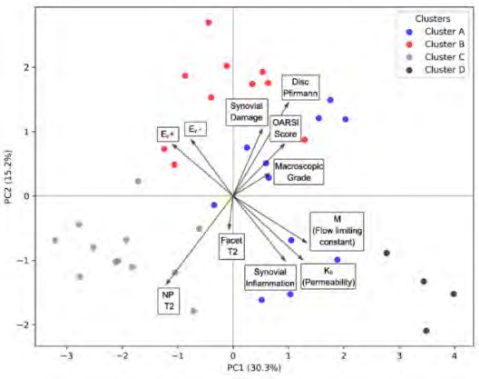

Fig 2: PCA biplot showing relationships between FJ cartilage properties, IVD structure, and FJ synovial pathology. Arrows in the same direction = direct correlation, arrows in opposite directions = inverse correlation, arrows at 90 degrees = no correlation.

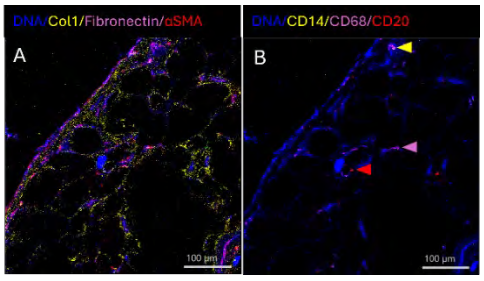

Fig 3: IMC of Facet Joint Synovium. A) tissue architectural markers in FJ synovium, **B)** Immune cell markers in FJ synovium.

Intra-Articular TAT-Cre-Mediated Deletion of Lats1/2 Induces Joint Pain and Synovial Dysfunction

Elizabeth Bernstein[1,2,3], Georgios Kotsaris[1,2,3], Gabriella Garza[2], Brett Croen[2, 3], Joel D. Boerckel[1,2], Nathaniel A. Dyment[1,2], Robert L. Mauck[1,2,3]
Depts. of [1]Bioengineering and [2]Orthopaedic Surgery, University of Pennsylvania; [3]CMC VA Medical Center, Philadelphia, PA
elizabeth.bernstein@pennmedicine.upenn.edu

Disclosures: RLM (5 – 4WEB Medical).

Introduction: The synovium is a bilayer membrane, composed primarily of fibroblasts and macrophages, that lines the joint capsule and produces synovial fluid.[1] During age-related and injury-induced osteoarthritis (OA) the synovium becomes fibrotic and stiffens. In response to this altered microenvironment, synovial cells become mechanoactivated:[2] fibroblasts transition to a myofibroblast-like phenotype, expressing fibrotic markers, and decreasing production of joint-lubricating factors,[3] while macrophages adopt a pro-inflammatory phenotype that exacerbates synovial dysfunction.[4] Although synovitis is known to correlate with pain and disease progression in OA,[5] the contribution of synovial pathology, and specifically that of mechanoactivated synovial cells, in the absence of cartilage damage or a destabilizing injury, remains unclear. To address this question, we focused on the Hippo pathway kinases, LATS1 and LATS2, which reduce nuclear translocation of the mechanoresponsive transcriptional co-activators YAP and TAZ. When present in the nucleus, YAP/TAZ can initiate fibrotic and inflammatory programs in synovial fibroblasts and macrophages, respectively.[3] Here, we delete LATS1/2 in the joint space via intra-articular injection of a membrane-permeable Cre recombinase to determine how YAP/TAZ gain-of-function affects synovial fibrosis, inflammation, and other joint pathologies, independent of an instigating injury.

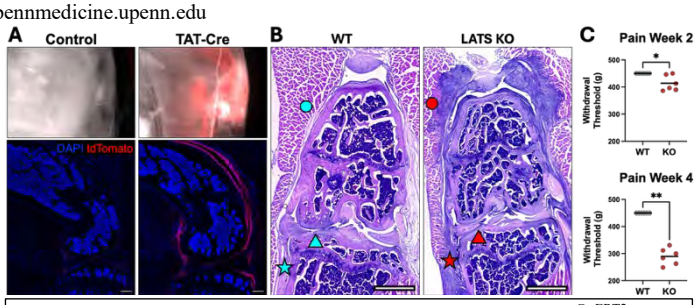

Figure 1. (A) Whole mount fluorescence and sections of Prg4^{CreERT2};R26R-tdTomato reporter knees 1 week after PBS or TAT-Cre injection. SB: 500μm. (B) WT and LATS1/2 KO knees at 4 weeks (H&E). Shapes indicate locations in Figs. 2-3. SB: 5mm. (C) Knee hyperalgesia at 2 and 4 weeks. *p<0.05, **p<0.01.

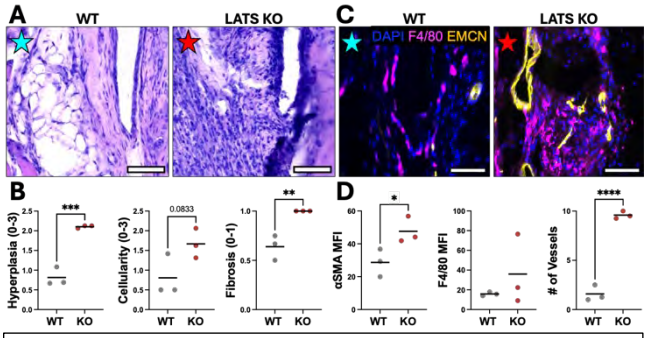

Figure 2. (A) H&E staining of synovium at 4 weeks. SB: 50μm. (B) Synovial scoring. (C) IF of synovium. SB: 50μm. (D) Quantification of αSMA and F4/80 staining intensity and vessel number. Stars indicate joint location from Figure 1. *p<0.05, **p<0.01, ***p<0.001, ****p<0.0001.

Methods: All animal work was IACUC approved. Assessment of intra-articular recombination efficiency: Prg4^{CreERT2};R26R-tdTomato reporter mice received 1 intra-articular injection of PBS (n=3) or the recombinant, membrane-permeable (TAT-modified) Cre recombinase (TAT-Cre) (n=3). After 7 days, hind limbs were sectioned and analyzed for tdTomato signal. Intra-articular Lats1/2 deletion: Lats1$^{f/f}$;Lats2$^{f/f}$ (n=3) and WT (n=3) mice received 2 intra-articular TAT-Cre injections 48 hours apart. Only male mice were used as males develop more severe OA in surgical models.[6] Pain assessment: Mice were tested for joint hyperalgesia using a pressure application measurement device before TAT-Cre injection and weekly for 4 weeks post-injection. Micro-CT: At 4 weeks, joints were harvested and bone morphology was evaluated by micro-CT. Histological scoring: Synovial scoring[7] was performed on coronal H&E-stained cryosections. OARSI scoring[8] was performed on coronal Saf O/Fast Green-stained cryosections. Immunofluorescence: Joints were stained for alpha smooth muscle actin (αSMA), fibroblast activation protein (FAP), F4/80 (macrophage marker), and endomucin (EMCN, vessel marker). Fibrosis and macrophage infiltration were assessed by measuring average fluorescence intensity of αSMA, FAP, and F4/80. Vascularity was measured by counting EMCN-positive vessels per synovial gutter. Statistics: Outcomes were compared using t-tests.

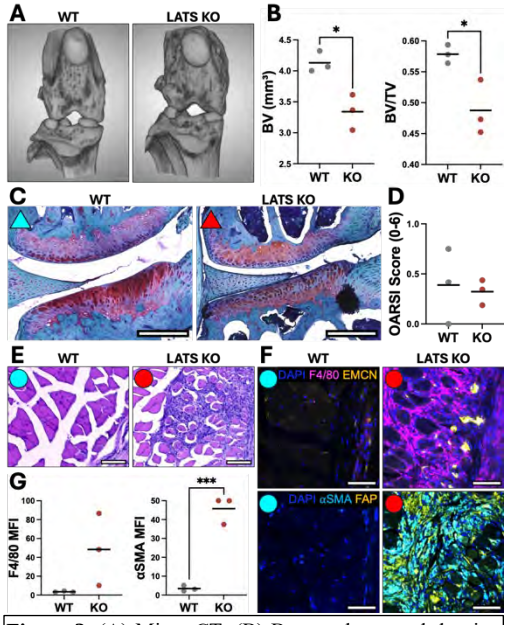

Figure 3. (A) Micro-CT. (B) Bone volume and density. (C) Cartilage staining (Saf O/Fast Green). SB: 250μm. (D) OARSI scoring. (E) H&E and (F) IF of muscle adjacent to the joint capsule. SB: 50μm. (G) Quantification of αSMA and F4/80 staining intensity. Triangles and circles indicate joint location from Figure 1. *p<0.05, ***p<0.001.

Results: Intra-articular Lats1/2 ablation alters joint architecture and induces pain. Through intra-articular injections of TAT-Cre recombinase, we achieved precise local recombination in the synovium (**Fig 1A**). H&E staining of WT and Lats1$^{f/f}$;Lats2$^{f/f}$ knees 4 weeks after injection, revealed marked changes in joint architecture, particularly in the synovium and adjacent muscle (**Fig 1B**). By 2 weeks, Lats1$^{f/f}$;Lats2$^{f/f}$ mice had reduced withdrawal thresholds and this joint hyperalgesia increased at 3 and 4 weeks (**Fig 1C**). Lats1/2 ablation drives synovial hyperplasia and fibrosis. 4 weeks after TAT-Cre injection, Lats1$^{f/f}$;Lats2$^{f/f}$ mice displayed marked increases in lining hyperplasia, sublining cellularity, and synovial fibrosis (**Fig 2A,B**). IF revealed the accumulation of αSMA$^+$ fibroblasts and increased angiogenesis (EMCN$^+$ vascular structures) in the synovium (**Fig 2C,D**). Lats1/2 ablation increases subchondral bone resorption and promotes fibrotic remodeling of adjacent tissues. Micro-CT showed decreased bone volume and BV/TV in Lats1$^{f/f}$;Lats2$^{f/f}$ mice, while the cartilage was unaffected (**Fig 3A-D**). Histology of muscle showed centrally nucleated fibers and infiltration of macrophages and αSMA$^+$ fibroblasts (**Fig 3E-G**).

Discussion: We found that targeted intra-articular depletion of LATS1/2, suppressors of YAP/TAZ activation, induces synovitis and synovial fibrosis, as well as pathological alterations in the subchondral bone and adjacent muscle, in the absence of joint injury. We hypothesize Lats1/2 ablation mimics synovial mechanoactivation by increasing nuclear translocation of YAP/TAZ, as has been shown previously in nephron progenitor cells.[9] Our findings suggest mechanoactivation of synovial cells as a driver of joint pathology, even in the absence of joint damage. Intriguingly, the cartilage remained unaffected by Lats1/2 deletion, despite extensive changes in surrounding tissues; this may suggest that synovial dysfunction precedes cartilage erosion in the absence of an instigating injury. Future studies will include analyses of disease progression, tissue mechanics, and fibroblast–immune cell transcriptional signatures and crosstalk, defining how aberrant Hippo–YAP/TAZ signaling drives synovial fibrosis to impact joint health.

Significance/Clinical Relevance: Intraarticular Cre-mediated recombination revealed a profound impact of Lats1/2 knockout on joint pain and structure. This study establishes a role for Hippo–YAP/TAZ in synovial fibrosis and inflammation and supports the hypothesis that synovial pathology is an active contributor to disease progression in OA.

Acknowledgements: This work was supported by the NIH (F30 AG094106 and R01 AR075418) and the VA (I50 RX004845).

References: 1. Scanzello, *Springer*, 2022; 2. Lemmon, *OAC*, 2024; 3. Bonnevie, *OAC*, 2024; 4. Knab, *Front Med*, 2022; 5. Mathiessen, *Arthritis Res Ther*, 2017; 6. Ma, *OAC*, 2007; 7. Obeidat, *OAC*, 2024; 8. Glasson, *OAC*, 2010; 9. McNeill, *JASN*, 2017.

In vitro development and in vivo evaluation of intra-articular GUSB mRNA therapy for Mucopolysaccharidosis VII

Karthikeyan Rajagopal[1], Kelsey L. Swingle[2], Keerthana Iyer[1], Zhirui Jiang[1], Emma Smith[3], Caitlyn M. Molony[3], George R. Dodge[1], Susan W. Volk[3], Margret L. Casal[3], Michael J. Mitchell[2], Lachlan J. Smith[1,4]

[1]Department of Orthopaedic Surgery; [2]Department of Bioengineering; [3]School of Veterinary Medicine; and [4]Department of Neurosurgery, University of Pennsylvania, Philadelphia, USA

Mucopolysaccharidosis VII (MPS VII) is a lysosomal disease characterized by deficient beta-glucuronidase (GUSB) activity, resulting in accumulation of poorly degraded glycosaminoglycans in cells and tissues. MPS VII patients exhibit significant synovial joint abnormalities, which result in reduced quality of life and which is not effectively treated by current systemic approaches, likely due to the dense and avascular nature of articular cartilage. Intra-articular delivery of therapeutic mRNA using ionizable lipid nanoparticles (LNPs) is a novel potential strategy to treat cartilage and joint disease in MPS. Advantages of LNPs are their modular design, whereby their properties can be optimized to improve biodistribution and intracellular delivery for specific tissues, and improved safety compared to viral vector-based gene therapy. The goal of this study is to investigate the use of intra-articular mRNA therapy to treat cartilage disease in MPS VII. LNPs encapsulating GUSB mRNA were fabricated using a formulation previously optimized to maximize chondrocyte transfection. Primary chondrocytes were obtained from the articular cartilage of 2-month-old MPS VII and healthy control dogs (each n=3), transfected in monolayer for 24-hours with GUSB mRNA LNPs (125-1000ng) and then maintained in pellet culture for up to 42 days. GUSB mRNA treatment resulted in a significant, dose-dependent increase in GUSB activity in MPS VII chondrocytes that persisted for up to 42 days. Furthermore, treatment significantly reduced chondrocyte lysosomal storage assessed using transmission electron microscopy compared to untreated cells. For in vivo evaluation, GUSB mRNA LNPs (25 µg/kg) in sterile saline were injected into the elbow and stifle joints of 1-month-old MPS VII dogs (n=4). Twenty-four hours after injection, treated joints exhibited significantly elevated GUSB enzyme activity in synovial fluid compared to contralateral joints that received saline injections only. These studies establish the therapeutic potential of intra-articular mRNA therapy for treating joint disease in MPS VII and other MPS subtypes. Funding: NIH and Penn Center for Musculoskeletal Disorders.

CD14 Deficiency in Mice Protects Against Age-associated Mobility Loss, Pain, and Multi-joint Degeneration

Kevin G. Burt[1,2], Vu Nguyen[1,2], Anna E. Rapp[2,3], Lance A. Murphy[2], Robert L. Mauck[1,2], Carla R. Scanzello[1,2,3]
[1]Department of Orthopaedic Surgery, Univ of Penn, Philadelphia, PA; [2] CReATE Motion Center, CMC VA Medical Center; Philadelphia PA; [3]Division of Rheumatology, Univ of Penn, Philadelphia, PA.
Disclosures: KGB (N) - kevin.burt@pennmedicine.upenn.edu, VN (N), AER (N), LAM(N), RLM (8), CRS (8)

INTRODUCTION: Osteoarthritis (OA) is a primary driver of pain and disability in the aging population, for which there are no available therapies that can halt or delay disease progression. Aging is a key risk factor for OA, where age-associated inflammation, or "inflamm-aging," is thought to be a contributing factor in disease progression, as both systemic and local joint inflammation are commonly associated[1]. One potential therapeutic target, soluble CD14, a co-receptor of inflammatory toll-like receptor signaling that is produced primarily by activated macrophages, is present in synovial fluid in patients with OA and positively associates with joint space narrowing, joint effusion, and pain[2,3]. We previously reported that targeting CD14 in mice via both genetic and therapeutic approaches protects against OA-associated pain across multiple models of PTOA (DMM, PMX, ACLR)[3-5]. **Expanding upon this work and given the broad inflammatory role of CD14, we tested the hypothesis that global genetic CD14 KO would protect against age-associated joint degeneration.**

METHODS: *Aged model (n=9-14):* Global genetic CD14 knockout (CD14 KO)[3-5] and WT mice were aged up to 24-months. *Evoked pain analysis (n=9-14):* Knee hyperalgesia was recorded using a pressure application measurement (PAM) device (Ugo Basile), measuring the withdrawal threshold in grams (capped at 450g). *Spontaneous* pain *behavioral analysis (n=9-13):* Spontaneous cage behavior was evaluated over a 14-hr overnight testing period using the Laboratory Animal Behavior Observation Registration and Analysis System (LABORAS™, Metris)[3]. *Histopathology (n=5-6):* Evaluations of knee[6] and spinal facet joint[7] cartilage damage and synovitis[8] were carried out on Safranin-O and H&E-stained sections, respectively. *Disc Height Index (DHI) (n=5-6):* DHI was calculated as an average of intervertebral disc (IVD) height normalized to adjacent vertebral body length using microCT images of the lumbar spinal column[9]. DHI is reported as the average across L2-L5 IVDs. *Statistical analysis:* Comparisons between strains were evaluated via multiple Mann-Whitney (nonparametric) or T-tests (parametric) with Holm-Sidak post-hoc, and across timepoints via two-way ANOVA, with $p<0.05$ considered significant.

RESULTS: Initial phenotype characterization of aged mice revealed that CD14 KO protected against age-associated weight gain, with a significant reduction in body weight at 12-($p<0.001$), 18-($p=0.004$), and 24-months ($p=0.011$) compared to WT (**Fig. 1A,B**). Evaluating spontaneous cage behavior, CD14 KO mice spent more time mobile ($p=0.009$)) and moving at max speed ($p=0.006$) at 24-months compared to WT (**Fig. 1C**). Evoked pain behavior analysis revealed that CD14 KO protected against age associated knee hyperalgesia ($p=0.002$) compared to WT at 18-months (**Fig. 1D**). Probing structural joint changes, CD14 KO provided a clear protection from age associated knee cartilage damage (**Fig. 2A**), with significantly lower max OARSI scores at 18-months ($p=0.038$) compared to WT (**Fig. 2B**). No protection of knee synovial histopathology was observed (**Fig. 2C,D**). Qualitative analysis of the lumbar spinal joints, revealed that CD14 KO protected against proteoglycan loss in both IVDs and facet joints, as evidenced by decreased Safranin-O staining in WT tissues (**Fig. 3A,C**). Quantitative analysis further revealed that CD14 KO protected against age-associated disc height loss, with increased DHI at 18-months ($p=0.0154$) compared to WT (**Fig. 3B**). Lastly, lower (but not significant) facet degeneration scores were observed within the CD14 KO group (**Fig. 3D**).

DISCUSSION: Our results expand upon prior reports of protections against age-related weight gain and bone mineral changes in global CD14KO mice, though these studies were only carried out to 14-months of age[10]. Evaluating CD14 in the context of age-associated joint degeneration, we first confirmed that CD14 KO protects against age-associated weight gain, and additionally observed protection against age-related mobility loss, providing an initial indication of broad protection against musculoskeletal functional decline. We next showed that CD14 KO significantly alleviated age-associated knee hyperalgesia, mirroring our prior demonstration of protection against painful behaviors across multiple surgical in models of PTOA[3,4]. In addition to the observed knee pain protection, we revealed protection against knee joint cartilage damage in the CD14 KO strain. Finally, expanding our analysis to the lumbar spinal joints, which we hypothesized to contribute to the general mobility losses with age, CD14 KO preserved proteoglycans across both aged IVD and facet joints. Lastly, CD14 KO provided a clear protection from age-associated disc height loss, a primary metric of degenerative IVD disease[9]. In addition to the inflammatory role of CD14 on innate immune cells, multiple mechanisms may be at play within this aged model, as increased inflammatory signaling from adipocytes is also thought to be a contributor to age-associated inflammation[1]. Future studies will probe how CD14 influences local joint and systemic inflammation across various cell types, and how this may contribute to musculoskeletal joint pathology and pain.

SIGNIFICANCE: The attenuation of mobility loss, pain, and multi-joint degeneration within aged mice lacking CD14 strongly supports the potential of targeting this receptor therapeutically for treating age-associated OA *across multiple joints* and suggests shared protective mechanisms throughout the musculoskeletal system. Whether the protective effects of CD14 loss are related to improved mobility, maintenance of a healthier weight through adult life, or mediated through broad local and systemic inflammatory mechanisms will be investigated in future studies.

REFERENCES: [1]Greene+ OAC (2015), [2]Sanchez-Lopez, Nat Rev Rheum (2022), [3]Burt+ BioRxiv (2025), [4]Burt+ ORS Annual Meeting (2025), [5]Sambamurthy, PLoS One (2018), [6]Glasson, OAC (2010), [7]Wang+ JBJS (2022), [8]Obeidat, OAC (2024), [9]Masuda+ Spine (2005), [10]Johnson FASEB J (2005)

ACKNOWLEDGEMENTS: Funding: I01 BX004912(VA BLR&D), R01 AR075737(NIAMS), and I01 RX002274-06S1, IK6 RX003416, and the CReATE Motion Center (VA RR&D).

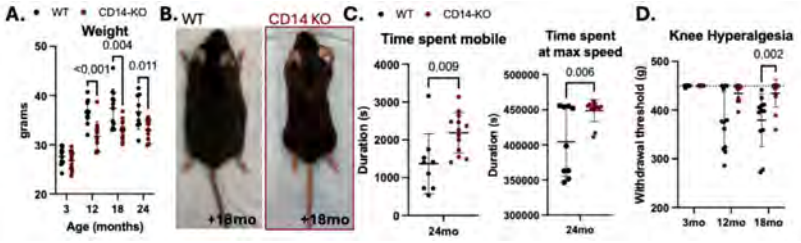

Figure 1: *(A) Weight (grams) with age. (B) Representative images of mice at 18mo sacrifice date. (C) Cage behavior was measured as duration (seconds, s) over a 14hr overnight testing period. (D) Evoked knee hyperalgesia measured as the withdrawal threshold (g), averaged across left and right knees/mouse. p-value indicated.*

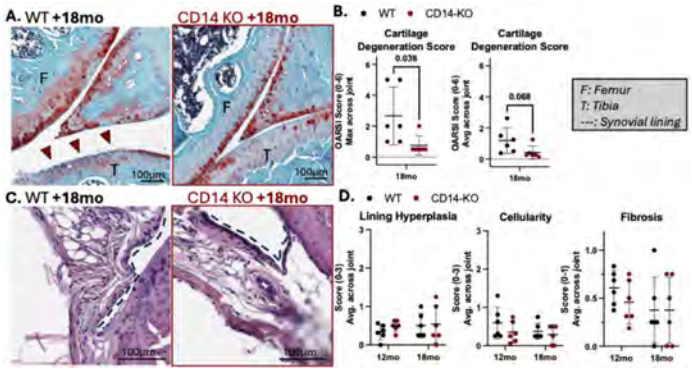

Figure 1: *(**A**) Safranin-O (cartilage) stained knee sections. (**B**) Max and average OARSI cartilage score taken across the knee joint. (**C**) HE-stained knee joint synovium. (**D**) Average synovial inflammation scores across sub-categories. p-value indicated.*

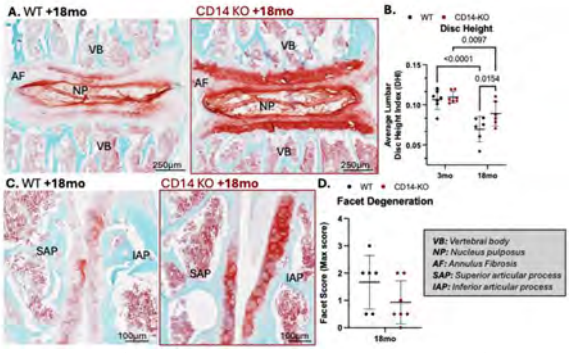

Figure 3: *Safranin-O stained lumbar (**A**) IVD and (**C**) facet joint sections. (**B**) Average lumbar disc height index (DHI) measurement calculated from microCT images (not shown). (**D**) Max L4/L5 facet cartilage degeneration scores. p-value indicated.*

YAP and TAZ Mediate Mechanical Load-Induced Bone Formation

Celine Adomakoh[1] , Yasaman Moharrer[2], Joel D.Boerckel[2]
[1]Department of Biophysics and Biochemistry, University of Pennsylvania
[2]Department of Orthopaedic Surgery, University of Pennsylvania

Bone adapts to mechanical stimuli through mechanotransduction; however, the molecular mechanisms underlying this response remain poorly understood. Yes-associated protein(YAP) and Transcriptional co-activator with PDZ-binding motif(TAZ) are key transcriptional co-activators that regulate gene expression through interactions with other proteins, although they do not bind directly to DNA. These proteins play a crucial role in bone mechanotransduction, facilitating bone formation in response to mechanical loading. Upon mechanical stimulation, YAP/TAZ are activated and translocate to the nucleus, where they interact with the TEAD binding domain. Our previous studies demonstrated that the deletion of YAP/TAZ in osteocytes (cells responsible for sensing mechanical signals) resulted in reduced bone formation and increased bone fragility in mutant mice.

To investigate the roles of YAP/TAZ and osteocyte mechanotransduction in mice with normal developmental histories, we employed pharmacological methods to acutely inhibit YAP/TAZ. For this, 14 weeks old C57/BL6 mice were injected by verteporfin (VP) which blocks YAP/TAZ co-activation or MGH-CP1 (CP1) which prevents TEAD from interacting with YAP/TAZ.

We applied cyclic compressive mechanical loading to one tibia for 5 days per week over two weeks. The other tibia remained unloaded as a control. Dynamic fluorochrome labeling (calcein and alizarin complexone) were used to quantify cortical bone formation at the site of maximal cortical strain and of trabecular bone in the proximal tibia metaphysis.

Our dynamic histomorphometry cortical analysis results for Mineralizing Surface/Bone Surface (MS/BS) revealed a significant effect of mechanical loading on DMSO-control samples, while this effect was abrogated in both VP and CP1 samples. Although mechanical loading had no effect in the latter groups, a drug effect was observed when comparing VP to DMSO-control and CP1 to DMSO-control. Mineral Apposition Rate (MAR) analysis showed a significant effect of mechanical load in DMSO-control samples, but this effect was again abrogated in VP and CP1. Additionally, there was a notable drug effect in CP1 compared to DMSO-control. Bone Formation Rate/Mineralizing Surface (BFR/MS) demonstrated a significant effect of mechanical loading across all three groups—DMSO-control, VP, and CP1. A drug effect was also observed in CP1 compared to DMSO-control. These findings suggest that YAP/TAZ inhibition in cortical bone abrogates the effects of mechanical loading.

Our dynamic histomorphometry trabecular analysis of MS/BS revealed that mechanical loading was abrogated in all groups: DMSO-control, VP, and CP1. MAR showed a significant mechanical loading effect in DMSO-control, while VP and CP1 were again abrogated. BFR/MS results indicated a significant mechanical loading effect in DMSO-control, but this effect was abrogated in both VP and CP1. Together, these results suggest that YAP/TAZ inhibition in trabecular bone also abrogates the response to mechanical loading.

Together our data suggests that YAP/TAZ signaling is crucial for regulating bone microarchitecture and formation in response to mechanical loading.

Mechanical Regulation of Muscle Stem Cells: Insights from Viscoelastic Hydrogel Models

Haiying H, Taeyoon K, Zichen G, Christopher M

Muscle stem cells (MuSCs) play a key role in muscle regeneration and growth. The mechanical properties of the extracellular matrix (ECM) are known to influence MuSC behavior. Previous studies have shown that MuSCs cultured on substrates that mimic the stiffness of healthy muscle tissue (elastic modulus, E ≈12 kPa) maintain their stemness and proliferative capacity better than those grown on rigid plastic. The ECM, however, is not purely elastic—it is viscoelastic, meaning its molecular components can rearrange over time to dissipate applied forces. Despite this, the role of ECM viscoelasticity in regulating MuSC function remains poorly understood.

In this project, we developed a novel viscoelastic hydrogel system based on strain-promoted azide–alkyne cycloaddition, hydrazone, and boronate ester chemistries. This system minimizes cytotoxicity, allows stable presentation of adhesive ligands, and provides precise control for fabricating 2D hydrogels. Freshly isolated primary mouse MuSCs were seeded on viscoelastic 2D hydrogels with varying stiffness (E = 12, 40 kPa) and stress relaxation rates ($\tau_{1/2}$ = 10^0, 10^2, 10^3, and >10^4 s) to investigate how changes in mechanical cues influence MuSC activation and differentiation. These studies may provide novel insights into the mechanobiology of muscle regeneration and identify new strategies for expanding therapeutically-relevant numbers of muscle stem cells.

Inappropriate Skeletal Muscle Progenitor Cell Fusion is a Major Contributor to Tongue Overgrowth in Beckwith-Wiedemann Syndrome

Tichy ED, Nguyen A, Bryne M, Fallon M, Pradieu RD, Tringola S, Nirgude S, Kinnear D, Kozakewich HPW, Kalish JM

Beckwith-Wiedemann syndrome (BWS) is a tissue overgrowth and cancer predisposition syndrome, which affects 1 in 10,000 live births. Macroglossia, or tongue overgrowth, is a cardinal feature and is present in over two thirds of cases. The causes of BWS macroglossia are unknown. Using our robust BWS Registry and Biorepository, which includes tongue specimens from debulking surgeries, and comparing them to tongue samples from pediatric autopsies, we found that BWS macroglossia is caused by skeletal muscle hypertrophy. We next examined skeletal muscle progenitor cell abundance and proliferation state in situ. We did not observe increased proliferation or increased muscle progenitor cell numbers in BWS tongue tissues. Isolation of satellite cells from tongues followed by in vitro culture similarly did not uncover any proliferative differences. However, inducing these cells to differentiate in vitro resulted in significantly larger myotubes and a hyper-fusion phenotype. These data demonstrate that BWS satellite cells exhibit cell autonomous defects that predispose them to form larger muscle fibers, which likely contribute to the observed macroglossia in patient tongues. In our next steps, we aim to identify altered signaling pathways in myogenic BWS cells undergoing differentiation, which may be targeted for future therapies.

Surgical revision of *S. aureus* infection increases virulence factor expression and activates a multi-tissue inflammatory response.

Carly J. Smith[1], Arianna J. Moniodes[1], Amanda R. Watkins[2], Autumn G. Melvage[1], Thomas P. Thompson[3], Eirene Choi[1], Abigail A. Lucas[1], Brendan F. Gilmore[3], Thomas P. Schaer,[2] Noreen J. Hickok[1], Theresa A. Freeman[1]

[1]Department of Orthopedic Surgery, Thomas Jefferson University, Philadelphia, PA

[2]University of Pennsylvania, School of Veterinary Medicine, Kennett Square, PA

[3]Queen's University Belfast, Belfast, UK

Theresa.Freeman@jefferson.edu

This study investigates the disruption of the host-pathogen interface of a biofilm-associated orthopedic infection using surgical revision. While these types of procedures are considered essential, the cellular and molecular mechanisms by which the immune system, musculoskeletal system, and bacteria coordinate their response to this secondary injury remains unclear. To investigate this, we performed histology, bulk RNA sequencing, and a cytokine array to define the dynamic interplay between host and microbe. Our results show that immunological niches already compromised with infection – such as the bone marrow, lymph nodes, and circulating blood – further upregulate pro-inflammatory programs in response to revision surgery. Following revision surgery, bone-resorbing osteoclasts increase in number at the site of injury and lead to overall bone volume losses in infected rats. Lymph nodes expand significantly in response to revision with increases in CD3+ and CD4+ T cells, but this expansion appears to restrict lymph flow and hinders long-term T cell activation. Circulating pro-inflammatory cytokines increase with surgical revision, and some levels remain elevated for up to 14 days, leading to increased systemic inflammation in infected rats. This enhanced inflammation at the incision site in response to revision has no effect on reducing bacteria numbers. Instead, it leads to increased expression of virulence factors, enhanced tissue remodeling, and damage. Some tissue types appear better equipped to recover from this inflammatory insult. Muscle tissue, for example, expresses significant increases in innate and adaptive immune cell transcriptional signatures including neutrophils, macrophages, T cells, and B cells 4-days post-revision, but these signatures are far less prominent 14-days post-revision. This finding corresponds with physiological improvements in muscle tissue morphology that are present on day 14. Conversely, bone appears poorly equipped to recover from the inflammatory insult of surgical revision. Revision leads primarily to increases in bone resorption and a worsening of bacterial infiltration and morphology within the bone marrow. These findings show that revision surgery negatively impacts all tissues within the surgical site, but how long these negative impacts are present is tissue specific. Understanding the timing and tissue changes associated with revision of infected orthopedic sites will help inform the design of additional interventions to minimize tissue damage and maximize bactericidal effects.

Distinct Molecular and Structural Traits of Permanent versus Transient Cartilage in Early Development

Jiaqi Xiang[1], Bryan Kwok[1], Meghan E. Kupratis[2], Mingyue Fan[1], Sara Tufa[3], Douglas R. Keene[3],
Robert L. Mauck[2], Nathaniel A. Dyment[2], Eiki Koyama[4], Lin Han[1]
[1]Drexel University, Philadelphia, PA; [2]University of Pennsylvania, Philadelphia, PA;
[3]Shriners Hospital for Children, Portland, OR; [4]The Children's Hospital of Philadelphia, Philadelphia, PA.

Disclosures: RL Mauck (4, *Mechano-Therapeutics*; 5, *4Web Medical*; 8, *JOR Spine*), L Han (8, *Osteoarthritis Cartilage*), no other disclosures.

INTRODUCTION: Hyaline cartilage is a family of cartilaginous tissues characterized by an extracellular matrix (ECM) of porous collagen II fibril networks entrapping densely packed proteoglycans [1]. Early skeletal development starts with formation of transient hyaline cartilage at the epiphysis (Fig. 1a), providing the template that remodels into bone [2]. In contrast, articular cartilage, which initiates at the cavitation sites defining future joint surfaces, is not replaced by bone and remains as hyaline cartilage throughout life, endowing joints with load transmission and energy dissipation functions [3]. These two hyaline cartilages thus follow distinct developmental trajectories and have different functions in vivo. However, due to their similar composition, there have been few attempts to delineate differences in their matrix structure-function relationships or assembly/remodeling paths. This study aims to distinguish the molecular, structural and mechanical traits of these two cartilages during the initial phase of matrix formation in both small (murine) and large (porcine) animal models.

MATERIALS and METHODS: Knee joints were harvested from wild-type (WT) C57BL/6J mice at embryonic day 15.5 (E15.5) and postnatal day 0 (P0), and from Yorkshire pigs at E42, E84 and P0. RNAscope in situ hybridization was applied to visualize the spatial expression profiles of *Col2a1* and *Acan* on P0 murine joint sections. Safranin-O/Fast Green histology was applied to evaluate joint morphology and sulfated glycosaminoglycans (sGAGs) distribution in sagittal and coronal paraffin sections of murine and porcine joints, respectively. Immunofluorescence (IF) staining was performed to assess the protein distributions of collagen VI, perlecan and collagen V. Transmission electron microscopy (TEM) was applied to quantify collagen fibril nanostructure in P0 murine joints. Atomic force microscopy (AFM)-nanoindentation was applied to 10 μm-thick, unfixed cryo-sections to quantify the tissue micromodulus, following our established methods [4]. Two-sample student's *t*-test was applied to detect differences in fibril diameter and modulus at $\alpha = 0.05$.

RESULTS and DISCUSSION: In the murine joint (Fig. 1a), we found active expression of *Col2a1* and *Acan* in both articular and epiphyseal cartilage at P0, with higher expression in epiphyseal chondrocytes (Fig. 1b). While histology showed stronger sGAG staining in epiphyseal cartilage (EC) in murine (Fig. 1c) and porcine knee (Fig. 2a), TEM images revealed thinner fibrils in EC (arrowhead, Fig. 1f). In turn, AFM showed similar modulus between AC and EC at P0 in murine (Fig. 1g). These two tissues also exhibited differential distribution of key matrix molecules in both animal models. Collagen VI, a pericellular matrix (PCM) biomarker [5], was only present in articular cartilage (AC). However, unlike murine joints, E84 porcine joints showed distinct collagen VI-exclusive PCM domains in AC (Figs. 1d,2b). Another PCM biomarker, perlecan [6], in contrast, was present throughout both tissues (Figs. 1d, 2b). Surprisingly, collagen V, the initiator of collagen I fibrillogenesis [8], was only found in developing AC (Figs. 1e, 2c), suggesting it may be involved in the initial templating of the permanent cartilage matrix, a role that extends beyond the traditional function of collagen II/IX/XI fibrils in hyaline cartilage (Fig. 1f). The differential localization of collagens V and VI in articular but not epiphyseal cartilage (Figs. 1d, 2b) suggests these two units constitute unique cellular microniches during initial establishment. In porcine knee, the modulus of EC was similar to that of AC at E42, but higher at E84 and P0 (Fig. 2d), supporting differential development traits of these two units. Currently, one key roadblock in treating diseases such as osteoarthritis (OA) or heterotypic ossification is the incomplete molecular understanding of cartilage matrix formation and its remodeling into bone. Understanding the initial traits that differentiate permanent versus transient cartilage may provide a path to address these challenges.

CONCLUSION: Our study identifies early molecular, structural, and mechanical distinctions between the matrices of permanent versus transient hyaline cartilage, providing a foundation for the development of new OA treatments and cartilage regeneration approaches.

References: [1] Han+ 2011. [2] Xie+ 2021. [3] Maroudas+ 1979. [4] Kwok+ 2023. [5] Poole+ 1988. [6] SundarRaj+ 1995. [7] Sun+ 2011. [8] Kim+ 2022. [9] Vincent+ 2007. [10] Staines+ 2013. [11] Medici + 2012.

Acknowledgements: This work was supported by NIH R01AR075418, NSF CMMI-2047073 and UPenn PCMD NIH P30AR06961.

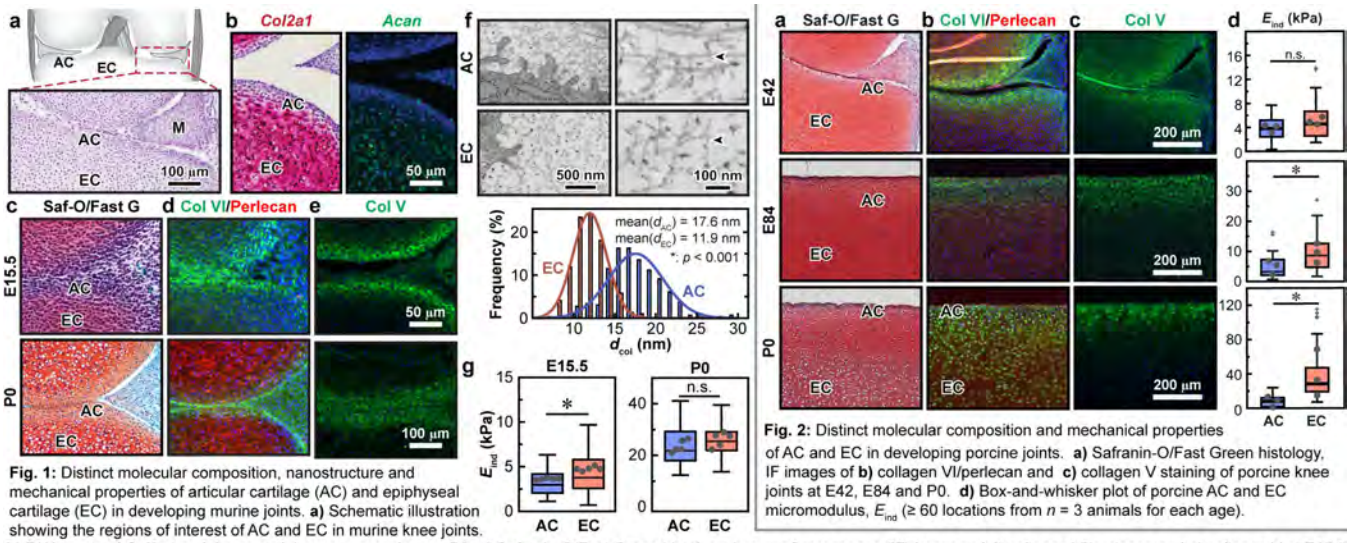

Fig. 1: Distinct molecular composition, nanostructure and mechanical properties of articular cartilage (AC) and epiphyseal cartilage (EC) in developing murine joints. **a)** Schematic illustration showing the regions of interest of AC and EC in murine knee joints. **b)** RNAscope of *Col2a1* and *Acan* spatial gene expressions at P0. **c)** Safranin-O/Fast Green histology, immunofluorescence (IF) images of **d)** collagen VI/perlecan and **e)** collagen V at E15.5 and P0. **f)** Representative TEM images of AC versus EC, and corresponding histogram of fibril diameter distribution (> 280 fibrils). **g)** Box-and-whisker plot of AC and EC micromodulus, E_{ind} (≥ 75 locations from $n = 5$ animals for each age).

Fig. 2: Distinct molecular composition and mechanical properties of AC and EC in developing porcine joints. **a)** Safranin-O/Fast Green histology, IF images of **b)** collagen VI/perlecan and **c)** collagen V staining of porcine knee joints at E42, E84 and P0. **d)** Box-and-whisker plot of porcine AC and EC micromodulus, E_{ind} (≥ 60 locations from $n = 3$ animals for each age).

Reduction of Type III Collagen During Healing has Minimal Impact on Young Adult Mouse Tendon Healing

Margaret K. Tamburro,[1] Jaclyn A. Carlson,[1,2] Emma E. Kroll, [1] Miranda K. Doro,[1] Stephanie N. Weiss,[1] Jeremy D. Eekhoff,[1] William Yen,[2] Louis J. Soslowsky[1], Susan W. Volk,[2]

[1]McKay Orthopaedic Research Laboratory, University of Pennsylvania, Philadelphia, PA

[2]School of Veterinary Medicine, University of Pennsylvania, Philadelphia, PA

Margaret.Tamburro@pennmedicine.upenn.edu

Disclosures: Margaret K. Tamburro (N), Jaclyn A. Carlson (N), Emma E. Kroll (N), Miranda K. Doro (N), Stephanie N. Weiss (N), Jeremy D. Eekhoff (N), William Yen (N), Louis J. Soslowsky (N), Susan W. Volk (N)

INTRODUCTION: Injured tendons heal poorly with fibrovascular scar, leading to functional deficits and high reinjury risk. As in skin, increased type III collagen (Col3) is a hallmark of the healing tendon matrix.[1] In healing skin, Col3 regulates cell activities and fate in the early healing niche and is a suppressor of scar formation.[2] However, the role of Col3 in tendon healing remains unclear. Therefore, the objective of this study was to elucidate the regulatory role of Col3 throughout tendon healing in young adult mice by reducing *Col3a1* expression at the time of tendon injury. We hypothesized that Col3 knockdown at time of injury would limit cell recruitment and differentiation, leading to poor structural and functional healing outcomes.

METHODS: At postnatal day 89 (p89), wildtype (WT, Rosa-CreER^{T2}; *Col3a1*$^{+/+}$) and Col3 knockdown (KD, Rosa-CreER^{T2}; *Col3a1*$^{F/F}$) mice (mixed sex) received a tamoxifen injection (200 mg/kg). Injured groups underwent bilateral patellar tendon biopsy punch injury[3] at p90 (IACUC approved). Injured patellar tendons were harvested at 1-, 3-, and 6-weeks post-injury (wpi), and uninjured tendons were harvested at the middle (3-wpi) timepoint. Tendons were randomized to composition assessment with gene expression and immunohistochemistry (IHC), structure assessment with second harmonic generation (SHG) imaging and transmission electron microscopy (TEM), and function assessment with tensile testing. Gene expression (n ≥ 8/group): RNA was processed, and expression of 96 genes was quantified with a Fluidigm 96.96 Dynamic Array.[4] Tamoxifen-treated knockdown samples used for gene expression analysis were confirmed to have >50% reduction in *Col3a1* expression relative to uninjured wildtype tendon. IHC (n ≥ 4/group): Tendons were fixed, cryopreserved,[5] and sectioned along the longitudinal axis of the tendon (8 µm thickness). Sections were blocked, permeabilized, and stained for Col3 (Goat Anti-Type III Collagen-UNLB, SouthernBiotech) and nuclei (SYTOX^{TM} Green, Thermo). Col3 fluorescence for regions of interest containing healing matrix was quantified with Fiji.[6] SHG (n ≥ 5/group): Tendons were optically cleared[7] and imaged (SP8 Multiphoton Microscope, Leica) with SHG. To quantify matrix alignment, regions of interest containing healing matrix were analyzed with OrientationJ.[8] TEM (n ≥ 4/group): Tendons were fixed, prepared, sectioned, stained, and imaged (60,000x).[9] Fibril diameter distributions were quantified. Tensile Testing (n ≥ 16/group): Tendons were prepared[10] and tested with a viscoelastic protocol: 1) preconditioning, 2) stress relaxation at 2% and 4% strain with a subsequent sinusoidal frequency sweep (10 cycles at 0.1, 1, 5, and 10 Hz) at each strain level, and 3) quasistatic ramp to failure (0.1% strain/s) with image capture (2 Hz). After outliers were removed (ROUT method, Q = 1%), data were compared with 2-way ANOVAs (genotype, healing timepoint). Fibril diameter distributions were compared with Kolmogorov-Smirnov tests. Significance was set at $p \leq 0.05$.

RESULTS: Col3 knockdown was effectively induced, as evidenced by gene expression and IHC (Fig. 1A-C). Col3 increases after injury and remains elevated compared to uninjured baseline throughout the 6-week healing period. Despite effective knockdown, principal component analysis (PCA) of gene expression did not show separation between WT and KD groups at any timepoint (Fig. 1D). Eleven genes were differentially expressed between WT and KD groups overall; post hoc comparisons of genotype at each timepoint showed five genes were differentially expressed at 3-wpi (Fig. 1E). Unlike skin, fibrillar collagen alignment (Fig. 2A-B) was unaffected by loss of Col3 in healing tendon, but fibril diameter distribution showed a shift toward larger fibrils in the KD group at 3- and 6-wpi (Fig. 2C). Tendon mechanics were not affected by genotype at any healing timepoint in p90 mice (selected properties shown, Fig. 3A-C).

DISCUSSION: We investigated the compositional, structural, and functional impacts of lasting reduction of Col3 at the time of tendon injury on tendon healing. Contrary to our hypothesis, reduction of Col3 during tendon healing had a nuanced impact on tendon healing in these young mice. This challenges the existing paradigm that persistent Col3 in the healing matrix directly contributes to poor tendon healing outcomes. Our results suggest Col3-independent mechanisms can contribute to poor physiologic tendon healing. Assessment of the molecular composition of the healing matrix in KD tendons will provide additional insight into possible compensatory production of other matrix molecules to form a provisional healing matrix that supports reparative cell recruitment and differentiation. We will also consider possible sex-specific effects of Col3 reduction and effects of different timing of Col3 reduction on healing outcomes.

SIGNIFICANCE: Understanding regulators of poor tendon healing is critical for design and use of improved tendon injury prevention and treatment strategies.

REFERENCES: [1] Dyment. PLoS One. 2013. [2] Volk. Cells Tissues Organs. 2011. [3] Beason. J Biomech. 2012. [4] Leiphart. J Biomech Eng. 2020. [5] Beach. Ann Biomed Eng. 2024. [6] Schindelin. Nat Methods. 2012. [7] Calve. PLos One. 2015. [8] Rezakhaniha. Biomech Model Mechanobiol. 2011. [9] Dunkman. Matrix Biol. 2013. [10] Leiphart. J Biomech. 2022. ACKNOWLEDGEMENTS: This study was funded by NIH R01GM124091, R01AR080029, F31AR082282 and the Penn Center for Musculoskeletal Disorders (P30AR069619).

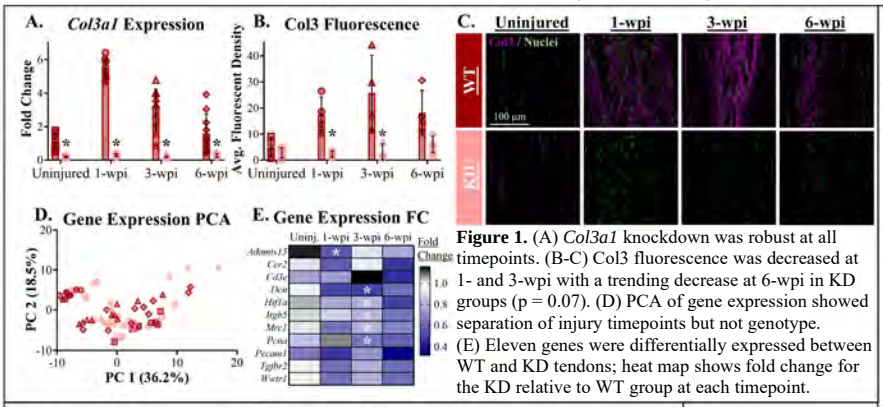

Figure 1. (A) *Col3a1* knockdown was robust at all timepoints. (B-C) Col3 fluorescence was decreased at 1- and 3-wpi with a trending decrease at 6-wpi in KD groups ($p = 0.07$). (D) PCA of gene expression showed separation of injury timepoints but not genotype. (E) Eleven genes were differentially expressed between WT and KD tendons; heat map shows fold change for the KD relative to WT group at each timepoint.

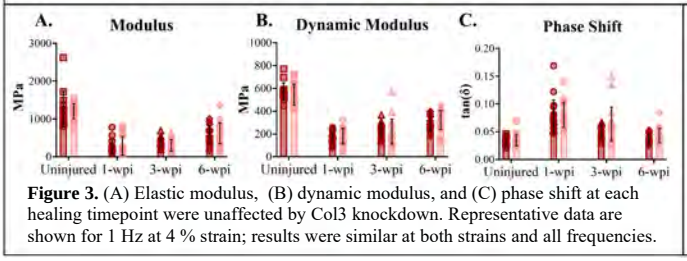

Figure 3. (A) Elastic modulus, (B) dynamic modulus, and (C) phase shift at each healing timepoint were unaffected by Col3 knockdown. Representative data are shown for 1 Hz at 4 % strain; results were similar at both strains and all frequencies.

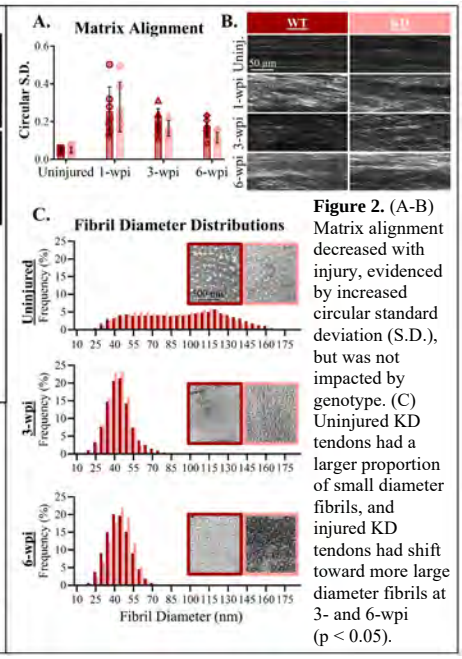

Figure 2. (A-B) Matrix alignment decreased with injury, evidenced by increased circular standard deviation (S.D.), but was not impacted by genotype. (C) Uninjured KD tendons had a larger proportion of small diameter fibrils, and injured KD tendons had shift toward more large diameter fibrils at 3- and 6-wpi ($p < 0.05$).

Lipid Nanoparticles Loaded with a Highly Potent sPLA$_2$ Inhibitor for Osteoarthritis Treatment

Qiushi Liang (qiushil@seas.upenn.edu)[1,2], Tao Gui[1], Lijun Luo[2], Anatoliy V. Popov[3], Qi He[1], Kyla Ortved[4], Andrew Tsourkas[2], Zhiliang Cheng[2], Ling Qin[1]
[1]Department of Orthopaedic Surgery, [2]Department of Bioengineering, [3]Department of Radiology, [4]School of Veterinary Medicine, University of Pennsylvania, USA

Disclosures: Z.C., L.Q., and A.T are inventors on a patent related to this work filed by the University of Pennsylvania (no. 63/043,025., filed 23 June 2020).

INTRODUCTION: Chronic unresolved inflammation plays a critical catabolic role in osteoarthritis (OA) development and progression. Pro-inflammatory cytokines (i.e., IL-1β and TNFα) up-regulate aggrecanases and collagenases in chondrocytes to degrade cartilage matrix. Secretory phospholipase A_2 (sPLA$_2$) is a heterogeneous group of enzymes that specifically hydrolyzes the sn-2 ester bond of membrane phospholipids to release free fatty acids, such as arachidonic acid and lysophospholipids, which are upstream mediators of inflammation in many chronic inflammatory diseases, including OA. Varespladib is a potent and clinically tested small molecule sPLA$_2$ inhibitor (sPLA$_2$i). In this study, we used lipid nanoparticles (LNPs) to deliver varespladib and evaluated the therapeutic efficacy of sPLA$_2$i-LNPs in attenuating OA progression in a mouse model.

METHODS: *Varespladib-lipid conjugation*– sPLA$_2$-cleavable varespladib-lipid conjugate was synthesized by reacting varespladib with lysophosphatidylcholine. The-COOH from varespladib and -OH from lysophosphatidylcholine form the sn-2 ester bond, which is selectively hydrolyzed by sPLA$_2$. *sPLA$_2$i-LNP generation*– The varespladib-lipid was incorporated into the lipid membrane shell by mixing with DSPE-PEG2K and DOTAP, a cationic lipid. *Horse cartilage explants* – Medial femoral condyle cartilage biopsies with a diameter of 6mm and a thickness of 2-3mm from horses were treated with one of the following: PBS, IL-1β+dimethyl sulfoxide (DMSO), empty LNPs, free sPLA$_2$i in DMSO, or sPLA$_2$i-LNPs for 7 days. *Animals*- All animal work was approved by the Institutional Animal Care and Use Committee at the University of Pennsylvania. 3-month-old male *C57Bl/6* mice underwent destabilization of the medial meniscus (DMM) in their right knees and received 10 µl of PBS, empty LNPs, free sPLA$_2$i, or sPLA$_2$i-LNPs via intra-articular (IA) injections starting immediately after surgery at once every 3 weeks for 12 weeks (n=6 mice/time point/group). In the loading model, 2-month-old male *C57Bl/6* mice were subjected to a single loading episode composed of 60 cycles of 6 N peak load on their right knees, and IA injected with 10 µl of PBS or sPLA$_2$i-LNPs starting immediately after surgery at once every 2 weeks for 4 weeks (n=6 mice/time point/group). Additional groups of mice (n=6/surgery) received sham surgery followed by PBS injections. *Histology*- Paraffin sections of knee joints were stained with H&E, Safarin O/fast green, or phosphor-NFκB p65 for immunohistochemisty. *Pain assessment*- Knee joint pain was evaluated weekly using von Frey filaments. *Statistics*- Data are expressed as means±SD and analyzed by one way ANOVA and unpaired, two-tailed Student's t-test.

RESULTS: The sPLA$_2$i-LNPs had a homogenous diameter around 12 nm (Figure 1A, B). They were stable in PBS over 7 days and in bovine fluid over 4 days, exhibiting satisfactory stability (Figure 1C, D). In vitro sPLA$_2$ activity assay demonstrated their sensitive response to environmental sPLA$_2$, with the inhibition effect being strongly correlated with the amount of varespladib.(Figure 1E). Treatment of horse cartilage explants with IL-1β induced OA-like degeneration after 7 days as shown by Safranin O staining (Figure 2). Strikingly, addition of sPLA$_2$i-LNPs at 60 µM (sPLA$_2$i concentration) to culture medium almost completely restored cartilage extracellular matrix (ECM) to a healthy level (Figure 2). Free sPLA$_2$i showed partial beneficial effects but this effect was minor compared to sPLA$_2$i-LNPs as the positively charged DOTAP significantly enhanced the penetration of sPLA$_2$i into the tissue, thereby increasing its local concentration and therapeutic effect. To test the in vivo efficacy of sPLA$_2$i-LNPs, we utilized two mouse models of OA induced by DMM and loading to mimic chronic OA and post-traumic OA, respectively. IA injections of sPLA$_2$i-LNPs into DMM knees greatly improved the morphology and structure of articular cartilage, leading to drastically reduced proteoglycan loss and synovitis at 3 months post-surgery (Figure 3A, B). Compared to free sPLA$_2$i group, mice receiving sPLA$_2$i-LNPs displayed 65% and 60% decreases in Mankin score and synovitis score, respectively (Figure 3C, 3D). Loading at 6N caused a lesion with proteoglycan loss in the lateral femoral articular cartilage surface in PBS-treated mice 1 month later (Figure 4A). Remarkably, compared to PBS, sPLA$_2$i-LNP treatment reduced the length of cartilage injury by 94% and Makin score by 83% to a level similar to sham group (Figure 4B). Synovitis was partially allievated (Figure 4C, D), leading to attenuated joint pain (Figure 4E). Mechanistically, sPLA$_2$i-LNPs significantly reduced levels of phospho-NFκB p65 in both the cartilage and synovium of loaded knees (Figure 4F, G), thereby inhibiting the pro-inflammatory NFκB pathway.

DISCUSSION: The delivery of small molecules like varespladib faces challenges such as rapid clearance, uncontrolled release, and low loading efficiency in drug delivery platforms. Our study addresses these issues by conjugating varespladib with lysophosphatidylcholine to create an sPLA$_2$-responsive LNP for OA therapy. Our results demonstrate that sPLA$_2$i-LNPs are stable and sPLA$_2$-sensitive. Additionally, they significantly reduced OA-related inflammation, cartilage degeneration, and synovitis symptoms in mouse OA induced by DMM and loading. Overall, the engineered, sPLA$_2$-responsive varespladib LNP offers controlled release and enhanced therapeutic efficacy, showing a great promise for OA treatment.

SIGNIFICANCE: This proof-of-principle study demonstrates the release profile and efficacy of LNPs with varespladib-lipid conjugation for OA treatment.

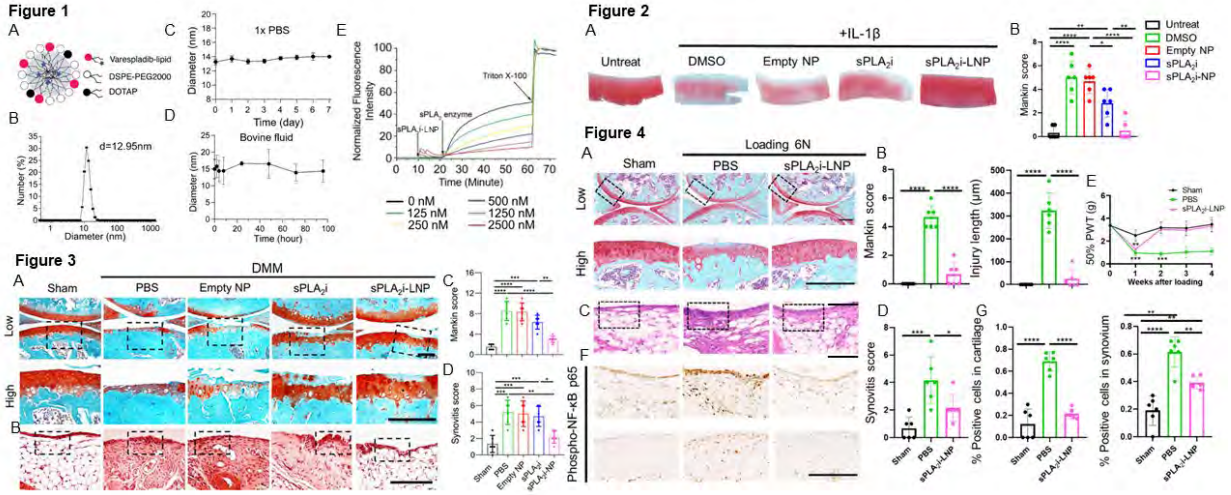

Figure 1. sPLA$_2$i-LNP synthesis and characterization. A: Schematic diagram of sPLA$_2$i-LNPs. **B**: diameter of LNPs by dynamic light scattering. **C, D**: Stability tests of the sPLA$_2$i-LNP. **E**: Inhibitory activities of sPLA$_2$i-LNPs at different concentrations of varespladib. **Figure 2. sPLA$_2$i-LNPs protect horse explants from OA degeneration. A**: SO/FG staining of the treated explants. **B**: Quantification of the Mankin scores across groups. **Figure 3. sPLA$_2$i-LNPs reduce joint destruction in DMM joints. A**, **B**: SO/FG results and Mankin scores of the cartilage. **C, D**: H&E staining of synovium tissue and quantification of synovitis scores. **Figure 4. sPLA$_2$i-LNPs attenuate joint destruction in loaded joints. A**, **B**: SO/FG and quantification of cartilage damage, represented by the Mankin scores and injury length. **C**: Von Frey results until 4 weeks after loading. **D, E**: H&E staining of synovium tissue and synovitis scores. **F, G**: Immunohistochemistry staining of phospho-p65 and its quantification. Scale bar, 200 µm. *P < 0.05, **P < 0.01, ***P < 0.001, ****P < 0.0001.

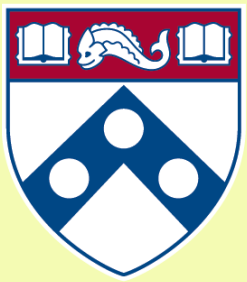

Penn Center *for*
Musculoskeletal Disorders
UNIVERSITY *of* PENNSYLVANIA

Micro CT Core Abstracts

AM Session

Poster 49 to 55

Age-dependent formation of heterotopic ossification in the ultra-rare disease Fibrodysplasia Ossificans Progressiva

Nadine Z. Großmann[1,3,4,5], Loreilys Mejías Rivera[1,3], Nava Schein[1,3], **Douglas W. Roberts**[1,3], Eileen M. Shore[1,2,3,*] & Petra Knaus[4,5,*]

Departments of [1]Orthopaedic Surgery, and [2]Genetics, the [3]Center for Research in FOP and Related Disorders, Perelman School of Medicine at the University of Pennsylvania, Philadelphia, PA, 19104, USA. [4]Freie Universität Berlin, Institute of Chemistry and Biochemistry, 14195 Berlin, Germany. [5]Berlin School for Regenerative Medicine, Charité - Universitätsmedizin Berlin, 13353 Berlin, Germany. (*co-senior authors)

Introduction: Activating mutations in the BMP receptor ACVR1/ALK2 cause the rare genetic disorder fibrodysplasia ossificans progressiva (FOP) and induce formation of extra-skeletal bone formation (heterotopic ossification; HO) in tissues such as skeletal muscle [1]. HO begins during childhood and continues throughout life [2]. The physiology of young and aged tissues is different, including their ability to properly repair and regenerate following injury [3]. Such considerations are highly relevant to treating HO since the ectopic bone formation is accompanied by impaired muscle repair in FOP [4].

Methods: To study age-dependent HO formation and muscle regeneration, we induced HO via cardiotoxin injury to the gastroc muscle of juvenile and adult control and FOP ($Acvr1^{R206H/+}$) mice. HO formation was analyzed using microCT imaging and quantification, and tissue samples underwent histologic analysis. Sections were stained with Hematoxylin/Eosin and Alcian Blue, to visualize inflammation, chondrogenic differentiation, and osteogenic differentiation.

Results: At 21 dpi, microCT analysis revealed that the youngest FOP mice formed significantly more HO. Histologic sections at 7 dpi indicated delayed muscle regeneration in adult FOP mice, with a persistent presence of fibroblasts. Increased immune cell response was observed in the youngest FOP mice

Conclusions: This is the first systematic investigation of age-related effects in FOP. Our data suggests that juvenile FOP tissues initiate HO rapidly, while adult tissues respond more slowly, though once initiated, progression rates are similar. However, overall HO formation is reduced in adult tissues. This study highlights age-related differences in tissue repair and HO formation, providing new insights into skeletal muscle regeneration. On-going studies identifying transcriptional changes and molecular pathways driving HO in young and adult mice will aid in pinpointing therapeutic targets and integrating them with known FOP-related mechanisms.

References:

[1] Shore EM, Xu M, Feldman GJ, Fenstermacher DA, Cho TJ, Choi IH, Connor JM, Delai P, Glaser DL, LeMerrer M, Morhart R, Rogers JG, Smith R, Triffitt JT, Urtizberea JA, Zasloff M, Brown MA, Kaplan FS. A recurrent mutation in the BMP type I receptor ACVR1 causes inherited and sporadic fibrodysplasia ossificans progressiva. Nat Genet. 2006 May;38(5):525-7. doi: 10.1038/ng1783. Epub 2006 Apr 23. Erratum in: Nat Genet. 2007 Feb;39(2):276. PMID: 16642017.

[2] Pignolo RJ, Baujat G, Brown MA, De Cunto C, Hsiao EC, Keen R, Al Mukaddam M, Le Quan Sang KH, Wilson A, Marino R, Strahs A, Kaplan FS. The natural history of fibrodysplasia ossificans progressiva: A prospective, global 36-month study. Genet Med. 2022 Dec;24(12):2422-2433. doi: 10.1016/j.gim.2022.08.013. Epub 2022 Sep 24. PMID: 36152026.

[3] Brack AS, Muñoz-Cánoves P. The ins and outs of muscle stem cell aging. Skelet Muscle. 2016 Jan 18;6:1. doi: 10.1186/s13395-016-0072-z. PMID: 26783424; PMCID: PMC4716636.

[4] Stanley A, Tichy ED, Kocan J, Roberts DW, Shore EM, Mourkioti F. Dynamics of skeletal muscle-resident stem cells during myogenesis in fibrodysplasia ossificans progressiva. NPJ Regen Med. 2022 Jan 14;7(1):5. doi: 10.1038/s41536-021-00201-8. PMID: 35031614; PMCID: PMC8760285.

Sexual dimorphism in skeletal responses to intermittent parathyroid hormone (PTH) treatment and discontinuation

Jin YV, Lee W, Azar T, Xu XX, Tseng WJ, Liu XS

Our recent study unexpectedly discovered that intact female and estrogen-deficient female rats had distinct responses to the discontinuation of PTH treatment. While significant bone loss and bone microarchitecture deterioration occurred in ovariectomized (OVX) rats, no adverse effect was observed in intact female rats, which sustained treatment benefits after PTH discontinuation. This motivated our current study on intact male and orchiectomized (ORX) rats to test the hypothesis that skeletal responses to PTH treatment and discontinuation are influenced by both sex and gonadal functions.

We performed an in vivo μCT study (Scanco vivaCT80, 11.6 μm, n=8/group) at the rat proximal tibia before ORX surgery (week -4), 4 weeks after surgery (baseline, week 0), after PTH/VEH treatment (week 3), and during treatment discontinuation (weeks 4, 5, 8, 10, and 12). VEH treatment had minimal impact on intact male rats (Fig C) while ORX caused a 33% decrease in BV/TV 4 weeks after surgery (week -4 to 0) and then remained stable for 12 weeks (Fig D). BV/TV of intact and ORX male groups increased by 85% and 95% after 3-week PTH treatment, respectively, and continued to increase for one week after PTH discontinuation (defined as the extended anabolic period, EAP), followed by a continuous decrease from week 4 to 12 (Fig C&D). By week12, BV/TV between PTH- and VEH-treated bone was no longer different ORX male group~~s~~. There was minimal change in BV/TV of VEH-treated Male, Female, and ORX rats, in contrast to a 34% decline in BV/TV in VEH-treated OVX rats (Fig E&F). Compared to intact females, intact males had a 2.5-fold greater percentage increase of BV/TV by PTH (Fig G). The increased BV/TV in intact females was sustained stably during PTH discontinuation; however, BV/TV continued to decline from weeks 6 to 12 in intact males (Fig G) due to a continuous decrease in trabecular number (Tb.N, data not shown). Comparing ORX to OVX rats, PTH treatments led to greater improvement in BV/TV (95% vs. 31%, Fig H) and trabecular thickness (Tb.Th, 55% vs. 39%) in ORX vs. OVX rats. Upon PTH discontinuation, BV/TV and Tb.Th continued to increase during the 1-week EAP in both groups. After the EAP, BV/TV had a greater decline in OVX vs. ORX rats (64% vs. 32%, Fig H) due to faster decreases in both Tb.Th and Tb.N (data not shown).

Overall, our current work exhibited a sexual dimorphism in the skeletal responses to PTH treatment and discontinuation in rats. Our results indicated that intact male rats, ORX male rats, and OVX female rats all had EAP upon PTH discontinuation, followed by significant withdrawal effects. In contrast, neither EAP nor withdrawal effect was observed in intact female rats, which sustained treatment benefit even after 9 weeks of discontinuation. Given that OVX rats, intact male rats, and ORX rats all had substantially lower levels of estradiol than intact female rats, we suspect that skeletal responses to PTH discontinuation may be estradiol level-dependent, which will be a focus of our future studies.

Lactation-induced Changes in Osteocyte Lacunae Are Spatially Heterogeneous and Persist After Weaning

Xiaoyu Xu[1], Srijani Datta[1], Yilu Zhou[1], Wonsae Lee[1], Liyun Wang[2], X. Sherry Liu[1]
[1] McKay Orthopaedic Research Laboratory, University of Pennsylvania, Philadelphia, PA
[2] Center for Biomechanical Engineering Research, University of Delaware, Newark, DE
xiaoyu.xu@pennmedicine.upenn.edu

Osteocytes (Ocys) play a central role in bone matrix homeostasis during female reproduction. They resorb their surrounding matrix during lactation to release calcium, and post-weaning recovery of lacunar-canalicular dimensions suggests a capacity for mineral redeposition. However, their ability to reversibly remodel bone matrix remains poorly understood. To address this, we conducted longitudinal DXA and μCT (14μm) tracking with multiple fluorochrome labels in C57BL6 mice (Fig1A). While virgin mice showed continuous skeletal growth, reproductive mice exhibited lactation-mediated bone loss with post-weaning recovery (Fig1B-D). Mineral labeling revealed endosteal-specific dynamics: suppressed anterior mineralization and increased posterior resorption during lactation, followed by post-weaning deposition (Fig1FH), suggesting that Ocys near the endosteum may be more responsive to lactation-induced remodeling than those in the central or periosteal cortex. Backscatter SEM analysis of anterior and posterior Ocys (Fig2A) revealed significant enlargement of lacunar dimensions during lactation in both regions, with no evident recovery following weaning (Fig2CD). The anterior and posterior midshaft cortices were each divided into five equal zones, and lacunae were assigned to zones based on their spatial location (Fig2EG). Lacunar enlargement during lactation was most prominent in the central-to-endosteal (C-E) zone of the anterior cortex and the endosteal (E) zone of the posterior cortex, suggesting that osteocytes near the endosteum are most responsive to lactation-induced mineral resorption (Fig2FH). Despite mineral re-deposition occurred after weaning (Fig2B), lacunae in the anterior B-C zone remained enlarged, while smaller lacunae near recovering endosteal surfaces likely represent newly embedded Ocys (Fig2F), suggesting the pre-existing Ocys in A-C zone lack restorative capacity. Similarly, enlarged lacunae did not recover in any posterior region (Fig2H), indicating that lactation-induced changes in lacunar dimension may be irreversible. Our results suggest that lactation induces spatially distinct lacunar alteration that could be permanent. The apparent 'recovery' likely reflects the incorporation of new osteocytes rather than remodeling of existing ones. This work redefines our understanding of Ocys plasticity during reproductive cycles, highlighting their functional heterogeneity based on cortical position and the enduring impact of lactation.

Figure1 (A) Experimental timeline for longitudinal tracking of skeletal morphology changes in reproductive mice (Repro) and age-matched virgin controls (Virgin). Longitudinal measurements of whole-body bone mineral density (BMD; B) and right femur BMD (C) by DXA and femoral Ct.Th by in vivo micro-CT (D,14 μm) in Repro and Virgin mice (n=3). Fluorochrome labels at anterior (E,F) and posterior cortices (G,H) of cryo-sectioned femur midshaft (8μm; P:periosteal, E:endosteal, dashed lines; blue:nucleus). **Figure2** (A) Experimental timeline of the osteocyte morphology dynamics in maternal skeletons. Ct.Th (B), lacunar area (C), and lacunar perimeter (D) at anterior and posterior femoral midshaft in Virgin, Lac, and Wean mice by bSEM images. Anterior (E) and posterior (G) bSEM sample images of a Wean mouse (grey dashed lines: newly formed mineral after weaning). Five equal zones (A to E) segmented in anterior and posterior mineral cortices, with lacunae assigned to each region based on their spatial locations (E,G). Lacunar area (n=100-120) was averaged for each zone and presented for both anterior (F) and posterior (H) sides. Significant differences compared to Pre-preg (Fig.1B-D) or between groups (Fig.2B-D) were indicated by asterisks (p<0.05 by Student's test or one-way ANOVA).

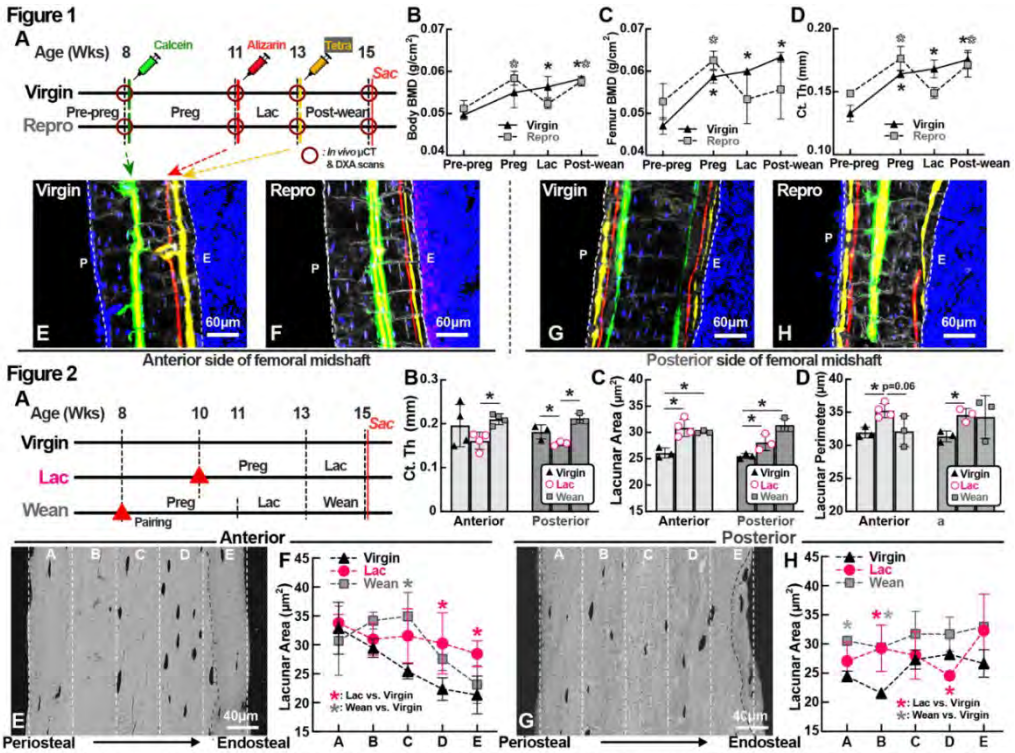

Figure1 (A) Experimental timeline for longitudinal tracking of skeletal morphology changes in reproductive mice (***Repro***) and age-matched virgin controls (***Virgin***). Longitudinal measurments of whole-body bone mineral density (BMD; **B**) and right femur BMD (**C**) by DXA and femoral Ct.Th by *in vivo* micro-CT (**D**,14 μm) in ***Repro*** and ***Virgin*** mice (n=3). Fluorochrome labels at anterior (**E**,**F**) and posterior cortices (**G**,**H**) of cryo-sectioned femur midshaft (8μm; P:periosteal, E:endosteal, dashed lines; blue:nucleus). **Figure2** (**A**) Experimental timeline of the osteocyte morphology dynamics in maternal skeletons. Ct.Th (**B**), lacunar area (**C**), and lacunar perimeter (**D**) at anterior and posterior femoral midshaft in ***Virgin, Lac,*** and ***Wean*** mice by bSEM images. Anterior (**E**) and posterior (**G**) bSEM sample images of a ***Wean*** mouse (grey dashed lines: newly formed mineral after weaning). Five equal zones (A to E) segmented in anterior and posterior mineral cortices, with lacunae assigned to each region based on their spatial locations (**E**,**G**). Lacunar area (n=100-120) was averaged for each zone and presented for both anterior (**F**) and posterior (**H**) sides. Significant differences compared to *Pre-preg* (**Fig.1B-D**) or between *groups* (**Fig.2B-D**) were indicated by asterisks (p<0.05 by *Student's ttest or one-way ANOVA*).

Regulation of fetal skeletal development by maternal exercise

Christopher J. Panebianco[1], Maha Essaidi[1], Brendan Tobin[2], Rebecca Simmons[1], Levi Wood[2], Nathaniel Dyment[1], Niamh C. Nowlan[3], Joel D. Boerckel[1]

[1]University of Pennsylvania, Philadelphia, PA, USA | [2]Georgia Institute of Technology, Atlanta, GA, USA | [3]University College Dublin, Dublin, IRL

INTRODUCTION: Fetal movements exert mechanical forces that shape the developing skeleton.[1] Conditions that impair fetal movements, termed "fetal akinesia", can cause debilitating skeletal defects (*e.g.,* joint contractures, impaired bone development). While it is possible to detect fetal akinesia-causing conditions prenatally, treatment options are limited. Previously, we reported that maternal exercise during gestation regulates fetal skeletal development and used the Splotch-delayed (Sp^d) mouse model of fetal akinesia to infer that maternal exercise induces fetal skeletal development, in part, by mechanical stimulation of the developing limbs.[2] However, the relative contributions of direct mechanical stimulation and indirect maternofetal communication, as well as the underlying cellular and molecular mechanisms, remain unclear. Here, we use a combination of morphometric, statistical, and molecular techniques to better understand how maternal exercise regulates fetal skeletal development in a clinically relevant model of congenital amypolasia.

METHODS: We used the muscular dysgenesis (*mdg/mdg*) mouse model of fetal akinesia.[4] *Mdg/mdg* mice feature a neuromuscular junction defect that renders the muscle non-contractile, resulting in amyoplasia. *Mdg/+* heterozygotes, which are phenotypically normal, were crossed to produce litters containing wildtype (WT), *mdg/+*, and *mdg/mdg* mutant progeny. Pregnant dams were subjected to 1 hr of daily wheel running exercise or sham exercise from E13.5 to E15.5, inclusive. Sham-exercised dams received equivalent treatment with locked wheels. Fetuses were harvested at E16.5, and joint and bone morphometry were evaluated via whole-mount optical projection tomography. We analyzed embryos from 10 litters: 9 WT Sham (3 male, 6 female), 8 *mdg/mdg* Sham (5 M, 3 F), 7 WT Exercise (5 M, 2 F), and 10 *mdg/mdg* Exercise (7 M, 3 F). Two-way ANOVA with Bonferroni correction were used to determine significant differences between groups ($\alpha = 0.05$). Contralateral limbs from 4-5 representative samples for each group were processed for single-cell RNA-sequencing (scRNA-seq). Briefly, embryonic forelimbs were digested, as previously described,[3] processed for scRNA-seq using the 10X Genomics GEM-X 3' gene expression chemistry, then sequenced using an Illumina NovaSeq 6000 sequencer. Samples from the same condition were integrated using pseudobulking and analyzed using the DESeq2 package in R.

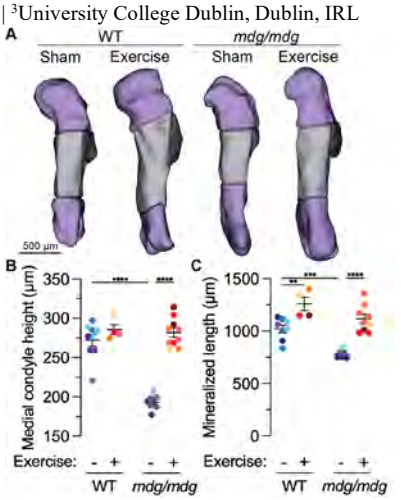

Figure 1. Maternal exercise rescues the effects of fetal akinesia-induced skeletal disorders. (A) *Optical projection tomography reconstructions showing E16.5 humerus morphogenesis.* ***(B,C)*** *Quantifications of medial condyle height and humerus mineralized length. Fetuses from the same litter are marked by the same color datapoint * = p<0.05.*

RESULTS: Maternal exercise rescued joint and bone morphogenesis defects in homozygous *mdg/mdg* mutant fetuses. Sham *mdg/mdg* fetuses had significantly impaired joint morphometry outcomes (*e.g.,* lateral condyle height) and reduced humerus mineralization length than Sham WT controls. Maternal exercise rescued the effects of muscular dysgenesis on both joint and bone morphogenesis (**Fig 1**). To determine the extent to which the effects of maternal exercise on fetal skeletal development can be explained by experimental co-variates related to maternofetal communication, we performed multivariate regression and analysis of covariance (ANCOVA). The best multivariate model, determined by maximized adjusted R^2 and minimized Akaike's Information Criteria (AIC), featured average running distance and fetal weight as predictors (adjusted $R^2 = 0.80$, AIC = 445). Follow-up ANCOVA analysis demonstrated that maternal exercise promoted limb mineralization after controlling for changes in fetal weight ($p < 0.0001$). Thus, the effects of maternal exercise on fetal bone growth cannot be fully explained by enhanced maternofetal communication. Therefore, we next analyzed the development of the deltoid tuberosity, an established hallmark of mechanoregulated morphogenesis. In *mdg/mdg* mice, the mesenchymal condensation that gives rise to the deltoid tuberosity forms normally at E13.5, but fully resorbs by E18.5 due to lack of mechanical stimulation.[4] As expected, Sham *mdg/mdg* mice exhibited deltoid tuberosity resorption, but this absorption was prevented by maternal exercise (**Fig 2**).

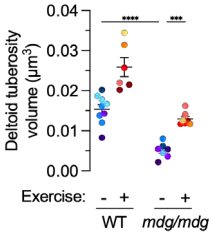

Figure 2. Maternal exercise prevents akinesia-induced resorption of the deltoid tuberosity. ** = p<0.05.*

We next sought to determine the cellular mechanisms by which fetal akinesia and maternal exercise influence fetal skeletal development. To this end, we employed scRNA-seq of E16.5 forelimbs. We captured high-quality transcriptomes from 353,517 cells. Using Louvain clustering, we identified 78 clusters and categorized them into 13 major cell populations by canonical gene expression. Each sample contained every cell population and there were no differences in the relative cellular distributions based on genotype or exercise condition. This suggests that the joint and bone phenotypes observed in *mdg/mdg* mice and their response to maternal exercise are unlikely to be explained by preferential expansion of any given cell type. Focusing on the chondrocyte and osteoblast lineages, we conducted differential gene expression analysis to assess whether the genes affected by the *mdg/mdg* mutation (*i.e.,* WT Sham vs. *mdg/mdg* Sham) were the same as those activated by the rescue (*i.e., mdg/mdg* Sham vs. *mdg/mdg* Exercise). We found limited overlapping differentially expressed genes (DEGs) in the chondrocyte and osteoblast lineage comparisons, which suggests that the rescue of skeletal development by maternal exercise may be indirect at the cellular level, or may involve subpopulations. However, two chondrocyte DEGs (*Larp1*, *Mtss2*) and three osteoblast DEGs (*Rab21*, *Larp1 Fam102b*) and were consistently downregulated by the *mdg/mdg* mutation and upregulated by maternal exercise, suggesting potential direct mechanistic targets (**Fig 3**).

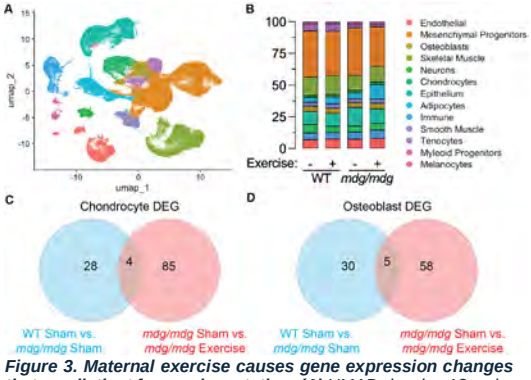

Figure 3. Maternal exercise causes gene expression changes that are distinct from mdg mutation. (A) *UMAP showing 13 major cell populations by Louvain clustering.* ***(B)*** *Proportion of cell types within conditions.* ***(C)*** *Chondrocyte and* ***(D)*** *osteoblast differentially expressed gene (DEG) comparisons.*

DISCUSSION: Fetal akinesia affects 1 in 3000 live births. Here, we show that maternal exercise can rescue skeletal defects caused by fetal akinesia in a clinically-relevant mouse model of amyoplasia. We conclude that the effects of maternal exercise are mediated both by enhanced maternofetal communication and by local mechanical stimulation. Our scRNA-seq analyses suggest that this rescue may be indirect, such that the cells impaired by akinesia are distinct from those activated by maternal exercise. However, it is also possible that the rescue is mediated by subpopulations of cells not captured by the clustering resolution of our initial analyses. Ongoing studies will directly explore these possibilities.

SIGNIFICANCE: Maternal exercise may serve as a non-invasive, *in utero* therapeutic to treat the effects of fetal akinesia on skeletal development and may provide a model for studying developmental mechanobiology *in vivo*.

REFERENCES: [1] Nowlan+ *Eur Cell Mater* 2015; **[2]** Panebianco+ *bioRxiv* 2025; **[3]** Collins+ *Dev Cell* 2023; **[4]** Blitz+ *Dev Cell* 2009

ACKNOWLEDGEMENTS: Work supported by the ERC EU's Seventh Framework Program [336306], NICHD [R01 HD113596], Penn IRACDA [NIH K12GM081259], Penn Center for Musculoskeletal Disorders [NIH P30-AR069691], and Penn Center for Undergraduate Research and Fellowships.

Vancomycin Coupled with Cold Plasma Treatment Inhibits Osteoclast Activity in *Staphylococcus Aureus*-Infected Bone

Arianna J. Moniodes, Carly J. Smith, Amanda R. Watkins, Genevieve Baldomero, Autumn G. Melvage, Thomas P. Schaer, Noreen J. Hickok, Theresa A. Freeman.

During osteomyelitis, *Staphylococcus aureus* (*S. aureus*) not only readily adheres to bone and implant surfaces, forming a biofilm, but also infiltrates the bone through canaliculi. Additionally, inflammation associated with *S. aureus* infection drives bone loss through osteoclast activity. This project analyzes femoral bones in a rat model of *S. aureus* infection, comparing no treatment, treatment with vancomycin, and a combination of vancomycin + cold plasma treatment. Cold plasma is known to be microbicidal through generation of reactive oxygen and nitrogen species, ions, electrons, heat, and UV radiation. Initially, our rat model undergoes surgical hardware implantation and infection with *S. aureus* (MSSA 25923). A second revision surgery is performed one week later to replace infected hardware and administer treatment. At 4- or 14-days post-revision, tissues and hardware are collected for CFU counts, microCT scans, and histology. Bacterial colonization of hardware steadily increases after revision up to day 14 when untreated. Vancomycin or combination of vancomycin + cold plasma decreases hardware CFU at end term. Cortical bone volume is decreased by infection as measured by micro-CT. TRAP staining of osteoclasts shows increased numbers along the endosteum of the diaphysis in infected compared to uninfected rats. Osteoclast number and size are decreased with vancomycin + cold plasma treatment. Brown and Hopps staining shows bacterial presence in both bone and marrow with infection. The femoral bone appears ill-equipped to respond to *S. aureus* infiltration, as bacterial number increases drastically after revision surgery, with significantly more bacterial clumping and a higher overall infection score observed by day 4 and maintained at day 14. However, vancomycin + cold plasma significantly reduced bacteria numbers and infection score in the bone. While vancomycin treatment with and without cold plasma decreased hardware colonization, only vancomycin reduced osteolysis at day 14. Cold plasma, as an additional treatment with vancomycin, may not preserve bone, but may mitigate bacteria within the bone. Taken together, these findings show vancomycin treatment is effective at slowing osteolysis, but other treatments such as cold plasma could synergize to provide better clinical outcomes.

CD14 modulates age- and injury-induced subchondral bone remodeling in osteoarthritis (OA) via Type I Interferon

Lance A. Murphy[1,2], Kevin G. Burt[1,2], Kate L Sharp[2], Baofeng Hu[1,2], Vu Nguyen[1,2], Robert L. Mauck[1,2], Carla R. Scanzello[1,2]
[1]University of Pennsylvania, Perelman School of Medicine, Philadelphia, PA; [2]CMC VA Medical Center, Translational Musculoskeletal Research Center, Philadelphia, PA. **Disclosures:** LAM (N) - Lance.murphy@pennmedicine.upenn.edu, BH (N), KGB (N), MW (N), VN (N), RLM (5), CRS (8)

INTRODUCTION: While arthritis is generally considered a disease of the joint, its impact on bone is fundamental to disease progression. In erosive arthritis (e.g., rheumatoid arthritis), inflammation impacts endogenous bone cell (osteoblast and osteoclast) activity, resulting in excessive bone resorption (1). Conversely, in osteoarthritis (OA), aberrant bone remodeling results in subchondral sclerosis and osteophyte formation (2). Inflammatory cytokines drive bone erosion and can be targeted in inflammatory arthritis, yet the cellular mechanisms driving aberrant bone formation in OA are not fully established. Our group demonstrated that CD14-deficient mice show less subchondral bone remodeling after joint injury in a destabilization of the medical meniscus (DMM)-model of OA (3). CD14 is a Toll-like Receptor (TLR) activating co-receptor that is highly expressed in myeloid cells, including the precursors of osteoclasts (OCs) (4). Toll-like receptor 4 (TLR4) activation is inhibitory to osteoclastogenesis and can act through multiple pathways, including the sequestration of NF-κB as well as the production of Type I Interferons (IFN-I) (5). Osteoblasts (OBs), on the other hand, are not known to highly express CD14, but TLR4 signaling has been reported to both activate and inhibit their formation (6). To further define the role of CD14 on subchondral bone remodeling, we evaluated subchondral bone formation in CD14-deficient mice in the context of aging- and injury-induced OA models *in vivo*. Further, to understand the signaling that underlies differential OA bone remodeling between CD14-deficient and sufficient strains we assessed OB and OC number *in vivo* and evaluated the capacity for OC differentiation *in vitro*. ***We hypothesized that deficiency or blockade of CD14 would reduce subchondral bone remodeling in murine OA models and protect against TLR4-dependent inhibition of osteoclastogenesis through reduced IFN-I signaling.***

METHODS: Aging Study: WT and CD14-deficient mice were aged to 12 months. Destabilization of the medial meniscus (DMM) (n=14/group): DMM was performed on male C57BL/6 (WT) mice at 12-wks of age. As the DMM model is most consistent in male mice, only male mice were used. For CD14 inhibitor studies, mice were treated intra-articularly with a CD14 inhibitor (.5 mg/kg) or isotype control 3 times within the first 3 weeks post-surgery and sacrificed 12-wks post-surgery. In the CD14KO DMM study, WT and CD14-deficient mice underwent sham and DMM surgeries, and sacrificed 2-wks post-DMM. Micro-CT Imaging: Bone assessments were performed using micro-computed tomography (micro-CT; SkyScan 1174, Bruker). Scanning parameters included an x-ray tube voltage of 50 kV, current of 793 μA, and an exposure time of 1600 ms, with a slice thickness and isotropic voxel size of ~ 9μm. Histology (n=4-5 per group): Mid-joint cryo-sections were stained with ELF97 in acidic buffer to identify Tartrate Resistant Acid Phosphatase (TRAP)-positivity (indicative of OCs), or in basic conditions to identify alkaline phosphatase (ALP) activity (indicative of osteoblasts, OBs). Trabecular surface area covered by OCs or OBs in the medial tibial plateau was measured across five 40X fields per mouse and was normalized by total trabecular surface area (ImageJ). All sections were counterstained with ToPro3 (TP3). Cell isolation and culture: For *in vitro* studies, bone marrow (BM) was pooled from the femorae and tibiae of 3-5 mice from each strain (WT, CD14KO, and Type I interferon receptor (IFNAR1) KO). Cells were cultured in complete αMEM + 30 ng/mL M-CSF for 5 days to expand OC precursors, before exposure to RANKL (100 ng/mL) to induce osteoclastogenesis over 4 days. In some studies, either soluble recombinant CD14 (Abcam, 0.005-0.5 μg/mL) or an anti-IFNAR1 antibody (MAR1-5A3, 1 μg/mL) was added. OC quantification: Cells were stained for TRAP 3 or 4 days after the addition of RANKL and imaged (5 images/well, 4 wells/timepoint), and OCs identified as TRAP+ multinucleated cells. Percent area of the field covered by OCs was reported (CellProfiler). Bulk RNA sequencing: RNA was harvested from WT and CD14-deficient osteoclasts 4 days after the addition of RANKL. Hallmark pathway analysis was used. Statistics: Unpaired t-tests were used to test between groups, with a Holm-Sidak correction for multiple comparisons.

RESULTS: In the aging model, at 12-months of age, the subchondral bone of CD14-deficient mice exhibited decreased bone volume fraction (BVF; bone volume (BV)/total volume (TV)) and trabecular thickness compared to WT mice (**1A**). In the injury-induced DMM model at 12-wks there was increased BVF and bone mineral density (BMD) in the Isotype-treated WT DMM group compared to unoperated mice, which was mitigated by treatment with anti-CD14 antibody (**1B**). At 2-wks following DMM, CD14-deficient mice also demonstrated decreased BVF compared to their WT counterparts. While there was no difference in OB staining area between strains, CD14-deficient mice showed a 3-fold increase in OC area compared to WT (**1C**). *In vitro*, CD14-deficient precursors differentiated into OCs more rapidly than WT cells (**2A**). Treatment of CD14-deficient cells with rCD14 inhibited OC formation in a dose-dependent manner (**2B**). Pathway analysis of bulk RNA sequencing data revealed downregulation of IFN-I signaling in CD14-deficient OCs (**2C**). Notably, OC differentiation of precursors from IFNAR1KO occurred more rapidly than WT cells, phenocopying results from CD14-deficient mice (**2D**). Similarly, treatment of WT cells with an anti-IFNAR1 antibody increased the rate of OC formation, matching that of CD14-deficient cells (**2E**).

DISCUSSION: Using both aging- and injury-induced models of OA, we demonstrated that CD14-deficiency or blockade protects against aberrant bone remodeling. In vivo analysis of subchondral bone demonstrates increased OCs in the absence of CD14, and in vitro functional assays support that this is likely due to aberrant osteoclastogenesis. Mechanistically, CD14-deficient osteoclasts differentiated earlier, and both genetic and pharmacologic approaches indicate that this is due to decreased IFN-I signaling downstream of CD14/TLR activation. Targeting this pathway using an anti-CD14 antibody showed protection against aberrant bone remodeling for up to 12 weeks post-injury in WT mice. These data indicate that CD14 acts to modulate IFN-I signaling to regulate bone remodeling in the setting of joint injury and age. Future studies will validate the role of IFN-I signaling on OA-related bone remodeling *in vivo*. **SIGNIFICANCE/CLINICAL RELEVANCE:** The protection against subchondral bone thickening observed in CD14-deficient mice may be due to the increased presence of OCs. Understanding the role and specific mechanisms of CD14/TLR signaling in osteoclastogenesis may lead to new therapeutic strategies for diseases characterized by pathologic bone remodeling. Additionally, targeting downstream pathways of CD14/TLR signaling, including IFN-I, identify new druggable therapeutic targets that could be used to treat OA and other diseases of aberrant bone remodeling.

REFERENCES: [1] Niu+ *Front Immunol* 2022 [2]Donell+ *EFORT* 2019; [3] Sambamurthy+ *PLoS ONE 2018*; [4] Zanoni+ *Front Cell Infect. Microbiol.* 2013; [4] Xue+ *Art Res Ther* 2020; [5] Souza+ *Front Immunol* 2019 [6] Alonso-Perez+ *Sec. Integrative Physiology* 2018

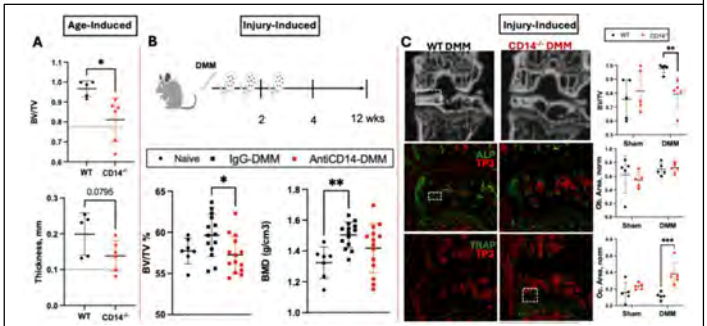

Figure 1: BVF and trabecular thickness of 12 month old (MO) WT and CD14$^{-/-}$ mice; dashed line denotes 4MO control (A). BVF and BMD of WT mice 16 weeks post-DMM following treatment with anti-CD14 antibody or isotype control (B). Images and quantification of BVF (box outlines region of interest), osteoblast area (box outlines area of positive ALP signal), and osteoclast area (box outlines area of positive TRAP signal) in WT and CD14$^{-/-}$ mice 2-wks post-DMM (C). *p<0.05, **p<0.01, ***p<0.005.

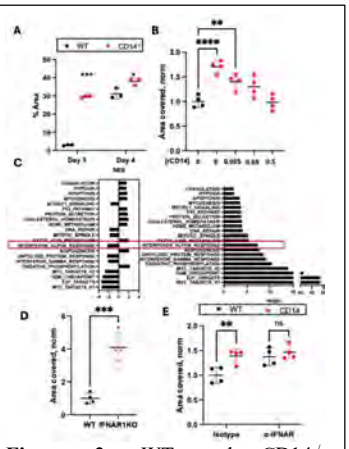

Figure 2: WT and CD14$^{-/-}$ osteoclastogenesis (OC-genesis) on days 3 and 4 post-RANKL addition (A). WT and CD14-deficient OC-genesis with rCD14 treatment for 3 days (B). Pathway analysis of DEGs for WT and CD14$^{-/-}$ OCs (C). OC-genesis of WT and IFNAR1$^{-/-}$ cells on day 3 (D). OC-genesis of WT and CD14$^{-/-}$ cells treated with anti-IFNAR1 antibody for 3 days (E).

Decellularized meniscal scaffolds combined with progenitor cells for temporomandibular joint repair

Authors: Hagar M. Kenawy, Hannah M. Bonelli, Yixiao Zhao, Sara Grasselli, Kyra W.Y. Smith, Jeffrey Chen, Dana Ragbirsingh, Eiman Abu Bandora, Cristina Barbella, Alexander Tucker, Eric Granquist, Riccardo Gottardi

Over 3 million children and young adults suffer from juvenile idiopathic arthritis, and up to 96% of this population will also experience temporomandibular joint (TMJ) osteoarthritis (OA)[1–6]. The hallmark of TMJOA is degeneration of condylar cartilage, but TMJOA often also presents with degradation of the subchondral mandibular bone[7]. Restorative therapies do not exist for TMJOA as treatments only focus on palliative care or on arthroplasties which do not accommodate pediatric patients' craniomaxillofacial growth[8]. Thus, there is a desperate need for regenerative TMJ therapies for both the condylar cartilage and bone[9].

Autogenous grafts are the go-to option for subchondral bone repair; however, this requires invasive surgeries and does not treat cartilage damage[10,11]. To engineer an approach for the repair of both cartilage and bone, our lab has developed a scaffold derived from porcine meniscal decellularization (MEND). Through selective removal of elastin, microchannels are formed that allow for uniform cell repopulation[12]. Using cell sources accessible by minimally invasive procedures [cartilage: human ear cartilage progenitor cells (CPCs) and bone: periosteal cells (PPCs)], our objectives are to confirm that MEND supports **1)** chondrogenesis **(Fig. 1A)** and **2)** osteogenesis (**Fig. 1D**).

Cartilage repair: CPC-MEND showed significant increases in glycosaminoglycan content post 21-days (d21) of chondrogenesis (**Fig. 1B**). For defect repair, the condylar cartilage area was punched and then filled by MEND, establishing a proof-of-concept repair for testing in subcutaneous implantation (**Fig. 1C**). *Bone repair:* After d21 of osteogenesis, PPC-MEND presented increased calcium and anionic deposits (not shown). One-way ANOVAs with Holm-Sidak *post-hoc* (N=3-4 donors) showed significant increases in gene expression for osteogenic genes *in vitro* for PPC-MEND at d21 compared to day 0 PPCs (p=0.001, **Fig. 1E**). After 4 weeks of subcutaneous implantation, microCT(N=4-5) showed 22% increased ossification compared to the implanted d21 control (**Fig. 1F**). Ongoing work focuses on implanting human TMJOA condyles subcutaneously in mice using CPC-MEND and PPC-MEND for mandibular cartilage and bone defect repair, respectively.

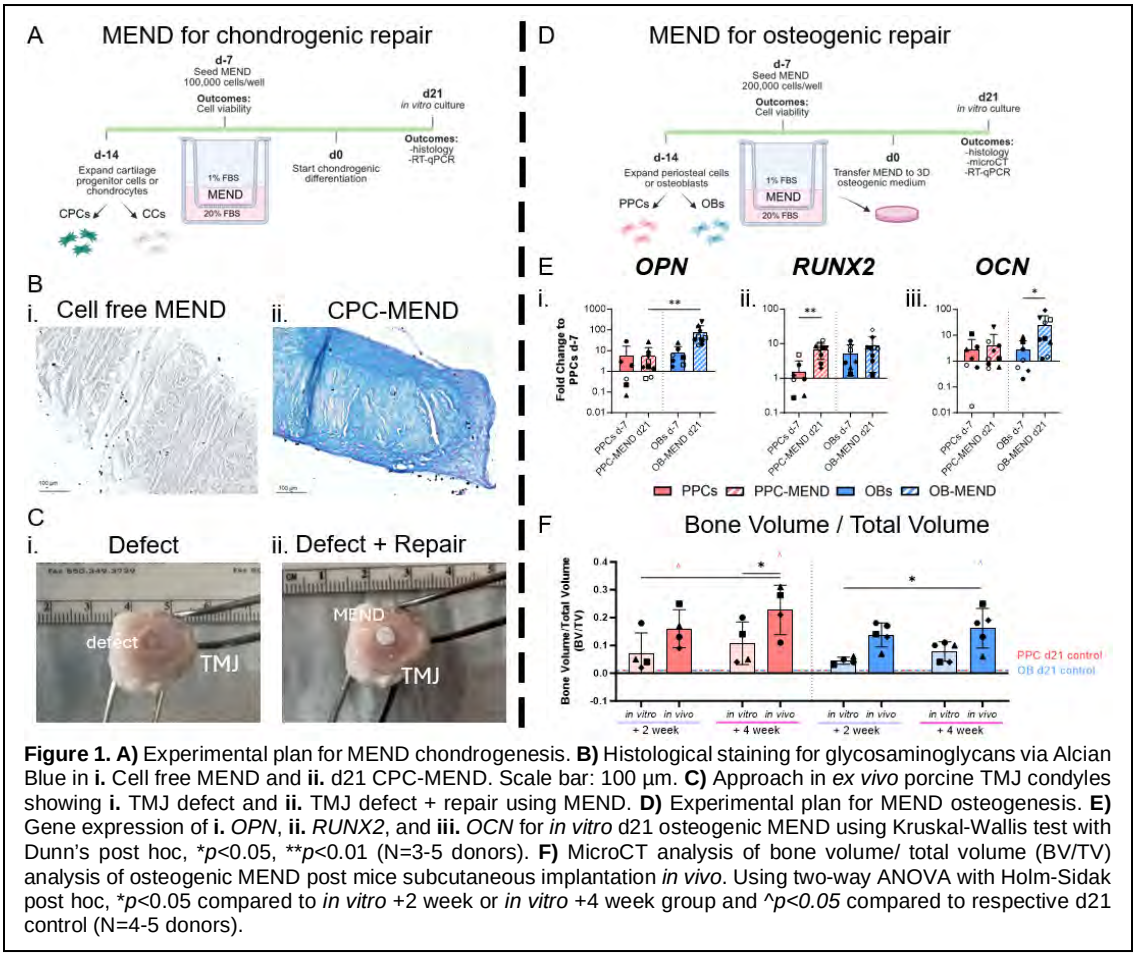

Figure 1. A) Experimental plan for MEND chondrogenesis. **B)** Histological staining for glycosaminoglycans via Alcian Blue in **i.** Cell free MEND and **ii.** d21 CPC-MEND. Scale bar: 100 µm. **C)** Approach in *ex vivo* porcine TMJ condyles showing **i.** TMJ defect and **ii.** TMJ defect + repair using MEND. **D)** Experimental plan for MEND osteogenesis. **E)** Gene expression of **i.** *OPN*, **ii.** *RUNX2*, and **iii.** *OCN* for *in vitro* d21 osteogenic MEND using Kruskal-Wallis test with Dunn's post hoc, *p<0.05, **p<0.01 (N=3-5 donors). **F)** MicroCT analysis of bone volume/ total volume (BV/TV) analysis of osteogenic MEND post mice subcutaneous implantation *in vivo*. Using two-way ANOVA with Holm-Sidak post hoc, *p<0.05 compared to *in vitro* +2 week or *in vitro* +4 week group and ^$p<0.05$ compared to respective d21 control (N=4-5 donors).

References [1] Dave+2020 [2] Zaripova+ 2021 [3] Stoll+ 2018 [4] Cannizzaro+ 2011 [5] Cedstromer+ 2014 [6] Stoll+ 2012 [7] Jiao+ 2011 [8] Lippincott+ 1998 [9] Wang+ 2023 [10] Melville+ 2023 [11] Knoedler+ 2023 [12] Gehret+ 2022

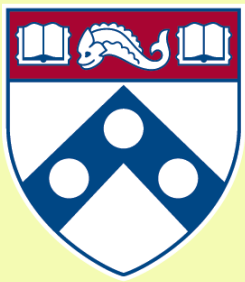

Penn Center *for*
Musculoskeletal Disorders
UNIVERSITY *of* PENNSYLVANIA

Other Research
(No P30 Core Use)
Abstracts

PM Session
Poster 56 to 76

Functional Asymmetries are Small and Varied in Achilles Tendinopathy: Implications for Clinical Assessment

Stanton Godshall[1], Devyn Russo[1], Andy K. Smith[2], Ryan T. Pohlig[2], Karin Grävare Silbernagel[2], Josh R. Baxter[1]
[1]University of Pennsylvania, Philadelphia, PA, [2]University of Delaware, Newark, DE
stanton.godshall@pennmedicine.upenn.edu

DISCLOSURES: Stanton Godshall (N), Devyn Russo (N), Andy K. Smith (N), Ryan T. Pohlig (N), Karin Grävare Silbernagel (N), Josh R. Baxter (N)

INTRODUCTION: The Achilles tendon is the strongest and largest tendon in the body and is responsible for transmitting forces up to 7.3 times bodyweight to facilitate locomotion [1,2]. Given this biomechanical role, injury to the Achilles tendon, like tendinopathy, is expected to impair plantar flexor function. Achilles tendinopathy is a painful and debilitating condition that is defined by localized pain and loss of function [3]. Several studies have shown that functional deficits, like strength and endurance, are present between limbs in Achilles tendinopathy patients [4,5]. Addressing functional deficits is often considered necessary for full recovery of tendon health. However, increasingly, studies show that between limb functional deficits are not as clear cut as originally understood. Several studies have found small or no differences between limbs in Achilles tendinopathy patients [6,7]. Thus, our objective was to assess functional asymmetries across a battery of functional tests to contribute to the ongoing study of between-limb functional deficits in Achilles tendinopathy. Our hypothesis was that patients would exhibit reduced performance across functional tests on their most symptomatic limb.

METHODS: We recruited 39 patients (20 female, age 47.7+\-11.4, BMI 28.6+\-6.1) to complete a functional test-battery in this IRB-approved study. Patients completed unilateral maximum voluntary contractions on an isokinetic dynamometer at three speeds (isometric, 30°/s, 150°/s) to capture a comprehensive range of ankle function. Additionally, clinically relevant task-based assessments were completed as patients did unilateral heel-rise and countermovement jump tests [4]. Patient surveys and ultrasound measurements were taken to contextualize functional asymmetries. We compared performance between the most and least symptomatic limb with paired t-tests when the underlying distribution was approximately normal, and used Wilcoxon ranked sign test elsewhere. Percent difference between limbs was calculated for each person to describe asymmetry patterns.

RESULTS: The most symptomatic limb showed statistically significant deficits in four out of five functional tests (**Figure 1**). Statistically significant between-limb differences include isometric torque (p=0.027), 30°/s isokinetic torque (p=0.002), 150°/s isokinetic torque (p=0.019), and calf raise fatigue work (p=0.032), with all tests having small-to-moderate effect sizes (0.342-0.523). The median between-limb percent difference ranged from -0.20% to 12.63% across the test battery (**Figure 2**). Notably, several patients exhibited asymmetries greater than 10% where the most symptomatic limb outperformed the least symptomatic limb: 9 during isometric testing, 5 during 30°/s isokinetic testing, 8 during 150°/s isokinetic testing, 7 during calf raise fatigue testing, and 3 during countermovement jump testing.

DISCUSSION: Our study partially confirmed the hypothesis that the most symptomatic limb would show reduced functional performance relative to the least symptomatic limb. Significant between-limb differences emerged in highly constrained plantar flexion torque tasks and calf raise fatigue tests. However, no group-level differences were found in countermovement jump performance, likely due to its multi-joint, skill-dependent nature. Effect sizes were modest, and individual variability was high. When we considered percent difference across tests, we found that several patients performed better on their most symptomatic limb, challenging the assumption that between-limb deficits are present in all individuals with Achilles tendinopathy. This may be due to subclinical bilateral symptoms, even when pain is unilateral. Exploratory analysis identified VISA-A score as the strongest predictor of asymmetry, while other factors like bilateral symptoms or tendon thickness asymmetry had minimal impact. A key limitation is the inclusion of patients with bilateral symptoms, which may reduce asymmetries. This was done to reflect real-world clinical populations. Additionally, patients who declined participation in certain tasks due to anticipated pain were excluded, likely biasing our results towards milder cases. Future research should test these associations in larger, more diverse cohorts and assess functional deficits relative to healthy controls.

SIGNIFICANCE/CLINICAL RELEVANCE: Despite widespread assumptions that tendinopathy decreases plantar flexor function, our findings show that functional asymmetries in Achilles tendinopathy are neither large nor consistent and often defy clinical expectations. Our results show that while group-level deficits exist, individual variability is substantial. Many patients perform equally well or better on their most symptomatic limb. These findings call into question the reliability of single-task assessments and supports the need for a battery of tests for evaluating tendon-related dysfunction. Our findings support clinical paradigms that carefully consider the initial functional deficits (or surpluses) of patients at their initial evaluations to design treatment plans aimed at addressing individual impairments along with promoting tendon recovery to restore pain-free function.

REFERENCES: [1] O'Brien+, *Foot Ank Clin*, 2005; [2] Baxter+, *Med Sci Sports Exerc,* 2021; [3] Scott+, *Brit J Sports Med.,* 2020; [4] Silbernagel+, *Knee Surg Sports Traumatol Arthrosc,* 2006; [5] Ohberg+, *Scand J Med Sci Sports,* 2019; [6] Hasani+, *Sports Med-Open,* 2021; [7] Sara+, *Exerc Sport Mov,* 2023

ACKNOWLEDGEMENTS: This research was supported by National Institutes of Health R01AR078898.

IMAGES AND TABLES:

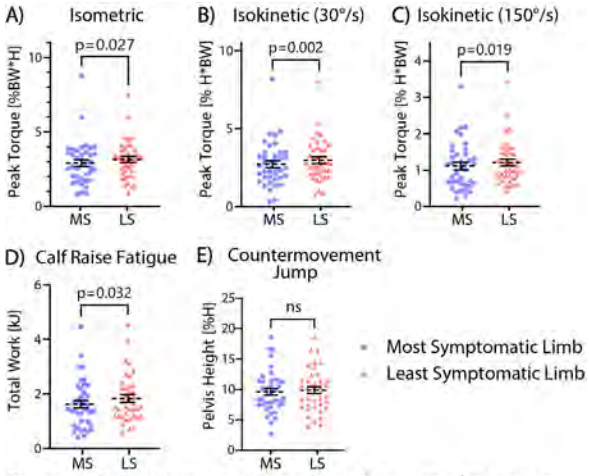

Figure 1. Paired comparison of performance between limbs across functional tests. Bars indicate mean±se

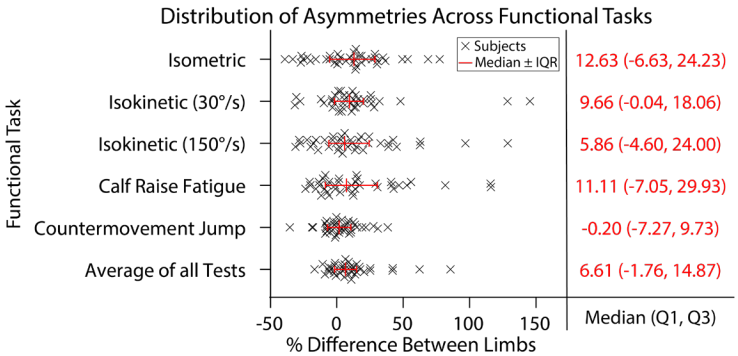

Figure 2. Distributions of asymmetries across functional tests. Percent differences below 0 indicate the most symptomatic limb outperforming the least symptomatic limb.

Sequential Macrolide Pretreatment Enhances Osteogenic Peptide-Induced BMP Signaling

Stacy A. Love[1,2], Myranda Sims[2], Matthias Recktenwald[2], Sebastián L. Vega[1,2]
[1]Department of Biomedical Engineering, Rowan University, Glassboro, NJ
[2]Department of Orthopaedic Surgery, Cooper Medical School of Rowan University, Camden, NJ

Introduction

Macrolide immunosuppressants FK506 (Tacrolimus) and Rapamycin (Sirolimus) bind FKBP12, an intracellular regulator that restrains bone morphogenetic protein (BMP) receptor activation. By sequestering FKBP12, both compounds sensitize BMP receptors to osteogenic ligands but also engage distinct secondary pathways. FK506 inhibits calcineurin, favoring SMAD-driven transcription, while Rapamycin inhibits mTORC1, enhancing ERK/AP-1-linked mechanotransductive signaling. Synthetic BMP-2 mimetic peptides, KIPKA (knuckle epitope) and DWIVA (wrist epitope) selectively activate these SMAD- and ERK- associated pathways, respectively. We hypothesized that macrolide pretreatment followed by peptide exposure would enhance BMP signaling compared to simultaneous dosing.

Methods

Pre-osteoblastic MC3T3-E1 cells expressing GFP reporters were used to quantify BMP signaling: BRE-GFP (SMAD-dependent) and SRE-GFP (ERK/AP-1-dependent). Serum-starved cells were exposed to osteogenic peptides, KIPKA (GCGGGKIPKASSVPTELSAISTLYLG) or DWIVA (GCGGGDWIVAG) (0.5-2 mM), after FK506 (5-25 μM) or Rapamycin (50-250 nM) pretreatment. GFP expression was measured by flow cytometry after 22-24 hours. Optimal concentrations (FK506 10 μM; Rapamycin 100 nM) were determined by dose-response profiling.

Results

Distinct pathway-specific selectivity was observed: KIPKA primarily activated BRE-GFP, while DWIVA activated SRE-GFP. Macrolide pretreatment enhanced these responses relative to peptide-only or simultaneous treatments. FK506 pretreatment increased KIPKA-induced BRE-GFP fluorescence, consistent with stronger SMAD signaling via calcineurin inhibition. Similarly, Rapamycin pretreatment before DWIVA exposure elevated SRE-GFP activity, reflecting potentiation of ERK/AP-1 signaling through mTORC1 inhibition. These findings demonstrate that timing-dependent FKBP12 modulation selectively enhances peptide-driven osteogenic signaling (US Provisional Application 63/866,043, 2025).

Conclusions

Sequential macrolide pretreatment strengthens osteogenic peptide signaling by first releasing FKBP12-mediated inhibition and then initiating more efficient receptor activation. FK506 preferentially augments KIPKA-SMAD signaling, whereas Rapamycin enhances DWIVA-ERK/AP-1 signaling, establishing pathway- and timing-specific mechanisms for macrolide potentiation. Ongoing work will extend these findings to 3D hydrogel systems and in vivo bone-repair models to optimize peptide-macrolide co-delivery for localized bone regeneration.

Engineered Peptide-Polyester Conjugates for Cell-Responsive Scaffold Degradation

Korina Vida G. Sinad[1], Natasha K. Hunt[2], Srujan Singh[4], Kelly B. Seims[2], Yingjie Wu[2], E. Thomas Pashuck[2], Warren L. Grayson[4], Lesley W. Chow[2,3]

Departments of [1]Chemistry, [2]Bioengineering, and [3]Materials Science & Engineering, Lehigh University, Bethlehem, PA, USA
[4]Department of Biomedical Engineering, Johns Hopkins University, Baltimore, MD, USA

Large bone defects caused by trauma, disease, or surgery remain a significant clinical challenge, with over two million bone grafting procedures performed worldwide each year.[1] While autologous bone grafts are the standard, donor shortages and complications underscore the need for engineered alternatives. Biodegradable polyesters like polycaprolactone (PCL) are promising scaffold materials due to their mechanical properties and ability to be 3D printed into patient-specific geometries. However, PCL exhibits a very slow degradation rate compared to new bone formation, which limits its effectiveness in supporting regeneration. In this study, a peptide–polyester conjugate platform was developed to create solid scaffolds that remodel in response to cellular activity. A functional proteomics approach was used to identify a protease-sensitive peptide sequence (Fast) that was degraded by multiple cell types present during bone regeneration.[2] We integrated the peptide into the PCL backbone to engineer scaffolds that are degraded by cell-secreted proteases. The Fast peptide and its scrambled control (ScrFast) were incorporated into PCL backbone to create linear, protease-sensitive peptide–PCL conjugates. The molecular design also included a fluorophore to quantify scaffold degradation and polyethylene glycol (PEG) spacers on either side of the peptide to enhance protease access. Fluorescence measurements were used to assess scaffold degradation in the presence of collagenase and human mesenchymal stromal cells (hMSCs). In both conditions, Fast-PCL scaffolds degraded significantly faster than ScrFast-PCL, demonstrating sequence-dependent and cell-mediated resorption. This study establishes a versatile framework for scaffolds that dynamically respond to cells, advancing new implantable materials designed for clinically relevant bone repair.

Reference:
[1] Laubach M, Whyte S, Chan HF, Frakenbach-Desor T, Mayer-Wagner S, Hildebrand F, Holzapfel BM, Kneser U, Delleck W, Hutmacher DW. *BMC Medicine*, **2024**, 22:517.
[2] Sinad KVG, Hunt NK, Singh S, Seims KB, Wu Y, Pashuck ET, Grayson WL, Chow LW. *bioRxiv* **2025**, DOI:10.06.680674.

Effect of prolonged NSAID exposure on osteocyte-like cell morphology

Lauren Caronia, Gavi Melman, Ryan E. Tomlinson

Department of Orthopaedic Surgery, Thomas Jefferson University, Philadelphia, PA 19107, USA

Introduction. Non-steroidal anti-inflammatory drugs (NSAIDs) are among the most used medications in the world. Though these medications can effectively provide short-term pain relief, the long-term effects of regular NSAID usage on bone are not well understood. Our laboratory has previously established that regular use of NSAIDs, particularly naproxen, impairs load-induced bone formation, diminishes stress fracture repair, and decreases bone toughness in mice. Similarly, we and others have found that regular NSAID usage is associated with increased stress fracture risk in humans. Of the commonly used NSAIDs, naproxen is non-selective and a widely used over-the-counter medication, while celecoxib is a selective COX-2 inhibitor and only available by prescription. We hypothesized that exposure to NSAIDs would significantly decrease osteocyte dendrite length within 10 days. This was based on findings from previous studies demonstrating naproxen use affecting the osteocyte dendritic network and perilacunar remodeling which has a role in bone toughness.

Methods. To examine this effect *in vitro*, murine osteocyte-like MLO-Y4 cells were cultured in naproxen or celecoxib and incubated for 10 days with concentrations ranging from 1 μM to 100 μM. Images were taken using an EVOS M5000 at multiple time points and analyzed using Simple Neuron Tracer to quantify dendrite length as a measure of cell morphology.

Results. Here, we observed cell dendrites significantly decreased in length for both the naproxen and celecoxib groups in a time- and dose-dependent fashion. The effect was more pronounced in the celecoxib group, suggesting that different NSAIDs have varying levels of effect on cell morphology. Furthermore, we observed an apparent increase in the thickness of the dendrites that is decreased after prolonged exposure to NSAIDs.

Discussion. In total, our results provide novel insight into the effect of NSAIDs on the osteocyte dendritic network. Specifically, we observed alterations to the osteocyte dendritic network after NSAID exposure that may decrease cell-cell communication and help explain previously observed decreases in bone toughness. Currently, the mechanism by which NSAIDs act on osteocyte dendrites is not yet fully understood. Future studies should focus on investigating this mechanism, both in vitro and in vivo. A potential limitation of this study is our inability to examine this effect over long periods of time that would resemble regular NSAID use in humans. Nonetheless, uncovering the mechanism by which NSAIDs affect osteocytes could lead to improved therapeutic strategies to relieve musculoskeletal pain without decreasing bone toughness.

Optogenetic Control of YAP/TAZ Nuclear Translocation for Mechanotransduction

Tianbai Wang[1,2], Erin E. Berlew[1,3], Paula Camacho Sierra[1], Ottman A. Tertuliano[2], Joel D. Boerckel[1,3]
Department of Orthopaedic Surgery[1], Department of Mechanical Engineering and Applied Mechanics[2], Department of Bioengineering[3]

Disclosures: All authors have no conflicts to disclose related to this research project.

Introduction: Cell migration is a fundamental process in morphogenesis, wound healing, and tissue regeneration. This dynamic behavior depends on the cytoskeleton and focal adhesions, which coordinate the mechanical forces necessary for movement. The assembly, reinforcement, and disassembly of these structures are mechanosensitive, responding to substrate stiffness and external mechanical cues [1]. The paralogous transcriptional coactivators Yes-associated protein (YAP) and transcriptional coactivator with PDZ-binding motif (TAZ) have emerged as central mechanotransducers that translate biophysical inputs into gene expression changes by their subcellular translocation from cytosol to nucleus [2]. We previously demonstrated that sustained gene expression is required for continuous cell migration and is maintained through a feedback loop mediated by YAP/TAZ signaling that could occur within 4 hours [3,4]. However, the kinetics of YAP/TAZ nuclear translocation and downstream transcriptional events remain elucidated.

Traditional approaches for studying YAP/TAZ signaling in migration, such as genetic or pharmacological perturbations, lack the spatiotemporal precision needed to resolve the dynamics of YAP/TAZ nuclear translocation and downstream signaling. Here, we have developed a novel two-component opto-YAP/TAZ toolbox that can release either YAP or TAZ from a membrane-tethered position via tobacco etch virus protease (TEVp) cleavage [5], for nuclear translocation in response to light exposure (Fig.1). We have developed two versions of these tools, one which features a nuclear localization sequence (NLS)-driven nuclear import and another which features wild type (WT) YAP or TAZ to preserve endogenous mechanoresponsivity upon light-mediated signaling activation.

Methods: Plasmid construction: The two-component opto-YAP/TAZ tools included a TEVp component and a membrane component containing YAP/TAZ. The TEVp component was composed of BcLOV4, mScarlet, and TEVp; membrane component was composed of LCK (membrane anchor), blue fluorescent protein (BFP), AsLOV2, TEV cleavage site (TEVcs), NLS (blank for the WT version), mNeonGreen (mNG), and YAP/TAZ. For optimization, variants of the membrane component with mutation on TEVcs (ENLYFQA/G) and AsLOV2 (original, hLOV [7], eLOV [7], and iLID [8]) were prepared. Cell transfection: HEK293T cells were plated in 35 mm cell culture dishes at ~15-20% confluency and cultured in high glucose DMEM with 10% FBS and 100 U/mL penicillin-streptomycin. Cells were co-transfected with both optogenetic components at ~30-40% confluency the next day using TransIT-293 transfection reagent (Mirus Bio). Optogenetic tool activation and imaging: Transfected cells were imaged through mCherry, GFP, and BFP channels (500 ms exposure) every 30 sec for 10 min (63× objective lens, Leica DMI6000B fluorescence microscope). Nuclei and cytosolic regions were segmented and mean fluorescence intensity was measured in CellProfiler, ratio between nuclear of cytosol (N/C ratio) fluorescence intensity was quantified.

Results: Upon light exposure, TEVp component containing BcLOV4 translocate to plasma membrane from cytosol (data not shown). For the NLS version of both opto-YAP and -TAZ tools, despite variants of TEVcs, strong nuclear signals were observed at dark state (Fig.2), indicating undesired leakage of the YAP/TAZ release in the absence of light activation. YAP/TAZ nuclear signals exhibited neglectable changes after 10 min of light exposure, likely due to the release of the majority of YAP/TAZ from the membrane component at dark. Wild type version of both opto-YAP and -TAZ showed no response to light activation. Next, using opto-YAP^{NLS} as a preliminary test, we observed significant enhancements in both leakiness and light responsiveness by replacing the original AsLOV2 with its mutated variants (Fig.3). We found that the membrane component with hLOV anchored to the plasma membrane at dark with nucleus empty of mNG tagged YAP, while substantial increase of YAP nuclear signal and decrease of membrane signal was observed after 10 min light activation. Similarly, the eLOV and iLID version of the membrane component exhibited mitigated leakiness at dark state. Quantified results demonstrated that the version with original AsLOV2 exhibited the highest N/C ratio at dark (2.6±1.5), in contrast, the other three mutated versions exhibited significantly lower N/C ratio (~1.0; $p<0.0005$). In addition, original AsLOV2 version exhibited moderate t1/t0 of N/C ratio (1.3±0.2), indicating limited light-induced YAP nuclear translocation. Alternatively, both hLOV and eLOV enabled significant enhancements in the t1/t0 of N/C ratio (1.8±0.3 and 1.7±0.4, respectively; $p<0.0005$). iLID version had similar t1/t0 N/C ratio level with the original AsLOV2 version. For the hLOV version, membrane-anchored YAP was released rapidly upon the first 30 sec of light exposure and continued within 10 min. Nucleus YAP did not increase until 1 min after light exposure and exhibited sustained increase over time. Cytosol nucleus remained a steady level within the first 5 min and dropped with the membrane levels after.

Discussions: This novel two-component optogenetic platform allows for precise spatiotemporal control of YAP/TAZ nuclear translocation. BcLOV4 moves to plasma membrane in response to light, bringing TEVp to the membrane component, where YAP/TAZ are anchored by the linkage of TEVcs. The proximity of TEVp induces enzymatic cleavage of TEVcs, leading to the release of YAP/TAZ. The undesired leakiness at dark state using the original AsLOV2 may result from the reduced stability of Jα helix of AsLOV2 by linking to the large mNG and YAP/TAZ molecules [9]. Therefore, we selected three mutated AsLOV2 with more stable structure and improved "gating" function at dark, efficiently prevented leakiness issue while maintaining light responsiveness. Among all three variants, we propose the hLOV is the best. For the wild type version, neither leakiness not light responsiveness was observed, which could be caused by the absence of NLS. The 22-residue NLS used in this study may also serve as a spacer between TEVcs and mNG, removing NLS may block the interaction between TEVp and TEVcs, disturbing the cleavage induced YAP/TAZ release. We are currently working on a WT version for opto-YAP/TAZ with a scrambled NLS as the spacer, we anticipate the outcome will be improved with the integration of hLOV. In the future, we are interested in measuring the kinetics of YAP/TAZ nuclear translocation for both NLS-driven and mechanosensitive WT versions in response to external mechanical stimuli, as well as the effects on the dynamics of cell motility machinery at a more accurate time-dependent manner.

REFERENCES: [1] Wu+ 2017 Biophys. J. 112:780-794. [2] Dupond+ 2011 Nature 474:179-183. [3] Mason+ 2019 J Cell Biol 218:1369-1389. [4] Mason+ 2023 eLife 12:RP86668. [5] Sanchez+ 2020 Nat Methods 17:167-174. [6] Kim+ 2017 eLife 6:e30233. [7] Wang+ 2017 Nat Biotechnol 35:864–871. [8] Guntas+ 2015 PNAS 112:112-117. [9] Strickland+ 2010 Nat Methods 7:623-626.

ACKNOWLEDGEMENTS: This work was supported by CPE4H, PCMD P30AR069619, R01GM143400.

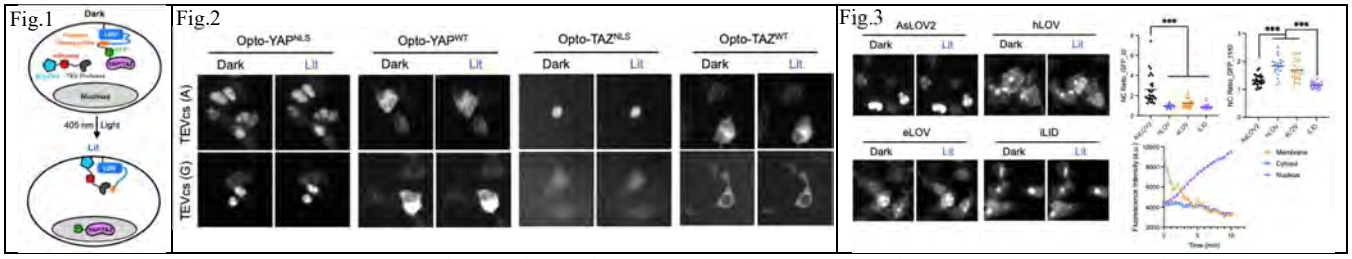

Fig.1: Schematic of the two-component opto-YAP/TAZ tools. YAP/TAZ are anchored on plasma membrane through TEV protease cleavage site (TEVcs), which is gated by AsLOV2 in dark. TEV protease is carried to membrane by BcLOV4 and cleave TEVcs that exposed during light exposure, leading to release and nuclear accumulation of YAP/TAZ. **Fig.2:** Localization of YAP/TAZ in the opto-YAP/TAZ$^{NLS/WT}$ tools with TEVcs variants (A or G) before (dark) and after (lit) 10 min light activation. **Fig.3:** Localization of YAP in the opto-YAP^{NLS} (TEVcs: G) tool with AsLOV2 variants (original, hLOV, eLOV, and iLID) before and after 10 min light activation. Nucleus/cytosol ratio of YAP was quantified for dark state (t0) and the ratio between lit and dark state (t1/t0). n=20 cells. *** $p<0.0005$. Dynamics of YAP translocation from membrane to nucleus of the hLOV version was quantified for 10 min light activation.

Controlling the Spatiotemporal Presentation of Growth Factor Mimetic Peptides in 3D-Printed Scaffolds for Osteochondral Tissue Engineering

F Gerardo Ortega Oviedo[1], Fenet Demissie[1], Alexis Kelerchian[1], Kelly B Seims[2], Lesley W Chow[1,2].
[1]Department of Bioengineering, [2]Department of Materials Science and Engineering, Lehigh University, Bethlehem, PA, USA.

Regenerating functional osteochondral (OC) tissue remains a significant challenge due to its poor intrinsic healing capacity and the complex biochemical and physical gradients that govern its function. During development, native osteochondral tissue formation is tightly regulated by the anisotropic and temporal presentation of growth factors (GFs), such as pro-chondrogenic transforming growth factor β1 (TGFβ-1) and pro-osteogenic bone morphogenetic protein 2 (BMP-2). Precise control of signaling presentation is necessary to successfully template the two distinct tissues (cartilage and bone) that form the integrated osteochondral structure. Biomaterials-based GF delivery strategies have shown great promise in OC tissue engineering, but conventional approaches often lack precise spatial and temporal control. Uncontrolled spatial presentation of these biochemical signals can lead to unwanted outcomes, such as hypertrophic phenotypes, low-quality tissue formation, and ectopic tissue growth. Additionally, the timing of GF delivery can influence stage-specific cellular differentiation. To address these challenges, our lab developed a 3D printing strategy with end-functionalized polycaprolactone (PCL) conjugates to control the spatial and temporal delivery of bioactive cues.

We hypothesized that controlling the spatiotemporal presentation of GF-mimetic peptides, such as restricting when and where they are delivered during culture, will mimic developmental processes to enhance stable tissue formation. We selected peptides derived from TGFβ-1 (CYGGGLIANAK; TGFβ1pep) and BMP-2 (CYGGGKIPKASSVPTELSAISTLYL; BMP2pep), which have been shown to promote cartilage and bone formation, respectively. These short, GF-derived sequences offer more stable, easier to synthesize, and cost-effective alternatives to the whole GF. Low molecular weight PCL (14 kDa) was modified to create conjugates bearing either the peptides or an azide group that enables selective attachment of dibenzocyclooctyne (DBCO)-modified peptides via click chemistry. Inks were formulated by codissolving a high molecular PCL (80 kDa) with different concentrations of the peptide-PCL or PCL-azide conjugates. The inks were 3D-printed into scaffolds and spatial control was demonstrated by printing with inks containing TGFβ1pep-PCL and BMP2pep-PCL in user-defined regions of the same scaffold. Fluorescent tagging of the peptides confirmed successful surface functionalization and spatial control over peptide localization within the scaffold.

Next, human mesenchymal stromal cells (hMSCs) were seeded into PCL and PCL-azide scaffolds to confirm GF-mimetic peptides can be delivered in the presence of cells. The media was supplemented with increasing concentrations of Cy3-labeled DBCO-TGFβ1 peptide ranging from 0.03 to 2.1 μM. We observed a gradual increase in fluorescence intensity over time in PCL-azide scaffolds, whereas PCL only scaffolds showed no sustained fluorescence. These results demonstrated our ability to dynamically and specifically modulate peptide presentation in the presence of cells.

Ongoing and future work focuses on investigating how the spatiotemporal presentation of BMP2pep and TGFβ1pep influences hMSC differentiation. Our versatile platform offers unprecedented spatiotemporal control over the delivery of multiple biochemical cues within a single scaffold, paving the way for dynamic and spatially organized approaches to drive osteochondral tissue regeneration.

Engineering a Drug-Peptide-Polymer for Localized Anti-Inflammatory, Chondrogenic, and Immunomodulatory Treatments for Osteoarthritis

Chiebuka Okpara[1], Zachary Weiser[1], Joshua Graham[1], Krishna Jayaram[1], E. Thomas Pashuck[1], Lesley Chow[1,2], Tomas Gonzalez-Fernandez[1].

[1]Department of Bioengineering, Lehigh University, Bethlehem, PA, USA and [2]Department of Materials Science and Engineering, Lehigh University, Bethlehem, PA, USA

Introduction: Osteoarthritis (OA) is a progressive musculoskeletal disease primarily characterized by inflammation-induced degeneration of the cartilage matrix, ultimately resulting in diarthrodial joint failure.[1] Mesenchymal stromal cells (MSCs) are promising candidates for cartilage regeneration in OA due to their multipotent differentiation potential and capacity to produce cartilage-specific matrix.[1] However, the chronic inflammatory microenvironment in OA impairs MSC differentiation and matrix deposition, hindering therapeutic efforts.[1] Corticosteroids such as dexamethasone (Dex) can reduce OA inflammation and pain, but long-term use leads to severe systemic side effects, undesired cartilage calcification, and chondrocyte apoptosis.[2] Moreover, Dex is rapidly cleared from the joint with an intra-articular half-life of less than 12 hours, underscoring the need for localized, inflammation-triggered delivery systems that minimize off-target effects.[2] To address this challenge, **our objective is to functionalize Dex to a 3D-printed poly(caprolactone) (PCL) scaffold using an inflammation-sensitive peptide linker and to validate whether the resulting Dex-peptide fragment preserves MSCs chondrogenic potential for OA cartilage repair, as a proof of concept for controlled release.**

Methods: *Peptide synthesis.* Dex was tethered to an inflammation-sensitive peptide[3] (Dex-peptide) using solid-phase peptide synthesis and purified via reversed-phase high-performance liquid chromatography. The synthesis was confirmed using matrix-assisted laser desorption/ionization time-of-flight (MALDI-ToF) and proton nuclear magnetic resonance spectroscopy (^{1}H NMR). *Peptide-PCL conjugation.* PCL diol and *p*-Maleimidophenyl isocyanate were dissolved in anhydrous 1-methyl-2-pyrrolidinone (NMP) and reacted overnight to synthesize PCL-maleimide.[4] Peptide-PCL conjugate was synthesized by reacting Dex-peptide with PCL-mal in anhydrous NMP overnight. The conjugates were confirmed with ^{1}H NMR and attenuated total reflectance Fourier transform infrared (ATR-FTIR). *3D printing and characterization*. Peptide-PCL conjugate inks were prepared by dissolving 370 mg/mL PCL and 40 mg/mL Dex-peptide-PCL conjugates in hexafluoroisopropanol and solvent-cast 3D-printed into scaffolds. 3D-printed scaffolds were imaged using scanning electron microscopy to characterize scaffold architecture. *In vitro cell culture*. A fragmented variant of the inflammation-sensitive peptide (Dex-pep fragment) was produced to assess whether the peptide coupling affected Dex activity. Dex-pep fragment was compared to free Dex under inflammatory, chondrogenic, and immunomodulatory conditions. MSCs were cultured in a 1:1 mixture of inflammatory macrophage-conditioned media[5] and chemically defined media to measure apoptosis. MSCs were seeded onto 3D-printed PCL scaffolds and cultured in chondrogenic media. Samples were harvested for biochemical analysis or fixed for histology to evaluate chondrogenic matrix deposition. Macrophages were polarized towards a pro- or anti-inflammatory phenotype to assess immunomodulatory effects with flow cytometry.

Results and Discussion: ^{1}H NMR and MALDI-ToF confirmed Dex was successfully modified to the inflammation-sensitive peptide. Dex-peptide was successfully conjugated to PCL-mal to produce Dex-peptide-PCL conjugates. ATR-FTIR spectra exhibited peaks for hydroxyl, alkyl, ester, and amide functional groups, confirming surface chemistry of the peptide-polymer conjugate. The peptide-PCL conjugates were incorporated into PCL inks and printed into scaffolds. No observable changes in scaffold architecture were noted between unmodified PCL and peptide-PCL scaffolds, confirming that the addition of the conjugates does not affect printing. Bioactivity testing of Dex-pep fragment revealed that 300 nM Dex-pep fragment reduced caspase-3/7 activity in MSCs exposed to inflammatory conditions, supported MSC chondrogenesis comparable to standard Dex treatment, and decreased both intra- and extracellular inflammatory macrophage markers. The 300 nM Dex-pep fragment demonstrated comparable efficacy to free Dex across multiple conditions and offers a promising strategy for dose optimization without relying on supraphysiological concentrations that can cause adverse effects. Future work will investigate Dex release profiles under inflammatory conditions, building on these results that demonstrate an inflammation-responsive platform capable of locally suppressing OA-associated inflammation while supporting MSC-mediated cartilage repair.

References: [1] Kennedy+ *Tissue Engineering: Part A*, 2024, [2] Madamsetty+ *ACS Biomater*. *Sci. Eng.*, 2022, [3] Sinad+ *bioRxiv*, 2025, [4] Camacho, *Biomater. Sci*., 2019, & [5] Witherel, *Biomaterials*, 2021

Nascent extracellular matrix converts biomaterial cues into cell fate decisions

J.Y. Liu[1,2], C. Loebel[1,2,3]
[1]Department of Bioengineering [2]Center for Precision Engineering for Health (CPE4H), University of Pennsylvania,
[3]Department of Materials Science & Engineering, University of Michigan

Statement of Purpose: Engineered hydrogels serve as well-defined niches for studying cell-matrix interactions. While chemical modification of polymer backbones provides a versatile strategy to tune hydrogel characteristics, how these modifications govern cell-hydrogel interactions remains unclear. An often-overlooked aspect is that cells actively remodel their environment through nascent extracellular matrix (nECM) deposition. Our previous work, along with others', has shown that mechanical confinement alters nECM deposition[1,2]; however, how the chemistry of the underlying hydrogel guides this process remains unknown. Importantly, we also aim to dissect how nECM functions within the cell-hydrogel system. To address this, we synthesized norbornene-modified hyaluronic acid (NorHA) polymers with varying degrees of modification to generate hydrogels with comparable mechanical properties, enabling systematic investigation of nECM formation, cell–nECM interactions, and the effects on cell fate.

Methods: Juvenile bovine chondrocytes (passage 1) were encapsulated in 5 kPa NorHA hydrogels with 'low' (~10%) or 'high' (~43%) modifications and cultured for 7 days in chondrogenic media supplemented with azidohomoalanine. nECM was labeled using dibenzocyclooctyne-amine-488, and mass spectrometry-based proteomics, followed by Gene Ontology (GO) enrichment using the full matrisome protein list as the reference background. Cell fate was assessed by SRY-box transcription factor 9 (Sox9) immunostaining. Early cell-hydrogel interactions were perturbed using a CD44 antibody, while cell-nECM interactions were perturbed using an integrin β1 antibody.

Results: Within 7 days, nECM formed a mesh-like structure, thicker in 'high' (2.49±1.13μm) versus 'low' hydrogels (1.51±0.63μm, Figure 1A). Compared to 'low' hydrogels, cells in 'high' hydrogels showed reduced Sox9 activity by nuclear localization (1.81 ± 0.40 vs. 1.57 ± 0.29 nuclear-to-cytoplasmic ratio, NC ratio, Figure 1B), indicating reduced chondrogenesis of chondrocytes.

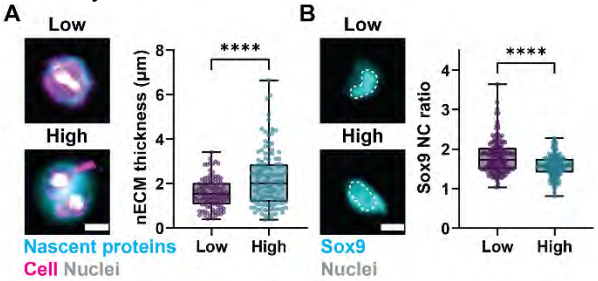

Figure 1. A. Representative nECM fluorescent images and thickness quantification. **B.** Representative Sox9 immunofluorescent images and NC ratio quantification. (**A-B:** Scale bar = 10 μm, n=100 cells.) ****p < 0.001

Proteomic matrisome analysis revealed distinct nECM profiles between 'low' and 'high' hydrogels, as shown by principal component analysis (Figure 2A). Among 182 identified matrisome proteins, 55 (30%) were differentially expressed (|fold change| > 2, *p-adjust* < 0.1) (Figure 2B). GO enrichment of these differentially expressed ECM proteins highlighted terms associated with cartilage and articular cartilage development (Figure 2C), suggesting that ECM composition correlates with cell fate regulation.

Blocking CD44-mediated early cell-hydrogel interactions reduced Sox9 nuclear localization in 'low' hydrogels (1.55 ± 0.29 N/C ratio) to levels seen in 'high' hydrogels but had no effect in 'high' gels (Figure 2D), indicating early hydrogel contact maintains chondrogenesis. Conversely, blocking ITGB1-mediated cell-nECM engagement decreased Sox9 nuclear localization in 'low' hydrogels (1.51 ± 0.38 N/C ratio) but rescued it in 'high' hydrogels (1.70 ± 0.35 N/C ratio, Figure 2E), revealing opposing, context-dependent roles of nECMs in cell fate.

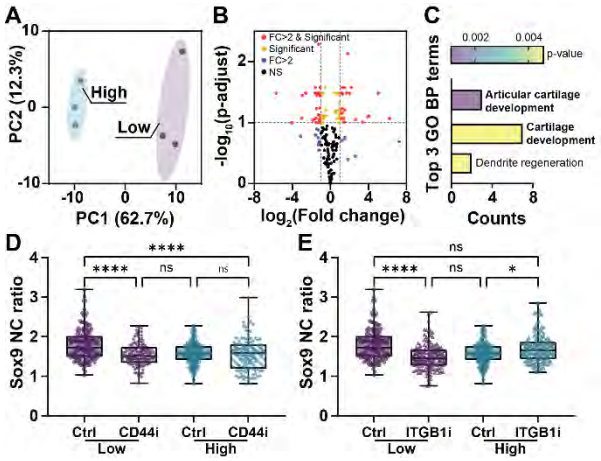

Figure 2. A. PCA of matrisome proteins deposited in low and high-modification hydrogels. **B.** Volcano plot showing differential expression of matrisome proteins. **C.** GO Biological Process (BP) enrichment of differentially expressed ECM proteins. **D-E.** Quantification of Sox9 NC ratio with CD44 (CD44i) or ITGB1 (ITGB1i) inhibition in low and high modification hydrogels. (A-C: n= 3 experiments, D-E: n=100 cells) **** p < 0.001, *p<0.05, ns=no significant

Conclusions: This work reveals a tri-directional relationship among hydrogel cues, nECM deposition, and cell fate, showing that polymer modifications alter nECM composition, which in turn influences cell fate (Figure 3). Ongoing work will evaluate this framework using varied cell types and hydrogel platforms.

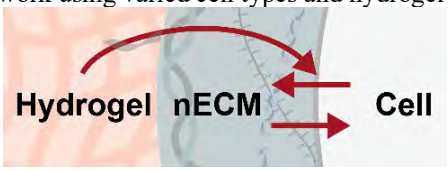

Figure 3. Schematic illustrating hydrogel–nECM–cell interactions identified in this study.

References:[1]C. Loebel + *Nat Mater.* 2019;18(8):883-891. [2]J. Cha+ *PNAS nexus* 3.9 (2024): pgae355.

Title: Muscle Repair and Immune-Regulating Proteins Show Sex-Specific Differences in an Aged Rat Model of Surgery-Induced Muscular Damage

Authors: Ayla G. Pearson*, Carly J. Smith*, Francis J. Ochman, Thomas P. Schaer, John C. Collins, Theresa A. Freeman
Dept. of Orthopaedic Research, Thomas Jefferson University, Philadelphia PA

Purpose:
Muscle injury is an often-overlooked consequence of many orthopedic procedures, particularly in older patients causing an increased risk of post-operative complications and delayed recovery. Furthermore, males and females display significant differences in immune modulation, including the acute inflammatory response, which plays a critical role in tissue repair and regeneration. To further understand how sex-specific differences in immune responses may impact muscle repair following surgery, we examined the differences in protein expression in muscle after injury associated with cartilage repair surgery with microfracture. Our studies were conducted on middle-aged rats, a clinically relevant model given that the majority of orthopedic surgery patients are middle-aged or older.

Methods:
Male (n=3) and female (n=3) middle-aged Brown Norway rats (18-month-old) underwent a femoropatellar arthrotomy of the right leg, receiving a full-thickness chondral defect to the medial condyle and microfracture 1 mm deep using a 25-gauge needle. 8 weeks post-surgery, rats were sacrificed and left and right quadricep muscles were harvested from all rats. Protein was extracted from muscles and was analyzed by mass spectrometry.

Results
Out of 584 proteins, 352 were significantly up- (180) or down- (172) regulated when comparing the female to male rat's response to surgical injury. The upregulated proteins were sorted into 2 main clusters using GSEA analysis of GO Biological Processes. Cluster 1 involved proteins associated with muscle function and cluster 2 containing proteins enriched in the adaptive immune response pathways and the innate activation, specifically the Type II antigen processing and presentation. Together this could indicate better muscle recovery and activation of adaptive immune response by females. Interestingly, immune related complement-activating proteins as well as blood coagulation, and wound healing responses were found to be downregulated in females compared to males. As this is a snapshot of a single timepoint after surgery and taking the presence of upregulated muscle function in females, this may indicate earlier resolution of innate immune responses and wound healing in response to surgery in aged female rats compared to males.

Conclusion
In a rat model of surgery-induced muscle damage in middle age, proteomic analysis revealed increases in proteins related to muscle function indicating enhanced repair and regeneration in females compared to males at 8 weeks following surgery. Limitations of this study are the small study size and single timepoint post-surgery. Studies like these are necessary to help highlight sexual dimorphisms in immune function which may significantly impact clinical outcomes. Understanding these differences can inform the development of new, immune-targeting therapies tailored for male and female patients following orthopedic surgery.

* These authors contributed equally to this work

RUNX2/RUNX3 have Critical Roles in Skeletogenesis, but are Not Required for Chondrocyte Hypertrophy

Halloran D, Feng X, Angelozzi M, Haseeb A, Voskamp C, Lefebvre V

Growth plates (GPs) are developmental templates for all endochondral bones. Their chondrocytes (GPCs) undergo a multi-step differentiation program that involves many types of regulatory factors, but our understanding of the activities of these factors remains incomplete. The current dogma, proposed two decades ago, is that the Runt-related transcription factors RUNX2 and RUNX3 are redundant master regulators of GPC maturation, i.e., prehypertrophic, hypertrophic and terminal osteoblast-like differentiation. Here, we decided to revisit this dogma, having found that *Runx2* and *Runx3* are co-expressed in GPCs only at the columnar proliferative stage. As previously shown for *Runx2/Runx3* global mutants, mice in which we inactivated *Runx2* and *Runx3* from an early limb bud skeletal progenitor stage, were born with much shorter legs than *Runx2* and *Runx3* single mutants. Their cartilage primordia only featured immature chondrocytes, whereas single mutants had formed GPs. While *Runx2/Runx3* global mutants died at birth, our mutants were viable. Chondrocytes in their cartilage primordia followed the same temporal and stepwise cell differentiation program as epiphyseal chondrocytes in control mice. They underwent hypertrophy en masse without ever proliferating in columns by postnatal day 14 and were replaced by a marrow cavity and poor-quality bone by day 21. They therefore lacked the typical pattern of limb long bones, in which a bone diaphysis is separated from epiphyses by growth plates. In another mouse model, we inactivated *Runx2* and *Runx3* in chondrocytes at day 21. This causes stunted mouse growth, as columnar GPC halted proliferation and became stuck at a hypertrophic stage. To decipher the molecular activities of RUNX2/RUNX3 in GPs, we performed single-cell profiling of transcriptomes in control and mutant GPCs. Our data reveal that RUNX2/RUNX3 control a wide spectrum of genes involved at different stages of GPC differentiation. In conclusion, our work challenges the current dogma on the roles of RUNX2/RUNX3 in GPCs. It provides novel evidence that the two factors play critical roles in columnar GPCs and are critically needed for timely rather than absolute GPC maturation. We anticipate that our work will help explain the molecular underpinnings of many forms of chondrodysplasias caused by variants in RUNX2, RUNX3 or genes controlled by these factors.

Developing an Inflammation-Responsive Drug Delivery System for Osteoarthritis

Juliana Magarelli[1], Chiebuka Okpara[1], E. Thomas Pashuck[1], Tomas Gonzalez-Fernandez[1], Lesley Chow[1,2]
Departments of [1]Bioengineering and [2]Materials Science and Engineering, Lehigh University

Background

Osteoarthritis (OA) affects over 32.5 million US adults and features progressive cartilage loss driven by chronic inflammation[3]. The inflammatory microenvironment accelerates cartilage degradation and undermines regenerative therapies, such as human mesenchymal stromal cell (hMSC)-based strategies. Anti-inflammatory drugs are highly effective, but frequent dosing increases risks of systemic side effects and further joint damage. Thus, there is a need for next-generation delivery platforms capable of responding to inflammatory cues to achieve controlled, localized release within the joint. This study aims to develop a biomaterials-based platform where drug release is triggered by inflammation.

Approach

We developed a scaffold platform with a fluorophore tethered to the surface via an inflammation-responsive degradable peptide linker as a model to quantify inflammation-triggered drug release[1]. This system will enable us to screen peptide sequences to fine-tune desired drug release kinetics. We designed 3D-printed poly(caprolactone) (PCL) scaffolds functionalized with an enzyme-sensitive peptide sequence (KRVKRRLMETGGGC, "Fast") to degrade under inflammatory conditions[2]. A scrambled version of this peptide (LTRLMEKRRKVGGGC, “ScrFast”) was used as a control to validate sequence specificity. Cy3 fluorophore was coupled to the peptides to quantify release kinetics and evaluate how cellular attachment or matrix accumulation affects therapeutic release profiles. Understanding how cell-material interactions and matrix deposition affect release is essential for predicting scaffold performance *in vivo* where tissue integration may alter local protease activity and degradation kinetics.

Methods

Peptide Synthesis: Fast and ScrFast peptides were synthesized via solid phase peptide synthesis and purified with reversed phase high-performance liquid chromatography (HPLC). Peptide masses were verified using matrix-assisted laser desorption ionization (MALDI). *Conjugate Synthesis:* PCL diol was modified with *p*-maleimidophenyl isocyanate (PMPI) in anhydrous 1-methyl-2-pyrrolidone (NMP) and reacted overnight to synthesize PCL-maleimide. Cy3-Fast-PCL and Cy3-ScrFast-PCL conjugates were created by reacting each peptide with PCL-mal in anhydrous NMP overnight. Each step was confirmed by proton nuclear magnetic resonance (^{1}H NMR). *Scaffold printing:* Peptide-PCL conjugate inks were prepared by dissolving 370 mg/mL unmodified PCL (80:25 kDa at an 80:20 ratio by weight) and 30 mg/mL Cy3-peptide-PCL conjugate in hexafluoroisopropanol (HFIP) on a shaker for 48 hours. Inks were rested for 24 hours before solvent-cast 3D printing using a 32-gauge needle to form 14-layer scaffolds (10 mm × 10 mm). Samples were prepared using a 3-mm diameter biopsy punch. *Cy3 release:* Scaffold tested included 3 groups: (1) Cy3-Fast-PCL, (2) Cy3-ScrFast-PCL, and (3) PCL with physioabsorbed Cy3. All groups were loaded with 8 nmol Cy3. hMSCs (200,000 cells/sample) were seeded onto scaffolds and incubated in Dulbecco's Modified Eagle Medium supplemented with Fetal Bovine Serum and Penicillin/Strepomicin (XPAN). Acellular scaffolds were incubated in XPAN, hMSC-conditioned XPAN, 2mg/ml collagenase in zymography buffer, or inflammatory macrophage-conditioned medium. Media was collected on Days 1, 3, 6, 9, 12, and 15. Cy3 fluorescence (λ_{ex} = 530 nm, λ_{em} = 570 nm) of the collection media was measured to quantify cumulative release.

Results and Discussion

Peptide masses were confirmed with MALDI. Successful conjugate synthesis was confirmed by ^{1}H NMR. After 15 days of incubation, Cy3 release was measured at low levels across all media types for Cy3-Fast-PCL and Cy3-ScrFast-PCL scaffolds, while Cy3 was released immediately from PCL scaffolds with physioabsorbed Cy3. These data demonstrated that the peptides successfully tethered Cy3 to the scaffold surface. However, the limited release suggested that the peptide was not accessible to the proteases present in the conditioned media or collagenase solution. Future work involves redesigning the conjugate by integrating a polyethylene glycol (PEG) spacer to increase protease accessibility. **References:** [1] Tolbert+ J. Biomed. Mater. Res., 2024 [2] Sinad+ bioRxiv, 2025 [3] Osteoarthritis Action Alliance+ UNC Report, 2024 [4] Camacho+ Tissue Eng. Part A, 2023

Cellular Uptake and Nuclear Localization of Biomimetic Proteoglycans

Annika R. Bergstrom[1], Anita Li[1], Sabrina Palumbo[1], Efthimia Rukis[1], Lin Han[2], Michele S. Marcolongo[1]
[1]Villanova University, Villanova PA; [2]Drexel University, Philadelphia, PA

Introduction: In early osteoarthritis (OA), stressors such as mechanical loading, inflammation, and oxidative stress disrupt chondrocyte homeostasis, leading to organelle dysfunction and catabolic activity that degrades the extracellular matrix (ECM), beginning with the microniche of the cell, the pericellular matrix (PCM). Our laboratory can molecularly engineer and modulate the biochemical properties of the PCM and territorial-ECM (T-ECM) using our suite of synthesized biomaterials: biomimetic proteoglycans (BPGs). BPGs, composed of natural chondroitin sulfate bristles (CS) and a poly(acrylic acid) (PAA) backbone, mimic the nano-architecture and water uptake of native proteoglycans [1]. Our most widely used BPG, BPG10, a ~250 kDa mimic with ~7-8 CS bristles attached onto a 10 kDa PAA core (Fig.1a), has been shown to passively diffuse through cartilage zones *in vivo* and *ex vivo,* with preferential localization to the PCM and T-ECM. Previous non-viable tissue studies also suggested potential cellular uptake of BPGs. Thus, we sought to determine (1) if BPGs can be cellularly uptaken in viable cells and, if so, (2) what organelle BPGs localize within at different dosage concentrations. This study will inform our understanding of the mechanism of action and implementation of BPGs for targeted repair of OA.

Methods: BPGs were synthesized and fluorescently labeled with Cy5.5. Human chondrocytes (C28/I2) were cultured and seeded in glass petri dishes (confocal microscopy) and 96-well plates (imaging flow cytometry, IFC). Cells were treated with BPG-Cy5.5 (0.025, 2.5, 5.0, and 10.0 mg/mL) or controls (untreated, Cy5.5 alone, and known positive 1 µm PLGA) for 24 h (confocal imaging) or 48/72 h (IFC, n=9/treatment, with n=3 biological replicates/treatment). Following treatment, cells were washed twice with PBS to remove any remaining BPGs and stained for viability (Calcein AM/ethidium homodimer) and nuclei (NucBlue, DAPI). 2D and 3D images were taken at 20, 40, and 63x magnification. IFC samples collected ≥15,000 events per well and analyzed in FlowJo by gating on untreated live cells in combination with the BD CellView Lens plugin. Percent parent (BPG10 + nuclei positive cells) and images were used to confirm nuclear overlap. Statistical analysis was performed via one-way ANOVA with Dunnett's post hoc test ($\alpha = 0.05$).

Results: Confocal imaging confirmed cellular uptake (Fig. 1a) and localization within the nucleus following 24 h (Fig. 1b) at all dosage concentrations, indicating all dosages are capable of cellular entry. Z-stack imaging confirmed BPGs were retained within cellular boundaries. Flow cytometry showed significant overlap between percent BPG-Cy5.5 and nuclei at 2.5, 5.0, and 10 mg/mL after 48 and 72 h compared to untreated controls (Fig. 1c-d), with mean (± 95% confidence intervals) uptake of

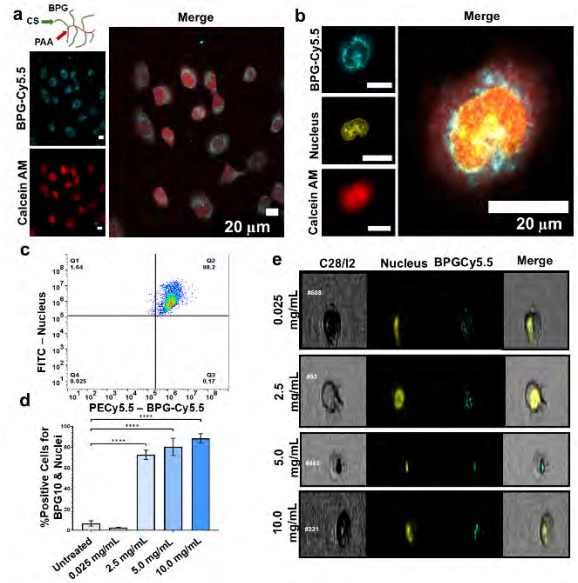

Figure 1. Uptake and nuclear localization of BPG10. a) BPG10 within cellular bounds 24 h post-treatment. **b)** Nuclear overlap with BPG10 at 24 h. **c)** Flow cytometry analysis of BPG10 and nuclei positive cells. **d)** Percent positive cells for BPG10 nuclear overlap at 48 h. **e)** Imaging flow cytometry of singlet cells for nuclear overlap with BPG10.

73% ± 19%, 80% ± 36%, and 89% ± 19% at 48 h, respectively. The 0.025 mg/mL group was not significantly different from untreated control samples (Fig. 1d), however, BPG10 was qualitatively observed within the bounds of chondrocytes imaged under IFC (Fig. 1e), suggesting entry with minimal nuclear saturation at the smallest concentration.

Conclusions: This study demonstrates that BPGs not only preferentially localize in the PCM but enter and localize within the nuclei of chondrocytes (Fig. 1a-e). Importantly, BPGs are retained within the nucleus and cellular boundaries for at least 72 h following BPG application. Singlet cell images from IFC (Fig. 1e) and mean fluorescence intensity values reveal BPGs enter chondrocytes. This suggests ≥ 2.5 mg/mL has the greatest chance of saturating the nucleus, thereby providing a novel and unexpected application of BPGs for direct cellular delivery. These results demonstrate a clear dose-dependent increase in BPG uptake by chondrocytes. Taken together, these findings point to a novel use of BPGs as an intracellular vehicle for targeted repair of damaged tissue that will subsequently inform our understanding of the mechanism of action of BPGs and redefine their relevance for targeted OA treatments.

References: [1] Prudnikova K. Acta Biomaterialia. 2018;75:93-104

Virtual Reality: The New Frontier of Orthopaedic Medical Student Education

Isaacs D, Croen BJ, Blaeser A, Cardwell M, Bernstein E, DePietro D, Cipriano C, Abramoff B

Objective: To assess the effectiveness of a virtual reality surgical simulation of total hip arthroplasties (THA) on first year medical students' self-perception of knowledge and orthopaedic interest.

Methods: First year medical students completed a two-hour virtual reality simulation session using VH Dissector Pro 6, Toltech software reviewing hip anatomy, and practicing a posterior and anterior approach to a THA. A pre and post-survey using Likert scales (1-5) was administered. Paired t-tests were performed to compare pre and post session responses and descriptive statistics were used for the rest of questions.

Results: Twenty-five students completed the simulation; 20 students completed both the pre and post-session survey, 24 completed just the pre-session survey, and 21 completed just the post session survey. Comparing pre and post-session surveys, participants endorsed increased comfort with anatomical direction terms (3.10 to 4.25; $p<0.001$), listing the major hip muscles (1.20 vs 3.15; $p<0.001$), identifying major hip muscles on a cadaver (1.15 vs 2.80; $p<0.001$) and explaining movements of each muscle (1.35 vs 3.35; $p<0.001$). In the post session survey, 85% of participants indicated increased interest in orthopaedics as a result of the session (average Likert 4.10 +/- 0.64), 76.19% indicated increased excitement about anatomy (4.14 +/- 1.01), and 76.19% wanted to continue to use VR for anatomy education (3.67 +/- 1.32).

Conclusions: Our study demonstrated that virtual reality simulation increased self-reported orthopaedic knowledge and was an engaging tool for medical student education. Participants indicated increased career interest in orthopaedics, suggesting VR technology can be a useful tool for early medical student exposure and engagement with the field of orthopaedics.

Genomic Occupancy Profiling of RUNX2 and RUNX3 in Growth Plate Chondrocytes Deepens Molecular Understanding of Skeletal Development

Authors: Xiaotian Feng, Daniel Halloran, Abdul Haseeb, Chantal Voskamp, and Véronique Lefebvre
Institution: Division of Orthopaedic Surgery, Children's Hospital of Philadelphia, PA

Abstract:

Transcriptional regulation is essential in governing the multi-step differentiation program of chondrocytes in the growth plate (GP), a cartilage structure that ensures the longitudinal growth of skeletal primordia and their subsequent endochondral ossification during fetal and postnatal development. Among key transcription factors, the RUNT family RUNX2 and RUNX3 proteins were previously shown to act redundantly to allow growth plate chondrocytes to mature into prehypertrophic, hypertrophic and then terminal osteoblast-like cells. Revisiting this dogma, we recently showed that the two genes are co-expressed only in proliferating columnar chondrocytes, thus prior to prehypertrophy, and act redundantly to allow immature chondrocytes to proceed through all steps of the growth plate chondrocyte differentiation program in a spatially and temporally controlled manner. To determine how RUNX2/RUNX3 control this process, we performed integrative genomic occupancy analysis for both proteins in a rat chondrosarcoma cell line (RCS) that exhibits a faithful phenotype of columnar and early pre-hypertrophic chondrocytes and in mouse GP primary chondrocytes. Consistent with their redundant actions in GP chondrocytes, we found that RUNX2 and RUNX3 exhibit substantial occupancy overlap across the genome and that their target genes are mainly related to molecular pathways involved in cartilage development and endochondral ossification. The RUNX2/RUNX3-bound regions mapped to both promoter and enhancer regions. They were enriched in both RUNT and SOX9 consensus binding sites, suggesting direct binding of RUNX2, RUNX3 and SOX9 to many of these sequences and functional interaction between the RUNT and SOX proteins. Reporter assays functionally validated the notion that RUNX2/RUNX3 and SOX9 can increase the activity of some enhancers synergistically and may thus act cooperatively to regulate specific events in growth plate development. In conclusion, our study deepens our understanding of the transcriptional regulation of growth plate development. They may thereby provide insights into mechanisms underlying skeletal disorders and suggest novel therapeutic strategies.

Investigating the Role of Environment Dimensionality on Cell Shape and Piezo1 Activation

Alexander Bolanos-Campos[1], Mistica Lozano Perez[1], Ottman Tertuliano[2]
[1] University of Pennsylvania, Bioengineering
[2] University of Pennsylvania, Mechanical Engineering and Applied Mechanics

Piezo1 is a mechanosensitive, transmembrane protein ion channel that transduces mechanical stimuli, such as substrate rigidity, surface roughness, and contractile forces, the cell experiences and generates into signal pathways. When the plasma membrane deforms, piezo1 transitions from a closed to open state, allowing cations, like Ca2+, to flow into the cell to be used in different signaling pathways. Previous studies have shown how piezo1 affects cell shape, proliferation, contractile forces, stemness, and differentiation potential like osteogenesis. However, most of these studies were primarily conducted in soft hydrogel systems that limit our understanding of how piezo1 affects cell processes within stiff 3D environments such as bone. Our aim is to investigate how cells cultured within well-defined nanoarchitectures of varying stiffnesses affect cell morphology and piezo1 activation of human bone-marrow derived mesenchymal stem cells (hBM-MSCs) in comparison to 2D environments.

We utilized two-photon polymerization to fabricate 2.5D and 3D architectures of varying stiffnesses within the hard and soft regime. After fabrication, scanning electron microscopy was utilized to image the structures prior to cell culture. hBM-MSCs were cultured on the architectures due to their sensitivity to mechanical cues. After culture, samples were fixed and stained for piezo1 and cytoskeleton components to determine the effect these different environments had on piezo1 presence and cell morphology. We observe that as dimensionality and stiffness increased, cell morphology increased for individual cells with strong piezo1 signal distributed throughout the cell body. Additionally, 2D topological features localized piezo1 signal while 3D topological features increased cell number throughout the architectures. These observations provide the motivation to investigate the contractile forces cells generate within the architectures and how it impacts the surrounding 3D environment.

Effectiveness of Glue Mesh Fixation Versus Tacker Mesh Fixation in Reducing Hernia Recurrence and Postoperative Pain Following the TEP Laparoscopic Approach for Inguinal Hernia Repair: Systematic Review and Meta-Analysis

Al Taie Faisal, OMS II; Thellapally Saikumar, OMS II; Rahmani Abdul, OMS II; Shah Umer, OMS II; Kazi Farhan

Introduction:
Inguinal hernia repair using the totally extraperitoneal (TEP) laparoscopic technique typically employs mesh fixation via staples or tackers. Concerns about chronic postoperative pain have created interest in tissue adhesives (glue) as an alternative. This study seeks to compare glue versus tacker mesh fixation in adult male patients undergoing TEP, focusing on postoperative pain, chronic pain (≥3 months), hernia recurrence, and infection rates.

Methods:
A systematic review of randomized controlled trials was conducted using PubMed, Embase, Cochrane Library, and Publish or Perish up to August 2025. Included trials enrolled adult male patients (age ≥18) undergoing TEP hernia repair and directly compared glue fixation to tacker or staple fixation. Studies reporting postoperative pain using standardized numeric scales were included. Random-effects pooled mean differences (MD) were calculated for early postoperative pain (postoperative day 1), intermediate pain (~1 month), and chronic pain (~3 months). Data extraction and risk-of-bias assessment were performed. Meta-analyses used random-effects models for outcomes with at least two homogeneous studies.

Results:
Seven randomized controlled trials met the inclusion criteria with a total of 1,060 participants, with 998 completing the follow-up. For early postoperative day 1, four studies (total n = 832; glue group = 177, tacker group = 655), reported mean pain scores of approximately 2.9 for glue fixation versus 4.0 for tacker fixation. Pooled effect results also favored glue (MD = −1.09, 95% CI −2.25 to 0.06; p = 0.06), demonstrating a clinically meaningful reduction in pain scores, but no statistical significance. Postoperative pain at 1 month, three studies (total n = 220; glue group = 110, tacker group = 110), also favored glue over tackers (MD = −2.10, 95% CI −4.57 to 0.37; p = 0.09). For chronic pain at ≥3 months, four studies (total n = 326; glue group = 161, tacker group =165) reported mean pain scores of 1.07 in the glue group versus 2.40 in the tacker group. Pooled results favored glue fixation (MD = −1.32, 95% CI −3.03 to 0.38; p = 0.26) again without achieving statistical significance. Recurrence and infection data were sparse and showed no major differences between fixation methods.

Discussion and Conclusion:
Glue mesh fixation in TEP hernia repair shows a consistent trend toward lower early and chronic pain compared to traditional tacker fixation, without an evident increase in hernia recurrence or infection. However, the evidence is not conclusive. Further high-quality randomized trials with standardized outcomes reported are needed to confirm whether glue fixation should become standard practice in this setting.

Demystifying Nerve Conduction Studies: An Automated Approach to an Arduous Assessment

Maggie M. Wagner[1*], Flavia Vitale[1], and Josh R. Baxter[2]
[1]Department of Bioengineering, University of Pennsylvania, Philadelphia, PA, US
[2]Department of Orthopaedic Surgery, University of Pennsylvania, PA, US
*Email: magwag@seas.upenn.edu

Introduction: Nerve conduction studies (NCS) provide lucrative insight into neuromuscular health but are critically underutilized in clinical settings. The procedure has demonstrated promise as a diagnostic for various neurological injuries or disorders, including polyneuropathy, radiculopathy, and spasticity. During NCS, by electrically stimulating a mixed peripheral nerve, clinicians and researchers elicit direct and reflexive responses from the innervated muscle, named the compound muscle action potential (M-Wave) and the Hoffmann reflex (H-reflex), respectively. The M-wave quantifies direct muscle activation through its maximum amplitude (M-max). On the other hand, the H-reflex is analogous to a spinal reflex test and, similarly, its maximum amplitude (H-max) approximates motoneuron excitability. H-reflex latency, measured as the elapsed time between stimulus delivery and the onset of the reflex, serves as the primary diagnostic measure, with irregular latencies denoting degeneration or injury to neural pathways. Despite its utility, the procedure is still relatively obscure, likely due to its difficulty and methodological variations. For example, depending on factors like posture and attention, the H-reflex experiences inhibition or sometimes complete suppression. Further, the stimulation parameters leveraged in NCS vary widely, with some parameters favoring the H-reflex over the M-wave and vice versa. To address these challenges, other groups have proposed controlled procedures for NCS, producing significantly more reliable evaluations [1]. However, NCS persists as a complicated and challenging procedure, requiring expert-level training for proper execution. Consequently, in this work, we aimed to introduce a new approach to NCS, which automates, simplifies, and expedites the procedure.

Methods: We have developed an automated nerve conduction study (ANCS) platform to conduct and simplify NCS. Through an extensive literature review, we have simplified NCS to three fundamental phases (**Figure 1**): 1) determining the optimal stimulation location, 2) determining H-max, and 3) determining M-max. The ANCS platform consists of a stimulator switchbox, dense stimulation electrode patch, programmable electrical stimulator, and user-friendly interface. Phase 1. We designed the dense stimulation patch and stimulator switchbox to address stimulator placement challenges. Conventionally, clinicians determine the optimal stimulation location through trial-and-error, which is time-consuming. Using the dense stimulation grid, the ANCS covers and evaluates the surface area proximal to the targeted nerve. To accomplish this, the stimulator switchbox cycles through each pair of stimulation electrodes, prescribing and delivering targeted stimulations. Following response analysis, the ANCS program selects the optimal stimulation electrode pair and uses it throughout Phases 2 and 3. Phase 2. The ANCS platform evokes and analyzes H-reflexes using varying stimulation intensities, identifying the largest peak-to-peak H-reflex amplitude and collecting three repetitions to calculate H-max. The program identifies the onset of the H-reflex and calculates its latency from these repeated stimulations. By inputting select electrode distances, the ANCS program also approximates inter-electrode distances and calculates the nerve conduction velocity, supporting diagnostic techniques requiring the metric. Phase 3. The ANCS platform applies increasing stimulus intensities to capture M-max, collecting three repetitions for repeatability.

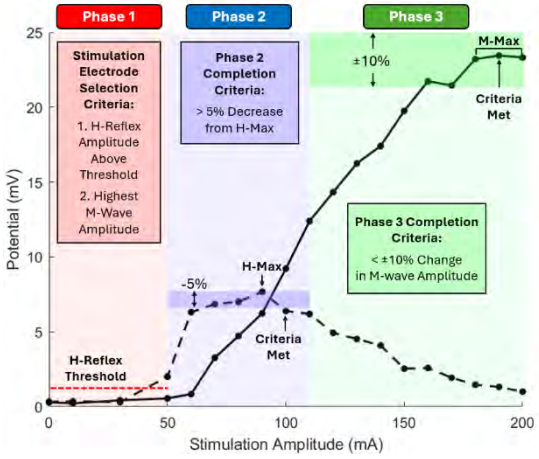

Figure 1. The three phases of the automated nerve conduction study platform superimposed over a sample H-reflex and M-wave recruitment curve.

In our preliminary evaluations of ANCS, we leveraged our flexible and customizable high-density surface electromyography (HDsEMG) grids composed of a carbon-based nanomaterial, $Ti_3C_2T_x$ MXene, to record the evoked responses; however, the system is compatible with other electrode types, including traditional metal and hydrogel electrodes. We placed HDsEMG grids bilaterally to the plantar flexor muscles, with 64 electrodes on each leg. The grids interfaced via a custom PCB to a wireless electrophysiology processor (Ripple Neuromed, Explorer Summit), which records HDsEMG at 7.5 kHz. After administering a stimulation, the ANCS program extracts the subsequent 100-ms of HDsEMG data, applies a 20-450 Hz 2nd order Butterworth bandpass filter, and separates the data streams based on known M-wave and H-reflex latency ranges for analysis [2]. Throughout ANCS execution, the program analyzes the evoked responses to prescribe the following stimulation parameters, autonomously assigning them using the programmable electrical stimulator.

Results and Discussion: The ANCS platform successfully executes all phases of the NCS procedure, collecting the primary output measures: H-max, H-reflex latency, and M-max. Consequently, it simplifies NCS, requiring minimal operator intervention and lowering the skill level required for the procedure. The ANCS platform also offers simplified and automated H-reflex measurements, expediting a previously challenging diagnostic approach and benefiting clinicians and patients. Further, the platform has promising applications for biomechanics research, as NCS yields information about one's underlying neuromuscular health and activity. M-max also serves as a potential approach to normalizing electrophysiological data, facilitating comparisons and interpretations between people.

Acknowledgements: Supported by NIH (R01AR081062, P50AR080581), Penn Health Tech Accelerator, and NSF Graduate Research Fellowship (DGE-2236662).

References: [1] R. Palmieri, et al., *Int. J. Neurosci.*, vol. 112, no. 7, 2002; [2] K. Tucker, et al., *Hum. Mov. Sci.*, vol. 24, no. 5, 2005

Transcriptomic and Epigenomic Atlas of Human Bone Marrow Reveals Gene Regulatory Networks and Cell-Cell Interactions Driving Mesenchymal and Hematopoietic Progenitor Fates

Michael Duffy[1], Kyung Jin Ahn[2], Wayne Lam[3], Austin Yang[2], Shovik Bandyopadhyay[1,2], Kai Tan[2] and Ling Qin[1].
(1)University of Pennsylvania, (2)Children's Hospital of Philadelphia, (3)Hunter College

Bone marrow is a highly complex and heterogeneous environment composed of hematopoietic, mesenchymal, and endothelial lineage cells. It is the site of many diseases affecting all its constituents, including blood and immune diseases, skeletal diseases, vascular diseases, and cancer metastases. Aging increases the occurrence of these diseases. Within the bone marrow, aging is characterized by myeloid and megakaryocyte skewing of hematopoietic progenitors and adipogenic bias of mesenchymal progenitors. Both play a role in reduced immune function and diminished skeletal integrity. Organization in cellular niches, mainly regulated by mesenchymal cells, is thought to orchestrate the array of critical functions in this highly diverse tissue. To develop a mechanistic understanding of the regulation of aging bone marrow, we simultaneously profiled human femoral head transcriptomic (snRNA-seq) and epigenomic (ATAC-seq) cell states and constructed an atlas of the gene regulatory networks involved in hematopoietic stem cell and mesenchymal differentiation. From ten samples, using a strategy to enrich rare cell populations, we captured 27,596 non-hematopoietic and 18,437 hematopoietic cells, including hematopoietic stem and progenitors, myeloid cells, lymphoid lineage, osteogenic and adipogenic cells, and mesenchymal progenitor cells The multiomic atlas captured increased non-hematopoietic cell clusters compared to scRNA-seq alone. Downstream analysis focuses on the non-hematopoietic and mesenchymal regulation of HSPC maintenance and differentiation potentiation. Using pseudo-time analysis (CytoTRACE), we predict markers regulating mesenchymal differentiation and find different gene markers in the transcriptomic and epigenomic data. We then construct signaling pathways between hematopoietic and mesenchymal cells and found 27 significant mesenchymal-HSPC interactions. Using CytoTALK, highlights the THY1+ MSC regulation of HSCs, particularly by CXCL12. Building a transcriptional regulatory network will further allow us to elucidate the differentiation and hematopoietic regulation programs of mesenchymal cells. Our human multiomic atlas represents the first to explore the epigenetic and signaling pathways of hematopoietic and mesenchymal differentiation biases in the aging bone marrow.

FLEX Ventilation Improves Pulmonary Function in a Rib-Tethered Mini-Pig Model of Thoracic Insufficiency Syndrome

Carly Ciociola[1], Jerrianne Brandly[1], Klaus Hopster[1], Madeline Boyes[1], Agathe Guillemet[1], Oscar H. Mayer[2], Alexander I. Gipsman[2], Brian Snyder[3], Thomas P. Schaer[1], Patrick Cahill[2]

[1]Department of Clinical Studies New Bolton Center, University of Pennsylvania School of Veterinary Medicine, Kennett Square PA, [2]Children's Hospital of Philadelphia, Philadelphia PA, [3]Boston Children's Hospital, Boston MA

ciociol1@vet.upenn.edu

Disclosures: All authors have no conflicts to disclose related to this research project

INTRODUCTION: In children with early onset scoliosis (EOS), the spine and associated rib cage deformities often result in thoracic insufficiency syndrome (TIS), where anatomic constriction of the thorax prevents uniform lung inflation and impedes lung growth, leading to extrinsic restrictive lung disease. A restrictive chest wall results in reduced respiratory system compliance, hypoventilation, hypoxemia, and significant morbidity with respiratory tract infections [2]. Untreated, children with TIS develop progressive respiratory and cardiovascular functional impairments, culminating in pulmonary hypertension and increased mortality [1]. Experimental models to study the pathophysiology and treatment of TIS remain limited. A rib-tethered large animal model simulating progressive scoliosis and thoracic deformity enables longitudinal evaluation of pulmonary function. We investigated the effects of a novel ventilation strategy, Flow-controlled Expiration (FLEX) [3,4], on lung function in a scoliotic mini-pig with TIS. The aim of this study was to assess long-term changes in pulmonary compliance and gas exchange in a rib-tethered large animal model of TIS, and to evaluate whether FLEX ventilation improves pulmonary mechanics and ventilation-perfusion matching when compared to conventional pressure ventilation (CPV).

Fig. 1. Dorsoventral 3D CT reconstruction of a tethered animal at 28 months post-op of the right hemithorax showing marked scoliosis.

METHODS: Under IACUC approval, rib tethering of the right hemithorax was performed in four female and castrated male Yucatan mini-pigs at 8 weeks of age to induce progressive thoracic deformity **(Figure 1)**. Two age- and weight-matched sham-operated animals served as controls. Longitudinal imaging and pulmonary function assessment were conducted over 9 months (cohort 1) and 3 months (cohort 2). CT imaging was used to measure Cobb angle and mean lung volume (MLV). Under general inhalant anesthesia, digital radiographs (DV, Right Lateral and Left Lateral) of the thorax and thoracic Computed Tomography (OmniTom® 8-slice small-bore mobile CT) were obtained. The inspiratory tidal volume (TV) was measured while animals were breathing spontaneously. Dynamic lung compliance (Cdyn), PaO_2/FiO_2 ratio, and lung dead space ($P_{ET}CO_2/PaCO_2$ ratio) were analyzed during CPV and FLEX ventilation. The mean lung volume (MLV) was measured using Sectra PACS software program from CT reconstruction. At study end, animals were anesthetized for pulmonary testing under spontaneous ventilation, CPV, and FLEX. Key endpoints included dynamic lung compliance (Cdyn), tidal volume (TV), PaO_2/FiO_2 ratio, and dead space ($P_{ET}CO_2/PaCO_2$).

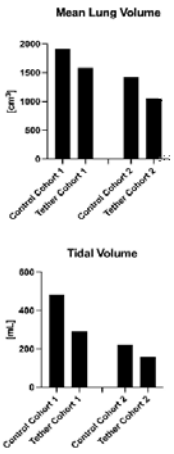

Fig. 2. Mean MLV and TV in the tethered animals (1586 cm³ and 290 mL) were significantly lower than in the control group (1912 cm³ and 485 mL).

RESULTS: The tethered animal in cohort 1 developed a sustained spinal curvature of 25° and marked asymmetry in thoracic growth. Mean MLV and TV in the tethered animals (1586 cm³ and 290 mL) were markedly lower than in the control (1912 cm³ and 485 mL) (**Figure 2**). During CPV, Cdyn was reduced in the tethered animals (32 mL/cmH_2O vs 55 mL/cmH_2O in control animals) and improved by 68% with FLEX. FLEX increased PaO_2/FiO_2 from 390 mmHg to 468 mmHg and reduced dead space from 18% to 3%, indicating more uniform ventilation and improved gas exchange. In the second cohort, the tethered animals failed to develop sustained spinal curvature and asymmetry in thoracic growth. Despite a lack of scoliosis, MLV and TV in the tethered animals (1,051 cm³ and 158 mL) were significantly different from those of the control (MLV 1,420 cm³ and TV 223 mL). During CPV, Cdyn was reduced in tethered animals (35 mL/cmH_2O) compared to the control (47 mL/cmH_2O). Cdyn improved during FLEX in the tethered (45 mL/cmH_2O) but not in the control animal. Further, during FLEX, the dead space was markedly reduced (4% during FLEX vs 12% during CPV).

DISCUSSION: It is well known that hypoxemia and impaired pulmonary perfusion are common complications in EOS patients with TIS [5]. Longitudinal studies of patients with untreated EOS reveal that 38% of patients die from respiratory failure [6]. Using our large animal untreated scoliosis model, we demonstrate that pulmonary function remains highly affected by chest deformity, likely due to decreased lung volumes and reduced chest compliance. As to why the tethered animals in the cohort without scoliosis still showed lower lung volumes compared to controls, plausible explanations include: Impaired Respiratory Muscle Function, where rib tethering changes the geometry and orientation of the ribs and intercostal muscles, even if a visible spinal curvature never develops. This altered orientation likely compromises the mechanical advantage of the intercostal and accessory respiratory muscles, reducing their efficiency in expanding the thorax during inspiration. As a result, tidal volume and mean lung volume would be reduced, despite preserved overall spinal symmetry. Increased Chest Wall Stiffness, where Rib tethering itself may cause fibrous remodeling, scarring, or altered rib biomechanics that stiffen the thoracic cage. Even in the absence of scoliosis, the rib cage could expand less effectively, producing a restrictive physiology with lower compliance and reduced lung volumes. The fact that dynamic compliance was already reduced during conventional ventilation in the tethered but nonscoliotic pigs suggests that chest wall stiffness is at least part of the explanation. Developmental Effects on Lung Growth - tethering is performed at a young age, when lung growth is tightly coupled to thoracic growth. By physically constraining thoracic expansion—even without scoliosis—the tethering may limit alveolar proliferation and lung parenchymal expansion, resulting in smaller absolute lung volumes later.

SIGNIFICANCE/CLINICAL RELEVANCE: Our findings from this and previous studies (**Figure 1**) confirm that both lung anatomy and function remain altered in the adult Yucatan mini-pig with induced spinal deformity up to two years post-tether. The rib tethering imposes structural restriction (chest wall stiffness and impaired growth) and simultaneously alters muscle mechanics (suboptimal fiber orientation and leverage). Together, these produce a restrictive defect even when overt spinal deformity does not occur. FLEX ventilation improved compliance and reduced dead space in the tethered, scoliotic, and non-scoliotic animals, suggesting that the lungs themselves remain recruitable, but the thoracic cage mechanics are the limiting factor. FLEX ventilation considerably improves lung function and dynamics by homogenizing the distribution of ventilation as well as gas and blood flow during expiration. The modulating and linearization of the expiratory phase further reduce the degree of atelectasis occurring during the second half of the expiratory period. Additionally, this ventilation mode might help optimize lung compliance and gas exchange in children with thoracic deformities undergoing general anesthesia for corrective surgery and be an option in children with TIS requiring long-term non-invasive ventilation.

REFERENCES: [1] Butler R, et. al, ORS, 2024 [2] Mayer O, et al, CPPAHC, 46(3), 2016. [3] Goebel U, et al. Br J Anaesth,113:474–483, 2014. [4] Wirth S, et al, Anesth Analg, 125: 1246-1252, 2017. [5] Wang Y, et al, JOSR 18(1), p.246, 2023. [6] Pehrsson K, et al, Spine, 17(9), pp.1091-1096, 1992.

ACKNOWLEDGEMENTS: Simpson Endowment of the University of Pennsylvania, School of Veterinary Medicine, the Program in Comparative Animal Biology (PICAB) Pilot Grants in Mechanisms of Pathology in Animal Models of Human Diseases, and the Wyss/Campbell Center for Thoracic Insufficiency (Children's Hospital of Philadelphia).

Comparison of Different Animal Models To Assess Pulmonary Function Using Hyperpolarized Xenon129 MRI.

C. Ciociola[1], A. Guillemet[1], K. Hopster[1]K. Ruppert[2], H. Hamedani[2], L. Loza [2], F. Amzajerdian[2], S. Kadlecek[2], R. R. Rizi[2], T. P. Schaer[1], B. Snyder[3], P. Cahill[4]

[1]University of Pennsylvania School of Veterinary Medicine, Kennett Square, PA, [2]University of Pennsylvania School of Medicine, Philadelphia, PA, [3]Boston Children's Hospital, Boston MA, [4]Children's Hospital of Philadelphia, Philadelphia PA

ciociol1@vet.upenn.edu

INTRODUCTION: Children with early onset scoliosis are often critically ill with failing respiratory function because of the associated spine and ribcage deformity. This thoracic dysfunction, termed Thoracic Insufficiency Syndrome (TIS), is manifest by decreased thoracic volume, increased chest wall stiffness, declining vital capacity, and overall failure to thrive. Surgical interventions that allow continued spinal growth while reducing thoracic distortion are promising, however, the respiratory status of these critically ill patients is not consistently improved by simply increasing the space available for the lung to grow. Normal pulmonary growth, defined by gains in lung parenchymal mass and alveolar multiplication, occurs until age 8. There is limited clinical data that lung function is favorably impacted if children are treated earlier, predicated on the assumption that treatment delay misses this developmental window of rapid alveolarization. Measurement of pulmonary function in early childhood by spirometry is the gold standard; however, it is limited by a patient's ability to actively participate in testing. There is an unmet need for new strategies to assess pulmonary function in pediatric patients with TIS to understand the underlying pathophysiology and determine the effectiveness of surgical treatments to preserve and rejuvenate pulmonary function. We previously reported on establishing several animal models of thoracic insufficiency concomitantly with developing imaging modalities: 1) hyperpolarized MRI using ^{129}Xe (HXe) gas diffusion to assess lung pathology via regional analysis of gas exchange and 2) dynamic CT/MRI to quantify dynamic lung volume and shape changes as a function of thoracic and diaphragmatic kinematics during the respiratory cycle under free breathing conditions. Herein, we report comparative findings from normative and scoliotic HXe MRI in pigs and rabbits, demonstrating that HXe MRI can diagnose respiratory pathophysiology at the parenchymal level. Moreover, we present preliminary work in lambs, that indicates that the xenon frequency shifts in the lung are essentially identical to human lungs[1], and that the lamb model of TIS may be of superior translational fidelity.

METHODS: Under IACUC approval, HXe MRI was performed in a prone position under general anesthesia in control juvenile pigs, rabbits, and lambs using a 1.5 Tesla magnet and custom 8-channel xenon-129 coil for pigs and lambs (Stark Contrast), and a custom birdcage designed coil in rabbits (Stark Contrast). Enriched xenon gas (87% xenon-129) was polarized using a commercial prototype (XeBox-E10). A gas mixture 20% oxygen and 80% HXe was administered with a tidal volume of 8-10ml/kg and images were acquired during inspiratory breath hold. 3D-spiral interleaves were acquired continuously over approximately three minutes. To quantify both ventilation and gas exchange, the frequencies of each RF excitation pulse were alternated between the gas phase (GP, 0 ppm) and dissolved phase (DP, 200 ppm) resonances with TR/TE = 7.63/0.62ms and GP/DP flip angles of 4°/30°. Images were reconstructed onto 80×80x80 grids. Phase-binning was used to retrospectively bin each interleave into 16 phases of a representative breathing cycle. Symmetric image normalization with cross-correlation metric in the ANTs toolbox was used to co-register all frames to the end-inhale frame to allow voxel-wise analysis. The 16 points of the GP signal representing an average breath were fit to piecewise sigmoid functions (**Fig 1**). The time points on each sigmoid curve at which the signal is 50% of the total amplitude were defined as arrival time (inhalation) and departure time (exhalation).

RESULTS: The pig and rabbit (**Fig 2C, D**) models presented with signal intensities [2] significantly inferior (10^4x) to the human spectrum (**Fig 2A**). Recent data acquisition in lambs revealed a signal intensity superior (**Fig 2B**) to humans with similar spectrum.

SIGNIFICANCE/CLINICAL RELEVANCE: This pilot study allows to determine a relevant and improved translational animal model for the use of HXe MRI in early onset scoliosis pre-clinical research.

REFERENCES: [1] Hilliard+*ORS* 2022, [2] Ismail+*ISMRM* 2024

ACKNOWLEDGEMENTS: This work was funded by the US National Institute of Health and Wyss-Campbell Center for Thoracic Insufficiency at Children's Hospital of Philadelphia

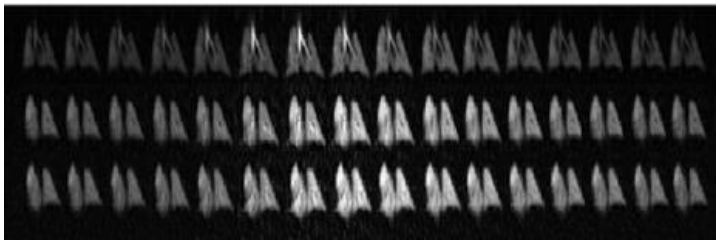

Figure 1: Raw HXe dynamic images for three representative coronal slices (from top to bottom depict anterior to posterior) in the TIS rabbit for one breathing cycle shown in 16 phases: from left to right is the end-exhale to end-inhale, returning to end-exhale.

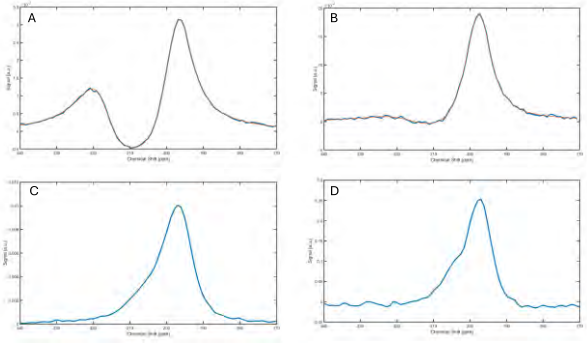

Figure 2: Comparison of the Human (**A**), Lamb (**B**), Rabbit (**C**) and Pig (**D**) spectra in entire normative lungs acquired during inspiratory breath hold. Note the different signal scales, with signals up to 20x10^4 a.u. in the lamb compared to rabbits and pigs with signal intensity <0.25 a.u.

Longitudinal Assessment of Trans-Endplate Diffusion in a Goat Model of Intervertebral Disc Degeneration

Carly Ciociola[1], Agathe Guillemet[1], Leslie Brewer[1], Harrah Newman[2], Sarah Gullbrand[2], Dawn Elliott[3], Thomas P. Schaer[1]
[1]University of Pennsylvania School of Veterinary Medicine, Department of Clinical Studies, Kennett Square PA, [2]University of Delaware, Newark, DE,
[3]Perelman School of Medicine at the University of Pennsylvania, PA
ciociol1@vet.upenn.edu

INTRODUCTION: Intervertebral disc degeneration (IVDD) is implicated as a leading cause of low back pain. Persistent, localized inflammation within the disc nucleus pulposus (NP) and annulus fibrosus (AF) is a key mediator of disc degeneration and is associated with downstream catabolic enzyme activity and extracellular matrix destruction. The IVD is the largest avascular structure in the body, its delivery of nutrients and oxygen and removal of waste is mainly conducted through the cartilaginous endplates (CEP) and peripheral AF. Pathologies affecting the CEP will induce oxygenation and nutritional changes in the AF and NP that can result in cellular death [4]. Chondroitinase ABC (ChABC) nucleolysis catalyzes the removal of chondroitin sulfate and dermatan sulfate side chains of proteoglycans in the extracellular matrix (ECM) of the NP. We previously described a goat model of disc degeneration by using different doses of ChABC injected into the NP, resulting in increased inflammatory cytokines and catabolic enzymes in the IVD, like the profiles found in human discs. These changes were also correlated with degeneration severity assessed histologically and using quantitative analysis of magnetic resonance imaging (MRI) using T2 and T1ρ relaxation times on explanted spines [7]. Previous studies have evaluated the use of different MRI relaxation measurements and scoring to assess IVD water content and molecular exchanges in ovine healthy lumbar spine [1] and caprine explanted ChABC degenerated lumbar spine [3]. The goal of this study was to longitudinally assess *in vivo* contrast-enhanced trans-endplate small molecule diffusion.

METHODS: Data was collected from fifteen skeletally mature goats (female and castrated males >4 years of age) who were enrolled in different studies that used the goat model of IVDD. With IACUC approval, goats underwent general anesthesia and received percutaneous ChABC injections (200µL of 2.5 - 5U) via a 22g spinal needle under 3D fluoroscopic guidance (Arcadis Orbis, Siemens, Munich, Germany). The remaining IVDs served as healthy controls. Post-operatively MR images (3 Tesla Siemens, Magnetom TrioTim) mid-sagittal T2-weighted series of images for T2 mapping (*25 echoes, TE=13.6ms, TR=4380ms, 5mm slice thickness*) and T1-weighted sagittal pre- and post-contrast images (*TE=2.1ms, TR=15ms, 5mm slice thickness*) using the non-ionic MRI contrast agent gadodiamide (*0.1 mmol/kg IV,* Omniscan, GE Healthcare; 30 min pre-post injection interval) were obtained at different time points from 2 weeks to 30 months post-ChABC injection. To quantify diffusive transport into the disc, T1 signals were measured with Image J (NIH; Bethesda), using the region-of-interest (ROI) drawing method delineating the NP on pre- and post-contrast mid-sagittal sections, and delta T1 was calculated and reported [8]. T2 relaxation time was obtained by circling the ROI, demarcating the NP, and calculating the average signal intensity in the ROI for each echo. Curve fits were then performed on these average intensities to obtain T2 relaxation time (ms). The first echo was excluded for curve fitting as standard practice [5].

RESULTS: None of the animals enrolled presented with postoperative complications, and all goats reached their time points. All data collected was organized in groups by postoperative time point: <1mos, 1-6 mos., 6-12 mos., and >12 mos. (**Fig. 1**). Gadodiamide is a T1 shortening agent, and thus, the reduction in the T1 relaxation time (pre- vs. post-contrast) provides a quantitative measure of small molecule diffusion into the disc. T1 data was heterogeneous, and *in vivo* T1 mapping demonstrated a reduction in T1 relaxation times in the spinal tissues of ChABC discs following contrast agent administration (**Fig. 1B-D**). Specifically, within the NP, gadodiamide diffusion into the disc progressively decreased until 12 mos. compared with healthy controls, suggesting that small molecule trans-endplate diffusion was reduced in these degenerating discs (**Fig. 1D**). T2 relaxation times decreased significantly from the first month after ChABC nucleolysis from native and continued to slowly decrease until 6 months post ChABC nucleolysis (**Fig. 2**) Interestingly, there then was a gradual increase of T2 relaxation time in groups from 6-12 months and above 12 months post nucleolysis (**Fig. 3**). This "recovery" was also reflected in the T1 relaxation time but lagged the recovery of the T2 signal intensity.

DISCUSSION: Histological evaluation of IVDD is the gold standard in assessing inflammatory and degenerative changes. MRI offers extensive interrogation *in vivo,* allowing for longitudinal, non-invasive visualization and quantification of IVD health. T1 mapping using contrast-enhanced MRI measures small molecule trans-endplate diffusion and, therefore, depends highly on the physiological homeostasis of the CEP. We previously reported that end-plate degeneration contributes to altered trans-endplate small molecule diffusion in the C-spine of goats and demonstrated that ChABC reduces the extracellular matrix, altering disc biomechanics and inciting an inflammatory cascade of matrix-degrading enzymes over time [2,6,7]. In these studies, T2 relaxation times have been shown to correlate with water and proteoglycan content as well as with Pfirrmann scoring and histopathology [2]. The findings in this present study are consistent with initial IVDD up to 6 months post nucleolysis that alters water and proteoglycan contents of NP ECM. Interestingly, 6 mos. post nucleolysis, there is a recovery of the IVD (**Fig. 3**). ChABC only acts on ECM but does not affect the NP cells, and goats lose their notochordal cells at birth [8]. While some discs degenerate past a point of regeneration with severe CEP lysis (data not shown), our data suggests that there is a subset of discs and perhaps animals where continued ECM production overcomes the inflammatory milieu, resulting in the restoration of the IVD. To our knowledge, there is no current evidence of IVD regeneration in the literature, and our findings require a multiscale approach to analyzing these structure-function alterations. The primary limitation of this study is its relatively small sample size, making statistical differences in disc imaging data difficult to detect, given the heterogeneity in these measures. Ongoing work is focused on increasing this sample size and performing correlations across quantitative measures of disc imaging and histopathology.

SIGNIFICANCE/CLINICAL RELEVANCE: There has been a paucity of long-term (>6mos.) IVDD studies in large animal models, and during the past 15 years, we have learned that the response to ChABC is highly heterogeneous from animal to animal and often not dose-dependent with doses >2.5U in 200µL. Intrinsic healing or restoration of the NP in the goat model of IVDD following ChABC nucleolysis is an important consideration when interpreting long-term data of cell-based and acellular IVD therapies. Quantitative post-contrast enhanced MRI may be a useful modality for longitudinal monitoring of structure–function alterations and associated trans-endplate small molecule diffusion into the NP.

REFERENCES: [1] Bouhsina+Scientific Reports2022, [2] Gullbrand+ECM2024, [3] Gullbrand+ OAC 2016, [4] Isma+Int. J. Mol. Sci.2022, [5] Meadows+JOR Spine2020, [6] Gullbrand+Acta Biomaterialia 2017, [7] Zhang+JOR2020, [8] Ashinsky+JBMR, 2020, [8] Williams+JOR 2023

ACKNOWLEDGEMENTS: Institute for Medical Translation New Bolton Center University of Pennsylvania School of Veterinary Medicine

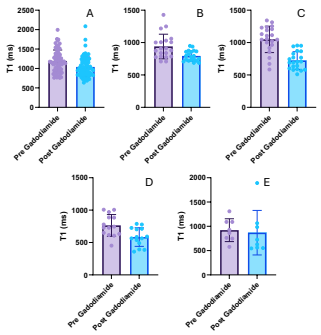

Figure 1: T1 (ms) pre and post contrast injection of native IVDs (**A**), ChABC degenerated disc for <1 month (**B**), 1-6 months (**C**), 6-12 months (**D**) and >12 months (**E**)

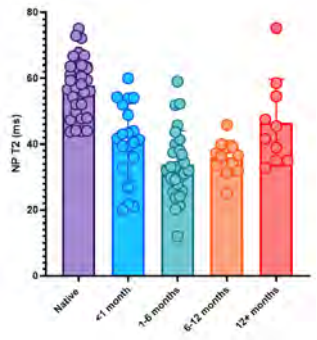

Figure 2: T2 relaxation time (ms) comparing native IVD (all time points) s that underwent nucleolysis with ChABC injection by time groups.

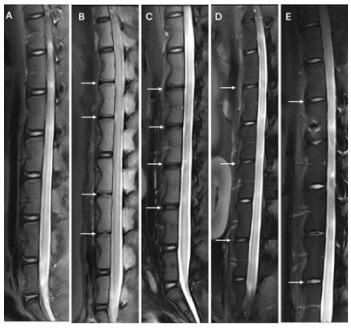

Figure 3: T2 Pfirmann sagittal sections of a healthy lumbar spine (**A**), and ChABC degenerated discs indicated by the white arrows at <1mos (B), 1-6mos (**C**), 6-12mos (**D**), and >12mos (**E**)

Are Total Wrist Arthroplasty Surgeries Being Performed More Frequently?

Jagger Godarzi MS, Shiraz Mumtaz MD, Elizabeth Blears MD, Kimberly Dong BS, Zachary Demetriou BS, Yousef Soliman BS, Asif Ilyas MD, MBA

Abstract

Background:

Patients with osteoarthritis (OA) of the wrist who have failed conservative management undergo surgical intervention. Although wrist arthrodesis has historically been the treatment of choice, recent efforts have been undertaken to improve the wrist arthroplasty procedure. Thus, this study was undertaken to better understand the trends in these two procedures. The study hypothesized that the number of total wrist arthroplasty (TWA) procedures and the TWA procedure rate would increase over time.

Methods:

The TriNetX database was retrospectively queried on February 27, 2024, for all patients diagnosed with wrist OA who then subsequently underwent either wrist arthrodesis or wrist arthroplasty from 2016-2023. Annual cohorts were defined by inclusion of ICD-10 codes and procedure CPT codes. Deceased patients during this period were excluded. Statistical analysis was performed using SPSS software to examine the trends in each procedure over the eight-year period.

Results:

Over the study period, total wrist arthrodesis remained the overwhelmingly more commonly performed procedure compared to total wrist arthroplasty. The annual number of arthrodesis procedures was relatively stable year to year, while arthroplasty procedure counts remained consistently very low. When examining incidence trends over time, the incidence of arthrodesis increased, particularly in the later years of the study period. In contrast, the incidence of arthroplasty remained low and did not demonstrate meaningful change over time. These findings indicate that arthrodesis continues to be the primary surgical approach for advanced wrist arthritis, and there has not been a measurable shift toward broader adoption of wrist arthroplasty.

Conclusion:

Total wrist arthrodesis remains the predominant surgical treatment for end-stage wrist arthritis, with its incidence increasing over the study period. Total wrist arthroplasty continues to be used infrequently, with incidence remaining low and stable. These findings indicate that arthroplasty has not replaced arthrodesis in contemporary practice, and broader adoption of motion-preserving wrist replacement has not yet occurred. Further investigation is warranted to identify the clinical, economic, and training factors influencing procedure selection.

Single Component Optogenetic Tools for Bi-Directional Control of RhoA Signaling

Erin E. Berlew[1,2], Paula Camacho Sierra[1], Tianbai Wang[1,2], Brian Y. Chow[2], Joel D. Boerckel[1,2]
[1]Department of Orthopaedic Surgery, University of Pennsylvania, Philadelphia, Pennsylvania
[2]Department of Bioengineering, University of Pennsylvania, Philadelphia, Pennsylvania

The Rho family of small GTPases coordinate actin cytoskeletal rearrangements and control fundamental cell processes including migration and mechanotransduction. Rho GTPase signaling is tightly controlled in space and time: GTPases are activated by guanine nucleotide exchange factors (GEFs) and inactivated by GTPase accelerating proteins (GAPs) at the plasma membrane. We have developed a novel suite of optogenetic tools for bi-directional control (i.e., activation and inactivation) of RhoA signaling. These tools are unique because they require expression of only a single plasmid for light-induced membrane recruitment of cargo proteins, enabled by a blue light-induced conformational change in the BcLOV4 photoreceptor from *Botrytis cinerea,* which results in plasma membrane recruitment via an electrostatic interaction. Here, we used this system to engineer tools to efficiently activate or inactivate RhoA signaling with subcellular precision in mammalian cells, including cell lines and primary cells (including endothelial cells, bone marrow stromal cells, and others). Blue light stimulation of either opto-RhoA or opto-ARHGEF11 drives robust cell contraction, actin polymerization, and transcriptional mechanotransduction mediated by Yes-associated protein (YAP). In contrast, opto-ARHGAP1 stimulation induced dynamic actin de-polymerization. We also generated guiding principles for creating optogenetic fusion proteins with BcLOV4, which will inform future tool development for optical control of membrane-based signaling pathways. This toolbox enables perturbation of the mechanical and transcriptional state of a cell using light with a single protein, reducing the genetic payload of plasmid delivery to targeted cells and eliminating the need for stoichiometric tuning of multiple components requiring more extensive optical bandwidth.

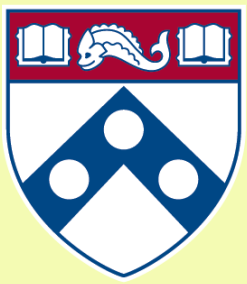

Penn Center *for*
Musculoskeletal Disorders
UNIVERSITY *of* PENNSYLVANIA

Biomechanics Core Abstracts

PM Session

Poster 77 to 88

Structural and functional adaptations of the rat Achilles tendon to long-term passive loading

Jonathon L. Blank, Eve I. Gibson, Mark M. Tarazi, Cassidy R. Landis, Louis J. Soslowsky, Josh R. Baxter
McKay Orthopaedic Research Laboratory, University of Pennsylvania, Philadelphia, PA
jonathon.blank@pennmedicine.upenn.edu

DISCLOSURES: None.

INTRODUCTION: Tendinopathy is a debilitating condition that affects 2.35 per 1000 individuals aged 21-60 years[1] and is common among athletes, workers, and the general population.[2] Risk factors for tendinopathy include sudden increases in or initiations of new activities, limited time for recovery, and repetitive movements.[3] Thus, highly and repetitively loaded tendons, such as the Achilles, are among the most afflicted tissues. Small animal models of running[4] or passive loading *in situ*[5] are common strategies to elicit and study overuse in the Achilles tendon. However, tissue stresses during running in humans far exceed those during rodent running,[6-7] and mechanical and compositional changes to the rat Achilles following high-stress long-term loading are unknown. Therefore, the purpose of this study was to determine the structural and functional response of the rat Achilles tendon to long-term loading using a novel small animal dynamometer. We hypothesized that our loading protocol would elicit degenerative changes to the Achilles tendon, leading to inferior mechanical properties due to changes in structure consistent with damage and overuse.

METHODS: Loading protocol: Twenty-four 10-week male Sprague Dawley rats were divided evenly into control and experimental groups (IACUC approved). Both groups were anesthetized with 1.5-2% isoflurane and the experimental group was mounted on a custom small animal dynamometer.[8] Hind limbs were fixed with the knee in full extension and the resting ankle angle at 90°. The ankle was driven continuously through 0-90 Nmm of torque for 5000 cycles at 2.5 Hz, where 90 Nmm is 2-3x greater than torques estimated during rodent running.[9] The experimental group received overuse treatment on one or both hind limbs and the control group was anesthetized in parallel with no treatment. This protocol was repeated three times per week for four weeks. Twenty-two rats completed the protocol and two were excluded due to anesthesia complications. All animals were euthanized the morning after the last loading bout. Mechanics (n=11/group): Tendon cross-sectional area (CSA) was measured using a laser device and Verhoeff stain lines were applied for optical strain analysis. The hindpaw was secured in polymethylmethacrylate at 120° and the proximal tendon clamped in sandpaper grips in a 37° C 1X PBS bath. Testing consisted of a 1 N preload, 10 cycles of preconditioning at 0.5% strain, stress relaxations at 3%, and 6% grip strain followed by frequency sweeps at 0.1, 1, 5, and 10 Hz, and a ramp-to-failure at 0.1%/s. Elastic (stiffness, optical modulus), viscoelastic (dynamic modulus (E*), phase shift (tan δ), and percent relaxation), and failure properties (max force) were measured. Fiber realignment was tracked at the insertion and midsubstance during the ramp to failure using reflectance mode polarized light imaging. Biochemistry (n=11/group): Following mechanical testing, tendons were digested in Proteinase K overnight at 60°C prior to quantifying glycosaminoglycan (GAG) content using the 1,9-dimethylmethylene blue assay and chondroitin sulfate as standard. Absorbance was read at 525 and 595 nm and normalized to the tendon dry weight.[10] Statistics: Data was assessed for outliers (2.2*IQR) and normality assessed using Shapiro-Wilks tests. Comparisons across groups were made using two-sided student's t-tests (GAG content, stiffness, max force) or two-way ANOVAs with Bonferonni post-hoc tests (CSA, optical modulus, viscoelastic data, fiber realignment). Significance was set at α=0.05.

RESULTS: There were no changes in overall GAG content (Fig. 1b) or CSA (Fig. 1c) in the tendon midsubstance following long-term loading. There was an increase in stiffness (p=0.018) (Fig. 1d) and tendon midsubstance modulus (p=0.02) (Fig. 1e). There were no changes in insertion modulus (Fig. 1e), max force (Fig. 1f), viscoelasticity (1 Hz results presented) (Fig. 1g-i), or fiber realignment in the insertion and midsubstance regions (Fig. 1j-k).

DISCUSSION: Contrary to our hypothesis, there was no evidence of degenerative changes to Achilles tendons undergoing long-term passive loading on our dynamometer. Instead, tendons had an increased stiffness and a higher modulus in the tendon midsubstance. These changes are consistent with those observed during running in humans, where higher running volume (and thus long-term Achilles tendon loading) leads to increased Achilles stiffness.[11] No changes to stiffness or midsubstance modulus were found in prior models of long-term rat running[4] and overuse,[12] indicating that our high-load dynamometer can produce load-related adaptations observed in humans and that the tendon stiffening response to long-term loading may be dose dependent. Interestingly, increased musculoskeletal tissue stiffness in humans due to training volume typically precedes degenerative changes associated with chronic overuse and Achilles tendinopathy.[13] However, there were no changes in GAG content or CSA typically observed with tendinopathy[3,14] suggesting that the protocol used in this study is not enough to generate a tendinopathy phenotype in the rodent Achilles tendon. Future work will examine the effects of loading dose, frequency, and duration on Achilles tendon, calcaneus, and triceps surae structure and function.

SIGNIFICANCE: This work studied biomechanical effects in the Achilles tendon following repeated loading bouts greater than those during rodent running. These studies can elucidate long-term adaptations of the Achilles tendon to repetitive loading.

REFERENCES: [1] Albers *et al.*, *BMC Musculoskel. Disord.,* 2016. [2] Hopkins *et al.*, *AP-SMART,* 2016. [3] Millar *et al.*, *Nat. Rev. Dis. Primers,* 2021. [4] Tamburro *et al.*, *JOR,* In Review. [5] Williamson *et al.*, *J. Biomech.,* 2023. [6] Konow *et al.*, *Front. Physiol.,* 2020. [7] Reiter *et al.*, *Med. Sci. Sport. Exerc.,* 2024. [8] Tang *et al.*, *J. Biomech.,* 2022. [9] Dienes *et al.*, *Sci. Report.,* 2022. [10] Zheng *et al.*, *Eur. Cell. Mater.,* 2015. [11] Siu *et al.*, *J. Sci. Med. Sport.,* 2016. [12] Legerlotz *et al.*, *J. Appl. Physiol.,* 2007. [13] Cook *et al.*, *Br. J. Sports Med.,* 2009. [14] Fu *et al.*, *Clin. J. Sport. Med.,* 2007.

ACKNOWLEDGEMENTS: Penn Achilles Tendinopathy Center for Research Translation (NIAMS P50-AR080581), NIAMS F32-AR082671.

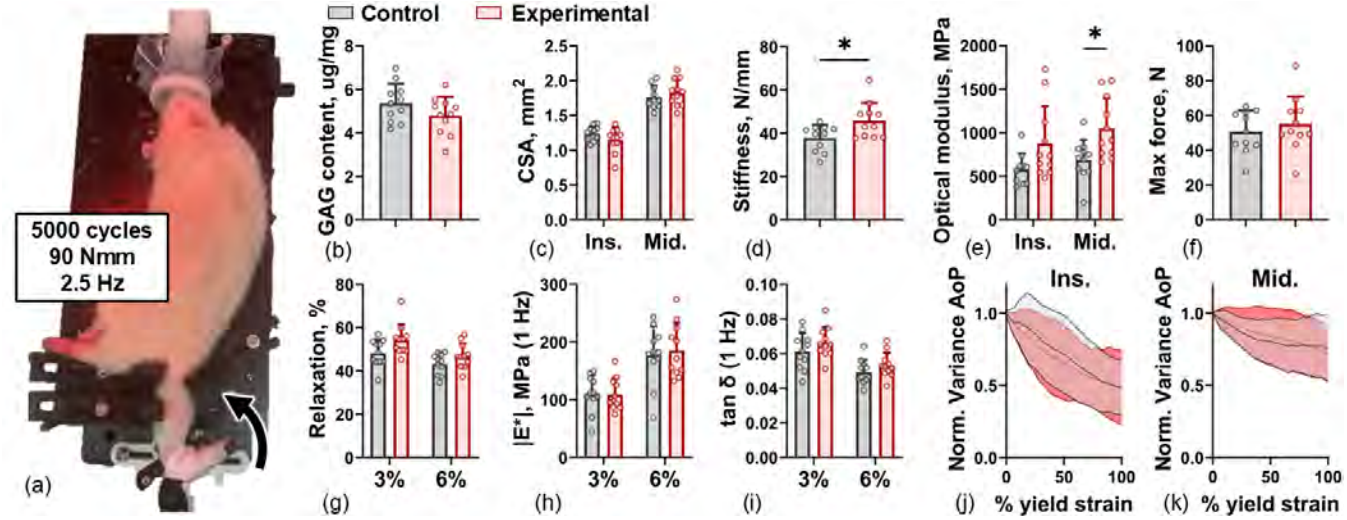

FIGURE 1: (a) Custom passive dorsiflexion system and treatment protocol for anesthetized rats. (b,c) There were no changes in GAG content or CSA following long-term loading. (d,e) Tendons were stiffer in the midsubstance (Mid.) without changes to insertion (Ins.) mechanical properties (e), failure force (f), viscoelasticity (1 Hz shown) (g-i), or fibril kinetics (j-k) following long-term loading (* $p \leq 0.05$).

Reduction of Type III Collagen During Healing Worsens Mechanical Properties in Aged Mouse Tendons

Margaret K. Tamburro,[1] Jaclyn A. Carlson,[1,2] Stephanie N. Weiss,[1] Jeremy D. Eekhoff,[1] William Yen,[2] Susan W. Volk,[2] Louis J. Soslowsky[1]
[1]McKay Orthopaedic Research Laboratory, University of Pennsylvania, Philadelphia, PA
[2]School of Veterinary Medicine, University of Pennsylvania, Philadelphia, PA
Margaret.Tamburro@pennmedicine.upenn.edu

Disclosures: Margaret K. Tamburro (N), Jaclyn A. Carlson (N), Stephanie N. Weiss (N), Jeremy D. Eekhoff (N), William Yen (N), Susan W. Volk (N), Louis J. Soslowsky (N)

INTRODUCTION: The incidence of tendon injury increases with age,[1] and aged tendons heal poorly.[2] Many age-related tendon changes have been described, including dramatic reduction of expression of the gene encoding type III collagen (Col3), *Col3a1*.[3] After injury, Col3 comprises a substantial component of the provisional healing matrix and contributes to regulation of matrix and cell behavior.[4] Despite its expression in tendon being commonly associated with poor tendon healing, the age-specific role of Col3 in tendon healing remains unclear. Therefore, the objective of this study was to elucidate the mechanical impacts of reduced *Col3a1* expression during healing in aged tendons. We hypothesized that reduced *Col3a1* expression would diminish formation of scar tissue and exacerbate age-related healing deficits, yielding mechanically inferior tendons.

METHODS: Wildtype (Rosa-CreER^{T2}; *Col3a1*$^{+/+}$) and Col3 knockdown (Rosa-CreER^{T2}; *Col3a1*$^{F/F}$) male mice received tamoxifen injection at postnatal day 364 (p364) followed by patellar tendon biopsy punch injury[5] at p365 (IACUC approved). Effective Col3 knockdown was previously confirmed by qPCR.[6] Left patellar tendons were harvested at 6-weeks post-injury, and patella-patellar tendon-tibia complexes were dissected and prepared[7] for mechanical testing ($n \geq 7$/group). Patellar tendon mechanics were quantified with viscoelastic tensile testing (nominal gauge length = 3 mm) including 1) preconditioning, 2) stress relaxation at 2% and 4% strain with a subsequent sinusoidal frequency sweep (10 cycles at 0.1, 1, 5, and 10 Hz) at each strain level, and 3) quasistatic ramp to failure (0.1% strain/s). Reflectance-mode quantitative polarized light imaging at 2 Hz captured the light reflected off the tendon midsubstance in real time during the ramp to determine average degree of linear polarization (DoLP), indicative of collagen fiber alignment, and variance of the angle of polarization (AoP), indicative of collagen fiber orientation.[8] Genotype-based differences were assessed with Student's t-tests (mechanical properties) or 2-way ANOVAs (normalized average DoLP and variance of the AoP at 10, 25, 50, 75, and 100% strain; genotype, normalized strain level). Significance was set at $p \leq 0.05$.

RESULTS: Tendons with Col3 knockdown were structurally different than wildtype tendons. Knockdown tendons showed a trending increase in cross-sectional area and a significant decrease in gauge length (Fig. 1A-B). Percent relaxation at both 2% and 4% strain was not affected by Col3 knockdown (Fig. 1C, F). At 2% strain, Col3 knockdown did not affect dynamic modulus or phase shift (Fig. 1D-E). At 4% strain, knockdown reduced dynamic modulus without affecting phase shift, at all frequencies (Fig. 1G-H). Col3 knockdown did not affect stiffness, but modulus was lower in the knockdown group (Fig. 1I-J). Consistent with expected fiber uncrimping and realignment, average DoLP increased and variance of AoP decreased with increasing strain, but knockdown did not affect strain-dependent changes in either property (Fig. 2A-B).

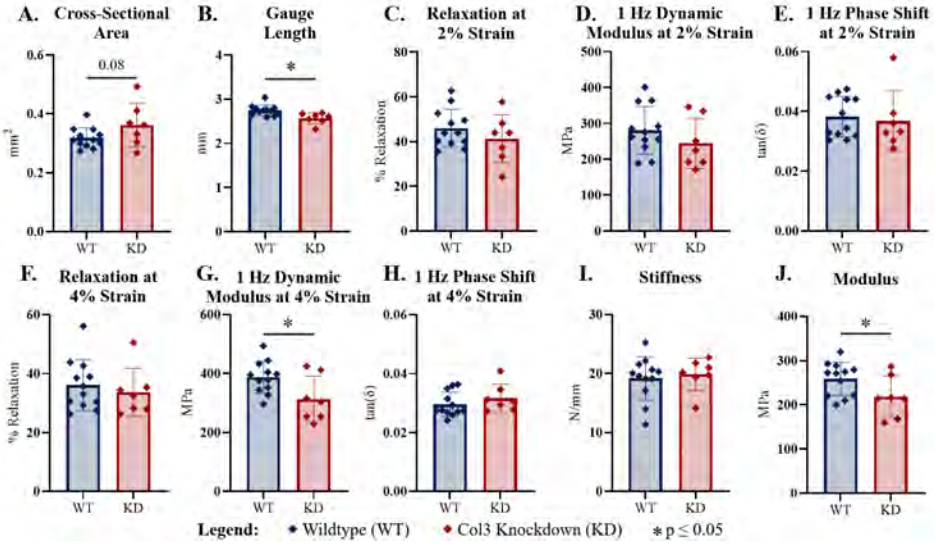

Figure 1. Col3 knockdown worsens tendon mechanics after injury. Knockdown tendons had a trend toward increased (A) cross-sectional area and had decreased (B) gauge length. At 2% strain, (C) percent relaxation, (D) dynamic modulus, and (E) phase shift were unaffected by knockdown. At 4% strain, (F) percent relaxation and (H) phase shift were unaffected while (G) dynamic modulus was reduced. Dynamic data is shown for the 1 Hz frequency (trends were consistent across frequencies). (I) Stiffness was unaffected by Col3 knockdown while (J) modulus was reduced.

DISCUSSION: This study investigated the mechanical impacts of reduced Col3 during tendon healing in aged male mice. As hypothesized, reduction of Col3 during tendon healing led to reduced mechanical properties. Interestingly, Col3 knockdown resulted in a shorter and possibly larger healed tendon. Because Col3 is the primary structural component of the provisional healing matrix, this finding is surprising and may indicate compensatory production of non-Col3 matrix in Col3 knockdown tendons. Material properties of knockdown tendons were inferior to wildtype. The possible increase in cross-sectional area in knockdown tendons may have compensated for poor material properties, yielding a comparable tendon stiffness. Because we only observed an effect of Col3 reduction on dynamic modulus at 4% strain, Col3 may be an important contributor to dynamic tendon mechanics at higher strains. Based on the similarities in collagen realignment between wildtype and knockdown groups, Col3 may not be an influential contributor to dynamic collagen realignment in healing tendon. In summary, these results highlight an important role for Col3 in promoting mechanical integrity after injury in aged tendons. Results are consistent with studies in other tissues that demonstrate pathologic changes with age in male mice with reduced Col3.[9] To fully understand contributions of Col3 to aged tendon healing, future studies will evaluate tendon structure and gene expression, include female mice, and investigate earlier healing time points.

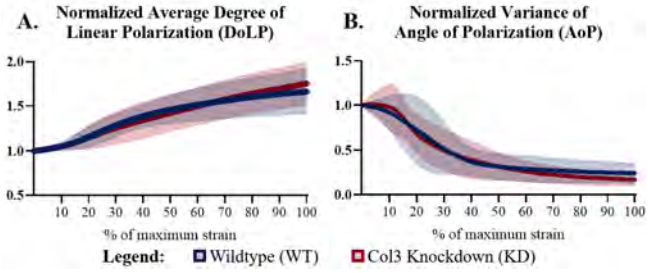

Figure 2. Col3 knockdown does not influence dynamic collagen realignment. (A) Average DoLP and (B) variance of AoP are unaffected by genotype across the strain profile. Data are presented normalized to the initial value as a percent of maximum strain. Initial values for average DoLP and variance of AoP were not different between groups.

SIGNIFICANCE: As therapeutic Col3 modulation through pharmacologic, biomaterial, and mRNA-based approaches becomes more feasible, understanding contributions of Col3 to tendon healing, particularly in aged tendons where injury is prevalent and devastating, is imperative for improving treatment strategies.

REFERENCES: [1] Korcari. Connect Tissue Res. 2023. [2] Ackerman. J Orthop Res. 2017. [3] Sugiyama. Biomed Rep. 2019. [4] Volk. Cells Tissues Organs. 2011. [5] Beason. J Biomech. 2012. [6] Tamburro. MSK Biol and Bioeng GRC. 2024. [7] Leiphart. J Biomech. 2022. [8] Iannucci. Biomed Opt Express. 2024. [9] Cooper. Vet Pathol. 2010. ACKNOWLEDGEMENTS: This study was funded by NIH R01GM124091, R01AR080029, F31AR082282 and the Penn Center for Musculoskeletal Disorders (P30AR069619). The authors thank Miranda Doro and Ashley Fung for their assistance.

Macrophage YAP/TAZ Signaling Mediates Mechanoregulation of Bone Fracture Repair

Georgios Kotsaris[1], Ana-Sofia Mongil[1], Madhura Nijsure[1], Elizabeth Bernstein[1], Annemarie Lang,[1] Nathaniel Dyment[1], Robert Mauck[1,2], Joel Boerckel[1]
[1]University of Pennsylvania; [2]CMC VA Medical Center
Georgios.kotsaris@pennmedicine.upenn.edu

Disclosures: RLM (5 – 4WEB Medical)

Introduction: Bone tissue can heal without scarring, but current treatments for fractures remain limited in efficacy and applicability. Harnessing biological mechanisms of repair, particularly the interplay between inflammatory signals and mechanical cues, offers a promising strategy to accelerate healing. In the early phase of fracture repair, macrophages (MΦs) infiltrate the fracture site. This phase of fracture repair is also mechanically dynamic, and these mechanical conditions impact the course of repair. Specifically, while rigid fixation induces intramembranous repair, early mechanical loading induces repair by endochondral ossification. Mechanical cues are transduced by a number of signaling pathways, including the transcriptional regulators Yes-associated protein (YAP) and transcriptional coactivator with PDZ-binding motif (TAZ). Our group has shown that YAP and TAZ mediate mechanotransduction in osteoblast-lineage cells during both bone development [1] and repair [2]. Recent studies also suggest that MΦs are actively sensitive to mechanical cues and that MΦ mechanotransduction can modulate tissue regeneration [3]. However, the role of macrophage mechanosignaling in bone fracture repair remains unclear. Here, we query whether ablation of YAP/TAZ signaling in macrophages modulates fracture repair in response to mechanical loading.

Methods: Bone fracture: Procedures were performed on skeletally mature male and female mice; all methods followed IACUC regulations. Femoral fractures were stabilized with external fixators (stiff: 18.1 N/mm; compliant: 3.2 N/mm). Early fracture cells (3 dpf) were isolated for scRNA-seq (GSE230260) (N=3–4/group). Triple Collagen reporter mice: (Col1-YFP; Col2-CFP; Col10-mCherry) marked osteoblasts, chondrocytes, and hypertrophic chondrocytes. F4/80 immunofluorescence localized macrophages in the callus. YAP/TAZ knockout mice: Macrophage-specific knockouts were generated using LysM-Cre. Fracture healing: At 2 weeks, femurs were analyzed by micro-CT and Saf O/Fast Green histology (N=6–12/group, both sexes). BMDM isolation: BMDMs were isolated from femora/tibiae of WT and YAP^{flox}/TAZ^{flox} mice (N=4-7/group, both sexes). In vitro recombination: TAT-Cre was applied to macrophage cultures for 6 h. Cell shape: Actin cytoskeleton was visualized using phalloidin staining, and cell morphology was quantified with CellProfiler. Phagocytosis: GFP–E. coli were added to cultures for 2 h, and uptake quantified by microplate reader. Statistics: Outcomes were compared using t-tests or 2-way ANOVA, with $p<0.05$ considered significant.

Results: MΦs in fracture repair: scRNA-seq showed that compliant fixation increased MΦ fractions at 3 dpf compared to stiff fixation or contralateral marrow **(Fig. 1A, B)**. MΦs rapidly invaded the fracture site, localizing to the hematoma at 4 dpf. By 7 dpf, they formed canopy-like structures over osteoblasts (Col1-YFP) and chondrocytes (Col2-CFP) in the soft callus. At 10–14 dpf, MΦs infiltrated the hard callus, associating with hypertrophic chondrocytes (Col10-RFP) during endochondral ossification **(Fig. 1C)**. MΦ-conditional YAP/TAZ deletion: Conditional deletion in MΦ did not affect cortical bone morphometry in intact adult bone (data not shown). The experimental design is shown in the graphical abstract **(Fig. 2A)**. At 2 weeks post-fracture, Saf O/Fast Green staining **(Fig. 2B)** revealed persistent cartilage in KO calluses, indicating impaired resolution between fixation groups. Consistently, microCT analysis **(Fig. 2C)** showed that WT mice exhibited the expected reduction in BV/TV with compliant fixation, whereas this effect was lost in KO mice. Effects of YAP/TAZ deletion on MΦ function: In vitro, YAP/TAZ deletion suppressed TEAD targets (*Cyr61, Ctgf*; **Fig. 3A**), increased *IL-6*, and reduced *Arg1* **(Fig. 3B)**. Phalloidin staining showed morphological changes: WT MΦs displayed protrusions and small bodies, while KO MΦs appeared larger and rounded **(Fig. 3C)**. Functionally, YAP/TAZ deletion impaired phagocytosis of GFP–E. coli **(Fig. 3D)**.

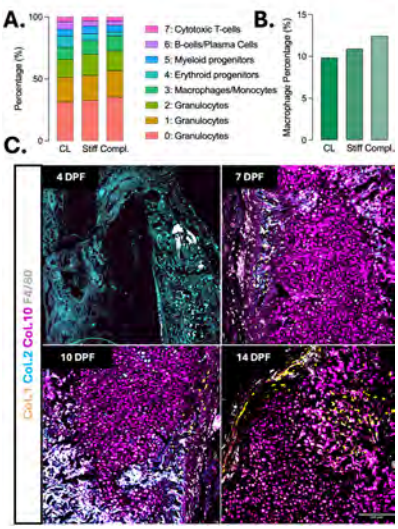

Figure 1: MΦ respond to mechanical stimuli in vivo. (A) scRNA-seq revealed eight subpopulations in the bone marrow. **(B)** Percentage of MΦs in contralateral unfractured (CL) limbs and in fractures with stiff or compliant fixation. **(C)** Immunofluorescence staining of the bone fracture callus. SB 100μm.

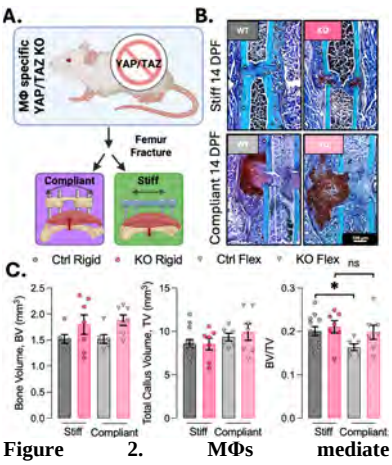

Figure 2. MΦs mediate mechanoregulation of fracture repair. (A) Experimental approach schematic. **(B)** Saf O staining of fractures with stiff vs. compliant fixation. SB 100μm. **(C)** Quantification of μCT parameters in fractured limbs. *p<0.05.

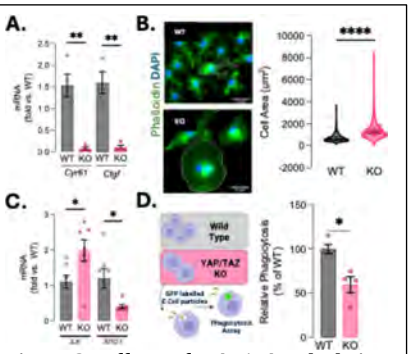

Figure 3: Effects of YAP/TAZ depletion on MΦ function. (A) qPCR of *Cyr61* and *Ctgf* expression in MΦs. (B) Actin cytoskeleton (phalloidin) and cell area quantification in of MΦs following TAT-Cre treatment. SB 25μm. **(C)** qPCR of *IL-6* and *Arg1* expression in MΦs. **(D)** Phagocytosis of GFP-labeled E. coli (% internalized GFP). *p<0.05, **p<0.01, ****p<0.0001.

Discussion: Our results reveal a critical role for YAP/TAZ signaling in macrophages in the mechanoregulation of fracture repair, shaping the cartilaginous callus milieu. MΦ-conditional YAP/TAZ deletion did not alter cortical bone morphometry, indicating that these signals are dispensable for skeletal development and homeostasis. During regeneration, however, MΦs infiltrated the callus early, co-localized with collagen-producing cells, and migrated dynamically between peripheral and central regions. Compliant fixation increased MΦ recruitment at 3 dpf, supporting mechanoregulated activation. Although cartilage callus formation was not abolished, YAP/TAZ deletion disrupted the mechanically driven endochondral response, consistent with WT MΦ localization to ossification sites. Mechanistically, we established an in vitro system using TAT-Cre to generate KO MΦs, showing that YAP/TAZ regulate cytoskeletal organization, cytokine profile, and phagocytic capacity. Together, these findings indicate that while YAP/TAZ signaling in MΦs is not required for skeletal development, YAP and TAZ direct MΦ recruitment during mechanoregulated fracture repair and regulate endochondral ossification. Ongoing studies will examine how MΦ mechanosignaling coordinates osteogenic–angiogenic coupling and functional repair.

Significance: Here we identify YAP and TAZ as mediators of MΦ activation by mechanical loading during bone repair and as regulators of MΦ state and function. Advancing our understanding of how mechanical and molecular cues regulate MΦ behavior may offer novel avenues for immunomodulatory and regenerative therapies.

References: [1] Collins+ *Dev. Cell. 2024*, **[2]** Kegelman+ *JBMR. 2020*, **[3]** Meli+ *Science Advances. 2020*.

Acknowledgements: This work was supported by the NIH [R01AR074948, P30AR069619] and the NSF [CMMI: 15-48571].

Metabolic Labeling Reveals a Critical Role for Decorin in the Assembly and Turnover of Cartilage Matrix

Thomas Li[1], Mingyue Fan[1], Annie Porter[2], Bryan Kwok[1], Chao Wang[1], David E. Birk[3], Renato V. Iozzo[4], X. Lucas Lu[1], Robert L. Mauck[5], Lin Han[1]
[1]Drexel University, Philadelphia, PA, [2]University of Delaware, Newark, DE, [3]University of South Florida, Tampa FL,
[4]Thomas Jefferson University, Philadelphia, PA, [5]University of Pennsylvania, Philadelphia, PA. Thomas Li: tl545@drexel.edu.

Disclosures: RL Mauck (4, *Mechano-Therapeutics*; 5, *4Web Medical*; 8, *JOR Spine*), no other disclosures.

INTRODUCTION: The development of effective cartilage regeneration is challenged by our incomplete understanding of molecular activities that regulate the assembly, turnover and degradation of its extracellular matrix (ECM) [1], a hydrated composite of collagen II/IX/XI fibrils and aggrecan macromolecules [2]. Our recent study identified a critical role for the small leucine-rich (SLRP) proteoglycan, decorin, in regulating the ECM integrity in both health and osteoarthritis (OA). In decorin-null ($Dcn^{-/-}$) mice, articular cartilage exhibits reduced aggrecan levels in both the pericellular matrix (PCM) and territorial/interterritorial (T/IT)-ECM, and perturbed chondrocyte mechanotransduction [3]. This role was attributed to a novel "physical linkage" function of decorin, acting to enhance aggrecan-aggrecan and aggrecan-collagen fibril molecular adhesion [4]. In cartilage ECM, aggrecan undergoes active turnover [5], with a higher turnover rate in the PCM [6]. Given the role of decorin in increasing aggrecan retention, we investigated how decorin mediates the turnover of newly synthesized proteins and glycosaminoglycans (GAGs) using a bio-orthogonal click-labeling method [7] and elucidated how decorin regulates the collagen-aggrecan integration by AFM-nanoindentation to cartilage after enzymatic GAG removal and infiltration of exogenous decorin.

METHODS: Femoral head cartilage explants were harvested from 3-week-old decorin-null ($Dcn^{-/-}$) and wild-type (WT) C57BL/6 mice. Explants were pre-cultured for 2 days, and then cultured for another 3 days with either 30 mM N-azidoacetylgalactosamine-tetraacylated (GAL) (1086, ClickChemistryTools) or L-azidohomoalanine (AHA) (1066, ClickChemistryTools) in chondrogenic DMEM [8] to metabolically label newly synthesized GAGs and proteins [7], respectively. Explants were then tagged with 30 mM AZDye 488 DBCO (1278, ClickChemistryTools) and then cultured for an additional 6 days in chondrogenic DMEM, with or without stimulation by the inflammatory cytokine IL-1β (10 ng/mL) to elicit chondrocyte catabolism [9]. GAL-labeled nascent GAGs and AHA-labeled nascent proteins released into the supernatant were collected every other day for quantification. At day 6, tissues were digested with 2% papain to quantify the nascent protein/GAG retained in the explant. Confocal images were taken at day 0 and 6 following click labeling to assess the spatial distribution of nascent proteins and GAGs within the explant, using a Zeiss LSM700 confocal microscope. Following our established procedure [4], AFM-nanoindentation was applied to quantify the indentation modulus, E_{ind}, of 3-week-old $Dcn^{-/-}$ and WT femoral condyle cartilage using a microspherical tip ($R \approx 5$ μm, $k \approx 5.4$ N/m) in PBS. The test was applied to untreated cartilage, samples in which sulfated GAG was depleted by 0.5 U/ml chondroitinase ABC and 500 U/ml hyaluronidase digestion for 24 hrs, and sGAG-depleted tissues infiltrated with exogenous bovine decorin (D8428, Sigma, 20 μg/mL for 24 hours). Repeated measure two-way ANOVA was applied to study the effects of genotype and IL-1β on GAG/protein release, and two-way ANOVA was applied to study the effects of genotype and treatment on E_{ind}, followed by Tukey-Kramer multiple comparison at $\alpha = 0.05$.

RESULTS: Fluorescence images showed clear differences in the distributions of nascent GAGs (Fig. 1a) and proteins (Fig. 1b). From the GAL-labeling, we observed a higher concentration of nascent GAGs surrounding the cells, illustrating the preferred localization of nascent proteoglycans in the PCM, with or without IL-1β stimulation. From the AHA-labeling, we observed nascent proteins distributed nearly homogeneously throughout the intercellular space. At both day 0 and 6, we did not observe appreciable differences between the WT and $Dcn^{-/-}$ explants. When stimulated with IL-1β, an increasing percentage of nascent GAGs were released from the explant for both genotypes (Fig. 2), concurrent with a substantial decrease in GAL-signal in the PCM (Fig. 1a). With and without IL-1β, a higher proportion of GAGs were released from $Dcn^{-/-}$ cartilage, with no differences noted for protein release (Fig. 1b). Under AFM-nanoindentation, for WT cartilage, sGAG removal significantly reduced tissue modulus; this could be partially restored by decorin infiltration. For $Dcn^{-/-}$ cartilage, the modulus of untreated tissue was lower than that of WT, and neither sGAG removal nor decorin infiltration had a significant impact (Fig. 3).

DISCUSSION: This study highlights a crucial role for decorin in regulating the active turnover and retention of newly synthesized aggrecan in healthy and degenerative cartilage. In cartilage ECM, the majority of GAGs constitute the side chains of aggrecan [10]. Thus, accelerated release of nascent GAGs from $Dcn^{-/-}$ cartilage (Fig. 2a) supports the essential role of decorin in the retention of newly synthesized aggrecan. Conversely, the lack of difference in nascent protein release (Fig. 2b) suggests that decorin does not directly impact collagen retention. Such role is crucial not only for the retention of aggrecan in healthy cartilage, but under OA-like conditions, when the fragmentation of aggrecan is aggravated by increased catabolism (e.g., IL-1β treatment).

The observation that exogenous decorin increased the modulus of sGAG-depleted WT cartilage (Fig. 3) suggests that decorin strengthens the collagen fibrillar network, likely by providing physical linkages through its leucine-rich, hydrophobic core protein to connect adjacent collagen II fibrils. In doing so, the decorin-strengthened collagen network provides higher resistance to the diffusive loss of aggrecan entrapped therein, which is driven by the high swelling pressure from the negative charges on sGAG [11]. Since the collagen fibril network is a prominent feature of both PCM and T/IT-ECM [3], decorin likely regulates the aggrecan-collagen integration in both domains. Indeed, while localization of nascent GAGs in the PCM (Fig. 1a) evidences specific interactions between aggrecan and PCM-specific molecules, this is not regulated by decorin, as nascent GAGs showed similar localization for both genotypes (Fig. 1a). Notably, addition of exogenous decorin did not rescue properties in $Dcn^{-/-}$ cartilage (Fig. 3). One explanation may be that loss of decorin alters collagen fibril structure, i.e., higher fibril heterogeneity [4], and thus, exogenous decorin is unable to effectively establish physical linkages with this altered network. In conclusion, our results highlight a critical role for decorin in both normal maintenance and disease-related cartilage remodeling.

SIGNIFICANCE/CLINICAL RELEVANCE: This study suggests a crucial role for decorin in increasing the retention of newly synthesized aggrecan by strengthening the collagen fibril network, enabling the development of decorin-based strategies for improving cartilage regeneration and OA intervention.

REFERENCES: [1] Huey+ 2012. [2] Han+ 2011. [3] Chery+ 2021. [4] Han+ 2019. [5] Lohmander+ 1999. [6] Quinn+ 1999. [7] Porter+ 2022. [8] Loebel+ 2020. [9] Li+ 2020. [10] Poole+ 1996. [11] Warren+ 2022.

ACKNOWLEDGEMENTS: This work was supported by NIH R01AR074490.

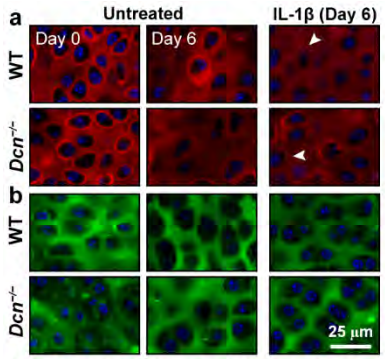

Fig. 1 Representative confocal images of click-labeled **a)** nascent GAGs by GAL and **b)** nascent proteins by AHA with (day 6) and without (day 0, 6) IL-1β stimulation.

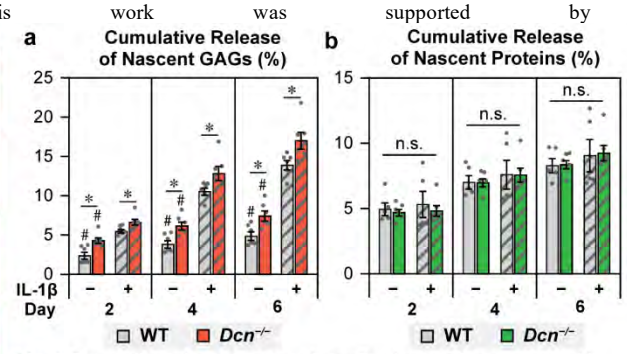

Fig. 2 Cumulative release of **a)** newly synthesized sGAGs measured by GAL and **b)** newly synthesized proteins by AHA click-labeling on WT and $Dcn^{-/-}$ P21 femoral head cartilage explants cultured with or without the stimulation of IL-1β at day 2, 4, and 6 of culture (mean ± S.E.M., $n \geq 5$, *: $p < 0.05$ between each genotypes; #: $p < 0.05$ between treatments).

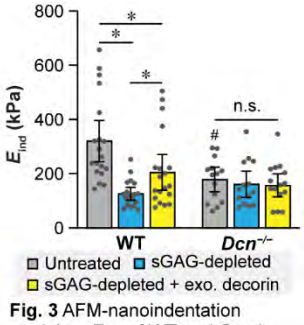

Fig. 3 AFM-nanoindentation modulus, E_{ind}, of WT and $Dcn^{-/-}$ cartilage for untreated, sGAG-depleted and decorin-infiltrated samples (mean ± 95% CI, $n \geq 14$, *: $p < 0.05$ between each treatment, #: $p < 0.05$ between genotypes).

A Novel Approach To Segmental Meniscus Repair - Can We Improve Biomechanical Performance Of Meniscus Transplants And Reduce The Risk Of Extrusion?

Hisham Omar[1], Akbar N. Syed[2], Kevin Landrum[2], Jacob Sommer[3], Kevin Shea[4], Theodore J. Ganley[2], Michael W. Hast[1,3]
[1]Dept. of Biomedical Engineering, University of Delaware, Newark, DE, [2]The Children's Hospital of Philadelphia, Philadelphia, PA, [3]Dept. of Mechanical Engineering, University of Delaware, Newark, DE, [4]Dept. of Orthopaedic Surgery, Stanford University School of Medicine, Palo Alto, CA,
ayasrah@udel.edu

Disclosures: HO (N), AS (N), KL (N), JS (N), MWH (N), KS (N), TG (N)

INTRODUCTION: Menisci act to reduce friction for knee articular cartilage, perform an essential role in load bearing by dispersing mechanical stress, and are crucial for normal knee kinematics [1]. Meniscal tears and excision of meniscal tissue have been shown to increase contact pressure in the tibiofemoral compartment, leading to accelerated osteoarthritis and other degenerative changes [2]. While meniscectomy often provides short-term symptom relief, its long-term effects on joint health are concerning [3]. Allograft meniscal transplantation is an option for adults but limited in pediatric patients due to donor scarcity and long-term survival concerns. Segmental meniscal transplantation could address these limitations; however, although various surgical repair techniques have been described, little is known about their biomechanical performance. The purpose of this study was to compare the biomechanical performance of two segmental repair techniques using cyclic loading and load to failure testing (**Fig.1**). We hypothesized that a novel suture technique will improve ultimate strength and resistance to cyclic fatigue compared to a recently described control technique.

METHODS: Twenty-four bovine meniscus explants (12 medial, 12 lateral) were prepared with a standardized segmental defect measuring approximately one-third of the meniscus length (12.6 ± 2.1 mm, **Fig. 1**). The defect was repaired using the native tissue. Two repair techniques were tested: 1) a novel technique that utilized two hashtag and two luggage tags and 2) a control technique that used four luggage tags, two horizontal and one vertical mattress suture repairs. To maintain shape of the menisci during testing, repaired specimens were mounted on custom 3D-printed PLA boards and secured with four 2.5 mm Kirschner wires. To allow for application of tensile forces on the excised segments, four additional LabralTape sutures were passed through the resected portion of the specimens. Alignment was carefully adjusted to ensure the load passed through the segment's center of mass along the desired axis. Quasi-static (n=6) and cyclic (n=6) uniaxial tension protocols were performed in universal test frames using custom jigs and grips. For the quasi-static experiments, specimens were loaded to failure at a rate of 1 mm/s. Cyclic tests consisted of 1000 loading cycles between 20 and 50 N, followed by a ramp to failure at 1 mm/s. Outcomes included stiffness, maximum force, and failure mode for all specimens, as well as plastic deformation and survival analysis for cyclic tests. Statistical analysis was performed using a one-way ANOVA with significance set at $p < 0.05$.

RESULTS: The novel repair technique demonstrated significantly higher maximum load to failure in both static (311.9 ± 26.2 N vs. 209.5 ± 82.6 N, $p = 0.0159$) and dynamic tests (339.0 ± 43.0 N vs. 181.0 ± 89.0 N, $p = 0.0029$) compared to the control group (**Fig. 2A**). Stiffness was not significantly different between groups in either test (not shown). During cyclic loading, plastic deformation increased significantly between 100 and 500 cycles in both groups, but no differences were observed between groups at any cycle count (**Fig. 2B**). Survival analysis showed that 33% of control specimens failed before completing 1000 cycles, whereas all novel repairs survived (**Fig. 2C**).

DISCUSSION: The results of this study confirmed our hypothesis that the novel repair provides superior biomechanical performance compared to the control technique. The significantly higher ultimate failure loads in both quasi-static and post cyclic testing suggest that this technique can better withstand forces experienced by the meniscus during routine knee loading. Although stiffness was not significantly different between groups, the ability of the novel repair to survive 1000 cycles without failure indicates that its suture configuration more effectively distributes load across the tissue. This study had several limitations. Repairs were performed in an open setting rather than arthroscopically which affects suture placement compared to clinical practice. In addition, cyclic loading was uniaxial and does not capture the complex, multi-directional forces experienced in vivo. Future work should focus on in vivo validation, including biological integration at the graft host interface, as well as arthroscopic implementation to replicate surgical conditions.

SIGNIFICANCE/CLINICAL RELEVANCE: The novel repair technique provides stronger fixation and greater resistance to cyclic fatigue. This approach could expand surgical options for pediatric patients who are poor candidates for total meniscal allograft transplantation by preserving native tissue and reducing long-term joint degeneration.

REFERENCES: [1] Mameri+, Curr. Rev. Musculoskelet. Med., 2022; [2] Caldwell+, Oper. Tech. Sports Med., 1994; [3] Ozeki+, Life, 2022. SS

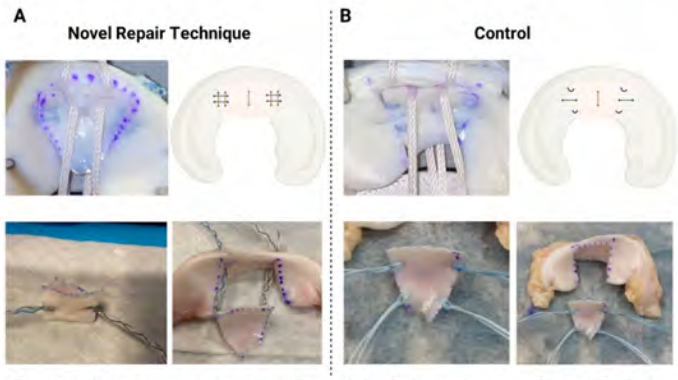

Figure 1: Two segmental meniscal repair techniques were evaluated. Left: Novel repair with two hashtag and two luggage tags. Right: Control repair with four luggage tags, two horizontal and one vertical mattress suture repairs.

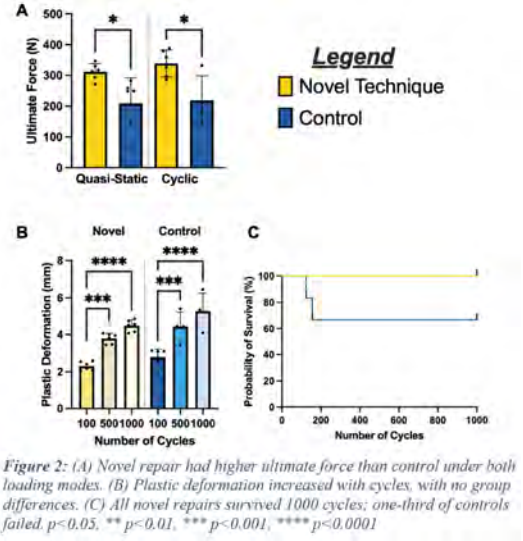

*Figure 2: (A) Novel repair had higher ultimate force than control under both loading modes. (B) Plastic deformation increased with cycles, with no group differences. (C) All novel repairs survived 1000 cycles; one-third of controls failed. p<0.05, ** p<0.01, *** p<0.001, **** p<0.0001*

Scleraxis-Targeted Collagen XII Knockout Alters Mouse Achilles Tendon Structure, Function and Gene Expression during Postnatal Development

Michael S. DiStefano, Srish S. Chenna, Louis J. Soslowsky
McKay Orthopaedic Research Laboratory, University of Pennsylvania, Philadelphia, PA
micdis@seas.upenn.edu

Disclosures: None

INTRODUCTION: Collagen XII is a Fibril-Associated Collagen with Interrupted Triple Helices (FACIT) primarily expressed during tendon growth and development [1]. Mutations in the *Col12a1* gene result in myopathic Ehlers-Danlos syndrome (mEDS), a connective tissue disorder in which patients exhibit weakness at birth, absence of deep tendon reflexes, and distal joint hypermobility and contracture [2]. We demonstrated that mature tendon-targeted knockout Achilles tendons (ATs) exhibited reduced elastic and viscoelastic mechanical properties and collagen fiber realignment relative to wild type control tendons [3]. Despite these differences in mature tendons, the roles of collagen XII on tendon structure, function, and gene expression throughout postnatal AT development remain unknown. Therefore, the objective of this study was to elucidate the roles of collagen XII on AT structure, mechanical function, and gene expression in developing postnatal mice. We hypothesized that tendon-targeted knockout of collagen XII would disrupt tendon homeostasis, leading to altered AT mechanics, morphology, and gene expression, with more notable differences at later postnatal developmental timepoints when ECM establishment and maturation are occurring.

METHODS: Animals: Male and female postnatal day (P) 10, 30 and 60 tendon-targeted collagen XII knockout (ScxCre;*Col12a1*$^{f/f}$; KO) and wild type Cre- littermate control mice (WT) were used (IACUC approved). Tendon Mechanics (n=10/group): ATs were measured with a laser displacement sensor to quantify cross-sectional area (CSA) and subjected to our mechanical testing protocol [3]. Tendon Morphology (n=5/group): Whole ankle and knee joints were fixed, decalcified, paraffin embedded, sectioned in the sagittal plane, and stained with toluidine blue to assess morphology and measure tendon length. Gene Expression (n=9-10/group): AT RNA was isolated and converted to cDNA, pre-amplified and loaded into Standard BioTools 96.96 Dynamic Array. Target genes included those of collagens, non-collagenous matrix, remodeling, cell-ECM, and cell-cell markers. Statistics: At each age, WT and KO data were compared using two-tailed t-tests with significance at $p \leq 0.05$ and trends at $p \leq 0.1$.

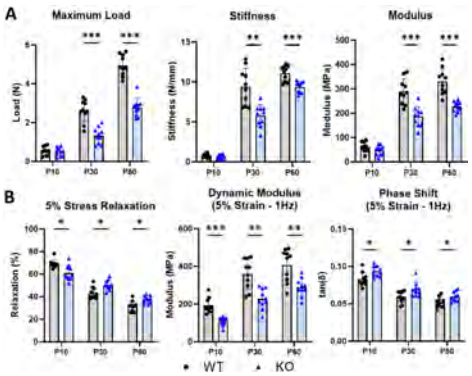

Figure 1. (A) KO tendons demonstrated reduced elastic mechanical properties at P30 and P60 and altered (B) viscoelastic mechanical properties across all ages. Data as mean ± standard deviation (*p≤0.05, **p≤0.01, ***p≤0.001).

RESULTS: Tendon Mechanics: CSA was not different across genotypes (data not shown). Elastic mechanical properties, maximum load, stiffness, and modulus (**Fig. 1A**) were reduced in KO tendons at P30 and P60. Percent relaxation was decreased in KO tendons at P10 and increased at P30 and P60 across all strain levels (5% strain shown in **Fig. 1B**). At all ages, dynamic modulus was decreased in KO tendons, while phase shift was increased in KO tendons across strain levels and frequencies (5% strain at 1Hz shown in **Fig. 1B**). Tendon Morphology: KO tendons exhibited elongation between the myotendinous junction (MTJ) and enthesis (E) relative to WT tendons at all ages (P30 shown **Fig. 2A**). Further, ATs in KO mice were longer than WT at all ages (**Fig. 2B**). Tendon Gene Expression: As expected, *Col12a1* expression was reduced in KO tendons (**Fig. 3A**). Principal Component Analysis (PCA) revealed clustering by genotype at P30 and P60 (P60 shown in **Fig. 3B**). Additionally, the volcano and deltaCt (dCt) plots at P60 highlight the magnitude of gene expression differences, with *Col12a1*, *Gja1* (Connexin43 gene), *Gdf5*, and *Sparc* downregulated and *Postn*, *Thbs4*, and *Mstn* upregulated in KO tendons relative to WT tendons (**Figs. 3C-D**).

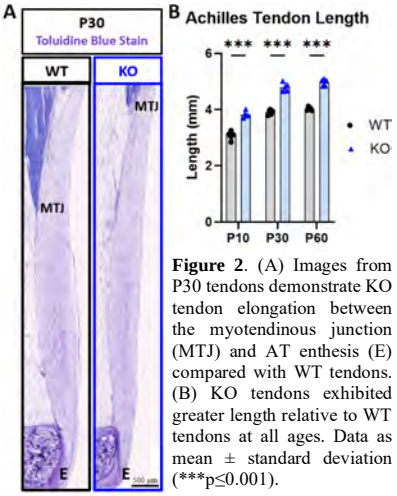

Figure 2. (A) Images from P30 tendons demonstrate KO tendon elongation between the myotendinous junction (MTJ) and AT enthesis (E) compared with WT tendons. (B) KO tendons exhibited greater length relative to WT tendons at all ages. Data as mean ± standard deviation (***p≤0.001).

DISCUSSION: This study highlights the regulatory roles of collagen XII in AT structure, mechanical properties, and gene expression. Consistent with our hypothesis, KO tendons demonstrated more notable alterations in elastic and viscoelastic mechanics, tendon morphology, and gene expression at later postnatal timepoints. Sustained increased length and decreased mechanics at later ages could be related to impaired development of the calcaneal enthesis of the AT, where the absence of an anchoring point disrupts mechanical cues critical for proper tendon development [4]. We observed decreased expression of *Gja1* and *Gdf5* in KO tendons at P60. Prior studies showed that *Gja1* and *Gdf5* are critical for regulating tendon mechanics, enthesis formation, and response to loading [4,5]. Additionally, work in osteoblasts demonstrated that absence of collagen XII resulted in decreased *Gja1* expression [6], further supporting our *Gja1* findings from P60 KO tendons. These results suggest that the absence of *Col12a1* may have a direct effect on normal AT and enthesis development. We also observed reduced *Sparc* expression in KO tendons at P60. Prior studies demonstrated load-induced regulation of AT maturation, homeostasis, and enthesis development by *Sparc* during postnatal development [7,8]. We previously showed that KO mice have reduced grip strength, indicating muscle weakness [1], which may be further supported by upregulated *Mstn*, a negative regulator of muscle mass [9], expression in the P60 KO tendons of this study. Given these results, future studies will identify the mechanisms involved with altered mechanical loading and absence of collagen XII on development of AT structure and function, particularly at its enthesis.

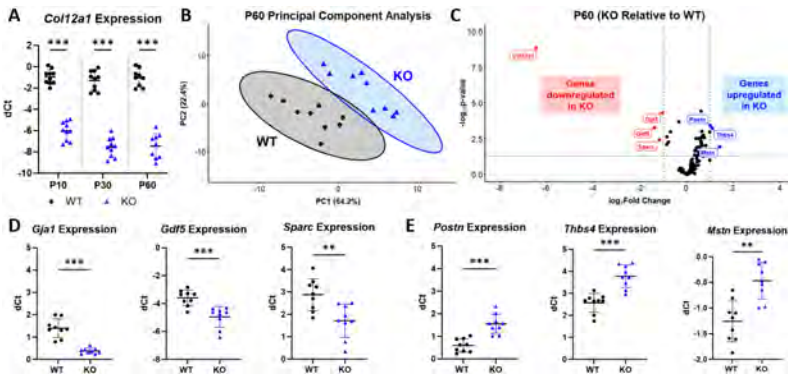

Figure 3. (A) *Col12a1* expression is reduced in KO mice at all ages. (B) PCA demonstrated clustering based on genotype at P60. (C) Volcano plot shows differential gene expression at P60, with (D) downregulated and (E) upregulated genes expressed in KO tendons relative to WT tendons. Data as mean ± standard deviation (**p≤0.01, ***p≤0.001).

SIGNIFICANCE/CLINICAL RELEVANCE: This study elucidates the critical role of collagen XII in regulating AT structure, function and gene expression during postnatal development which will inform the pathogenesis of mEDS in tendon and potentially inform future treatments.

ACKNOWLEDGEMENTS: Study supported by NIH/NIAMS F31AR083255, NIH/NIAMS R01AR078790 and NIH/NIAMS P30AR069619.

REFERENCES: [1] Fung et al. *Matrix Biol Plus*. 2022. [2] Punetha et al. *Muscle Nerve*. 2017. [3] DiStefano et al. ORS. 2022. [4] Shen et al. *J Bone Miner Res*. 2020. [5] Mikic et al. *J Orthop Res*. 2006. [6] Izu et al. *The J Cell Biol*. 2011. [7] Gehwolf et al. *Sci Rep*. 2016. [8] Wang et al. *Sci Transl Med*. 2021. [9] Tobin et al. *Curr Opin Pharmacol*. 2005.

The Temporal Role of Collagen XII in Mouse Tendon Healing

Jacob C. Nixon[1], Stephanie N. Weiss[1], Nathaniel A. Dyment[1], Louis J. Soslowsky[1]
[1]McKay Orthopaedic Research Laboratory, University of Pennsylvania, Philadelphia, PA
jacobnix@seas.upenn.edu

Disclosures: Jacob C. Nixon (N), Stephanie N. Weiss (N), Nathaniel A. Dyment (N), Louis J. Soslowsky (N)

INTRODUCTION: Collagen XII is a non-fibrillar collagen involved in cell and matrix interactions [1]. Mutations of the *Col12a1* gene are clinically associated with myopathic Ehlers-Danlos syndrome (mEDS), a congenital disorder characterized by symptoms such as distal joint hypermobility, an absence of deep tendon reflexes, and abnormal wound healing [2] – implicating a role for collagen XII in the response to tendon injury. Our previous work has shown that the patellar tendons (PTs) of tendon-targeted *Col12a1* knockout mice have increased matrix disorganization and altered cell morphology during early postnatal growth and reduced modulus and fiber re-alignment near maturity [3], indicating that collagen XII plays a critical role in cell and extracellular matrix (ECM) organization and, thus, the proper structure and function of tendons. However, the role of collagen XII in re-establishing cell and ECM organization during tendon healing remains unknown. Therefore, the objective of this study was to determine the temporal roles of collagen XII in restoring the structure, function, and composition of the healing murine tendon. We hypothesized that collagen XII knockdown would result in disrupted structure and composition and in concomitantly reduced improvements in tendon mechanical properties during healing and that knockdown at time of injury would impair the tendon healing response more than knockdown 1-week post-injury.

METHODS: Male and female global inducible collagen XII knockdown mice (*Rosa-CreER^{T2};Col12a1$^{flox/flox}$*; KO) and *CreER^{T2}*- littermate control mice (Ctrl) were used (IACUC approved). At 90 days old, mice underwent bilateral patellar tendon injury surgery as described [4], and *Cre* excision of the conditional alleles was induced via 4 consecutive daily IP injections of tamoxifen beginning at 1 day pre-injury (TM0) or 6 days post-injury (TM7). TM0 mice were sacrificed at 1-, 2-, or 4-week(s) post-injury; TM7 mice were sacrificed at 2- or 4-weeks post-injury. An additional group of uninjured control mice received tamoxifen at either of the previously mentioned time points and were sacrificed at 110 days old. Mechanical testing: PTs (n=10-12/group) were prepared and evaluated mechanically using a viscoelastic testing protocol, as described [4]. Briefly, tendons were pre-conditioned; subjected to two stress relaxations at 1% and 4% nominal strain, each followed by a dynamic frequency sweep at 0.1, 1, 5, and 10 Hz; and then loaded in a ramp to failure at 0.1%/s nominal strain rate. Transmission electron microscopy (TEM): PTs (n=4-5/group) were prepared and imaged as described [4]. The injured tissue was uniformly sampled to measure fibril diameter distribution. Gene expression: RNA was extracted from whole PTs (n=6/group), converted to cDNA, pre-amplified, and submitted to a Fluidigm Dynamic Array IFC against a panel of 93 genes (plus housekeepers *Abl1* and *Rps17*). Statistical treatment: Outliers were removed before performing analyses. For mechanical parameters, two-factor ANOVAs by genotype and healing time point with post-hoc Tukey's HSD for each induction time point were conducted. For TEM distributions, Kolmogorov-Smirnov tests by genotype for each healing time point and induction time point were conducted. For gene expression, t-tests by genotype for each healing time point and induction time point were conducted. Significance was set at $p < 0.05$.

RESULTS: Mechanical testing: No differences were detected between genotypes for any mechanical properties at any healing or induction time point (**Fig 1**). TEM: Knockdown resulted in an initial minor shift toward smaller fibril diameters at 2-weeks post-injury (**Fig 2A**) and a later minor shift toward larger fibril diameters at 4-weeks post-injury (**Fig 2B**). This finding was present for both induction time points. Gene expression: Tamoxifen injection resulted in an expected downregulation of *Col12a1* expression for all healing time points and induction time points. For TM0, *Acan* was downregulated due to knockdown at 2-weeks post-injury (**Fig 3A**). For TM7, *Mmp9*, *Fbn2*, *Spp1*, and *Mki67* were downregulated and *Ctgf* and *Serpine1* were upregulated due to knockdown at 2-weeks post-injury (**Fig 3B**); *Has1* was downregulated and *Col2a1* was upregulated due to knockdown at 4 weeks post-injury (data not shown).

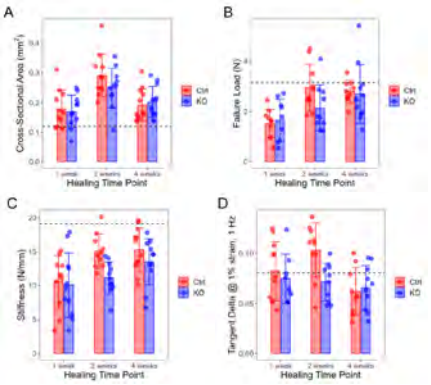

Figure 1. Knockdown of collagen XII had no effect on tendon (A) cross-sectional area, (B) failure load, (C) stiffness, or (D) tangent delta at 1% strain, 1 Hz at any healing or induction time point. Data represented as mean ± standard deviation. The average of the uninjured group is plotted as a dashed

DISCUSSION: This study investigated the temporal role of collagen XII in tendon structure, function, and composition following injury using conditional deletion both at the time of injury and at 1-week post-injury. Surprisingly, knockdown of collagen XII had no effect on the mechanical properties of injured PTs and had minimal effects on the expression of genes related to tendon healing, consistent with the effect of collagen XII knockdown on the mechanical properties and gene expression of skin granulation tissue [5]. Knockdown of collagen XII did, however, alter tendon structure during healing, resulting in an early shift to smaller fibril diameters and a later shift to larger fibril diameters. While our previous work showed a critical role of collagen XII in regulating cell arrangement rather than initial ECM assembly during tendon development [3], surprisingly, this study suggests that collagen XII may not play a similar role during tendon healing. Furthermore, our induction time points were chosen to isolate the role of collagen XII in the proliferation and arrangement of peritenon-derived stem cells during the first week post-injury. Thus, the lack of differences between induction time points indicates that collagen XII may instead play a more substantial role in ECM deposition, fibril growth dynamics, and subsequent remodeling during the later phases of healing. Further studies will assess the role of collagen XII in cell and ECM organization during tendon healing using histological methods.

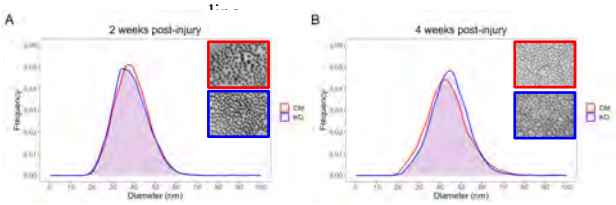

Figure 2. (A) Knockdown of collagen XII resulted in slightly decreased fibril diameters at 2-weeks post-injury. (B) Knockdown of collagen XII resulted in slightly increased fibril diameters at 4-weeks post-injury. Only TM0 data is shown. Representative images are inlaid at the top right.

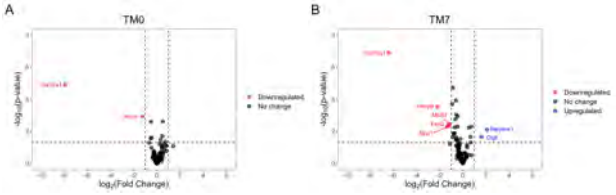

Figure 3. Knockdown of collagen XII had minimal effects on tendon gene expression at 2-weeks post-injury (A) for TM0 and (B) for TM7. Genes that were significantly ($p < 0.05$) upregulated or downregulated compared to littermate controls are labelled.

SIGNIFICANCE: Collagen XII does not regulate tendon mechanical function and composition but does alter tendon structure during tendon healing, suggesting that collagen XII may have minimal importance in re-establishing tendon structure-function at this age following injury.

REFERENCES: [1] Izu and Birk. *Front Cell Dev Biol*. 2023. [2] Zou, et. al. *Hum Mol Genet*. 2014. [3] Fung. University of Pennsylvania. 2023. [4] Leahy, et. al. *J Orthop Res*. 2023. [5] Schönborn, et. al. *Matrix Biol*. 2020.

ACKNOWLEDGMENTS: The authors acknowledge the assistance of Courtney Nuss in sample preparation for TEM. This study was supported by NIH/NIAMS R01AR078790 and T32AR007132 and the Penn Center for Musculoskeletal Disorders (P30AR069619).

Computed Tomography-Based Assessment of Subtrochanteric Cortical Density in Bisphosphonate-Related Atypical Femoral Fracture

Christiana L. Cottrell[1], Chiara M. Oshiro[2], Sujay S. Garlapati[1], Mahdi M. Hurreh[2], Alyssa C. Rosen[2], Sri Drishaal Kumar[2], Holly D. Nguyen[1], Dylan L. Bellissimo-Meade[2], Allison Y. Tang[2], Hansen Liu[2], Jonathan L. Gao[2], Rashad Madi[2,3], Ani Ural[4], Rebecca Willcocks[5], Bruce Kneeland[2], Neil Sheth[2], Elena Taratuta[2], Rui Feng[2], Haviva M. Goldman[1], Chamith S. Rajapakse[2]
[1]Drexel University College of Medicine, Philadelphia, PA, [2]University of Pennsylvania, Philadelphia, PA, [3]Saint Vincent Hospital, Worcester, MA [4]Villanova University, Villanova, PA, [5]University of Florida, Gainesville, FL
clc456@drexel.edu

Disclosures: Christiana L. Cottrell (N), Chiara M. Oshiro (N), Sujay S. Garlapati (N), Mahdi M. Hurreh (N), Sri Drishaal Kumar (N), Holly D. Nguyen (N), Alyssa C. Rosen (N), Dylan L. Bellissimo-Meade (N), Allison Y. Tang (N), Hansen Liu (N), Jonathan L. Gao (N), Rashad Madi (N), Rebecca Willcocks (N), Ani Ural (N), Bruce Kneeland (N), Neil Sheth (N), Elena Taratuta (N), Rui Feng (N), Haviva M. Goldman (N), Chamith S. Rajapakse (N)

INTRODUCTION: Chronic bisphosphonate therapy has been linked to atypical femoral fracture (AFF), a rare but serious subtrochanteric fragility fracture. The risk factors underlying AFF susceptibility remain poorly understood, and the use of minimally invasive medical imaging to characterize cortical properties at AFF-prone sites remains largely unexplored. The current standard clinical protocol for assessing osteoporotic fracture risk includes DXA-derived bone mineral density (BMD) and fracture risk assessment but is limited in evaluating AFF risk. Computed Tomography (CT)-derived bone mineral density, expressed in Hounsfield Units (HU), is a key biomarker for fracture risk and may characterize cortical changes that predispose patients to AFF. The purpose of this research is to identify clinically measurable factors associated with AFF risk in bisphosphonate-treated patients. Specifically, this study aims to characterize subtrochanteric properties in AFF patients with long-term bisphosphonate use.

METHODS: Pelvic CT scans from 30 AFF patients (3 male, 27 female) on bisphosphonates for 6.8 ± 3.9 years treated at Penn Medicine were retrospectively analyzed in this IRB-approved protocol. Digital Imaging and Communications in Medicine (DICOM) voxel dimensions were standardized to 0.5 mm^3 in 3D Slicer, and cortical HU measurements were obtained using ImageJ, utilizing 1-mm^2 region of interests (ROIs) placed in anterior, posterior, medial, and lateral cortical locations. HU values at each cortical location were recorded at 16 consecutive 1-mm intervals from the inferior border of the lesser trochanter and extending distally. Statistical analyses were performed using JMP Pro 17 (SAS Institute Inc., Cary, NC). One-way ANOVA was used to evaluate the effects of cortical location, sex, and race on bone mineral density (estimated by HU), and bivariate fits were used to assess associations between distance from the lesser trochanter, age, and BMI with respect to HU.

RESULTS: A one-way ANOVA demonstrated that cortical region had a significant effect on HU ($F(3, 2596) = 196.22$, $p < 0.0001$, $\eta^2 = 0.19$, $R^2 = 0.18$). Mean HU values varied across locations, as the lateral cortex (M = 1444.6, SE = 9.1) and medial cortex (M = 1438.2, SE = 9.2) were higher in density compared to the anterior cortex (M = 1338.1, SE = 9.1) and posterior cortex (M = 1168.4, SE = 9.2). Across 2600 cortical measurements, mean HU was 1348 ± 259, and HU increased distally ($r = 0.067$, 95% CI [0.029–0.105], $p = 0.0006$). Bivariate linear regression showed an average increase of 3.8 HU per millimeter ($F(1, 2598) = 11.75$, $p < 0.0001$, $R^2 = 0.005$), and an average decrease of 5.74 HU per one-point increase in BMI ($F(1, 2598) = 24.55$, $p < 0.0001$, $R^2 = 0.009$). One-way Anova highlighted that HU varied significantly by race ($F(3, 2596) = 55.15$; $p < 0.0001$; $R^2 = 0.060$), with African-American patients demonstrating the lowest HU (n = 6, 1226.8 ± 11.2), followed by Asian patients (n = 8; 1361.2 ± 9.7) and White patients (n = 14; 1371.4 ± 7.3), while Hispanic/Latino patients had the highest HU (n = 2, 1443.3 ± 15.7).

DISCUSSION: This study demonstrates that subtrochanteric cortical location contributes significantly to HU-derived cortical bone density patterns among chronic bisphosphonate users with AFF. Cortical location accounted for 18% of the variance in HU, whereas distance from the lesser trochanter explained less than 1% of the variance, indicating that cortical location has greater influence on HU than the distance distal to the lesser trochanter. The medial and lateral cortices demonstrated higher HU values compared to the anterior and posterior regions, which is consistent with previous literature that recorded lateral cortical thickening and bone heterogeneity as predictive factors for AFF in long-term bisphosphonate users.
The limitations of this study include limited sample size due to the rarity of AFF, which may have affected statistical power. Furthermore, variability in scan timing relative to fracture, scanner kVp and contrast parameters, and the presence of joint replacement artifacts may have impacted imaging results. Despite these limitations, this study offers novel insights through monitoring in vivo BMD estimates at sixteen incremental distances in 4 different cortical locations, creating a highly detailed characterization not previously reported in AFF research. Future research will standardize scan methodology and examine demographically matched bisphosphonate-treated patients without AFF to determine femoral traits associated with increased fracture susceptibility.

SIGNIFICANCE: Cortical location has greater influence in bone density measurement variation than distance from the lesser trochanter when assessing the risk of AFF in long-term bisphosphonate users. These findings underscore the need to standardize the methodology for determining AFF risk. Given that CT scans are performed for various reasons, opportunistic analysis of these scans can be used to identify patients at an elevated risk for AFF. Further studies are required to validate these observations and establish which cortical location best predicts AFF susceptibility.

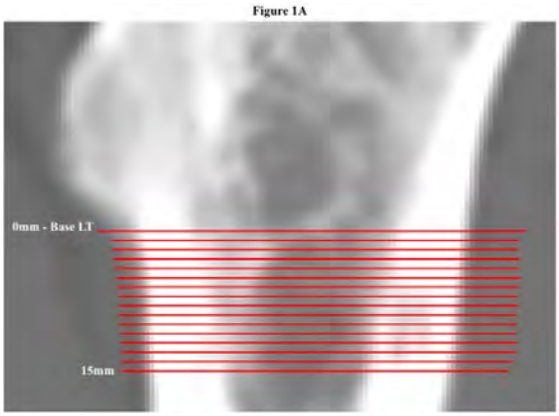

Figure 1. Method of conducting HU measurements: **1A.** Starting position for cortical HU measurements: from the base of the lesser trochanter distally at 1mm increments for 15 mm. **1B.** ROI placement by cortical location (Anterior, Posterior, Medial, Lateral).

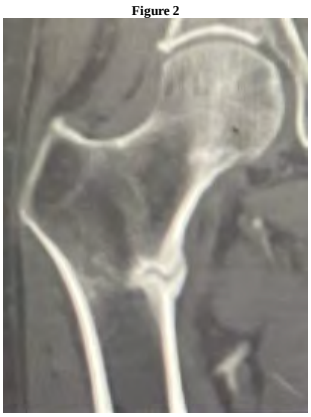

Figure 2. AFF at the level of the lesser trochanter in a patient on chronic bisphosphonate therapy

Cell-Instructive Hydrogel Platform with On-Demand Mechanical Regulation for Modeling Myelofibrosis

Authors: Kexin ZHANG[1*], Hardik MAKKAR[2*], Nghi TRAN[3], Kyle H. VINING[1,2,4]

Affiliations:

1 Department of Materials Science and Engineering, School of Engineering and Applied Sciences, University of Pennsylvania

2 Center for Innovation & Precision Dentistry (CiPD), School of Dental Medicine, University of Pennsylvania.

3 Department of Bioengineering, School of Engineering and Applied Sciences, University of Pennsylvania

4 Department of Preventive and Restorative Sciences, School of Dental Medicine, University of Pennsylvania

[*] Equal contribution as first author

Correspondence: Kyle Vining, viningk@upenn.edu

Myelofibrosis (MF) is a progressive bone marrow disorder characterized by excessive extracellular matrix (ECM) deposition that disrupts hematopoiesis and drives chronic inflammation. While fibrosis-associated ECM remodeling is a hallmark of MF, how the evolving mechanical microenvironment contributes to stromal cell dysfunction remains poorly understood. We hypothesize that progressive ECM stiffening can reprogram the phenotypes of bone marrow mesenchymal stromal cells (BM-MSCs) and direct their immunoregulatory functions.

To investigate how extracellular mechanical cues regulate BM-MSCs behavior, we developed a dynamically tunable biopolymer-based hydrogel that captures the mechanical evolution of the fibrotic BM niche. An interpenetrating network (IPN) was formed using ionically crosslinked tetrazine-functionalized alginate (Tz-VLVG) and self-assembled collagen type I, which was subsequently stiffened by the addition of norbornene-functionalized polyethylene glycol (PEG-Nb) crosslinkers. This on-demand stiffening approach enables a tenfold increase in storage modulus (G') and significantly slower stress relaxation, mimicking the transition from healthy to fibrotic BM tissue *in situ*.

3D encapsulated BM-MSCs within the hydrogel exhibited spreading ability pre- and post-stiffening. Inhibition of actomyosin contractility, integrin β1 binding, or focal adhesion kinase (FAK) signaling resulted in confined cell morphology. To probe inflammatory responsiveness, a toll-like receptor (TLR) agonist, lipopolysaccharide (LPS), was applied concurrently with the treatments, unveiling a stiffness-dependent change in the secretion profile of IL-6, IL-8, and CCL2.

Our study establishes a mechanically dynamic 3D model that directly links ECM stiffening to stromal inflammatory activation in MF. This platform provides a physiologically relevant testbed for dissecting the mechanobiological regulation of disease progression and for evaluating anti-fibrotic and immunomodulatory therapies.

Title: Designing Tunable Elastin-Like Protein Hydrogels to Study Skeletal Muscle Tissue Differentiation

Authors: Andre Roots, Christopher Madl

Skeletal muscle responds to changes in the extracellular matrix, the polymeric meshwork surrounding cells that is responsible for providing structure and regulating cell behavior. Forces transmitted by the extracellular matrix result in intracellular changes, a dynamic process known as mechanosensing. Improper mechanosensing may be associated with heritable muscle-wasting conditions, muscle injuries, and aging-related muscle loss. Previous 3D in vitro models have used purified animal proteins as hydrogel components, which do not permit independent chemical and mechanical tunability. Thus, studying independent effects from stiffness, viscoelasticity, degradation, and cell adhesive ligand presentation on in vitro muscle tissue assembly and regeneration has been hampered by the nature of the ECM materials used. To provide greater control over ECM-related signaling, we aim to design a platform with the ability to independently tune bulk stiffness, stress relaxation rate, proteolytic degradability, and cell adhesive ligand presentation. We are engineering a family of elastin-like proteins (ELPs), genetically encodable and modular intrinsically disordered proteins, that have independent primary covalent crosslinking sites, tunable network connectivity, and modular adhesive and degradation motifs. We employ poly(ethylene glycol) crosslinkers to produce covalently crosslinked ELP hydrogels with RGD adhesive cues to assess the effect of changes in stiffness, viscoelasticity, and network architecture on the assembly of functional in vitro muscle microtissues, focusing on re-quiescence of satellite-like cells and terminal differentiation of myotubes. We anticipate that these model systems will provide novel insight into the biophysical regulation of muscle regeneration in the context of aging and disease.

Plasma-Assisted AgNP Functionalized 3D-Printed Lattice Scaffolds with Tunable Stiffness and Surface Curvature for Enhanced Osteogenic Differentiation

Pratheesh K Vijaya Kumari[1], Jasmine Carpenter[1], Derrick Dean[1], Vineeth M Vijayan[*1]

Department of Biomedical and Mechanical Engineering, Alabama State University, Montgomery, AL 36104, USA

Email: pkumari@alasu.edu, jcarpenter6040@myasu.alasu.edu, ddean@alasu.edu, vviijayan@alasu.edu

Replicating the hierarchical architecture and dynamic properties of native bone remains a central challenge in bone tissue engineering.[1]. The limitations of current bone grafting techniques including donor site morbidity, limited tissue availability, and inconsistent integration underscore the need for synthetic scaffold-based alternatives. In this study, we developed 3D-printed triply periodic minimal surface (TPMS) gyroid lattice scaffolds fabricated from polylactic acid (PLA) and functionalized with silver nanoparticles (AgNPs) using a low-temperature plasma-assisted process. The approach aims to create scaffolds that emulate the mechanical performance of trabecular bone while introducing nanoscale bioactivity.

Building on the hypothesis that silver nanoparticle–mediated plasma nano structuring enhances osteogenic differentiation by improving interfacial chemistry, we systematically investigated a range of AgNP precursor concentrations to identify the optimal non-cytotoxic, bioactive silver level. Independently, computationally designed gyroid scaffolds with varying strut thicknesses and surface curvature were fabricated to tune stiffness within the trabecular bone range and evaluated how lattice geometry–driven mechanical cues, in combination with surface nanocoating and influence osteogenic outcomes. To further improve nanoparticle adhesion and bioactivity, all scaffolds were pre-coated with polydopamine (PDA), enabling uniform AgNP deposition and synergistic enhancement of surface chemistry and topography. To optimize the plasma-assisted silver functionalization process, six AgNP precursor concentrations (0.7–25 mM) were evaluated. Using hydrogen plasma treatment, silver nanoparticles were uniformly deposited on 3D-printed PLA scaffolds with hexagonal infills. In parallel, scaffolds were pre-coated with polydopamine (PDA) to produce PDA-AgNP composite coatings that enhance nanoparticle adhesion. SEM imaging revealed that lower precursor concentrations (≤1.5 mM) produced evenly distributed, spherical nanoparticles with strong surface attachment, whereas PDA pre-coating enabled uniform AgNP coverage even at higher concentrations (25 mM). Laser-Induced Breakdown Spectroscopy (LIBS) confirmed the presence of silver with a characteristic peak at ~546.5 nm, with peak intensity increasing proportionally to the $AgNO_3$ concentration.

Cytotoxicity testing using MTT (ISO 10993-5) and Alamar Blue assays showed high metabolic activity at ≤0.7 mM AgNP, confirming cytocompatibility on L929 fibroblast cells. Based on these findings, the optimized 0.7 mM AgNP coating was applied to 3D-printed gyroid lattice scaffolds with strut thicknesses ranging from 0.6–1.5 mm. Increasing lattice thickness elevated the compressive modulus and reduced surface curvature. Finite Element Analysis (FEA) verified that thinner lattices distributed von Mises stress more evenly, while both experimental and simulated Young's moduli increased with lattice thickness, indicating geometry-dependent stiffness.

Confocal microscopy revealed enhanced cytoskeletal organization and cell attachment on thinner lattices with PDA–AgNP coatings, highlighting the interplay between bulk stiffness and surface bioactivity. Alizarin Red staining at 7, 14, and 21 days confirmed significantly higher mineralization in 0.6 mm PDA–AgNP–coated scaffolds compared to uncoated controls. These results demonstrate that osteogenesis is strongly influenced by scaffold stiffness, curvature, and plasma-based nano-coatings. Ongoing studies aim to further explore the mechanobiological mechanisms underlying these responses, providing deeper insight into how mechanical and surface cues cooperatively regulate stem cell differentiation for bone regeneration.

Reference

1. Zhang, W. *et al.* The synergistic effect of hierarchical micro/nano-topography and bioactive ions for enhanced osseointegration. *Biomaterials* 34, 3184–3195 (2013)

Opportunistic Osteoporosis Screening through Cervical Spine Analysis on Dental CT Scans

Nilan Nandish[1], Shilpa Shree Kuduva Ramesh[2], Weihan Chen[1], Sally Farnham[1], Dan Del Collo[1], Nikhil Maddirala[1], Michael Chang[1], Elaina Truong[1], Jaxson Nield[1], Devon Thomas[1], Lily Chen[1], Alyssa Rosen[1], Lilian Wang[1], Zara Bhatt[1], Felicia Tang[1], Alejandro Sierra[1], Steven Graham[1], Adrienne Kim[1], Iris Yang[1], Hansen Liu[1], Steven Wang[3], Anh Le[3], Chamith Rajapakse[1]

1 Department of Radiology and Orthopedic Surgery, UPenn School of Medicine, Philadelphia, USA, 2 Department of Diagnostic Sciences, UNC Adams School of Dentistry, Chapel Hill, USA, 3 Department of Oral and Maxillofacial Surgery, UPenn School of Dental Medicine, Philadelphia, USA

INTRODUCTION: Osteoporosis is a skeletal disease characterized by low bone mass and reduced bone strength, predisposing individuals to an increased risk of fractures, particularly in the elderly. Bone mineral density (BMD), typically measured using dual-energy X-ray absorptiometry (DXA), remains the clinical standard for osteoporosis diagnosis. However, many cases of low bone mass remain undiagnosed until fractures occur. With the increasing accessibility of cone-beam computed tomography (CBCT), there is growing potential for opportunistic assessment of bone quality in patients undergoing CBCT imaging for other indications. This study aims to evaluate the feasibility of using CBCT to estimate bone strength in the C2 and C3 cervical vertebrae as a means of opportunistic screening for low bone mass.

METHODS: A retrospective cross-sectional study was conducted using 600 CBCT scans (235 males, 365 females). Scans with motion artifacts or from patients with medical conditions known to affect bone metabolism were excluded. Trabecular bone strength of the C2 and C3 vertebral bodies was estimated using a finite element–based BoneHealth software tool (Precision Radiomics, University of Pennsylvania/NYU) employing an internal calibration technique. Age-related trends in bone strength were analyzed. In a subgroup of participants (n = 50) with DXA performed within ±5 years of CBCT acquisition, CBCT-derived bone strength was correlated with DXA-derived BMD and T-scores at the lumbar spine (L1–L4), femur, and hip. Statistical analyses were performed using JMP Pro 17 (SAS Institute, Cary, NC, USA).

RESULTS: Bone strength at both C2 and C3 demonstrated a significant negative correlation with age in both sexes ($p < 0.001$; C2: $r = -0.33$ females, $r = -0.31$ males; C3: $r = -0.26$ females). Peak bone strength was observed around age 50, with mean values of 1.1 ± 0.4 mg/cm³ at C2 and 1.7 ± 0.6 mg/cm³ at C3. Significant declines were evident by age 72 ± 2.5 years at C2 (0.6 ± 0.33 mg/cm³) and by age 68 ± 1.1 years at C3 (1.1 ± 0.3 mg/cm³). In the DXA subgroup, CBCT-derived C2 and C3 strength values showed moderate positive correlations with DXA-based femur and hip BMD and T-scores ($r = 0.29–0.50$, $p < 0.05$).

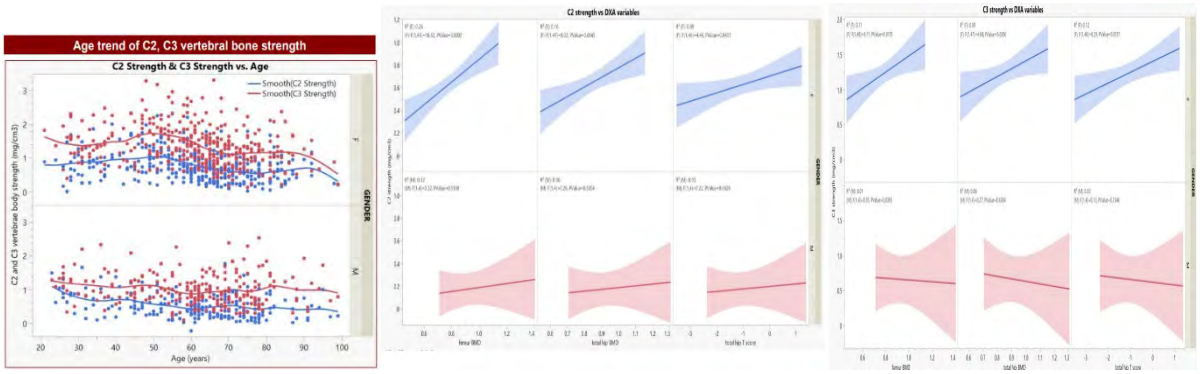

Figure 1. Age Trend of C2, C3 Vertebral Strength. Figure 2: Correlation of C2 Vertebral Bone Strength vs DXA Variables. Figure 3: Correlation of C3 Vertebral Bone Strength vs DXA Variables.

DISCUSSION: This study provides novel insights into age-related declines in cervical vertebral bone strength. The strong negative correlation between age and bone strength at C2 and C3 mirrors established patterns of decreasing BMD with aging. Peak bone strength was observed during the third decade of life, consistent with previous literature identifying this period as critical for achieving maximal bone mass. The notable decline in bone strength between ages 50 and 60 coincides with the menopausal transition, underscoring the influence of hormonal changes on skeletal health and corroborating findings from longitudinal BMD studies. Importantly, this study demonstrates the potential of CBCT—commonly acquired for dental and maxillofacial purposes—as a low-dose, readily available tool for opportunistic bone health assessment. Because most large field-of-view CBCT scans encompass cervical vertebrae C1–C3, such images could enable early identification of individuals with low bone mass who might otherwise remain asymptomatic. Establishing bone strength reference percentiles across age groups, particularly around menopause, provides a valuable framework for clinical assessment. Nonetheless, the study's cross-sectional design does not account for confounding factors such as physical activity, genetic background, or dietary influences, which may affect bone strength.

SIGNIFICANCE/CLINICAL RELEVANCE: Despite inherent limitations in CBCT Hounsfield unit accuracy and gray-value uniformity, this study demonstrates that C2 and C3 vertebral bone strength varies predictably with age and sex and correlates with BMD in weight-bearing sites. CBCT therefore represents a practical, low-radiation, three-dimensional alternative to DXA for opportunistic screening of low bone mass. As CBCT use continues to expand, this approach may facilitate earlier detection and management of osteoporosis in broader patient populations.

Penn Center *for* Musculoskeletal Disorders

University *of* Pennsylvania

Histology Core Abstracts

PM Session

Poster 89 to 102

Intra-Articular Non-Muscle Myosin II Knockout Mitigates Pain and Synovial Hyperplasia After Joint Injury

Elizabeth Bernstein[1, 2, 3], Gabriella Garza[2], Kevin Burt[2, 3], Brett Croen[2, 3], Rachel Flaugh[2, 3], Liane Miller[2, 3], Robert Mauck[1, 2, 3], Nathaniel Dyment[1, 2]
Depts. of [1]Bioengineering and [2]Orthopaedic Surgery, University of Pennsylvania; [3]CMC VA Medical Center, Philadelphia, PA
elizabeth.bernstein@pennmedicine.upenn.edu

Disclosures: RLM (5 – 4WEB Medical)

Introduction: OA progression is characterized by changes in the mechanical properties of both the cartilage and synovium,[1,2] and these changes can impact mechanoactivation and alter the phenotype of resident cells.[3,4] Prior research has shown that disrupting mechanosignaling via intra-articular injection of either Rho or non-muscle myosin (NM-II) inhibitors improves cartilage integrity after destabilization of the medial meniscus (DMM).[4] While that study focused on the response of chondrocytes to such perturbations, the effects on other joint tissues and functional outcomes have not yet been explored. We recently developed a mouse model in which *Myh9* and *Myh10*, the genes encoding NM-IIA and NM-IIB, respectively, are both floxed allowing for their conditional deletion. Here, we sought to evaluate the effect of intra-articular NM-II ablation on cartilage, subchondral bone, and synovium, as well as pain behavior after joint injury.

Methods: All animal work was IACUC approved. DMM: To induce OA, DMM was performed on the right hind limb of Myh9$^{f/f}$;Myh10$^{f/f}$ (n=14) and WT mice (n=10). Only male mice were used as males develop more severe OA after DMM.[5] Intra-articular NM-II knockout: Mice received 2 bilateral intra-articular injections of PBS or TAT-Cre (a recombinant membrane-permeable Cre recombinase) 72 and 24 hours prior to DMM[6] (**Fig 1A**). Pain assessment: Joint hyperalgesia was assessed with a pressure application measurement device before DMM and 8 weeks after DMM. Micro-CT: 8 weeks post-DMM, joints were harvested and bone morphology was evaluated by micro-CT. Histological scoring: Synovial scoring[7] was performed on coronal H&E-stained cryosections. OARSI scoring[8] was performed on coronal Saf O/Fast Green-stained cryosections. Fibroblast-like synoviocyte (FLS) isolation: FLS were isolated from the hind paws of WT mice. *In vitro* NM-II knockdown: FLS were transfected with non-targeting or *Myh9*- and *Myh10*-targeted siRNA, and knockdown was confirmed via RT-qPCR at 48 hours. Immunofluorescence: Cells were fixed and stained for actin, αSMA, FAP, and paxillin. Morphometric analysis: Cell morphometry was analyzed using CellProfiler. RT-qPCR: Expression of αSMA (*Acta2*) and fibronectin (*Fn*) was assessed by RT-qPCR. Statistics: Outcomes were compared by two-way ANOVA with Tukey's post-hoc comparisons.

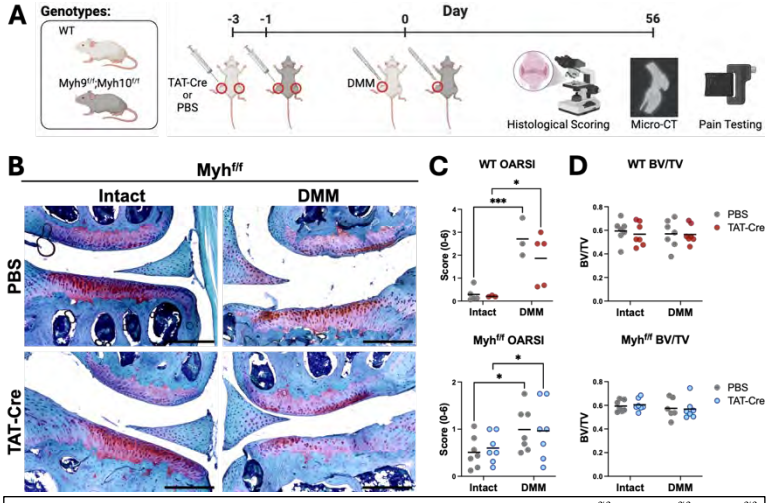

Figure 1. (A) Study design. (B) Saf O/Fast Green staining of Myh9$^{f/f}$;Myh10$^{f/f}$ (Myh$^{f/f}$) mice 8 weeks post-DMM. Scale: 250μm. (C) OARSI scoring of WT and Myh$^{f/f}$ joints. (D) Quantification of subchondral bone density via micro-CT. *p<0.05, ***p<0.001.

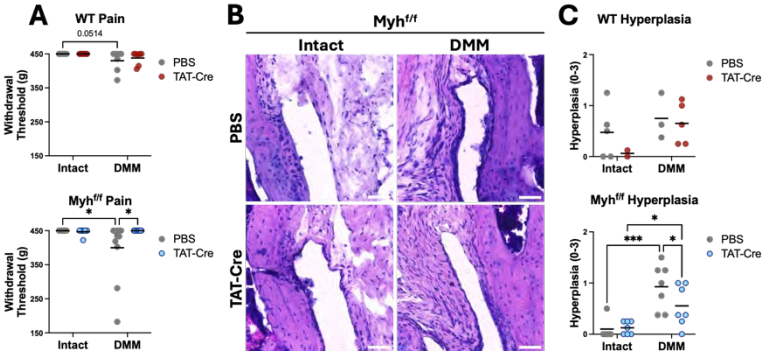

Figure 2. (A) WT and Myh9$^{f/f}$;Myh10$^{f/f}$ (Myh$^{f/f}$) knee hyperalgesia 8 weeks post-DMM. (B) Histological scoring of synovial hyperplasia. (C) H&E of Myh9$^{f/f}$;Myh10$^{f/f}$ synovium. Scale: 50μm. *p<0.05, ***p<0.001.

Results: Intra-articular NM-II ablation does not alter cartilage or subchondral bone morphology after DMM. TAT-Cre injection did not alter cartilage pathology, as OARSI scoring 8 weeks after DMM showed significant cartilage pathology in both WT and Myh9$^{f/f}$;Myh10$^{f/f}$ mice (**Fig 1B-C**). NM-II ablation also did not alter subchondral bone volume or density (**Fig 1D**). NM-II knockout mitigates pain and synovial pathology after joint injury. In WT mice, DMM reduced the pressure required to elicit paw withdrawal, indicating increased pain, with no difference observed when comparing PBS and TAT-Cre injected mice. Conversely, in Myh9$^{f/f}$;Myh10$^{f/f}$ mice, TAT-Cre injected mice had significantly higher withdrawal thresholds than PBS controls, indicating decreased pain with NM-II knockout (**Fig 2A**). TAT-Cre also reduced lining hyperplasia in Myh9$^{f/f}$;Myh10$^{f/f}$ synovium compared to PBS controls, while having no effect in WT mice (**Fig 2B-C**). NM-II knockdown disrupts FLS mechanoactivation. To investigate a potential mechanism underpinning these changes, we explored the effect of NM-II knockdown on FLS *in vitro*. Treatment with *Myh9*- and *Myh10*-targeted siRNA reduced cell spreading, increased aspect ratio, and decreased expression of αSMA and fibronectin, even under conditions that promote FLS mechanoactivation (TGFβ supplementation) (**Fig 3 A-C**).

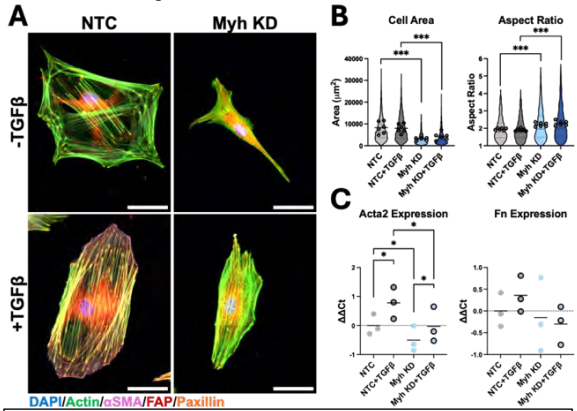

Figure 3. (A) IF of FLS without or with Myh knockdown. Scale: 50μm. (B) Quantification of cell morphology. (C) Gene expression. *p<0.05, ***p<0.001.

Discussion: Our findings demonstrate that intra-articular NM-II ablation mitigates joint hyperalgesia and lessens synovial pathology, despite persistent cartilage damage. This suggests that NM-II–mediated synovial mechanotransduction may facilitate pathological remodeling and pain in OA. Our *in vitro* data further support this, as NM-II knockdown disrupted morphological signs of mechanoactivation and expression of fibrosis-related genes. While the lack of cartilage protection was surprising given previous data on the efficacy of pharmacologic NM-II inhibition,[4] this may be due to potential poor penetration of TAT-Cre into cartilage. Ongoing work aims to understand the efficiency of TAT-Cre in various joint tissues. Future studies will also include additional functional outcomes, explore tissue micromechanics, and utilize scRNA-seq and co-culture systems to characterize cell and tissue crosstalk in the context of injury.

Significance/Clinical Relevance: This study identifies NM-II as a driver of synovial pathology and pain in OA and indicates that targeting synovial cell mechanoactivation may ameliorate OA symptoms, independent of effects on the cartilage and bone.

Acknowledgements: This work was supported by the NIH (F30 AG094106 and R01 AR075418) and the VA (I50 RX004845).

References: 1. Stolz, *Nature Nanotech*, 2009; 2. Kim, *ORS*, 2024; 3. Bonnevie, *OAC*, 2024; 4. Kim, *PNAS*, 2015; 5. Ma, *OAC*, 2007; 5. Bernstein, *ORS*, 2025; 6. Obeidat, *OAC*, 2024; 7. Glasson, *OAC*, 2010.

Bone marrow late mesenchymal progenitors regulate bone remodeling, hematopoiesis, and vasculature

Qi He[1], Qiushi Liang[1], Yanhua Lan[1], Hanli Guo[1], Kyu Sang Joeng[1], Ernestina Schipani[1], Nathaniel Dyment[1], Ivo Kajazic[2], Ling Qin[1]
[1]Department of Orthopaedic Surgery, University of Pennsylvania, [2]Center for Regenerative Medicine and Skeletal Development, University of Connecticut, USA. Presenting author: qi.he@pennmedicine.upenn.edu

Bone marrow mesenchymal progenitors play vital roles in bone turnover and serve as a microenvironment for hematopoiesis. Our previous scRNA-seq of these cells identified a late mesenchymal progenitor (LMP) population with specific αSMA (Acta2) expression. To examine this population in adult mice, we subjected 10-week-old αSMA-CreER Rosa-Tomato (αSMAER/Td) mice to Tamoxifen (Tam) injections. One week later, Td+ cells appeared in the bone marrow throughout long bones and vertebrae. They were rare in bone marrow (0.38%), composed of Pdgfrb+ mesenchymal cells and Sca1+ periarteriolar cells, with the former being the majority (88%, n=4). Over 3 months of tracing, Td+ cells were greatly diminished. These cells rarely formed CFU-Fs in vitro and did not significantly contribute to osteoblasts/osteocytes and adipocytes in vivo, suggesting they are not progenitors with self-renewal and multidifferentiation ability. Ablation of these cells in 10-week-old αSMA-CreER DTA mice by Tam injections (n= 5/group) did not affect body weight but reduced trabecular bone mass by 58.1% 6 weeks later due to decreased bone formation (54.5% in osteoblasts) and increased bone resorption (1.45-fold in osteoclasts). mTORC1 signaling is a critical regulator of bone formation. To study LMP function in vivo, we depleted Tsc1, the central upstream inhibitory regulator of mTORC1, in αSMA+ cells (Tsc1 iCKO Td) starting from 10 weeks of age. These mice (n= 5/group) had drastically increased trabecular bone mass (1.6- and 2.6-fold at 1 and 6 weeks, respectively) after Tam injections due to increased osteoblasts (2.2-fold) and reduced osteoclasts (29.2%). Td+ cells in bone marrow were transiently expanded, forming CFU-Fs in culture. However, osteoblasts remained mostly Td-, suggesting that αSMA+ cells regulate bone formation through a cell-non-autonomous manner. Additionally, marrow Cd45+ hematopoietic cells and vasculature were increased, accompanied by an increased amount of VEGFa, a growth factor critical for hematopoiesis and angiogenesis, in Td+ cells. On the contrary, inhibiting mTORC1 signaling by depleting Raptor, an mTORC1 scaffolding protein, in αSMA+ cells (Raptor iCKO Td) showed opposite bone and marrow phenotypes (n= 5/group). In summary, our data demonstrate that αSMA+ mesenchymal cells in adult bone marrow are a transient and regulatory subset critical for bone remodeling and hematopoiesis via regulating mTOR signaling pathway.

Comparative temporomandibular joint cartilage analysis to guide repair

Hannah M. Bonelli[1,2], Cristina Barbella[2,3], Dana D. Ragbirsingh[2], Hagar M. Kenawy[1,2], Riccardo Gottardi[1,2]

1. University of Pennsylvania, Philadelphia, PA 19104
2. Children's Hospital of Philadelphia, Philadelphia, PA 19104
3. Brown University, Providence RI 02912

Juvenile idiopathic arthritis is the most common form of arthritis diagnosed in children, and of that population, up to 96% can experience osteoarthritis of the temporomandibular joint (TMJOA), characterized by degeneration of the mandibular condylar cartilage. Unlike other joints, the TMJ can simultaneously function as a hinge joint and as a gliding joint. Consequently, this requires the joint to have a complex cartilage bilayered structure which consists of hyaline cartilage covered by a layer of fibrocartilage. Like other articulating joints, the TMJ is often studied using mice for genetic models and pigs or goats for reparative strategies. However, unlike other articulating joints, very little is known regarding the composition of this distinctive bilayered cartilage. In order to develop regenerative approaches for TMJOA, we first need to better understand this complex cartilage structure and how it may change across species. Notably, our preliminary data indicate that there is more elastin content within the hyaline cartilage region compared to the fibrous region, which is counterintuitive. In this work we will be presenting condylar cartilage changes across species including collagen distribution and organization, glycosaminoglycan (GAG) content, and elastin content. We will also compare native TMJ cell phenotypes from both the hyaline cartilage and fibrocartilage layers to other neural crest derived cells such as ear chondrocytes (eCCs) which could serve as a reparative cell source accessible via a minimally invasive procedure. Our results show how condylar cartilage organization and elastin content increase while GAG content decreases with increasing species size. Comparison of native TMJ cells extracted from hyaline cartilage (hyaline cartilage chondrocytes, hCCs) and fibrocartilage (fibrochondrocytes, fCCs) with eCCs suggests that with targeted modulation by growth factors in the culture medium, eCCs can secrete key cartilage components of the two native TMJ cell phenotypes. These findings demonstrate the need to study cartilage composition across species in order to better choose relevant animal models and benchmark cartilage components to assess the efficacy of selected cell sources for TMJOA repair.

Title: Regulatory T-cell targeting biomaterials for treating ischemic muscle injuries

Authors: Brennagh Shields,[†] Lauren Mottel,[†] Caroline LaSalle, Lindsay Gallagher, Brian J. Kwee

Affiliations: Department of Biomedical Engineering, University of Delaware, Newark, DE, United States

[†]These authors have contributed equally to this work
Denotes presenting author

Regulatory T-cells (Tregs) are potent anti-inflammatory immune cells that suppress pro-inflammatory immune responses, polarize regenerative macrophages, and secrete tissue specific growth factors. However, Tregs are recruited to chronic, non-healing injuries at low frequencies, resulting in degenerating pro-inflammatory microenvironments and fibrosis. We engineered injectable, oxidized (degradable by hydrolysis), calcium-crosslinked alginate hydrogels to provide sustained release of interleukin-33 (IL-33), to recruit $ST2^+$ Tregs, or amphiregulin (AREG), to activate the immunosuppressive function of $EGFR^+$ Tregs. These hydrogels were engineered to enhance the recruitment or activation of Tregs at sites of severe, ischemic muscle injuries to suppress inflammation and promote tissue repair. By incorporating charged laponite nanoparticles into the hydrogel, we enhanced the burst release and long-term rate of release of IL-33 from the hydrogel. For controlled delivery of AREG, enhancing the oxidation and degradation rate of the alginate enhanced the release of AREG. These two hydrogels were then tested in a murine model of hindlimb ischemia in BALB/c mice, where the alginate was intramuscularly injected into ischemic muscle. Treatment with the IL-33-releasing hydrogel enhanced blood perfusion recovery, trended toward enhancing the contractile muscle function, and reduced limb necrosis compared to treatment with a blank hydrogel. Application of the AREG-releasing hydrogel reduced necrosis, enhanced motor limb function, and induced structural muscle repair compared to a blank hydrogel. Furthermore, the AREG hydrogel significantly reduced the number of CD4+ T-cells and the pro-inflammatory macrophages in the ischemic muscle compared to a blank hydrogel. On-going work with the PCMD Histology Core will evaluate how these hydrogels regulate histological blood vessel, muscle, and nerve repair. Overall, this work demonstrates the immunomodulatory regenerative capacity of our Treg-targeting biomaterials as a treatment for severe skeletal muscle ischemic injuries.

A novel strategy for epigenetic and metabolic reprogramming of aged human mesenchymal stem cells

Eirene Choi[1], Matheus Moreira Perez[1], Alzbeta Chabronova[2], Amber Slaweski[1], Mandy Peffers[2], John Collins[1] and Theresa A Freeman[1].

[1]Department of Orthopedic Surgery, Thomas Jefferson University, Philadelphia, PA, United States.
[2]Department of Musculoskeletal and Ageing Science, University of Liverpool, Liverpool, United Kingdom.

Adverse cellular changes in DNA, mitochondria, and protein processing occur with cellular aging. Epigenetic and metabolic reprogramming are two strategies to slow/reverse these processes. Apoptosis Signal-Regulating Kinase 1 (ASK1) is a MAP kinase whose inhibition has been shown to slow degenerative diseases. Activation of Sirtuin 6 (SIRT6), a NAD-dependent histone deacetylase epigenetically enhances longevity. Given these respective effects, this study explores the use of an ASK1 inhibitor (Selonsertib) and a Sirtuin 6 activator (MDL-800) together to regeneratively reprogram aged human bone marrow-derived mesenchymal stem cells (hBM-MSCs). Spheroidal micromasses made from hBM-MSCs of younger (27 ± 6yo) and older (79 ± 5yo) donors of both sexes (n=4-5 per group,17 total) were used. Transforming growth factor-beta 3 (TGFβ3) treatment was added to induce differentiation and treatment groups included TGFβ3 alone or in combination with Selonsertib, MDL-800, or both (dual treatment). Controls included no TGFβ3. Every 2 days, fresh media with treatments were added until day 10 when masses were collected for RNA/protein isolation and histology. Proteomics by Sequential Window Acquisition of all Theoretical Mass Spectra was used. Analysis using principal components, differential expression and Gene Set Enrichment (GSEA) analyses with UNI-PROT was performed. Significant downregulation of gene sets associated with ECM and ATP synthesis with upregulated DNA damage were observed in older untreated hBM-MSC micromasses. Confirmation of chondrogenesis with the addition of TGFβ3 treatment was indicated by increased enrichment of gene sets such as protein translation, ECM and decreased mitochondrial activity in both age groups. This result was confirmed using histology and alcian blue staining (proteoglycan) of the micromasses. Comparison of the effects of TGFβ3 treatment of micromasses from aged donors to younger donors showed significant downregulation in mitochondrial processes, NAD, Lipid/Fatty-acid metabolism and peroxisomes. Upregulated gene sets included cell signaling, and endoplasmic reticulum/golgi processes. When the dual treatment was administered with the TGFβ3, these gene sets reverted to similar levels as those observed in the younger donors. In addition, dual treatment significantly upregulated NAMPT (Nicotinamide phosphoribosyltransferase) 3.5 fold in older hBM-MSCs. Functionally, ECM staining of donor micromasses for denatured collagen (using binding to the Gly-X-Y motif) showed increased staining with age that decreased with the dual treatment. Together these results demonstrate the dual treatment of Selonsertib and MDL-800 administered to older hBM-MSCs restores cellular and molecular processes to those of younger hBM-MSCs.

Mechanical Unloading via Sciatic Nerve Resection Delays Proliferative and Matrix-Driven Achilles Tendon Growth during Early Postnatal Development

Talayah Johnson[1], Natalie L. Fogarty[2], Alisia Lin[1], Destiny Miller[1], Madison Dennis[1], Jiaqi Xiang[3], Xi Jiang[1], Lin Han[3], Robert L. Mauck[1], Nathaniel A. Dyment[1]

[1]University of Pennsylvania, Philadelphia PA, [2]Children's Hospital of Philadelphia, Philadelphia, PA, [3]Drexel University, Philadelphia, PA.

Talayahj@seas.upenn.edu

Disclosures: Mauck (5 - 4Web Medical), Han (8, Osteoarthritis Cartilage).

INTRODUCTION: Musculoskeletal tissues, including tendons, are highly responsive to mechanical cues. Both excessive and insufficient loading can alter tendon composition, and drastic shifts in the mechanical environment are implicated in tendon pathology [1]. While the influence of loading on adult tendons and tendon healing is well established, much less is known about how the forces that arise with the activities of daily living regulate tendon growth in early postnatal development, a period marked by a shift from cell proliferation to increasing extracellular matrix (ECM) accrual. To investigate the role of mechanical unloading during early postnatal growth, we employed surgical sciatic nerve resection (SNR) at P1 to reduce hindlimb loading. Our approach targets the time when both proliferative and ECM-driven tendon growth are active. We hypothesize that mechanical loading is a critical driver of both proliferative-driven growth and ECM-driven growth in the Achilles tendon.

METHODS: All animals and procedures were IACUC approved. Sciatic Nerve Resection. Unilateral left sciatic nerve resection (SNR) was performed on post-natal day 1 (P1) in male and female *Col1a1(3.6 kb)-CFP* reporter mice with evaluation at post-natal days 14, 42, and 84 (*N*=28, 12 males, 16 females). SNR results in sustained gait abnormalities as we reported previously [2]. Cryohistology. Hindlimbs were harvested, formalin-fixed, embedded in OCT, and cryosectioned (8 μm) in the transverse plane. Fluorescent imaging with a nuclear counterstain, followed by brightfield imaging with toluidine blue staining were performed. Scanning Electron Microscopy was used to assess collagen fibril diameter. Sections were fixed, dehydrated, and coated with 6 nm thick platinum-palladium mixture prior to imaging. Image Analysis. Achilles tendon cross-sectional area and cell density were quantified using Fiji. Statistics. SNR limb vs. contralateral limb groups were compared via paired t-tests at α=0.05.

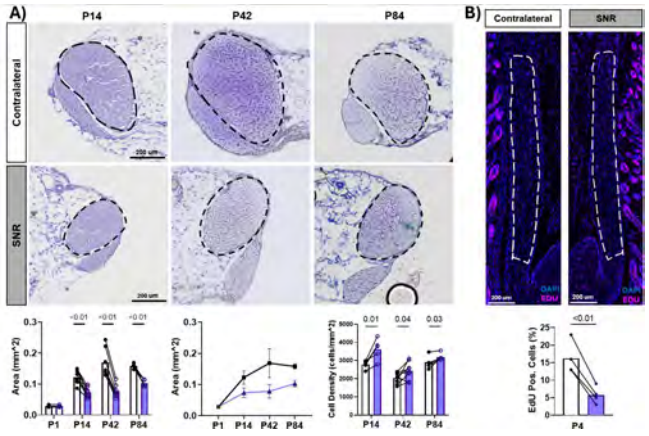

Fig. 1: Neonatal SNR significantly decreased Achilles tendon cross-sectional area (CSA, shown in rep. images) while increasing cell density (A) P1 samples were prior to surgery*. Cell proliferation was also reduced at P4 (B).

RESULTS: SNR resulted in smaller Achilles tendons. Our results indicate that the sustained gait abnormalities arising from SNR [2], alters the growth of the Achilles tendon in neonatal mice. Neonatal SNR significantly decreased Achilles tendon cross-sectional area (CSA) in the SNR limb at all timepoints (**Fig. 1A**, p<0.01). The contralateral limb exhibited steady CSA expansion from P14 to P42, whereas the SNR limb showed minimal growth between P14 and P42. Interestingly, the SNR limb displayed a surge in growth between P42 and P84, achieving ~25% of its total growth during this interval. The CSA reduction in the SNR limb was accompanied by a significant increase in cell density in the SNR tendon at all timepoints (**Fig.1A**, p<0.05). To determine whether early deficits in tendon growth corresponded with altered cell proliferation, we administered EdU injection at the time of SNR surgery. At P4, EdU labeling revealed a reduction in proliferating cells in the SNR tendon compared to the contralateral limb (**Fig. 1B**, p<0.01**)**. SNR delays temporal decline in (Col1a1 3.6kb) expression: At P14, the contralateral limb displayed significantly higher CFP intensity than the SNR limb (**Fig. 2,** p < 0.001), consistent with reduced CSA at this time point. By P42, however, the SNR limb exhibited significantly higher CFP intensity compared to the contralateral side (p < 0.001). At P84, the contralateral limb showed a steeper reduction in signal, whereas the SNR limb maintained higher CFP intensity at this later point **(Fig. 2)**. SNR reduces collagen fibril diameter: Fibril diameters were significantly smaller in the SNR tendon compared to contralateral controls at P14 (9.5% reduction) and P42 (29.4% reduction), with the effect more pronounced at P42 (p < 0.001, **Fig. 3**).

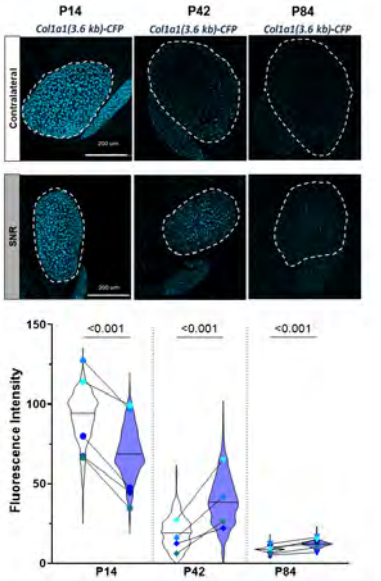

Fig 2: Col1a1(3.6kb)-CFP expression was reduced in SNR tendons at P14 however the SNR limb exhibited significantly higher CFP intensity at later time points (P42 & P56) compared to the contralateral limb.

DISCUSSION: We targeted periods of active cell proliferative- and matrix-driven growth using an SNR model and found that mechanical unloading acutely suppresses cell proliferation, collagen expression, and fibril thickening, ultimately impairing tendon growth. Early unloading via SNR led to rapid reductions in tendon CSA and cell number by P14, aligning with the known window of active cell proliferation. While the SNR tendon remained significantly smaller than the contralateral tendon at all time points, SNR may actually extend the growth period of the Achilles tendon since CSA of the contralateral tendon plateaued at P42, whereas the SNR tendon continued expand through P84. The altered temporal dynamics of Col1-CFP expression, which correlate with changing rates found in tendon CSA, reinforce that mechanical loading is a key regulator of tendon cell phenotype during postnatal growth. The slower decline of Col1a1 expression in the SNR limb suggests that mechanical unloading extends the period of this matrix-synthesizing cell phenotype. The reduced fibril diameter suggests that diminished loading limits fibril thickening, leading to progressive architectural defects. This corresponds with reduced material properties that we previously reported [3].

SIGNIFICANCE/CLINICAL RELEVANCE: Together, these findings demonstrate that mechanical cues are required to sustain both the proliferative and matrix-accumulating phases of postnatal tendon growth. The marked reductions in structural and material properties confirm that SNR is an effective model for unloading the Achilles tendon during a mechanically sensitive developmental window, offering a powerful platform to study how chronic unloading influences tendon maturation and long-term mechanical integrity.

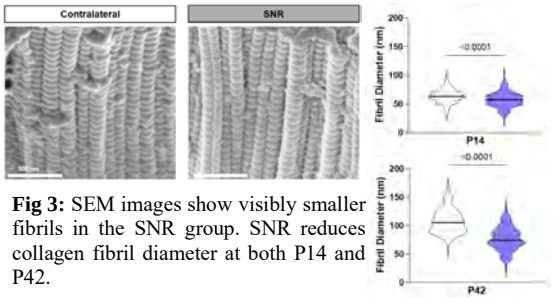

Fig 3: SEM images show visibly smaller fibrils in the SNR group. SNR reduces collagen fibril diameter at both P14 and P42.

REFERENCES: 1. Lavagnino, JOR 2015; 2. Fogarty, JOR 2023; 3. Johnson, ORS 2024.

ACKNOWLEDGEMENTS: NIH R01-AR075418, P50-AR080581, and P30- AR069619.

Macrolide Rapamycin Enhances DWIVA-Induced Osteogenesis in 3D Degradable Hydrogels

Umu S. Jalloh[1], Niva Shah[1], Sebastián L. Vega[1,2]
[1]Department of Biomedical Engineering, Rowan University, Glassboro, NJ
[2]Department of Orthopaedic Surgery, Cooper Medical School of Rowan University, Camden, NJ

Introduction

Long bone fractures are among the most common traumatic injuries and a major cause of disability in young adults. Although most heal naturally, over 100,000 U.S. patients each year experience non-unions requiring revision surgery with inconsistent outcomes. Bone morphogenetic protein-2 (BMP-2) is the only FDA-approved osteoinductive factor, but its supraphysiological dosing causes severe complications. Synthetic BMP-2 mimetic peptides such as DWIVA mimic the BMP-2 wrist epitope and activate Smad-independent osteogenic signaling, yet activation is limited by FKBP12 binding to BMP receptor complexes. We hypothesized that the macrolide Rapamycin (Rap), which binds FKBP12, would relieve this inhibition and enhance DWIVA-induced osteogenesis.

Methods

Hyaluronic acid-norbornene (HANor) hydrogels were crosslinked with a protease-degradable peptide (GCNSVPMS↓MRGGSNCG) via thiol-norbornene photopolymerization (I2959 0.05 wt%, 10 mW/cm², 5 min). Degradable hydrogels enable cell-mediated matrix remodeling during osteogenesis. Precursor solutions contained HANor (3 wt%), crosslinker (2.5 mM), RGD (2 mM), DWIVA (2 mM), and Rap (100 nM). Mesenchymal stem cells (MSCs, 2 x 10^6 cells/mL) were encapsulated in cylindrical hydrogels and cultured for up to 14 days in growth (GM) or osteogenic (OM) medium. Cell viability and morphology were assessed by Live/Dead and phalloidin/Hoechst staining. Mechanotransduction was quantified from changes in cell volume and sphericity, while alkaline phosphatase (ALP) activity and calcium deposition were measured at days 7 and 14.

Results

DWIVA-functionalized hydrogels maintained high MSC viability and promoted spreading compared to GM controls. Rapamycin further enhanced mechanotransduction, reflected by greater cell volume and reduced sphericity. ALP-positive cells rose from 9.9 ± 3.9% (GM) to 68.0 ± 2.4% (DWIVA) and 93.8 ± 2.2% (DWIVA + Rap), matching OM (94.8 ± 3.1). At day 14, calcium deposition was further enhanced, with DWIVA + Rap (16.3 ± 1.8 mg/dL) exceeding DWIVA alone (9.1 ± 1.5 mg/dL) and OM (14.8 ± 1.3 mg/dL).

Conclusions

Protease-degradable thiol-norbornene hydrogels functionalized with DWIVA peptides support robust 3D osteogenic differentiation of MSCs. Rapamycin amplifies DWIVA-induced mechanotransduction, ALP activation, and mineralization by relieving FKBP12-mediated inhibition of BMP receptor signaling. Ongoing work will examine downstream Smad-independent pathways using BMP-2 reporter cell lines and evaluate DWIVA + Rap hydrogels in a rat femoral defect model with support from the PCMD MicroCT and Biomechanical cores.

Temporal Dysregulation of Chondrocyte Maturation and Extracellular Matrix Modification Following Neonatal Type III Collagen Loss in Murine Femoral Head Cartilage

Tiffany C. Wu[1-3], Daniel C. Stewart[1], William Yen[1], Yuchen Liu[5], Sidney Wong[1,4], Lin Han[5], Robert L. Mauck[2,3,6], and Susan W. Volk[1]
[1]Dept. of Clinical Studies & Advanced Medicine, School of Veterinary Medicine, [2]Dept. of Bioengineering, [3]Dept. of Orthopaedic Surgery, [4]School of Arts and Sciences, University of Pennsylvania, Philadelphia, PA, [5]School of Biomedical Engineering, Science and Health Systems, Drexel University, Philadelphia, PA, [6]Translational Musculoskeletal Research Center, Corporal Michael J. Crescenz VA Medical Center, Philadelphia, PA
tif5353@seas.upenn.edu

INTRODUCTION: Osteoarthritis (OA) is a degenerative joint disease characterized by the breakdown of cartilage extracellular matrix (ECM).[1] Regenerative strategies for cartilage repair remain elusive due to a limited understanding of ECM assembly and chondrocyte-matrix interactions.[2,3] Recent evidence implicates type III collagen (COL3), an understudied fibril-forming collagen present in low concentrations (~1-5%) in healthy human cartilage, as a key regulator of ECM structural integrity and cartilage health.[4] Other work has shown a critical role for COL3 in regulating matrix architecture and mechanoresponses in other tissues.[5,6] In this study, we hypothesize that COL3 is a critical component of cartilage extra- and peri-cellular matrix maintenance and repair via its roles in neo-matrix assembly and integrin-mediated mechanotransduction.

METHODS: *Conditional* Col3a1 *knockout mice*: Systemic knockout of COL3 (*Col3a1* gene) was induced by intragastric injection of tamoxifen (TM) to neonatal (P0-2) conditional *Col3a1* knockout mice (*Col3a1*$^{F/F}$/RosaCre^{ER}, or F/F).[6] Control wild-type mice (*Col3a1*$^{B6/B6}$/RosaCre^{ER}, or B6/B6) were similarly injected with TM (IACUC approved). *RT-qPCR*: Femoral head articular cartilage was harvested either on post-natal day 21 (P21) or days 50-60 (P50-60) and snap frozen. Relative gene expression of *Col3a1*, *Col2a1, Col10a1, Acan*, *Itga10*, *Itga11*, *Mmp3, Mmp9*, and *Mmp13* were measured in F/F and B6/B6 mice (*Gapdh* was used as a housekeeper). *Histology*: Cartilage at P21 or P50-60 was fixed overnight in glutaraldehyde, embedded in paraffin, and 5 µm sections were stained with Safranin-O/Fast Green. Quantification of areal cell density (number of cells/unit area) and chondrocyte cell area was accomplished with wheat germ agglutin stained slides (to identify cell membranes) with DAPI, using ImageJ and CellProfiler in five regions of interest in the hypertrophic zone. *In situ zymography (ISZ)*: Cartilage sections were incubated with Invitrogen DQ™ collagen type IV (COL4) and collagen type I (COL1) to assess matrix metalloproteinase (MMP) activity against these substrates. *Statistical Analysis*: All statistics were conducted in GraphPad Prism with a significance level of α=0.05. Outliers were removed from each dataset using Grubbs' Test and significant differences were detected using unpaired Student's t-tests.

RESULTS: Efficient knockout of the floxed *Col3a1* allele in F/F mice was achieved, as demonstrated by a reduction of *Col3a1* mRNA levels to < 1% following neonatal TM treatment compared to TM-treated B6/B6 control mice at both P21 ($p<0.0001$) and P50-60 ($p=0.0031$). Histological analysis of cartilage revealed an expanded hypertrophic chondrocyte zone in P21 COL3-deficient mice compared to controls. (**Fig. 1A, 1B**). Both areal cell density and average cell area were increased in F/F relative to B6/B6 cartilage of P21 mice (**Fig. 1C, 1D)**, although these histomorphometric differences were resolved by P50-60 (**Fig. 1E, 1F**; images not shown). qPCR analysis revealed significant decreases in *Col2a1* ($p=0.0164$), *Col10a1* ($p=0.0013$), *Acan* ($p=0.0315$), and *Itga10* ($p=0.0022$) mRNA levels in F/F tissues compared to controls; no significant differences in *Itga11* ($p=0.7022$), *Mmp3* ($p=0.1917$), *Mmp9* ($p=0.6250$), or *Mmp13* ($p=0.1766$) expression levels were observed. To further investigate induction of catabolic activity after COL3 loss, ISZ was performed, which revealed an increase in MMP activity against COL1 substrates (**Fig. 2A-C**), but not COL4 substrates (**Fig. 2D-F**) in COL3-deficient cartilage relative to controls. In contrast to the differential gene expression induced by COL3 loss at P21, at P50-60, qPCR data revealed no differences in *Col2a1* ($p=0.4684$), *Col10a1* ($p=0.3334$), *Acan* ($p=0.9439$), *Itga10* ($p=0.7885$), or *Mmp3* ($p=0.3306$) expression levels in COL3-deficient cartilage compared to controls. However, there were suggested increases in *Itga11* ($p=0.0908$), *Mmp9* ($p=0.0988$), and *Mmp13* ($p=0.0574$). At this P50-60 timepoint, there was a significant increase in MMP activity in the ECM space assessed by ISZ against COL4 substrates in COL3-deficient cartilage compared to controls (**Fig. 3D-F)**, but not against COL1 (**Fig. 3A-C**), in contrast to the observations at P21.

DISCUSSION: Our findings reveal a role for COL3 in temporally regulating chondrocyte maturation and ECM remodeling during postnatal development of murine femoral head cartilage. At P21, COL3 knockdown resulted in increased hypertrophic chondrocyte areal density and cell area and a reduction in *Col2a1*, *Acan*, and *Itga10* expression. This suggests an altered dynamic of how and when chondrocytes undergo and progress through hypertrophy in the ossification center. By late development (P50-60), both histology and altered cell phenotype markers normalized across genotypes, suggesting that COL3 is critical during early endochondral ossification but less so as the cartilage matures. COL3 also modulated ECM modification through temporally distinct MMP activity: COL3 loss induced an early increase in MMPs targeting COL1 substrates (relevant to cartilage: MMP-1, -13, and -14)[7] and shifted towards activation of COL4-degrading MMPs (MMP-2, -9, and -12)[8] later in development.

SIGNIFICANCE: These findings identify COL3 as a critical regulator of early chondrocyte phenotype and cartilage matrix remodeling during postnatal development and suggest a potential role for COL3 loss in accelerating cartilage degeneration and OA progression. Future studies will explore COL3's therapeutic relevance in cartilage repair and disease prevention.

REFERENCES: [1]Goldring, *HSS J.*, 2012; [2]Huey+, *Science*, 2012; [3]Bielajew+, *Nat. Rev. Mater.*, 2020; [4]Wang+, *Matrix Biol.*, 2020; [5]Brisson+, *Am. J. Pathol.*, 2015; [6]Stewart+, *J. Invest. Dermatol.*, 2024; [7]Van Doren, *Matrix Biol.*, 2015; [8]Murphy+, *Biochem J.*, 1991.

ACKNOWLEDGEMENTS: This work was supported by the NIH (T32 GM148377 and R01 AR083666).

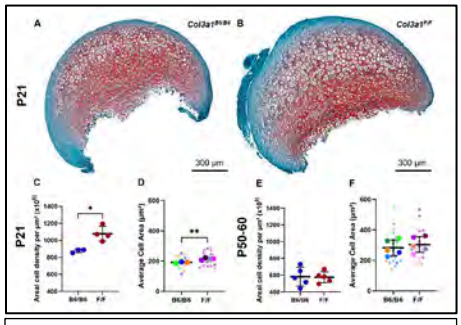

Fig. 1. Representative Safranin-O/Fast Green staining of P21 femoral head cartilage of P21 *Col3a1*$^{B6/B6}$ **(A)** and *Col3a1*$^{F/F}$ **(B)** mice, revealing expansion of hypertrophic chondrocytes. Quantification of areal cell density per µm^2 and average cell area (µm^2) at P21 **(C, D)** and P50-60 **(E, F)**. Mean ± SD, n ≥ 3, unpaired Student's T-test (* p ≤ 0.05, ** p ≤ 0.01).

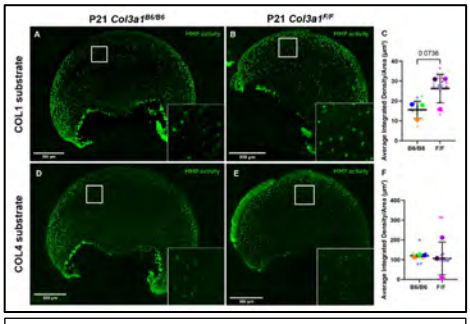

Fig. 2. Representative P21 in situ zymography staining of MMP activity against COL1 substrates (MMP-1, -13, -14) **(A, B)** and COL4 substrates (MMP-2, -9, -12) **(C, D)** in *Col3a1*$^{B6/B6}$ and *Col3a1*$^{F/F}$ murine femoral head cartilage. Quantification of staining intensity normalized to area (µm^2) **(C, F)**. Mean ± SD, n ≥ 3, unpaired Student's T-test (* p ≤ 0.05).

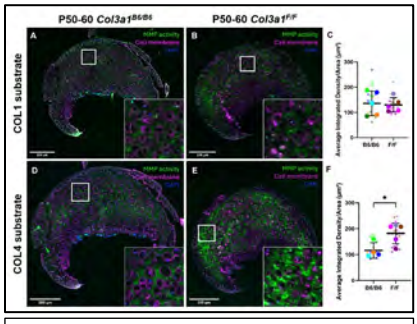

Fig. 3. Representative in situ zymography staining of MMP activity (green) against COL1 **(A, B)** and COL4 **(C, D)** substrates (green) in P50-60 murine femoral head cartilage. Quantification of staining intensity normalized to area (µm^2) **(C, F)**. Mean ± SD, n ≥ 4, unpaired Student's T-test (* p ≤ 0.05).

Effects of the Combined Treatment of MDL-800 (a SIRT6 activator) and Selonsertib (an ASK1 inhibitor) on Muscle Repair after Surgical Injury

Francis J. Ochman[1], Ayla Pearson[2], Matheus M. Perez[2], John A. Collins[2], Theresa A. Freeman[2]
[1] Cooper Medical School, Camden, NJ
[2] Dept. of Orthopaedic Research, Thomas Jefferson University, Philadelphia PA

Introduction: Muscle repair and regenerative potential decrease with age. Consequently, muscle injury during orthopedic or other surgical procedures can impair function and recovery in older patients. Preliminary data from our laboratory indicate that aged female rats exhibit better muscle recovery after surgical injury compared with aged male rats. In this study, we investigate whether combined treatment with MDL-800 (a SIRT6 activator) and selonsertib (an ASK1 inhibitor) enhances muscle tissue repair in a sex-dependent manner at a clinically relevant time point of middle age.

Methods: Aged (18-month-old) Brown Norway rats were randomized into groups of 3 male and 4 female samples for either treatment with intraperitoneal injection of MDL-800 (75 mg/kg) and selonsertib (50 mg/kg; MDL-SEL) or control groups. The MDL-SEL treatment was administered weekly for 4 weeks pre-surgery and 8 weeks post-surgery. Quadriceps muscles were harvested for analysis of inter-fiber collagen deposition and muscle fiber size by histology (Pico Sirius Red staining) as well as by qPCR and proteomics.

Results: Histological analysis showed the muscle fibers of males were significantly larger than females (with or without treatment). Treatment with MDL-had no effect on either collagen fiber deposition or fiber size compared to control groups. Molecular analysis by qPCR revealed downregulation of NOS2 in MDL-SEL treated males only (< 0.05). Proteomic analysis by mass spectrometry indicated significant differential expression of 133 proteins in female MDL-SEL vs. control rats (85 up, 48 down). GSEA analysis of KEGG pathways indicated upregulation of extracellular matrix interactions and downregulation of thermogenesis, oxidative phosphorylation, and metabolic pathways in females with MDL-SEL. In males, 98 proteins were significantly changed (34 up, 64 down), with upregulation of amino acid biosynthesis, metabolism, and oxidative phosphorylation, and downregulation of calcium signaling and calmodulin binding.

Conclusion: Overall, at 8 wks. post-injury our data demonstrates males may respond better to the dual MDL-SEL treatment, as indicated by proteomic changes showing significant increases in oxidative phosphorylation and decreased NOS2 expression. Caveats of these results are the small study size and the single timepoint at 8 weeks. Additionally, MDL-SEL dosage concentration and administration should be considered.

Peptide-functionalized 3D-printed biomaterial scaffolds direct *in situ* osteochondral tissue regeneration

Andrew Kitson[1], Marina M. Santos[2], Scott L. Korte[2], Brandon A. Krick[3], Julie B. Engiles[2,4], Thomas P. Schaer[2], Lesley W. Chow[1,5,6] (lesley.chow@lehigh.edu)

[1]Department of Materials Science and Engineering, Lehigh University, Bethlehem, PA, [2]Department of Clinical Studies and [3]Department of Pathobiology, New Bolton Center, School of Veterinary Medicine, University of Pennsylvania, Kennett Square, PA, [5]Department of Bioengineering & [6]Polymer Science and Engineering Program, Lehigh University, Bethlehem, PA

INTRODUCTION: Osteoarthritis (OA) is a debilitating disease characterized by progressive osteochondral (OC) tissue degeneration that affects over 30 million adults in the U.S.[1] The gold-standard treatment for end-stage OA is total joint replacement, which is not suitable for younger patients that may outlive their implant.[2] Early-stage interventions for cartilage repair, such as microfracture and autologous chondrocyte implantation, can delay disease progression.[2] However, the newly formed tissue is mechanically inferior to native cartilage and poorly integrated with the subchondral bone, leading to unsatisfactory long-term clinical outcomes.[1,2] Biomaterials offer promising strategies to direct OC tissue formation and organization to augment early-stage treatments. To achieve this, we developed a 3D printing strategy to fabricate biodegradable polymer scaffolds spatially functionalized with multiple bioactive peptides.[3,4] Peptide-poly(caprolactone) (PCL) conjugates bearing hyaluronic acid (HA)-binding (HAbind-PCL) or mineralizing (E3-PCL) peptides were designed to promote human mesenchymal stromal cell (hMSC) chondrogenesis or osteogenesis, respectively.[4] We hypothesized that scaffolds presenting both peptides in discrete regions will direct OC matrix organization. PCL and dual-peptide scaffolds were implanted in a critically sized osteochondral defect model in rabbits to evaluate scaffold-directed tissue formation and integration *in vivo*.

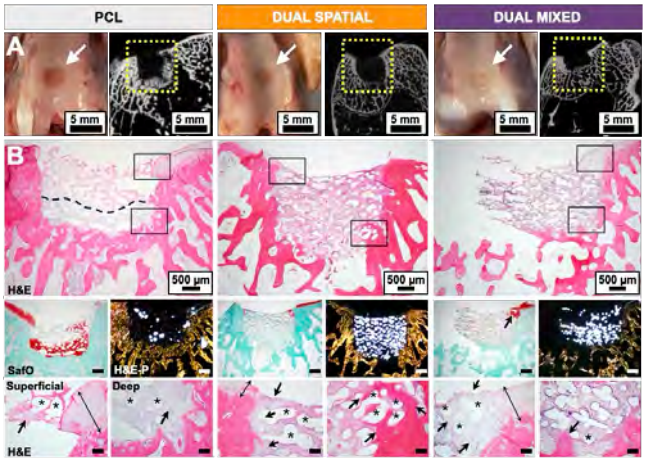

Fig. 1: (A) Macroscopic images correlated with microCT of scaffolds harvested at 3 months from critically sized osteochondral rabbit defects (left: arrow; right: box). (B) Histology showed proteoglycan-rich matrix at the base of PCL scaffolds while dual spatial and dual mixed scaffolds showed proteoglycan-rich matrix within superficial regions (upper box) and osteogenesis at the base (lower box). Corresponding high-magnification images showed PCL (asterisks) surrounded by loose primitive mesenchyme (arrow) at the interface of the flanking articular cartilage (double-headed arrows) compared to chondrogenesis and osteogenesis found in respective superficial and deep regions of both dual-peptide scaffolds. Central regions of all implants showed scaffold surrounded by primitive mesenchymal cells admixed with bland adipose islands, multinucleate giant cells, and few lymphoplasmacytic infiltrates. (Rows 1 and 2: scale bar = 500 µm; Row 3: scale bar = 100 µm)

METHODS: *Scaffold fabrication*: HAbind-PCL and E3-PCL conjugates were synthesized using methods previously described.[3,4] Conjugates were dissolved with unmodified PCL in hexafluoro-2-propanol (HFIP) to fabricate 3 scaffold groups: (1) PCL; (2) dual spatial (HAbind and E3 in discrete zones); and (3) dual mixed (both peptides presented homogeneously). Inks were solvent-cast 3D printed into 3-mm thick, 4-mm diameter scaffolds. Under IACUC approval, bilateral, full-thickness (3-mm depth, 4-mm diameter) critically sized osteochondral defect sites in 4 rabbits (female only for pilot study) were prepared in the femoral trochlear grooves comparing dual-peptide scaffolds to PCL. Scaffolds were incubated in autologous bone marrow aspirate concentrate obtained during the same procedure before implantation. Samples harvested at 3 months were analyzed using microCT and histology.

RESULTS: Macroscopic images correlated with microCT and histology confirmed scaffolds remained in the defects in all groups for the entire 3-month study with minimal lymphohistiocytic inflammation (**Fig. 1**). Spatial cartilage and bone formation and adjacent tissue integration was observed in respective superficial and deep zones of both dual spatial (Fig. 1B center) and dual mixed (Fig. 1B right) implants while unfunctionalized PCL scaffolds resulted in displaced cartilage matrix formed at the base of the defect (Fig. 1B left).

DISCUSSION: The dual-peptide scaffolds enhanced spatial tissue formation and integration compared to PCL scaffolds. These exciting results underscore how our peptide-functionalized scaffolds drive spatial tissue formation with endogenous cells and tissue. This work advances a novel biomaterial-based approach for functional osteochondral tissue regeneration towards clinical relevance as an early-stage treatment for osteoarthritis.

REFERENCES: [1] Osteoarthritis (OA), CDC. [2] Di Luca A+ *Birth Defects Res. Part C.* 105:34-52, 2015. [3] Camacho+ *Biomater Sci* 7:4237-4247, 2019. [3] Camacho+ *Biomater Sci* 9:6813-6829, 2021.

ACKNOWLEDGEMENTS: This study was supported by NSF (DMR 1944914; DGE 2234658) and Lehigh's Vice Provost Office of Research.

Visible Near-Infrared (VNIR) Spectroscopy of OARSI-Scored Human Joint Tissues

Amanda Spurri[1], Shu-Jin Kust[1], Petra Baylin[1], Binyam Fentaw[1], Alex Arnold[1], Leslie Barnes[1], Daniela Proca[1], Nancy Pleshko[1]

[1]Temple University, Philadelphia, Pennsylvania

Introduction: While assessment of joint tissues using VNIR spectroscopy demonstrates the potential to provide quantitative chemical information from joint tissues, further methodology development is required for implementation *in vivo* applications. The objectives of this work are to both assess the potential for correlation of VNIR spectra with gold standard histologic grading (OARSI) using multivariate analysis techniques, such as principal component analysis (PCA) and linear discriminant analysis (LDA) and to advance the understanding of the molecular changes that contribute to differences in VNIR spectra across OARSI grades using infrared (IR) spectral imaging.

Methods: Tissues: The tissues utilized during this study for spectra collection and histologic grading were segments of human osteochondral tissues from 35 joint arthroplasty procedures (Temple Hospital IRB Protocol 31644). VNIR Spectra Collection: Regions for data collection were identified visually to span a range of disease severity. Three spectra per region were collected in contact with the tissues using a custom fiber optic probe with a 90 degree bend at the tip. The spectra were collected in diffuse-reflectance mode with 50 co-added scans per spectrum over the visible (28,571 cm^{-1} – 14,286 cm^{-1}) (350 – 700 nm) and NIR (12,500 – 4,000 cm^{-1}) regions using an ASD Labspec 4 spectrometer. Data processing included normalization, smoothing and second derivative processing to sharpen underlying peak absorbances. Histological Preparation and Analysis: Following spectra collection, segments were marked with a histology pen to note data acquisition locations on the tissue section. These segments were fixed, decalcified, paraffin-embedded and sectioned followed by hematoxylin & eosin staining at Temple Hospital and Safranin O staining by the PCMD histology core. Histological grading was completed by three graders using the OARSI scoring criteria (0-6.5, with 0 being pristine and 6.5 being most severe), and the assigned grade for each location was determined by group consensus. A stage was not included in the grading as specific mm-size regions corresponding to where fiber optic spectra were acquired was the focus of the grading. Select tissues were also prepared for IR spectral imaging. Multivariate analyses (PCA and LDA) were performed to assess spectral data separation based on OARSI score. **Results and Discussion**: Qualitative differences are observed in both the histological sections (Figures 1A, 1B) and VNIR spectra (Figure 1C) based on the degree of cartilage degradation, providing motivation for more advanced method development for spectral classification based on histological grading standards. Multivariate analysis demonstrates potential for classification of spectra, particularly in supervised techniques such as LDA (Figure 2). Additionally, IR imaging data of the tissues provided quantifiable outcomes related to cartilage PG content and collagen fiber orientation, expanding the potential number of metrics for correlating VNIR spectra with cartilage integrity. With this information, further data analysis will assess whether OARSI score is the optimal gold-standard for calibration of VNIR data as opposed to a histological matrix score, such as is found with a modified Mankin grade.

Figure 1

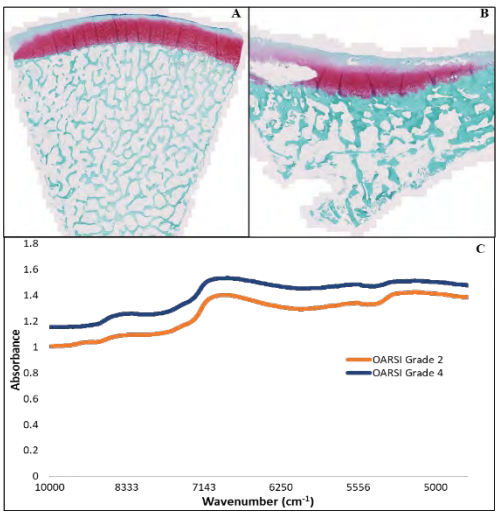

Figure 2

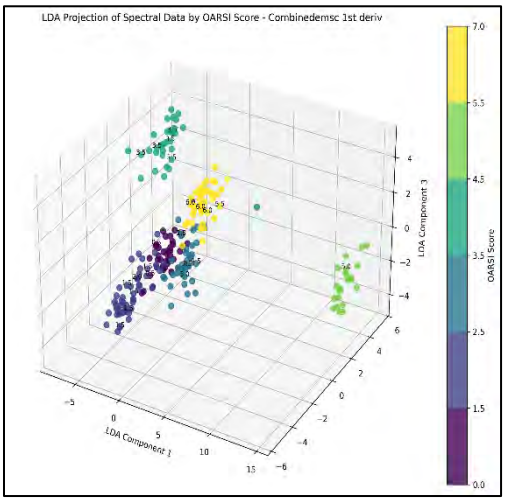

Figure 1: Safranin O-stained sections demonstrating OARSI grades 2 (1A) and 4 (1B). Comparison of averaged raw spectra show qualitative differences in overall spectral contour and baseline offset (1C).

Figure 2: LDA projection showing group separation based on OARSI grade.

Acknowledgements: Supported by NIH R01AR056145; We gratefully acknowledge the Penn Center for Musculoskeletal Disorders (NIH AR069619) for technical and financial support.

Spatial Transcriptomics Reveal Unique Molecular Signatures of the Developing Achilles Tendon

Grey Hallstrom[1], Xi Jiang[1], Nathaniel Dyment[1]
[1]McKay Orthopaedics Research Laboratory, Department of Orthopaedic Surgery, University of Pennsylvania, Philadelphia, PA
greyhall@pennmedicine.upenn.edu

Disclosures: None.

INTRODUCTION: Despite the vast knowledge of the structure and mechanical function of mature tendons, the understanding of tenogenic cell differentiation, including markers that define specific stages of the lineage, is limited. Cells within the tendon body (i.e., internal tendon fibroblasts) have traditionally been considered a homogeneous population. From the discovery of the tenogenic transcription factor Scleraxis (Scx) and other markers (e.g., Mkx, Tnmd) that are enriched in tendons, several advancements have been made in understanding this lineage. For instance, recent work utilizing single-cell RNA sequencing (scRNA-seq) has revealed greater cell heterogeneity than previously appreciated. Despite these advancements, we still lack an accepted list of markers that delineate cells within the different regions of tendon (e.g., myotendinous junction, peritenon, enthesis), and much less cells at multiple differentiation states (progenitor, tenoblast, tenocyte) [1]. Indeed, *in vivo* tools are needed to identify the progenitors and more mature cell types to better understand this lineage, as *in vitro* differentiation assays do not maintain the tenogenic fate of isolated cells. Spatial transcriptomics has been used to attempt to address this need. However, many methods lack true single-cell spatial resolution and are also cost-prohibitive for many labs. Our group has advanced the 10x Xenium platform to improve transcript quality while also markedly reducing costs. This study demonstrates our ability to define discrete cell populations based on anatomical location while also uncovering shifting tenogenic cell populations with age, all while using an "off-the-shelf" gene panel not tailored to musculoskeletal tissues.

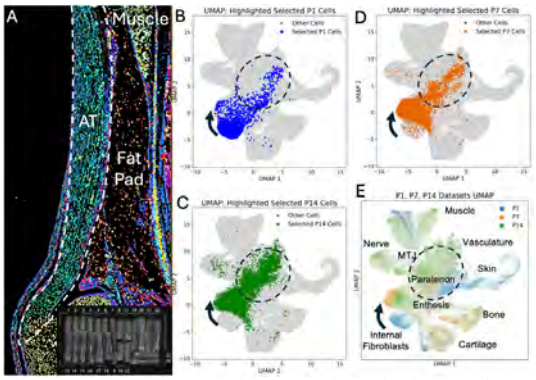

Figure 1: (A) Xenium Spatial Transcriptomics image of a P7 AT (dotted outline) with colored cells indicating different clusters. Inset shows 24 sections on 1 slide. (B) UMAP of selected AT at P1, (C) P7, and (D) P14. Arrow indicates shifting population and dotted line indicates growing population with age. (E) UMAP of all timepoints with cell types annotated.

METHODS: Animals: Hindlimbs were harvested from postnatal days 1 (P1), 7 (P7), and 14 (P14) wildtype mice (n=3/group with 2 slides per mouse, sex unknown for pilot study). Histology: Hindlimbs were fixed in 10% formalin, embedded in OCT, and Achilles tendon (AT) was sectioned (8μm thick) in sagittal plane with Cryofilm. Within the 12 x 24 mm space, 24 sections (inset in **Fig. 1A**) were glued to 10x Xenium slides using UV-curable adhesive (many more sections than used in the standard FFPE pipeline). Xenium spatial transcriptomics were performed using the mouse tissue atlassing panel containing probes for 379 genes and processed using standard 10x protocols through the University's single-cell sequencing core. Subsequent processing and analysis of 18 of the sections were performed using Xenium Explorer browser and Python scripts. For data presented in this abstract, we generated UMAPs from the Xenium data by normalizing and filtering low-abundance cells, performing principal component analysis to generate a probabilistic model of cell-to-cell relationships based on their similarity and differences in highly variable gene expression. Nearest neighbor analysis was also performed, where for a given "target" cell the cluster of the nearest "neighbor" cell was identified and cluster association percentages were computed.

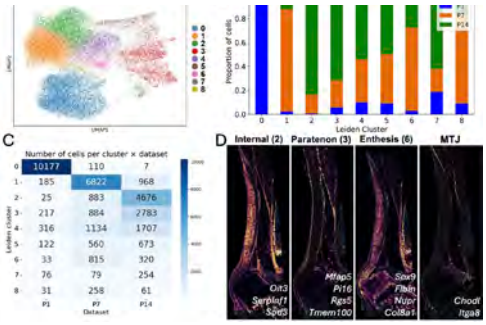

Figure 2: (A) UMAP of reanalyzed P1, P7, P14 AT selections. (B) Proportion of each timepoint per cluster. (C) Breakdown of cell numbers per cluster per age. (D) Representative image from a P7 AT highlighting genes from cluster 3 showing enrichment in the paratenon.

RESULTS: Shifting tenogenic cell populations with postnatal growth. We first defined our region of interest around the Achilles tendon, including the enthesis, peritenon, MTJ, and midsubstance to capture the tenogenic population (white dotted line in **Fig. 1A**). Next, we combined each timepoint into one UMAP highlighting the selected tendon regions to see how these three populations change with age (**Fig. 1B-E**). Largely, we identified a population that shifted (black arrows) and another population that grew in number (dotted lines) with age. Cell clusters mapping to specific tendon regions. To identify what cells were contributing to these growing populations and where in the tissue those cells are located, we reanalyzed the P1, P7, and P14 selected tendon cells as new clusters (**Fig. 2A-C**). We found the shifting population was clusters 0, 1, and 2 and were predominantly internal tendon fibroblasts, while the growing population was mostly in cluster 3 and localized to the peritenon. Additional clusters were enriched in the enthesis (cluster 6), while 2 genes *Chodl* and *Itga8* localized to the MTJ (**Fig. 2D**). Each of the three timepoints had a predominant internal fibroblast population: (Cluster 0 for P1, Cluster 1 for P7, and Cluster 2 for P14 (**Fig. 2B**). Internal fibroblast clusters have distinct spatial associations. Given the shift in the internal fibroblast population (clusters 0-2) with age (**Fig. 3A**), we next determined the spatial associations between these clusters using nearest neighbor analysis. We identified the cluster for the nearest "neighboring" cell of each "target" cell and then calculated percentages for each association. For example, 97% of cluster 1 cells were adjacent to cluster 0, whereas only 5% of cluster 0 cells were adjacent to cluster 1 at P1. We also found that clusters 1 and 2 were spatially intermixed in the tendon midsubstance with 17% of cluster 1 cells adjacent to cluster 2 cells and 70% of cluster 2 adjacent to cluster 1 cells at P7 and switches at P14 (**Fig 3B**).

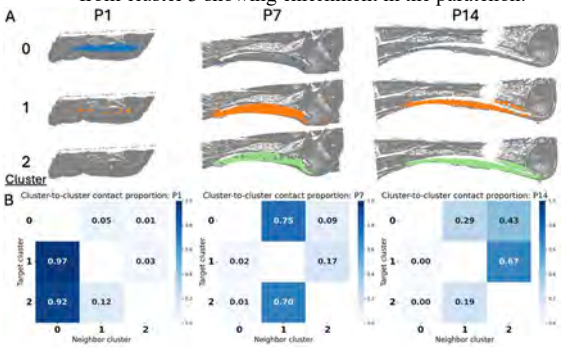

Figure 3: (A) Highlights of Clusters 0, 1, and 2 on representative AT section at P1, P7, and P14. (B) Cluster-to-cluster contact maps for Cluster 0, 1, and 2 for P1, P7, and P14 AT.

DISCUSSION: Taken together, these data highlight an innovative method to study tenogenic cell differentiation with precise spatial context at a truly single-cell level. Clustering data indicates that, as the tendon develops, there are major shifts in gene expression from P1 to P14 across the tendon. Currently, we are in the process of generating Xenium data with genes involved in tenogenesis and tendinopathy to further establish markers at different stages of the tenogenic lineage. In addition, we will use lineage tracing models to define clonal tendon cell arrays to establish how these arrays differentiate over time. In fact, given the close spatial association between clusters 1 and 2 in this study, there may indeed be a clonal relationship where cluster 1 cells differentiate into cluster 2.

SIGNIFICANCE/CLINICAL RELEVANCE: This study provides a novel understanding and establishment of a protocol for identifying distinct molecular signatures of tendon cells with single-cell spatial resolution with a marked increase in throughput with cryofilm sections. This technology can be applied to clinical samples with specific markers for studying tenogenesis and disease.

REFERENCES: 1. Huang, et al, J Orthop Res, 2023.

ACKNOWLEDGEMENTS: NIH P50-AR080581, P30-AR069619, and R01-AR082810.

The Role of Hypertrophic Chondrocyte YAP/TAZ Mechanosignaling in Fetal Bone Development

Devin C. Gottlieb, Christopher J. Panebianco, Dr. Joel D. Boerckel

Introduction: Endochondral ossification is a critical process in fetal long bone development, beginning with mesenchymal condensation at embryonic day (E)11.5 and progressing through chondrocyte maturation and hypertrophy.[1] By E15.5, the primary ossification center (POC) emerges, and vascular invasion drives the replacement of hypertrophic chondrocytes with bone. YAP (Yes-associated protein) and TAZ (transcriptional co-activator with PDZ-binding motif) are mechanosensitive transcriptional co-activators downstream of the Hippo pathway. They integrate cytoskeletal and extracellular cues to regulate gene programs, including targets such as Cyr61, that influence chondrocyte maturation and osteoblast differentiation. Combinatorial deletion of YAP and TAZ in skeletal progenitors severely impairs ossification and matrix organization, leading to perinatal lethality.[2] Conditional YAP/TAZ depletion from osterix-positive osteoprogenitor cells (YAP/TAZ cKO^{Osx}) also disrupts cartilage-to-bone transition and delays mineralization.[3] It has also been shown that YAP/TAZ cKO^{Col2a1} results in altered growth plate organization, with an expanded round chondrocyte zone and an elongated hypertrophic zone (HZ).[4] Together, these studies establish YAP/TAZ as central regulators of both osteoblast activity and chondrocyte maturation during endochondral bone formation.

Hypertrophic chondrocytes (HCs), once thought to solely undergo terminal apoptosis, are now recognized as capable of differentiating into osteoblasts and osteocytes.[5] They also exhibit mechanosensitivity during fracture healing, where loading influences HC differentiation during endochondral bone healing.[6] Previous studies indirectly ablated YAP/TAZ mechanosignaling in HCs by deleting YAP and TAZ in proliferating chondrocyte precursor cells (Col2a1-Cre) or simultaneously deleted YAP and TAZ in osteoprogenitor cells (Osx-Cre). In both mouse models, there was a distinct phenotypic change in the hypertrophic zone. These findings suggest that HC YAP/TAZ mechanosignaling is important for proper endochondral ossification; however, the direct role of YAP/TAZ signaling within hypertrophic chondrocytes during development remains unresolved.

Mechanosignaling plays an important role in fetal skeletal development. Fetuses that lack mechanical stimulation, termed fetal akinesia, have impaired bone growth and skeletal deformities.[7] In Sp^{d} mice, which model fetal akinesia, maternal exercise partially rescued skeletal defects by promoting earlier vascular invasion and stimulating remodeling of the chondro-osseous junction. These findings indicate that *in utero* loading via maternal exercise can stimulate skeletal development and partially rescue ossification defects in Sp^{d} mice. The purpose of this work is to determine the extent to which HC YAP/TAZ mechanosignaling guides this fetal skeletal response to maternal exercise.

Materials and Methods: Pregnant female C57Bl/6 mice underwent daily wheel running from E13.5 to E16.5 to provide in utero mechanical stimulation, while controls were exposed to locked wheels. At E17.5, embryos were collected, forelimbs cryoembedded, and sectioned at 10 µm. Immunofluorescent staining for Col10a1 (HCs), ALP (osteoblast activity), Endomucin (vascularity), DAPI/Phalloidin, and YAP/TAZ was performed, with slides imaged using a Zeiss Axioscan and quantitative length and intensity analyses conducted in Fiji/ImageJ. Pregnant dams carrying YAP/TAZ $cKO^{Col10a1}$ and wild-type controls underwent one hour of wheel running daily from E13.5–E15.5. At E16.5, embryos were collected for comparable cryoembedding, sectioning, and histological analysis.

Results and Conclusions: In C57BL/6J embryos, maternal exercise resulted in an increase of F-actin intensity within the primary ossification center, indicating enhanced cytoskeletal organization. Additionally, Col10a1 staining showed a decreased HZ length, consistent with stimulated endochondral ossification and accelerated skeletal maturation. For the YAP/TAZ $cKO^{Col10a1}$ experiments, sample collection for all four experimental groups (YAP/TAZ $cKO^{Col10a1}$ Exercise/Sham and Control Exercise/Sham) has been completed, providing a strong basis for downstream histological analysis. In ongoing work, Col10a1 staining will enable quantification of HZ length specifically within the YAP/TAZ $cKO^{Col10a1}$ mice, where it is hypothesized that maternal exercise will fail to elicit the enhanced ossification observed in C57BL/6J mice.

References: [1] Kozhemyakina+ *Development* 2015; **[2]** Kegelman+ *FASEB J* 2018; **[3]** Collins+ *Dev Cell* 2023; **[4]** Vanyai+ *Development* 2020; **[5]** Yang+ *PNAS* 2014; **[6]** McDermott+ *Sci Transl Med* 2019; **[7]** Nowlan+ *Eur Cell Mater* 2015

Elucidating the Effects of Yap Overexpression in Tendon Remodeling and Cytoskeletal Re-tensioning

Mariah Pabon, Elizabeth Siedl, Joel Boerckel

Abstract

Tendon function is dependent on extracellular matrix (ECM) composition and the maintenance of tensional homeostasis. Remodeling of the ECM alters mechanical properties, leading to impaired tissue function in patients (Dyment, 2011; Zhang, 2005; Lake, 2009). Previous work has shown overexpression of Yes associated protein (YAP) represses accessibility of matrix metalloproteinases (MMPS) *in vitro* (Jones, 2023). Prior studies implicate YAP signaling in cytoskeletal dynamics and endothelial mechanotransduction (Mason, 2019), but the mechanisms of cytoskeletal re-tensioning in tenocytes are not understood.

In this project, we seek to establish and validate a novel YAP overexpression mouse model (YAPCA Prx1-Cre) to investigate the impact of YAP on tendon structure and function. Both homozygous and heterozygous transgenic mice for a YAP constitutively active mutation will be characterized by histology, immunofluorescence, and RNA in situ hybridization to confirm YAP/TAZ overexpression and downstream target activation (Cyr61, Ctgf). We will also employ a Collagen1 inducible-Cre system to conditionally knock out YAP/TAZ, and use the Ai9 fluorescent reporter allele to visualize Cre-mediated recombination and confirm cell targeting across all sample groups.

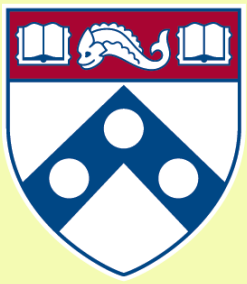

Penn Center *for*
Musculoskeletal Disorders
UNIVERSITY *of* PENNSYLVANIA

Micro CT Core Abstracts

PM Session

Poster 103 to 108

MDL-800-induced activation of SIRT6 regulates chondrogenic differentiation and cartilage formation

[1]Matheus Moreira Perez, [1]Eirene Choi, [1]Autumn Melvage, [1]Amber Slaweski, [2]Mandy J. Peffers, [1]Theresa Freeman, [1]John A. Collins

[1]Thomas Jefferson University, Philadelphia, PA, USA. [2] The University of Liverpool, Liverpool, UK

Precise stem cell signaling cues are needed to induce chondrocyte differentiation and articular cartilage repair. Current stem cell therapies to form stable articular cartilage are suboptimal and can form bone through endochondral ossification. Our prior data demonstrates that activation of sirtuin 6 (SIRT6) can regulate chondrocyte and stem cell function, but its role in chondrogenic differentiation is unclear. In this study, we assessed the effect of MDL-800, a small molecule activator of SIRT6, to regulate chondrogenic differentiation and endochondral ossification processes *in vitro* and *in vivo*.

Animal studies were approved by the Thomas Jefferson IACUC. We utilized our previously described 'Matrigel with BMP2 endochondral ossification model' which has been shown to promote ectopic bone formation *in vivo*. Twelve-week-old C57BL/6 mice were subcutaneously injected with 300 µl of Corning Matrigel Matrix Basement Membrane containing BMP2 (6µg/ml) or BMP2 plus MDL-800 (25 µM). After 14 days, mice were euthanized and Matrigel masses were analyzed by RT-PCR, microCT and Safranin-O/fast green staining. To define the effect of MDL-800 to transcriptionally regulate chondrogenesis *in vitro*, human bone marrow derived mesenchymal stem cells (hBM-MSCs) were cultured in 3D micromasses (n=9) and incubated in basal media or chondrogenic differentiation media (containing TGFß3) in the presence or absence of MDL-800 (10 µM) for 10 days. After experimental incubations, RNA-sequencing was performed, followed by gene set enrichment analysis (GSEA).

Supplementation of MDL-800 into Matrigels containing BMP2 significantly decreased endochondral ossification processes and bone formation ($p=0.0154$), when compared to BMP2 controls. Matrigels displayed robust cartilage formation that was unchanged between groups. However, MDL-800 containing Matrigels displayed significantly increased COL2A1 and ACAN gene expression levels, compared to controls. In our chondrogenic differentiation model, RNA-sequencing and GSEA analysis demonstrated that administration of MDL-800 to chondrogenic media significantly decreased pathways associated with 'bone development' and 'activation of matrix metalloproteases' while enriching pathways associated with 'histone activity', 'FOXO signaling', and 'DNA repair'.

This study demonstrates that SIRT6 activation represses BMP2-mediated endochondral ossification and maintains stable cartilage formation *in vivo*. Mechanistically, RNA sequencing revealed that SIRT6 activation promotes pro-anabolic signaling cascades and represses bone development processes. In conclusion, our findings demonstrate that SIRT6 may exert preferential effects on stem cell chondrogenesis to increase cartilage formation.

HydroBone: An Injectable BMP-2 Peptide Hydrogel for Bone Fracture Repair

Matthias Recktenwald[1], Stacy A. Love[1,2], Myranda Sims[1], Umu Jalloh[1], Tae Won B. Kim[1,2], Sebastián L. Vega[1,2]

[1]Department of Biomedical Engineering, Rowan University, Glassboro, NJ, USA

[2]Department of Orthopaedic Surgery, Cooper University of Rowan University, Camden, NJ, USA

Introduction

Bone fractures and non-unions remain a major clinical challenge, affecting millions worldwide. Biochemical interventions such as bone morphogenetic protein-2 (BMP-2) are the only clinically approved osteoinductive growth factor, yet their use is limited by safety concerns, variable efficacy, and high cost. These challenges highlight the need for alternatives capable of localized and sustained osteogenic stimulation. HydroBone is an injectable hydrogel platform developed by the team at HydroPep Therapeutics to deliver bone-forming peptides in an injectable biomaterial.

Methods

HydroBone consists of a HANorPeptide solution and a HATet solution that, upon 1:1 mixing, self-assemble into a hydrogel through catalyst-free Diels-Alder cycloaddition. This modular chemistry enables independent control of gelation kinetics, mechanics, and peptide incorporation (Gultian et al., *Macromolecular Bioscience* 2023; WO 2024/020558 A1). Hydrogels were functionalized with BMP-2 mimetic peptides DWIVA and KIPKA, alone or combined with the macrolide rapamycin, which potentiates BMP receptor signaling and enhances osteogenic differentiation. MC3T3 reporter lines were virally transduced to fluoresce by either SMAD or ERK activation. *In vitro*, these MC3T3 cells or human mesenchymal stem cells (MSCs) were cultured in the presence of peptides and macrolides, in solution or tethered to hydrogels (3D), to assess alkaline phosphatase (ALP) activity, calcium deposition, and SMAD or ERK activation. *In vivo*, hydrogels were injected into rat femoral intramedullary canal defects and analyzed by microCT and histology.

Results

DWIVA-functionalized hydrogels significantly enhanced trabecular bone formation within 4 weeks, with highest bone volume observed with MSC delivery (Love et al., *Journal of Orthopaedic Research* 2024). In vitro, FK506 amplified BMP-2 mimetic peptide signaling and increased ALP activity and calcium deposition (US Provisional Patent Application 63/866,043, 2025). Together, these results demonstrate that HydroBone enables localized bone formation with excellent injectability, *in situ* gelation, and confined regenerative response at the defect site.

Conclusions

We are currently optimizing peptide and macrolide dosing in vitro and have initiated an IACUC-approved study supported by the Foundation Venture Capital Group to evaluate bone bridging in a 5 mm critical-size femoral defect. Analysis will be performed with the assistance of the PCMD MicroCT and Biomechanical cores to quantify bone volume, integration, and mechanical strength. Collectively, these efforts advance HydroBone toward clinical translation as a next-generation therapeutic for musculoskeletal fracture repair and bone regeneration.

YAP and TAZ Mediate Mechanical Load-Induced Bone Adaptation and Osteocyte Mechanosensing

Yasaman Moharrer [1], Daniel Horan[2], Tala Azar[1], Annemarie Lang[1], Alexander Robling[2], X. Sherry Liu[1], Joel D. Boerckel[1].
[1]University of Pennsylvania, [2]Indiana University

Bone adapts to mechanical stimuli; however, the underlying mechanotransductive mechanisms remain poorly understood. We hypothesized that the transcriptional co-regulators YAP and TAZ mediate bone adaptation to mechanical loading. Deletion of YAP and TAZ from osteocytes has previously been shown to alter bone architecture and the lacunar–canalicular network. Therefore, we used pharmacologic approaches to acutely inhibit YAP/TAZ signaling in skeletally mature mice with normal developmental history.

Two orthogonal inhibitors were selected: verteporfin (VP), which blocks YAP/TAZ co-activation, and MGH-CP1 (CP1), which prevents TEAD binding to YAP/TAZ. Fourteen-week-old male C57BL/6 mice received i.p. injections of VP, CP1, or DMSO for two weeks. During treatment, the left tibiae were subjected to in vivo cyclic compressive loading (4 Hz, 1200 cycles/day, 5 days/week, 1200 με peak strain), while contralateral limbs served as non-loaded controls. Bone formation was quantified by microCT and dynamic fluorochrome labeling (calcein and alizarin complexone) at both cortical and trabecular sites.

Cyclic loading significantly increased cortical thickness in DMSO-treated tibiae, but this anabolic response was abolished by both VP and CP1. Neither loading nor YAP/TAZ inhibition significantly altered trabecular bone morphometry (BV/TV, Tb.Th, Tb.N, Tb.Sp). At the periosteum, loading increased mineralizing surface and bone formation rate, and this effect persisted despite YAP/TAZ inhibition. However, at the endosteum, both VP and CP1 eliminated the load-induced increases in mineral apposition and bone formation rate.

Cytoskeletal analysis of osteocytes further showed that mechanical loading markedly increased osteocyte dendritic branching in the femoral intercortex of DMSO-treated mice, while this response was abolished by VP and blunted by CP1. These findings align with the view that osteocyte dendritic processes serve as primary mechanosensors and that the actin cytoskeleton is a core transducer of mechanical cues into biochemical responses. Notably, loading increased branch number without altering cell oblatness or stretch, suggesting that adaptation primarily involves remodeling of the pericellular F-actin and dendritic networks rather than changes in overall cell body morphology.

Together, these results provide the first in vivo evidence that YAP and TAZ mediate the mechanotransduction of anabolic loading through cytoskeletal and osteocyte network remodeling. By blunting endosteal but not periosteal bone formation, pharmacologic YAP/TAZ inhibition uncovers regional differences in mechanosensitive signaling and highlights potential skeletal risks associated with anti-YAP/TAZ therapies in oncology.

Mechanical Stress and Heterotopic Ossification Progression in Fibrodysplasia Ossificans Progressiva

Diego Ocaranza Nuñez[1], Loreilys Mejias Rivera[1], Douglas Roberts[1], Eileen M Shore[1]
[1]Department of Orthopaedic Surgery and Center for Research in FOP and Related Disorders

Fibrodysplasia Ossificans Progressiva (FOP) is a rare genetic disorder affecting 1 in every 1-2 million people. In most cases, FOP caused by the *ACVR1*^{R206H} mutation, resulting in dysregulated BMP signaling and abnormal bone formation in skeletal muscle and other soft tissues. Heterotopic ossification (HO) in FOP is often triggered by soft tissue injury and progressively limits joint mobility. Previous clinical studies have suggested that limb immobilization after fractures in FOP patients is associated with less ossification than expected, suggesting that mechanical loading may promote HO formation. This concept was evaluated in this study using a FOP mouse model by inducing a defined muscle injury and comparing freely moving mice to mice with the injured limb immobilized. After 14 days, immobilized limbs demonstrated significantly lower HO volume at the injury site ($p=0.0008$) and lower overall HO compared to non-immobilized controls ($p=0.064$). However, immobilization was also associated with new HO at non-injury locations, mainly at the hip, but also at the shin. These results support mechanical offloading as a potential strategy to reduce HO in FOP, while indicating possible redistribution of ossification as a result of the immobilization approach.

Effect of Fluoride Treatments on Dental Implant Osseointegration in Mice

Eri McLaughlin, Hattanas Kumchai, Robert Diecidue, Ryan E. Tomlinson
Thomas Jefferson University, Philadelphia, PA

Introduction: Dental implants are widely regarded as the gold standard for replacing non-restorable teeth. However, implant failure remains a significant clinical concern, with reported failure rates of 4.4% at 5 years and 6.9% at 10 years. Early failures occur prior to prosthetic attachment and account for approximately half of all implant failures. The primary cause of an early failure is usually either failed osseointegration or an implant-associated infection. Our overall objective is to develop therapeutic strategies that can address both primary causes of implant failure. One promising avenue involves the use of fluoride-based agents, which possess both osteogenic and antimicrobial properties. In this study, we have explored two fluoride delivery systems: Silver Diamine Fluoride (SDF) and Sodium Fluoride Gel (NaF). SDF is a newer therapy designed to arrest dental caries by halting and reversing cavity progression. In contrast, NaF gel is a common and established treatment modality in the oral cavity.

Methods: Adult male and female C57BL/6J mice received titanium implants using an established submerged dental implant model. SDF, NaF, or PBS (control) were applied to the site immediately before implantation. The maxilla was harvested intact after either 2 or 4 weeks, fixed in neutral buffered formalin and then either stored in 70% ethanol at 4 °C or PBS-soaked gauze at -20 °C. Samples were scanned using a MicroCT (Bruker Skyscan 1275) at 10 micron resolution with scanning parameters of 100 kV and 100 uA and a copper filter. Analysis was conducted in a 1 x 0.5 mm (W, H) cylindrical region of interest centered on the implant. After MicroCT, samples were decalcified in 14% EDTA, sunk in 30% sucrose, and embedded in OCT for histology. Cryosections were stained using standard methods for H&E or TRAP. Imaging was performed using a Nikon E800 at 4x, 10x, and 20x magnifications and images were analyzed using FIJI. Statistical analysis was performed using Prism (GraphPad), with p-value less than 0.05 considered significant.

Results: MicroCT analysis of dental implants revealed a negative effect of SDF and positive effect of NaF on measures of osseointegration. Specifically, bone volume fraction (BV/TV) was significantly different in SDF-treated implants (-32%) and NaF-treated implants (+36%) as compared to PBS-treated controls. Similarly, bone volume (BV) was also significantly different in SDF-treated implants (-40%) and NaF-treated implants (+39%) as compared to PBS-treated controls. Histological evaluation revealed that osseointegration may be impaired due to significant fibrous encapsulation in SDF-treated implants. Specifically, we observed a significantly larger fibrous layer between implant and underlying bone in SDF-treated implants (+82%) as compared to PBS-treated controls.

Discussion: Although SDF has previously been used to powerfully arrest dental carries, no studies have considered dental implant association. In contrast, the application of NaF was previously shown to enhance osseointegration of titanium implants in a rabbit ulna model. In contrast to our hypothesis, our results show that application of SDF in a submerged dental implant model in mice results in less osseointegration. In contrast, NaF application significantly increased osseointegration measures. Therefore, future work will focus on the relative effects of these therapeutic strategies on cells present at the bone-implant interface as well as their role in mitigating implant-associated infection.

Determining the Role of NRF2 in NGF-TrkA signaling in Bone

Shaniqua Martin, Ryan E. Tomlinson

Department of Orthopaedic Surgery, Thomas Jefferson University, Philadelphia, PA 19107, USA

Introduction. Nuclear factor erythroid-2-related factor 2 (Nrf2) is a transcription factor that acts as a central regulator of the cellular stress response. In response to oxidative stress, Nrf2 translocates to the nucleus to initiate transcription of antioxidant response genes, such as Nqo1, Srxn1, and HO-1. Although Nrf2 generally opposes inflammation by turning NF-κB signaling down, recent studies have shown that NGF is a direct transcriptional target of Nrf2 in astrocytes and dermal macrophages. Our lab has previously shown that NGF-TrkA signaling is required for normal load-induced bone formation following osteogenic mechanical loading. Therefore, we hypothesized that Nrf2 expressed in the osteoblast lineage supports osteogenic mechanical loading by increasing NGF expression, potentially protecting against oxidative stress.

Methods. Male and female conditional knockout (CKO) mice were generating by crossing $Nrf2^{fl/fl}$ (Jax: #025433) mice or $Ngf^{fl/fl}$ (*courtesy Minichiello Lab*) with Osteocalcin-Cre (Jax: #019509) mice. $Nrf2^{fl/fl}$ or $NGF^{fl/fl}$ littermates without Cre were considered wildtype (WT). All mice were maintained on a C57BL/6J background and were used in accordance with the IACUC of Thomas Jefferson University (Protocol #02204). Axial forelimb compression of the right forelimb was performed using a material testing system (TA Instruments Electroforce 3200 Series III) with custom designed fixtures. For analysis of skeletal phenotype by microCT, the left and right femurs were dissected from Nrf2 WT and CKO adult mice and frozen at - 20°C in PBS-soaked gauze. Each bone was scanned using a Bruker microCT system fixed with a 1 mm aluminum filter, and with scanning parameters of 60kv, 166 μA at a resolution of 11.5 microns. To assess load-induced bone formation by dynamic histomorphometry, adult (16-18 weeks) male and female mice were given calcein (10mg/kg, Sigma C0875) on D3 and alizarin red s (30mg/kg, Sigma A3882) on D8 of the loading protocol by IP injection. Animals were euthanized on D10. The left and right ulnae from adult, male and female Nrf2 mice were harvested 4 hours and D7 after a single bout of compressive loading on D0 to extract RNA for gene expression analysis. The left and right ulnae from adult, male and female NGF mice were harvested 4 hours after a single bout of compressive loading for HPLC-UV and Protein Carbonyl.

Results. By dynamic histomorphometry, Nrf2 CKO mice exhibited a significant increase in osteoblast activation MS/BS (%) on the periosteal surface compared to WT controls. However, the mineral apposition rate (MAR) was similar between groups, indicating no change in individual osteoblast function. Trabecular bone analysis revealed a sex-specific effect with male CKO mice showing trends towards increased bone mass in which female mice showed no response. By microCT, cortical bone geometry was largely unaffected although minor increases were observed in male CKO mice. During three-point bending, male and female CKO groups had modestly higher Young's Modulus values, indicating a slight increase in bone stiffness. Male CKO femurs and both female groups ultimate bending energy was significantly increased in compared to the male WT counterparts. The trend continued for Toughness, Post Yield Toughness, and Post yield energy with the male WT mice having the lowest values while the CKO and female WT groups showed small but consistent increases. Finally, HPLC-UV and analysis of protein carbonyls were used to characterize the effect of oxidative stress following mechanical loading, focusing on the Glutathione Antioxidant system. First, we observed that 16-week-old adult mice have increased levels of GSH in the controlled left limb, compared to the right limb. GSSG levels are slightly elevated in the left control limb when compared to the loaded right limb. Next, the glutathione ratio shows a slight increase in the right loaded limb and decrease in the left limb. Results for the 52-week-old adult mice reveal that GSH and GSH/GSSG ratio values were decreased in the right loaded limb and the GSSG is increased.

Discussion. Contrary to our hypothesis and literature, mice lacking Nrf2 in the mature osteoblast lineage had enhanced response to osteogenic mechanical loading, particularly regarding mineralizing bone surface (MS/BS). As a result, the function of Nrf2 in the skeleton may be confined to early osteoprogenitors rather than mineralizing osteoblasts. Nonetheless, we find that osteogenic mechanical loading is associated with significant oxidative stress in the loaded limb. Thus, loss of Nrf2 in the mature osteoblast may activate a compensatory mechanism that enhances osteoblast activation in response to mechanical load. Future work will characterize the relationship of Nrf2 and NGF in load-induced bone formation as well as examine the role of NGF-TrkA signaling in protecting bone cells from load-induced oxidative stress.

Penn Center *for* Musculoskeletal Disorders
University *of* Pennsylvania

YOUR FEEDBACK IS IMPORTANT!

Please take a minute to complete the survey to help with future Symposiums

https://upenn.co1.qualtrics.com/jfe/form/SV_eQgmegtrvHV4aSa